INFORMATION TO USERS

This manuscript has been reproduced from the microfilm master. UMI films the text directly from the original or copy submitted. Thus, some thesis and dissertation copies are in typewriter face, while others may be from any type of computer printer.

The quality of this reproduction is dependent upon the quality of the copy submitted. Broken or indistinct print, colored or poor quality illustrations and photographs, print bleedthrough, substandard margins, and improper alignment can adversely affect reproduction.

In the unlikely event that the author did not send UMI a complete manuscript and there are missing pages, these will be noted. Also, if unauthorized copyright material had to be removed, a note will indicate the deletion.

Oversize materials (e.g., maps, drawings, charts) are reproduced by sectioning the original, beginning at the upper left-hand corner and continuing from left to right in equal sections with small overlaps. Each original is also photographed in one exposure and is included in reduced form at the back of the book.

Photographs included in the original manuscript have been reproduced xerographically in this copy. Higher quality 6" x 9" black and white photographic prints are available for any photographs or illustrations appearing in this copy for an additional charge. Contact UMI directly to order.

UMI

A Bell & Howell Information Company
300 North Zeeb Road, Ann Arbor MI 48106-1346 USA
313/761-4700 800/521-0600

Reproduced with permission of the copyright owner. Further reproduction prohibited without permission.

CAPILLARY INSTABILITY OF JETS

by

ANUJ CHAUHAN

A dissertation submitted to
the Graduate Faculty in Engineering
in partial fulfillment of the
requirements for the degree of
Doctor of Philosophy,
The City University of New York

1998

UMI Number: 9908303

UMI
300 North Zeeb Road
Ann Arbor, MI 48103

This manuscript has been read and accepted for the Graduate Faculty in Engineering in satisfaction of the dissertation requirements for the degree of Doctor of Philosophy.

9/17/98 David S. Rumschitzki

Date

David S. Rumschitzki

Co-Chair of Examining Committee

9/17/98 Charles Maldarelli

Date

Charles Maldarelli

Co-Chair of Examining Committee

Sept. 18, 1998 Mumtaz K. Kassir

Date

Executive Officer

Andreas Acrivos

Demetrios T. Papageorgiou

Yiannis Andreopoulos

Supervisory Committee

THE CITY UNIVERSITY OF NEW YORK

ABSTRACT

CAPILLARY INSTABILITY OF JETS

by

ANUJ CHAUHAN

Advisors:

Charles Maldarelli
David S. Rumschitzki
Demetrios T. Papageorgiou

This thesis studies the capillary instability of a compound jet. A compound jet comprises an inner core of a primary fluid surrounded by an annulus of an immiscible secondary fluid. The compound jet is unstable due to capillarity. A compound jet finds applications in a variety of fields, such as, ink jet printing, particle sorting, extrusion, molding, particle production etc. In some of these applications such as molding, the disturbances that could cause the jet breakup start as periodic spatial disturbances of Fourier wave number k and grow in time. This is the temporal instability. In some other applications, such as, ink-jet printing, the disturbances initiate at the edge of the nozzle from which the jet issues out. These disturbances grow in space. This is the spatial instability. At small velocities, even if the initial disturbances are periodic in time, they grow exponentially in time. This is the absolute instability. We perform the temporal, spatial and the absolute stability analysis of an inviscid compound jet in a unified framework using the theory of transforms. Further, we solve the temporal instability problem for a viscous jet to understand the effect of viscosity on breakup dynamics. In the temporal analysis, we show that each interface of the compound jet contributes one mode to the instability. The modes contributed by the inner and outer interfaces grow for waves longer than the inner and the outer circumference of the undisturbed jet, respectively. The inner interface mode has a higher growth rate and hence dominates the breakup. The two interfaces grow exactly in phase in this mode and hence it is refereed to as the stretching mode. The other mode is the squeezing mode because the two interfaces grow exactly out of phase. The same two modes are also present in the spatial analysis. At high Weber numbers the predictions of the spatial theory reduce to those of the temporal theory because the waves simply convect with the jet velocity and there is no dispersion. At Weber numbers below a critical value, the compound jet becomes absolutely unstable. There are three absolutely unstable modes and as the Weber number approaches zero, one of them is stabilized and the other two reach growth rates that are same as the maxima of the stretching and the squeezing modes in the temporal theory. Viscosity reduces the spatial and the temporal growth rates and also the critical Weber number. Experimentally, we verify the predictions of the spatial theory for a single jet at high and intermediate Weber numbers and observe a backward propagating modes at smaller Weber numbers which could signify absolute instability.

TABLE OF CONTENTS

PREFACE

In the Fall of 1993, when we began working on this research project, we were motivated to study the stability of compound jets due to their potential use in ink jet printers. The traditional ink jet printers create a single jet of the fluid ink that breaks due to surface tension. The resulting drops are moved around by application of rapidly varying electric field to generate the desired character on the paper. Due to the need of very small drops, one needs very small nozzles and this creates the problem of clogging. Hertz and Hermanrud during the course of an experimental investigation designed a printer based on compound jet in which the inner fluid is some colorless volatile liquid and the outer fluid is the ink. The nozzle is permanently inside the outer fluid, i.e., ink and thus there is no clogging.

We began our project by studying the temporal stability of an inviscid compound thread in the absence of gravity, which seemed to be the obvious first step towards modeling the flow coming out of the compound ink-jet printer. However, in due course, we first decided to include viscosity and later perform the spatial analysis, which is the more appropriate approach to solve the problem because the jet is moving in space and disturbances introduced at the nozzle tip grow axially.

Throughout the course of this work, we solve the stability problem as an initial value problem in the Fourier Laplace domain and invert the solution to the real space time domain. This is the same approach as adopted by many before us. Most available literature on such problems performs first the Fourier inversion followed by the Laplace inversion. Our dispersion equation being explicit in s(k) is ideally suited for performing the inversion the other way, i.e.. Laplace first followed by the Fourier. While investigators before us have adopted this approach, we did not find any literature on the intricacies involved in this method. This motivated us to construct the required theory for performing the above inversion. Not to our surprise and actually to our relief, we found that all the stability results do not depend on the route adopted for the inversion.

Having done the theoretical analysis we wanted to verify our results experimentally. Our efforts to find available experimental data on compound jets were fruitless. The only experiments that we found were a couple performed by Hertz and Hermanrud. This prompted us to develop an experimental setup to verify our results. While working on developing the experimental setup we realized that though there has been a lot of experimental work done on single jets there still remain a few gaps. First, most investigators used the temporal theory to compare the experimental results to the theoretical predictions. Second, the measurement of the wavelengths and the growth rates of the disturbances based on the breakup lengths or utilizing the disturbance at the maxima is not robust. Thirdly, it is known that the single jet is absolutely unstable, but the experimental evidence in this regard is lacking.

This prompted us to device a new method of measuring the wavelengths and growth rates based on digitization of the jet images, use the convective theory while comparing the theory to the experiments and to attempt to observe the onset of absolute instability in a single jet. In the process we also desired to develop a setup in which one could obtain a good control on the breakup size and the breakup length of the jet on-line.

The first chapter of the thesis is devoted to the literature review and an introduction to the main issues involved in the problem. In the second chapter we solve the temporal problem for a viscous and an inviscid compound jet. The third chapter is devoted to solving the spatial problem for an inviscid compound jet. In the forth chapter we investigate the absolute instability of an inviscid compound jet. The fifth chapter contains the experimental technique to measure the wavelengths and growth rates. It also compares the experimental results to theory and shows that the breakup size of the jet can be controlled precisely on-line. In the last chapter we investigate the experimental manifestation of the absolute instability in a single jet. We observe backward propagation of very short waves, which is ascribed to absolute instability.

ACKNOWLEDGEMENT

First and foremost, I would like to thank my advisors for making this research, 'a very pleasant experience'. I am extremely grateful to Charles, David and Demetrios for giving me a lot of freedom while at the same time being very helpful and encouraging. They not only taught me lessons of Chemical Engineering but also plenty of equally important lessons of life. I would also like to express my gratitude for Professor Andreas Acrivos for agreeing to be a part of my thesis committee. His presence at City College is a source of inspiration for all of us.

In addition, I want to thank the entire faculty of the Chemical Engineering department for being very friendly and helpful.

I also want to thank Andy Eng and Xu for their help in setting up the experimental apparatus.

I had a very pleasant stay at City College. For this I need to thank all my friends especially Sharona, Anubhav, Mayank, Jana, Stephanie, Deepti and all the other graduate and undergraduate students at City College.

Finally I want to thank my family whose love and affection from millions of miles away has been a constant source of strength and motivation. I love you all.

LIST OF FIGURES

CHAPTER II

CHAPTER III

CHAPTER IV

CHAPTER V

CHAPTER VI

CHAPTER 1

INTRODUCTION

A liquid thread is unstable to axisymmetric interfacial disturbances due to destabilizing capillary forces. The linear stability of a base state consisting of a doubly infinite, circular, inviscid, liquid thread with tension σ. radius a and density ρ was first studied by (Rayleigh 1879). Rayleigh analyzed the temporal instability of this base state by imposing, at t=0, an interfacial disturbance with Fourier wavenumbers k and n in z and θ directions, respectively. He determined the evolution of this initial disturbance using normal modes ($e^{i(kz+n\theta)+s(k,n)t}$, where z is along the thread axis and s(k,n) is complex). Rayleigh established that only axisymmetric (n=0) wavelengths ($2\pi/k$) larger than the undisturbed thread circumference ($2\pi a$) grow in time ($s_r(k,n=0) > 0$), and that there is a maximum in the growth rate at a wavenumber (k_m) equal to 0.696/a. The disturbances grow without traveling, (s_i ($k \leq 1/a, n=0$)=0). The circumferential curvature destabilizes the jet and the longitudinal curvature stabilizes it. If the waves are longer than the jet circumference, the circumferential curvature is bigger than the longitudinal curvature. Hence, it dominates and makes the jet unstable. If the waves are shorter than the jet circumference the longitudinal curvature dominates and hence, stabilizes the jet. It can also be argued that for waves longer than the jet circumference, the surface area of the disturbed jet is less than the surface area of the base state of undisturbed jet. Hence, growth of disturbances leads to a decrease in surface area and hence a reduction in surface energy. This causes the jet to be unstable to waves with wavelength longer than the jet circumference.

The temporal stability of the static thread was reconsidered for the case in which the thread fluid is viscous (Chandrasekhar 1961), and is surrounded by a second immiscible viscous liquid (Tomotika 1935). As capillarity drives the instability, the range of unstable wavelengths remains the same when viscous effects are included, but growth rates are reduced and maximally growing waves are shifter to longer wavelengths. All the above studies were done by using the normal mode analysis. Berger (1988) carried out the stability analysis of a single jet as an initial value problem and concluded that the normal mode analysis, in certain circumstances, predicts incorrect breakup times; he corrected it with the initial value formulation.

The temporal linear stability of static threads finds applications in predicting the collapse of liquid bridges, particularly in microgravity contexts where fluid tethers and bridges arise naturally, or polymer processing of thin walled-molds in terrestrial applications where the high viscosity of the polymer permits free standing annular threads as the configuration sets. But the primary motivation for the analysis of the capillary stability of threads is its application to the breakup into drops of jets emerging from nozzles. In this case disturbances continually imposed at the nozzle tip (either intentionally through periodic oscillations, or through tip imperfections) grow by the destabilizing capillary action as they are convected downstream, until they cause the jet to breakup into drops. Drop breakup from jets is important in the technological processes of atomization, ink jet printing (Sweet 1964), fuel injection, particle sorting (Hertzberg et al. 1976) and polymer fiber spinning (where it is desirable to arrange for reduced growth rate so that the jets can polymerize before breakup).

To be more applicable to the breakup of a jet into drops, the temporal analysis of the static thread base state can be changed to a thread translating with velocity V. For the static thread base state, unstable waves grow with no dispersion; for a uniformly translating jet base state it is easy to show that the growing disturbances therefore simply convect with the velocity V ($s_i(k)=-ikV$) and with the same growth rate ($s_r(k)$). Based on this analysis, one could conclude that the spatial growth of disintegrating jets is $e^{(sr(k)/V)z}$, where z is the distance from the nozzle tip. However, as first suggested by (Keller et al. 1973), the fact that the disturbances are continually imposed on the jet should be accounted for in the stability analysis. He suggested a base state in which the jet is modeled as a circular (doubly) infinite jet moving with uniform velocity, and interfacial disturbances are imposed locally in space (z=0, for example) and periodic in time with Fourier frequency modes ω. For an inviscid jet and axisymmetric disturbances, Keller et al. determined the spatial growth for the harmonic response ($e^{ik(\omega)z+i\omega t}$; $k(\omega)$ complex, $k_i<0$ for spatial growth) as a function of the Weber number ($W=\rho V^2 a/\sigma$). Keller et al. demonstrated that for W>3.2 and dimensionless frequencies or Strouhal numbers ($\omega a/V$) between zero and approximately one (the cutoff being a function of W), the localized periodic disturbances grow axially. Thus the spatial analysis allows for the calculation of stable and unstable frequencies. For frequencies in the unstable range, the drop size and distance to breakup can be predicted (assuming the linear theory is valid up to break-up; see the experimental verification discussed below) since the drops which are formed then have size which scales as $1/k_r(\omega)$, and the distance downstream from breakup is of order $1/k_i(\omega)$.

For W<3.2, a change in form of $k_i(\omega)$ was observed by Keller *et al*. (Leib and Goldstein 1986b) demonstrated that below this value of the Weber number, growth in time as well as space occurs owing to a pinch singularity of the dispersion equation, and the jet is absolutely unstable with the harmonic response augmented by temporal growth at a particular k^* ($e^{ik^*z+s^*t}$, $\mathrm{Re}(s^*)>0$) The curve $k_i(\omega)$ is then discontinuous, only part of Keller et al.'s branch is valid, and is joined by a second branch. Further studies by (Leib and Goldstein 1986a) examined the effect of fluid viscosity, and demonstrated that the critical Weber number (above which the instability is convective and below which it is absolute) decreases with decreasing Reynolds number ($Re = \rho Va/\mu$). (Lin and Lian 1989) demonstrated that for a viscous jet (for fixed Re), the critical Weber number increases as the density of the surrounding phase (treated as an inviscid gas) increases.

Keller et al examined asymptotically the convective instability for large Weber number, and found that in this limit $k_r(\omega) = \omega/V$ and $k_i(\omega) = -s_r(k_r)/V$, where $s_r(k_r)$ is the temporal growth rate function. Thus the disturbance travels downstream with the base velocity (and no dispersion), and grows with the temporal growth rate. Therefore in this limit, for a given frequency, we would expect drops to form with a size scaling as V/ω and a distance downstream from the orifice of order $1/(-k_i) = V / s_r(\omega/V)$. Hence in the limit of large Weber number, the temporal analysis is sufficient in determining the wavelength and break-up length of the jet issuing from an orifice, although it cannot give insight into absolute instability. In particular, for the case in which the jet is subject to a broad range of frequencies, the frequency corresponding to the wavenumber which grows the fastest will dominate, the size of the drops will be of order $1/k_m$ of the temporal analysis and the distance downstream from breakup of order $V/s_r(k_m)$.

A large body of experiments studying the breakup of jets into drops have been undertaken, usually with a sinusoidal periodic disturbance of frequency ω applied at the nozzle tip (see particularly, (Donnelly and Glaberson 1966), (Goedde and Yuen 1970), (Rutland and Jameson 1970), (Taub 1976), (Pimbley 1976), (Chaudhary and Maxworthy 1980b), (Kowalewski 1996) and the review monograph by (Yarin 1993).) These studies (usually at sufficiently high Weber numbers so that the flow is convectively unstable and $k_r = \omega/V$ and $k_i\ V = -s_r\ (k_r)$) have verified that the visible growing waves have wavenumbers equal to ω/V, and that the distance to breakup correlates well with $|k_i^{-1}| = -V/s_r\ (k_r)$ with the temporal rate given by the inviscid result since at these high velocities viscous effects are usually negligible. Although the breakup process is clearly nonlinear, the surprising reach of the linear theory when a single harmonic is applied is usually attributed to the fact that the influence of additional harmonics generated through nonlinear effects, usually arise only very near the break-off point.

The fine structure of the jet at breakup involves the formation of thin ligaments, which attach the main body of the jet to the detaching drops. These ligaments snap to form a satellite drop in addition to the main drop. Satellite formation and the ligament dynamics is beyond the scope of linear theory. Attempts to describe this structure have been undertaken using weakly higher order expansions in the interfacial deformation ((Wang 1968), (Yuen 1968), (Nayfeh 1970), (Lafrance 1975) and (Chaudhary and Redekopp 1980)) , and these have been shown to predict satellites and agree with observations of satellite sizes (Rutland and Jameson 1970) and (Chaudhary and Maxworthy 1980b). Other efforts at describing the structure at breakup have focused on developing one dimensional fully nonlinear equations for a jet either through (1) a perturbation in orders of the radius to the disturbance lengthscale (Lee 1974), (Pimbley and Lee 1977), (Ting and Keller 1990), (Schulkes 1993), (Eggers and Dupont 1994), and (Bechtel et al. 1995), or (2) from a director (Cosserat) continuum theory (Bogy 1978), (Bogy 1979). Still other efforts have resorted to direct numerical computations, or the examination of finite time singularities.

This thesis studies the capillary driven linear instability of compound threads and jets. In its base state, a compound thread comprises an inner core fluid of radius R_1 surrounded by an annulus of another immiscible fluid with radius R_2. Two interfaces provide destabilizing capillary forces which can cause unstable fluid motions and drop formation: The inner interface between the two immiscible liquids has interfacial tension σ_1 and the outer liquid/gas surface has surface tension σ_2 . Compound jets find application in the same fields as single jets, but they has the added flexibility of having two fluids and two interfaces whose physical properties can be manipulated in order to get the desired drop breakup size and breakup distance from the nozzle. The initial motivation for stability studies of compound jets was (Hertz and Hermanrud 1983) investigation of these jets for improving ink jet printing. Their experiments showed that the compound jets are unstable to varicose and sinuous instabilities besides the capillary instability, which apparently arise from large internal shear forces in the fluids. But low velocities favor the capillary instability. Current interest in compound jets arises from the use in the production of compound fibers, and compound spherical particles.

The temporal stability of a compound static thread was first studied in the limit in which the core and annular fluids were inviscid, and the axial velocity and pressure in both the fluids are independent of the radial and the azimuthal directions. Sanz and Masseguer (Sanz and Masseguer 1985) and Radev and Shkadov (Radev and Shkadov 1985). These one dimensional temporal analysis for axisymmetric disturbances found that there are two growing modes: One mode is driven by the destabilizing capillary forces at the outer surface R_2, and becomes unstable for wavelengths larger than the outer circumference, and the second is driven by the inner interface (R_1) and is unstable to the longer waves greater than this circumference. Sanz and Masseguer (Sanz and Masseguer 1985) demonstrated that the mode driven by the inner interface has an amplitude ratio, which is positive indicating a stretching vibration, while the mode driven by the outer interface has a negative amplitude ratio, and hence is a squeezing vibration. Both (Sanz and Masseguer 1985) and (Radev and Shkadov 1985) found that the growth rates of the stretching mode as a function of the wavenumber are much larger than those of the squeezing mode, so that the stretching mode dominates the linear dynamics.

Inclusion of viscous effects, and full axisymmetric motion (i.e. radial as well as axial motions) in a temporal linear stability analysis was undertaken by (Radev and Tchavdarov 1988) and by (Shkadov and Sisoev 1996) for a base state of a circular compound jet moving with a uniform velocity V. As with the one-dimensional analysis, the jet becomes unstable to the stretching mode, with unstable band ($0<k<1/R_1$), and the squeezing mode with band ($0<k<1/R_2$). The disturbances were found to convect with the base velocity ($s_i=-ikV$). These studies examined the dependence of the growth rate curves ($s_r(k)$) on the surface tension ratio ($\gamma=\sigma_2/\sigma_1$), and the ratios of the densities and viscosities of the annular fluid to the core ($d=\rho_2/\rho_1$) and ($m=\mu_2/\mu_1$), respectively) for values of γ, d and m in the range of approximately .1 to 10. The results indicate that the wavenumbers for maximum growth are particularly sensitive to the density and surface tension ratios, with k_m decreasing for increasing γ or decreasing d. The dependence of the viscosity ratio was found to be much less sensitive, although the maximum growth rate is reduced significantly with increasing viscosity ratio. The important inference from these results is that the density, viscosity, and surface tension ratio may be used to tune the drop size or the breakup distance in a compound jet subject to broad frequency (wavenumber) disturbances, thus allowing one to take advantage of the intended versatility of the second phase which the compound jet affords. Radev and Tchavdarov (Radev and Tchavdarov 1988) and Shkadov and Sisoev (Shkadov and Sisoev 1996) do not provide calculations of k_m or the maximum growth rate s_m as a function of the system ratios. More importantly, few calculations are presented on the ratio of the amplitudes of the outer interface disturbance to that of the inner interface at k_m. (This ratio, denoted as amp_m, is, in the temporal analysis, fixed by the eigenfunctions of the normal modes.) The amplitude ratio at k_m is important in determining how the compound jet breaks up through the stretching mode, assuming linear theory is applicable to the breakup point, and the jet is subject to a wide enough spectrum of frequencies so that this wavenumber can be realized. Radev and Tchavdarov (Radev and Tchavdarov 1988) note that the distance to the first breakup point is given by the minimum of L_1 and L_2 where $L_1 = [V/s_r(k_m)] \ln(R_1/\xi_1)$ and corresponds to core breakup first, and $L_2 = [V/s_r(k_m)] \ln((R_2 - R_1)/(\xi_2 - \xi_1))$ and corresponds to the annular fluid breaking first. (Here ξ_1 and ξ_2 are the amplitudes of the inner and outer interface, respectively, at $z=0$.) The former is ideal for composite drop production since it leads to the formation of drops of core liquid in a continuous phase of the annular fluid first, and then to composite drops as the outer interface snaps-off. Snap-off of the film first is problematic for composite formation since the subsequent snap-off of the core may not lead to composite drops unless the annular liquid rapidly wets the core fluid after the core finally breaks. In any case, conditions under which the amplitude of the inner interface is much larger than that of the outer interface ($amp_m<1$) are those favorable for composite formation and knowledge of how the tension, viscosity and density ratios control amp_m would technologically be quite instructive. Radev and Tchavdarov (Radev and Tchavdarov 1988) provide only a dependence on the tension ratio, and while (Sanz and Masseguer 1985) provide a more complete study, it is for their one dimensional inviscid model. All the studies on compound jets only analyzed the temporal instability.

The aims of this thesis are twofold, firstly to develop the temporal and the spatial theory for a compound jet and secondly to experimentally verify the theoretical predictions of the stability analysis of the jet in all the velocity regimes. We expect and we shall later show that the basic physics and the mechanisms of instability are the same for the single and the compound jet. Thus, we choose to use a single jet in our experiments for the purpose of verifying the theoretical results.

This thesis is divided into four chapters. The present chapter contains the introduction and the literature review. In the second chapter we discuss the temporal instability of an inviscid and a viscous jet and compare the theory with available experimental data. In particular we attempt to understand the stability mechanisms and the effect of the presence of two interfaces. We believe that the presence of the second liquid presents us with manipulatable variables which if controlled properly can result in the desired breakup characteristics, namely, breakup size and breakup times. Thus, we study the effect of all the system parameters on the stability characteristics. In temporal applications, it is not a common and certainly not an easy practice to impose specific wavelength disturbances. Thus, the breakup is usually on account of the growth of disturbances introduced by the noise. In the presence of wide band disturbances, such as random noise, the system follows the breakup dynamics of the fastest growing mode. Hence, we focus on the effect of system parameters on the fastest growing mode. We also develop thin film and long wave asymptotic expressions. These expressions in addition to verifying the numerics serve as starting tools for the non-linear simulations. These also help us understand the mechanism of the instability and the effect of various physical properties on the stability. We perform the temporal stability analysis for viscous and inviscid fluids. Thus, we can compare the results from the two simulations to see the effect of viscosity on the stability characteristics. In the third chapter we analyze the spatial instability of an inviscid jet and compare the available experimental results to the spatial theory. This is the first attempt in literature to analyze the spatial instability of a compound jet. The stability problem is solved in the Fourier Laplace domain and inverted to the real space time domain. Following Briggs, we first invert the Fourier transform followed by the Laplace transform. We compare the results of the spatial analysis to those of the temporal analysis that we obtain earlier in Chapter II. As mentioned earlier, Keller ascertained that for a single jet, one of the spatial roots merge with the temporal solution at high velocity. However, according to him, the root that merges with the temporal solution is not the fastest growing mode. He hypothesized that the modes with the faster growth have much longer wavelengths and the finite length of the jet prevents the manifestation of these modes. We first check the validity of this hypothesis and show that the modes which Keller considered to be the faster growing modes are actually evanescent modes, i.e., they should not be included in the inversion and hence do not contribute to the instability. We further resort to asymptotic analysis and numerical simulations to verify if the compound jet behaves in a similar manner, i.e., the spatial modes merge into the temporal modes at high jet velocities. The spatial analysis of an inviscid single jet predicts that it becomes absolutely unstable below a critical Weber number of approximately 3.2. One would expect the compound jet to do likewise. We reduce the Weber number in our spatial analysis of the compound jet to see if we do obtain a 'pinch' type of a singularity that gives rise to the exponential growth in time, i.e., the absolute instability. The origin of absolute instability can be detected either in the k plane by locating the pinch singularity or in the s plane by cusp formation. We use both the mappings to detect the absolute instability and verify that they are equivalent. We show that the compound jet is absolutely unstable below a critical Weber number, which is a function of the system parameters. Having established that the compound jet is absolutely unstable, we analyze the absolute instability in greater details in the next chapter. In all the studies involving absolute instability of jets, the authors only concentrated on obtaining the critical velocities, i.e., the velocities below which the jets become absolute unstable. No attempt has yet been made to follow the instability below the critical velocity and observe how the stability characteristics of the absolute instability change. We follow the merging patterns in the k plane below the critical velocity and show that there are multiple absolutely unstable modes. Each of the modes possesses a different absolute growth rate. The mode with the highest of these growth rates will dominate at any given Weber number. Interestingly, the behavior of some of these modes changes from being absolutely unstable to being not absolutely unstable in certain ranges of Weber numbers. We also note that different modes are dominant in different ranges of Weber numbers. Further, we calculate the phase velocity of the dominant absolutely unstable wave and compare it with the velocity of the maximally growing convective wave. We also compare the wavelengths of the absolutely unstable and the fastest convectively unstable waves. We make these comparisons to ascertain how easy it would be to differentiate between the absolutely unstable and the convectively unstable waves and to find out the conditions best suited to experimentally observe absolute instability in a compound jet. In this chapter too, we solve the problem in the Fourier Laplace domain and invert the solution to the real space time domain. But here while performing the inversion we invert the Laplace inversion first and then the Fourier inversion. We expect that the order of inversion should not affect the final solution. We compare our solution obtained this way with the one obtained by following Briggs, i.e., Laplace inversion first and then the Fourier inversion. We do this comparison to verify that the order of inversion is immaterial. In the next chapter we compare our experimental findings with theoretical results for single jet instability. Although a wealth of experimental data is available for single jets, some of the issues pertaining to the stability analysis remain unresolved. One of them is the experimental manifestation of absolute instability. Also, most of the experimental studies on the jets have focused on the temporal instability. In the last chapter of the thesis, we discuss our experimental findings in context to the temporal, spatial and absolute instability of a single jet. We develop a setup in which we can attenuate the base state of a jet coming out of a nozzle with periodic disturbances. The frequency and the amplitude of the input disturbance can be varied to study the effect of frequency modulation on the stability characteristics. Our study differs from the previous experimental studies in atleast two regards. Firstly, we compare our experimental results to the spatial predictions. The previous studies assumed that the waves introduced at the nozzle tip convect with the jet velocity. Thus the frequency of the oscillations is related to the wavelength of the waves by the relation, $V=\omega/k_r$. The temporal analysis was then used to obtain the temporal growth rates which were related to the spatial growth rates by $s_t=|k_i|V$. These results are true only at high velocities. Secondly, most of the earlier studies relied on measuring the breakup length to obtain the spatial growth rates. We develop a new method of using the entire jet profile to measure the growth rates. This serves two purposes. First it gives a more reliable value of the spatial growth rate and second it serves as a tool to verify if the jet profile is similar to that predicted by the linear stability analysis. It would not be entirely unexpected if that were not the case because the measurements are made in a non-linear regime. However, the fact that the growth rates obtained by linear analysis agree well with the experimental values suggests that inspite of being in the non-linear regime, the jet profile predicted by the linear analysis might also be in agreement with the experimental profile. This has not been verified in the past. Our method of measurements of the axial growth rates allows this comparison. We also vary the jet velocity and the fluid comprising the jet to investigate the jet behavior in different Weber number regimes. In our theoretical analysis, we neglect gravity. In the experiments, we analyze the effect of gravity to find out if gravity has a significant effect. We also develop a simple model to predict the effect of gravity on the base state of the jet. In addition, we analyze the velocity profile of the jet as it exits from the needle tip. Inside the needle it is in poiseuille flow and as it comes out the profile slowly relaxes to the plug flow. The model that we develop in this transition region predicts the radius of the jet as it relaxes to the plug flow and the distance it travels before it relaxes to the plug flow. Finally, in the last chapter, we reduce the Weber number of the jet to below the critical Weber number to observe the experimental manifestation of absolute instability. We see a remarkable difference in the region near the breakup on lowering the Weber number. This could potentially be the absolute instability. We also propose an alternative explanation to account for this different behavior in the small Weber number regime.

CHAPTER 2

TEMPORAL INSTABILITY OF A COMPOUND THREAD

I. Introduction

A single jet is unstable due to capillarity, i.e., disturbances introduced either at the interface or in the bulk will grow. The stability analysis of single jets has been approached in two different ways:(1) The jet is modeled as a doubly infinite thread, either at rest or moving with a constant velocity. In this scenario, periodic disturbances are introduced to the jets' interface at t=0 and are followed in time. This is the temporal instability. The disturbances grow as $e^{ikz+s(k)t}$. The jet is unstable if Real(s(k)) is positive. (2) The jet is modeled as a cylinder of liquid issuing out of an orifice. In this formulation, time periodic disturbances are introduced at some spatially localized position and are followed in space as they convect with the jet. The disturbances grow as $e^{ik(s)z+st}$; $s=i\omega$. The disturbances grow if Imag (k)<0 for z>0 {The source is assumed to be located at z=0}. This is the convective or the spatial instability.

In this chapter we analyzed the temporal instability of a compound thread or a jet traveling with a uniform velocity. In its base state, a compound thread comprises an inner core fluid of radius R_1 surrounded by an annulus of another immiscible fluid with radius R_2. Two interfaces provide destabilizing capillary forces which can cause unstable fluid motions and drop formation: The inner interface between the two immiscible liquids has interfacial tension σ_1 and the outer liquid/gas surface has surface tension σ_2.

The temporal linear stability of static threads finds applications in predicting the collapse of liquid bridges, particularly in microgravity contexts where fluid tethers and bridges arise naturally, or polymer processing of thin walled-molds in terrestrial applications where the high viscosity of the polymer permits free standing annular threads as the configuration sets. In addition, given the spatial analysis of Keller et al., which established the equivalence of the spatial and the temporal analysis at high Weber numbers, the temporal analysis is also relevant in context to the breakup of fast flowing jets.

This chapter is divided into two parts. In the first part we analyze the instability of an inviscid compound thread. All the previous studies cited above used normal modes to analyze the temporal instability. We model the stability problem as an initial value problem and solve it in the Fourier Laplace domain and invert the solution to space time domain. We examine the effect of various system parameters on the stability characteristics. We develop the long wave asymptotic expressions, which serve as a check on numerics and can also serve as useful tools to initiate non-linear analysis. We will examine the limit of thin annular films $(R_2 - R_1)/R_1 = \varepsilon << 1$, in order to develop analytic asymptotic equations for the growth rates. These type of calculations, not as yet undertaken in the literature, serve several uses apart from being directly applicable to technologies which use thin annular fluids: First, because they are analytic, the expressions help in understanding the mechanism of the instability. They also differentiate the physics of the two growing modes. Second, the thin film expansions also serve as the starting point of the weakly non-linear evolution of the instability (Papageorgiou 1993). An outline of either section is as follows. The linear stability equations are presented first in the Stability Formulation section. We develop the temporal problem as an initial value problem and compare it with normal mode analysis. (The idea of treating the stability problem as an initial value problem has been used successfully by (Prosperetti 1980), and (Berger 1988)). In the next section, we detail the asymptotics for thin annular films, and the long wave asymptotics, discuss compound threads with order one annular thickness, and detail the dependence of the stability curves on the tension, viscosity and density ratios for the viscous and on the tension and density ratios for the inviscid compound jet. Finally, we compare the available experimental data in literature with the inviscid and the viscous temporal theories that we develop in this chapter.

The aims of our study, as differentiated from those already in the literature, are as follows: (i) As we have already discussed, previous calculations of $s_r(k)$ by (Radev and Tchavdarov 1988) and by (Shkadov and Sisoev 1996) have indicated that maximum growth rates and wave numbers for maximum growth are sensitive to the viscosity, density and tension ratios. However simulations of s_m and k_m were not undertaken. Our focus will be on calculating these dependencies so that it will become clear how to use the second fluid of a compound jet to tune drop size and breakup distances from the nozzle tip. (ii) Detailed calculations will be presented of the amplitude ratio amp_m of the maximally growing wave as a function of the system ratios so that it will be easier to predict the sequence by which the dominant stretching mode breaks up. As we have mentioned, for composite particle formation, it is desirable to have the core snap first, which will be favored by large amplitudes of the inner interface relative to the outer surface ($amp_m < 1$). As we discussed above, the amplitude ratio has only been studied in detail by (Sanz and Masseguer 1985) for their one dimensional inviscid model.

II.I TEMPORAL ANALYSIS OF AN INVISCID COMPOUND THREAD

II.I.I Formulation of the linear stability theory

Governing equations and boundary conditions

A doubly infinite jet of an inviscid fluid A, of density ρ_1 is surrounded by a coaxial annulus of an immiscible inviscid fluid B, of density ρ_2 (figure 1.1 pg. 65). Choose a cylindrical coordinate system (r, θ, z), whose z axis is coincident with the fluid cylinder's axis. We neglect gravity in our analysis. The compound jet is moving in a vacuum with a uniform velocity in the positive z direction. The undeflected inner interface is $r=R_1$ and the outer interface is $r=R_2$. The interfacial surface tensions are σ_1 and σ_2, respectively. We will solve the problem in a reference frame moving with the jet velocity, with respect to the stationary lab frame. Thus, in our moving frame, the jet is stationary and is like a compound thread. The dimensionless equations of motion and continuity are:

$$\beta_i \frac{D\, v_i}{Dt} = -\nabla\, P_i \qquad (1.1)$$

$$\nabla \cdot v_i = 0 \qquad (1.2)$$

(i=1,2)

where in fluid i, P_i is the pressure and $\mathbf{v}_i$ is the velocity vector. In the governing equations and the boundary conditions, we non-dimensionalize lengths by $[R_1]$, time by $[(\sigma_1/\rho_1 R_1^3)^{-1/2}]$, pressure by the surface tension pressure $[\sigma_1/R_1]$ and velocity by $[(\sigma_1/\rho_1 R_1)^{1/2}]$. The dimensionless parameters are $a=R_2/R_1$, $\gamma=\sigma_2/\sigma_1$, $\beta_2=\beta=\rho_2/\rho_1$ and $\beta_1=1$. The interfaces are denoted by $r=h_i(z,t)$. Define the mean curvature H_i of interface i (i=1,2) by,

$$2H_i = -\frac{1}{h_i(1+h_i'^2)^{\frac{1}{2}}} + \frac{h_i''}{(1+h_i'^2)^{\frac{3}{2}}} \tag{1.3}$$

Aside from the centerline condition ($\mathbf{v}_i$,P finite at r=0), the boundary (the jump in normal stress and the continuity of velocity) and kinematic conditions in dimensionless form are:

$$[[P]]_i = 2H_i\gamma_i \text{ at } r = h_i(z,t) \quad i = 1,2 \tag{1.4}$$

$$[[n.v]]_i = 0 \text{ at } r = h_i(z,t) \quad i = 1,2 \tag{1.5}$$

$$[\frac{\partial}{\partial t} + v_i.\nabla](r - h_i) = 0 \text{ at } r = h_i(z,t) \quad i = 1,2 \tag{1.6}$$

where $[[\ ]]_i$ denotes the difference between inside and outside of interface i and **n** is the vector normal to the interface.

In the base state there is no forcing disturbance in the bulk and the interfaces are undeflected. Let u and w denote the radial and axial velocities, respectively. Any solution of the form, w=F(r), where F is completely arbitrary, satisfies the base state equations (1.1)-(1.6) exactly. Since we are interested in capillary driven instabilities, we restrict the analysis to the solution in which w=constant in the same in both the core and the annulus. With this assignment, there is no slip at the interface, thereby preventing the Kelvin Helmoltz type of instability. Thus, we concentrate on the base state:

$$u_i^0 = 0, \quad w_i^0 = V; \qquad i = 1,2 \tag{1.7}$$

$$P_2^0 = \frac{\gamma}{a}, \qquad P_1^0 = 1 + \frac{\gamma}{a} \tag{1.8}$$

If a small (~ λ), <u>axisymmetric</u> disturbance is introduced into the jet, the disturbances to the velocities and the interface from the base state are also of order λ. For i=1,2, we have

$$v_i(r,z,t) = (0,V) + v_{i,1}(r,z,t)\lambda + O(\lambda^2) \tag{1.9}$$

$$h_1(z,t) = 1 + \zeta_1(z,t)\lambda + O(\lambda^2) \tag{1.10}$$

$$h_2(z,t) = a + \zeta_2(z,t)\lambda + O(\lambda^2) \tag{1.11}$$

$$P_i(r,z,t) = P_i^0 + P_{i,1}(r,z,t)\lambda + O(\lambda^2) \tag{1.12}$$

Substituting these in the governing equations. one gets the leading order equation for the perturbation quantities,

$$\beta_i\left(\frac{\partial v_i}{\partial t}\right) = -\nabla P_i \tag{1.13}$$

$$\nabla . v_i = 0 \tag{1.14}$$

where we delete subscript 1 for simplicity. We choose the origin to coincide with the location of source; thus z_0=0.

In the temporal analysis the instability is initiated by the initial conditions. In our moving reference frame, we choose the initial conditions:

$$v_i(r,z,0) = 0; \zeta_i(z,0) = \zeta_{i,0}(z) \tag{1.15}$$

Taking the divergence of the momentum balance and using the equation of continuity, we get

$$\nabla^2 P_i = 0 \tag{1.16}$$

We shall now take the Fourier Laplace transform of the equation.

Define the transforms as

$$\hat{f}(k) = \int_{-\infty}^{\infty} f(z) e^{-ikz} dz \tag{1.17}$$

$$\tilde{f}(s) = \int_{0}^{\infty} f(t) e^{-st} dt \tag{1.18}$$

In the transformed domain, the pressure equation is,

$$\frac{d^2\tilde{\hat{P}}}{dr^2} + \frac{1}{r}\frac{d\tilde{\hat{P}}}{dr} - k^2\tilde{\hat{P}}_i(r,k,s) = 0 \tag{1.19}$$

where $\tilde{\hat{P}}_i$ is the pressure in the Fourier-Laplace domain. The general solution of (1.19) is,

$$\tilde{\hat{P}}_i = A_i I_0(kr) + B_i K_0(kr) \tag{1.20}$$

where I_o and K_0 are the modified Bessel functions of order 0 and A_i, B_i are constants of integration which can be functions of k and s.

The boundary and kinematic conditions (1.4-1.6) in dimensionless form in the Fourier-Laplace domain are:

$$\tilde{\hat{P}}_1 - \tilde{\hat{P}}_2 = -(1-k^2)\tilde{\hat{\zeta}}_1 \quad \text{at } r = 1; \tag{1.21}$$

$$\tilde{\hat{P}}_2 = -\gamma\left(\frac{1}{a^2} - k^2\right)\tilde{\hat{\zeta}}_2 \quad \text{at } r = a; \tag{1.22}$$

$$\tilde{\hat{u}}_2 = s\tilde{\hat{\zeta}}_2 - \hat{\zeta}_{2.0} \quad \text{at} \quad r = a \; ; \tag{1.23}$$

$$\tilde{\hat{u}}_1 = s\tilde{\hat{\zeta}}_1 - \hat{\zeta}_{1.0} \quad \text{at} \quad r = 1 \; ; \tag{1.24}$$

$$\tilde{\hat{u}}_1 = \tilde{\hat{u}}_2 \quad \text{at} \quad r = 1 \tag{1.25}$$

The velocity and pressure are finite at r=0.

Upon solution of the equation of motion in the r direction to get $\tilde{\hat{u}}_1$ and substitution of $\tilde{\hat{P}}_1$ and $\tilde{\hat{u}}_1$ into the boundary conditions, the solution takes the form, A(k,s)**x**=**b**(k,s), where

$$A(k,s) = \begin{vmatrix} I_1(k) & -\dfrac{I_1(k)}{\beta} & \dfrac{K_1(k)}{\beta} & 0 & 0 \\ \dfrac{kI_1(k)}{s} & 0 & 0 & s & 0 \\ 0 & \dfrac{kI_1(ka)}{s\beta} & \dfrac{-kK_1(ka)}{s\beta} & 0 & s \\ 0 & I_0(ka) & K_0(ka) & 0 & \gamma(\dfrac{1}{a^2} - k^2) \\ I_0(k) & -I_0(k) & -K_0(k) & (1-k^2) & 0 \end{vmatrix} \tag{1.26}$$

$$\tilde{\hat{x}}^t = [A_1, A_2, B_2, \tilde{\hat{\zeta}}_1, \tilde{\hat{\zeta}}_2] \tag{1.27}$$

$$b^t = [0, \hat{\zeta}_{1.0}, \hat{\zeta}_{2.0}, 0, 0] \tag{1.28}$$

The solution of this system of 5 equations for $\tilde{\hat{\zeta}}_1$ and $\tilde{\hat{\zeta}}_2$ is,

$$\tilde{\hat{\zeta}}_1 = \frac{1}{|a_{mn}|}[a_{22}\hat{\zeta}_{1.0} - a_{12}\hat{\zeta}_{2.0}] \tag{1.29}$$

$$\tilde{\hat{\zeta}}_2 = \frac{1}{|a_{mn}|}[-a_{21}\hat{\zeta}_{1,0} + a_{11}\hat{\zeta}_{2,0}] \qquad (1.30)$$

where a_{mn} are the components of the matrix a and are given in the appendix (pg. 34).

To get the solution in the time and space domain, one must invert the solution from the Fourier-Laplace domain, i.e.,

$$\zeta_1(z,t) = \frac{1}{4\pi^2 i}\int_{-\infty}^{\infty} e^{ikz}\left[\int_{c(k)-i\infty}^{c(k)+i\infty} \tilde{\hat{\zeta}}_1(k,s)e^{st}ds\right]dk \qquad (1.31)$$

where c(k) is a real number that lies to the right of all singularities of $\tilde{\hat{\zeta}}_1$ in the s plane for each k.

The Laplace inversion can be done by converting the line integral to a Bromwich contour integral and using the residue theorem to evaluate the integral. The residues have to be calculated at all the poles of $\tilde{\hat{\zeta}}_1$ in the s plane for a given k. From Eqs. (1.29,1.30), the poles in the s plane arise either when det(a)= $|a|=0$ or when any of the terms a_{mn} is singular or both. The terms of the matrix a stay finite in the s plane except when s=0. If s=0, a_{mn} diverge as 1/s and det(a_{mn}) diverges as $1/s^2$. Thus s=0 is not a pole of ζ. The poles that contribute to instability arise from the roots of f(k,s)=det(a)=0. This is the dispersion equation of the system. Given a k, the poles $\{s_n(k)\}$ in the s plane are the roots of the dispersion equation. When these poles are all simple,

$$\hat{\zeta}_1(k,t) = \sum_{n=1}^{4}\frac{1}{\partial|a_{mn}(k,s)|/\partial s}\bigg|_{k,s_n}[a_{22}(k,s_n)\hat{\zeta}_{1,0}(k) - a_{12}(k,s_n)\hat{\zeta}_{2,0}(k)]e^{(s_n t)} \qquad (1.32)$$

But $a_{11}(k,s_n)a_{22}(k,s_n)=a_{12}(k,s_n)a_{21}(k,s_n)$, since $\det(a_{mn})=0$ at (k,s_n). Using this in Eq. (1.32), one gets,

$$\hat{\zeta}_1(k,t)=\sum_{n=1}^{4}\frac{1}{\partial|a_{mn}(k,s)|/\partial s}\bigg|_{k,s_n}\frac{-a_{12}}{a_{11}}[-a_{21}(k,s_n)\hat{\zeta}_{1,0}(k)+a_{11}(k,s_n)\hat{\zeta}_{2,0}(k)]e^{(s_n t)} \qquad (1.33)$$

$$\hat{\zeta}_2(k,t)=\sum_{n=1}^{4}\frac{1}{\partial|a_{mn}(k,s)|/\partial s}\bigg|_{k,s_n}[-a_{21}(k,s_n)\hat{\zeta}_{1,0}(k)+a_{11}(k,s_n)\hat{\zeta}_{2,0}(k)]e^{(s_n t)} \qquad (1.34)$$

where

$$\frac{\partial|a_{mn}|}{\partial s}=2s-2\frac{(s-a_{11})(s-a_{22})-a_{12}a_{21}}{s}$$

To carry out the Fourier inversion, we complete the contour in the k-plane (see figure 1.2) and appeal again to the residue theorem:

$$\zeta_1(z,t)=\frac{1}{2\pi}\int_{-\infty}^{\infty}\hat{\zeta}_1(k,t)e^{ikz}dk=i\sum(\text{Residues})_k \qquad (1.35)$$

The poles of $\hat{\zeta}(k,t)$ in the k plane arise from the poles, e.g., k_0, of the initial conditions, i.e., $\hat{\zeta}_{1,0},\hat{\zeta}_{2,0}$, or when some $a_{mn}(k,s_n)$ becomes infinite. This can happen only if $G(k)=0$ for $G(k)$ defined in the appendix. $G(k)$ has no zeroes on the real k axis for $\beta>0$. Note that as $k\to 0$, all the solutions to the dispersion equation, i.e., $s_n(k)\sim k$ and all the terms in the matrix a, i.e., $a_{mn}\sim k$. Thus, $|a_{mn}|\sim k^2$ and $a_{mn}/(\partial|a|/\partial s)$ stays finite. Hence, $k=0$ is not a pole of $a_{mn}/(\partial|a|/\partial s)$. The only poles of $\hat{\zeta}_1(k,t)$ in the k plane are the poles k_0 of the initial conditions. If $\hat{\zeta}_{1,0}$ has no poles on the real k axis, the method of stationary phase gives,

$$\zeta_1\sim\sum_{n}\text{coeff}(k_m,s_n(k_m))\frac{e^{ik_m z-s_n(k_m)t}}{\sqrt{t}} \quad \text{as } t\to\infty \qquad (1.36)$$

where ds/dk=0 at $k=k_m$ and k_m lies on the real k axis.

If $\zeta_{i,0}$ is of the form $\sum_{k_0} \Delta_{i,k_0} \sin(k_0 z)$, then $\zeta_{i,0} = \sum_{k_0} \Delta_{i,k_0} \delta(k-k_0)$. The Fourier inversion can then be done explicitly because $\hat{\zeta}_i(k,t)$ has no other pole on the real k axis except at $k=k_0$. The Fourier inversion (1.35) gives,

$$\zeta_i = \sum_{k_0} \sum_{n} \text{coeff}(k_0, s_n(k_0))\, e^{ik_0 z + s_0 t} \tag{1.37}$$

where the coefficients follow from Eqs. (1.33)-(1.34). The details of the inversions are presented in the Appendix in the second part of this chapter. The principle ideas in the inversion are the same in both the inviscid and the viscous case, hence, we avoid presenting them twice.

By multiplying out the terms in the appendix, one can reduce the dispersion equation, $f(k,s)=a_{11}a_{22}-a_{12}a_{21}=0$, to the form $W(k)s^4+X(k)s^2+Y(k)=0$. This equation can be solved to give $s=g(k)$. There are four roots for a given k. We shall now show that s^2 must be real.

To investigate the characteristics of this system, consider the homogeneous eigenvalue problem for this system of governing equation and boundary conditions. The governing equation in terms of $\tilde{u}_i$ is,

$$(D-k^2)\tilde{u}_i = 0 \quad ; \quad D = \frac{d^2}{dr^2} + \frac{1}{r}\frac{d}{dr} \tag{1.38}$$

By multiplying the governing equation by $\tilde{\hat{u}}_i^*$ where * denotes complex conjugate, integrating over r and making use of the boundary conditions, one finds

$$\frac{1}{s^2}\left[(1-k^2)\left|\tilde{\hat{u}}_1\right|^2\Big|_{r=1}+\gamma a\left[\frac{1}{a^2}-k^2\right]\left\|\tilde{\hat{u}}_2\right\|_{r=a}\right]=I$$

$$I=\frac{1}{k^2}\int_0^1 r(k^2\left|\tilde{\hat{u}}_1\right|^2+D_1\tilde{\hat{u}}_1 D_1\tilde{\hat{u}}_1^*)dr+\frac{1}{k^2}\int_1^a r(k^2\left|\tilde{\hat{u}}_2\right|^2+D_1\tilde{\hat{u}}_2 D_1\tilde{\hat{u}}_2^*)dr+\frac{1}{k^2}\tilde{\hat{u}}_1\tilde{\hat{u}}_1^*\Big|_{r=0}\geq 0 \quad (1.39)$$

$$D_1=\frac{1}{r}(\frac{\partial}{\partial r}r)$$

This implies s^2 is real when k is real. From Eq. (1.39) s^2 is positive for $k<1/a$ and is negative for $k>1$. Thus, the dispersion equation, $W(k)s^4+X(k)s^2+Y(k)=0$. is such that $X^2>4WY$.

II.I.II RESULTS AND DISCUSSION

The dispersion equation is quadratic in s^2 and thus allows explicit solutions for s(k). There are 4 roots, but two of them are the negative of the other two. Figure 1.3 shows two of its four roots along with their long wave (k→0) limits. All the modes are linear in k as $k\to 0$, i.e., $s\sim s_1 k$, where s_1 satisfies

$$4s_1^4-s_1^2(2+\frac{2\gamma}{a\beta}+\frac{2(\beta-1)\gamma}{\beta a^3})+\frac{\gamma}{\beta a}-\frac{\gamma}{\beta a^3}=0 \qquad (1.40)$$

As shown earlier, s^2 as a function of k is purely real. Thus the growth rate s is either purely real or purely imaginary. If the growth rate is real and positive the disturbances grow in time and the system is unstable; if the growth rate is imaginary, the disturbances oscillate in time with fixed amplitude. This behavior is a manifestation of the inviscid nature of the fluids because no dissipation, which dampens oscillations, is present. Two of the modes are stable for all wave numbers and two have k bands where they are unstable. One unstable mode grows for all k<1, i.e., for waves with wavelengths greater than the core circumference. The other mode is unstable for k<1/a, i.e., for waves with wavelengths greater than the outer circumference. Both the modes become purely imaginary beyond their respective cutoffs.

The amplitude ratio in Fourier Laplace domain, i.e, the ratio of the interfacial deflections of the outer to the inner interface, from Eqs. (1.29) and (1.30), becomes,

$$\frac{\tilde{\hat{\zeta}}_2}{\tilde{\hat{\zeta}}_1}(k, s) = \frac{[-a_{21}\hat{\zeta}_{1.0} + a_{11}\hat{\zeta}_{2.0}]/|a_{ij}|}{[a_{22}\hat{\zeta}_{1.0} - a_{12}\hat{\zeta}_{2.0}]/|a_{ij}|} \tag{1.41}$$

At the roots of dispersion equation, $f(k,s_n)= a_{11}a_{22}-a_{12}a_{21}=0$. Using this in (1.41), we get for mode n,

$$\frac{\tilde{\hat{\zeta}}_2}{\tilde{\hat{\zeta}}_1}(k, s_n) = \lim_{s \to s_n} \frac{\tilde{\hat{\zeta}}_2}{\tilde{\hat{\zeta}}_1}(k, s) = -\frac{a_{11}}{a_{12}} = -\frac{a_{21}}{a_{22}} \tag{1.42}$$

For both the modes, the amplitude ratio is purely real. So, the interfaces are exactly in or out of phase (see Fig. 1.4). The mode that grows for k<1 grows in phase but oscillates out of phase for k>1; the other growing mode grows out of phase for k<1/a but oscillates in phase for k>1/a. Out of phase interfacial growth squeezes the film and hence the name "squeezing" mode. Similarly the in phase growing mode is named the "stretching" mode. Several other authors have found the stretching and the squeezing unstable modes in studies of planar or cylindrical films [e.g., (Taylor 1959) and (Felderhof 1968)].

The growth rates of both the modes go to zero as the wavelength of the disturbance becomes very large, i.e., k→0. This happens because as k→0, there is no axial pressure gradient to accelerate the fluid, hence, the growth rate goes to zero. It is interesting to examine the interfacial shapes of each of these modes. At k=1/a, the circumferential curvature of the outer interface exactly balances its longitudinal curvature. Since the growth rate of the squeezing mode goes to zero at k=1/a, it is necessary that the surface tension forces balance on the inner interface as well. The only way this is possible, when $k \neq 1$, is if $\tilde{\hat{\zeta}}_1 = 0$. So, $\tilde{\hat{\zeta}}_2 / \tilde{\hat{\zeta}}_1 = \infty$. Similarly, for the stretching mode at k=1, $\tilde{\hat{\zeta}}_2 / \tilde{\hat{\zeta}}_1 = 0$. This is illustrated in Figure 1.6. These two neutral states, at k=1/a for the squeezing mode and k=1 for the stretching mode, correspond to the two eigenfunctions for the equilibrium shapes of finite annular menisci obtained by Tsamopoulos et. al.(Tsamopoulos et al. 1988).

There is a maximum, s_{max}, in growth rate for each mode with corresponding wave number k_{max}. s_{max} of the stretching mode is greater than that of the squeezing mode for all parameter values explored. If the linear theory turns out to characterize the jet break-up, as it does for the single jet, then s_{max} determines the breakup time and k_{max} the size. In this linear scenario, the stretching mode growth will result in breakup of the core first, resulting in drops of primary fluid within a secondary fluid jet. If the jet still follows the linear dynamics of the original compound jet, the film will then rupture, resulting in the formation of compound drops. In contrast, linear squeezing mode growth can lead to either the core or the film rupturing first depending on the film thickness and the amplitude ratio. If the film is thin, the out of phase growth of the squeezing mode can cause film breakup resulting in dewetting, even though the growth rate is small.

It is possible to choose specific initial conditions such that one of the modes, say n, disappears. From Eqs. (1.29), (1.30), this happens when

$$-a_{21}(k,s_n)\hat{\zeta}_{1,0}(k)+a_{11}(k,s_n)\hat{\zeta}_{2,0}(k)=0\Rightarrow\frac{\hat{\zeta}_{1,0}(k)}{\hat{\zeta}_{2,0}(k)}=\frac{a_{11}(k,s_n)}{a_{21}(k,s_n)} \tag{1.43}$$

Using the dispersion equation it can be shown that,

$$\frac{a_{11}(k,s_1)}{a_{21}(k,s_1)}=-\frac{a_{12}(k,s_2)}{a_{11}(k,s_2)}=\frac{\tilde{\hat{\zeta}}_1}{\tilde{\hat{\zeta}}_2}(k,s_2) \tag{1.44}$$

where if mode 1 is stretching, mode 2 is squeezing and vice versa. This implies that if the initial disturbance has an in-phase amplitude ratio corresponding to the stretching mode, the compound jet continues to grow in phase and squeezing mode remains absent. If the initial disturbance has an out of phase amplitude ratio corresponding to the squeezing mode, the compound jet stays out of phase at all times.

For the film to rupture in the squeezing mode, $|\zeta_2|+|\zeta_1| \sim a-1$; for the film to rupture in stretching mode, $|\zeta_2-\zeta_1| \sim a-1$; and for the core to rupture in either mode, $\zeta_1 \sim 1$. Such results, in principle, are beyond the range of validity of the linear theory.

Most applications aim to control the breakup size and time. The manipulatable variables are the system parameters, the most important of which are, γ, β and a. We now examine their effects on the growth rate.

Surface tension drives the capillary instability. The circumferential curvature provides the destabilizing force whereas the longitudinal curvature provides the restoring force. The driving force provided by the outer-interface is the product $\sim\gamma(1/a^2-k^2)$ of the surface tension and the curvature. Since the destabilizing curvature of the outer interface dominates for waves longer than the outer circumference in the squeezing mode, the growth rate increases with the increase in driving force that increasing γ achieves; see figure 1.5. For the stretching mode, the outer interfacial deflections have a net destabilizing effect for $k<1/a$ and a net stabilizing effect for $k>1/a$. Since the non-dimensionalization requires one to interpret an increase in γ as an increases in σ_2, it follows that the growth rate increases for $k<1/a$ and decreases for $k>1/a$ (figure 1.6).

An increase in outer fluid's density leads to an increase in its inertia. Thus the growth rate decreases for either mode (curves not shown).

II.I.III THIN FILM LIMIT

In order to get a clear understanding of the physics of each of the modes it is useful to examine the temporal instability problem in the thin film limit, i.e., when $\varepsilon = (R_2-R_1)/R_1 = a-1 \ll 1$. The non-dimensional radial length scales in the film become very small ($O(\varepsilon)$) compared with the radial length scales ($O(1)$) in the core and the axial length scales ($O(1)$) in both the core and the annulus. As a result, the radial derivatives in the film become very large. To rescale this rapid variations in the film, we define a scaled film variable $y := (r-1)/\varepsilon$ which is $O(1)$ in the film. The y derivatives in the film are $O(\varepsilon^0)$. One can expand the equations themselves or their solutions in powers of ε and match core and annular solutions via the boundary conditions at each order in ε.

On substituting $a=1+\varepsilon$ in the dispersion equation and solving for the growth rates to leading order in ε, one finds , $s=s_0\varepsilon^0$ for the stretching mode and $s=s_{1/2}\varepsilon^{1/2}$ for the squeezing mode, where

$$s_{1/2} = \pm\sqrt{\frac{k^2(1-k^2)}{\beta}\frac{\gamma}{1+\gamma}} \tag{1.45}$$

Figures 1.7 illustrate this result.

In the squeezing mode, the pressure in the film is $O(\varepsilon^0)$ to support the capillary pressure caused due to perturbation to the outer interface. The linearized equations of motion show that the axial pressure gradient accelerates the film fluid to produce a significant axial velocity ($w \sim O(\varepsilon^{-1/2})$). By continuity, $u \sim \varepsilon w \sim \varepsilon^{1/2}$. The radial component of the equation of motion reduces to $\partial P/\partial y=0$, i.e., P is independent of y to leading order. This is typical of thin layers, as in lubrication or boundary layer theory. In order to avoid a trivial solution in the core $P \sim O(\varepsilon)$. As a result, the normal stress conditions at both interfaces contain only film quantities. The large perturbation film pressure balances the capillary pressure at both interfaces and accelerates the film fluid axially; the film problem closes independently of the core. In the core, $u \sim \varepsilon^{1/2}$ to match the film radial velocity and from continuity $w \sim \varepsilon^{1/2}$.

In the stretching mode, recall $s=s_0\varepsilon^0$ with

$$s_0 = \pm\sqrt{(1+\gamma)(1-k^2)k\frac{I_1(k)}{I_0(k)}} \tag{1.46}$$

(see fig 1.8) and the film's perturbation pressure is $O(\varepsilon^0)$ to balance the capillary pressure. From the axial equation of motion, the film pressure drives a strong, but less significant axial film velocity $w \sim O(\varepsilon^0)$. Even though continuity implies, $\partial u/\partial y \sim \varepsilon$, clearly a stretching mode must have a significant radial velocity as well. Thus to leading order $u \neq u(y) \sim 1$ and, as a result, the leading order of ψ in the film is also independent of y. From the next order Orr-Sommerfeld equations, the next order of ψ is linear in y, i.e.,

$$\psi_2 = A_0 + (A_1 + B_1 y)\varepsilon + O(\varepsilon^2) \tag{1.47}$$

and thus w is also independent of y to leading order. Since the radial velocity is independent of y, the kinematic condition requires $\zeta_2 = \zeta_1$. Finally, as in the squeezing mode, the radial component of the equation of motion gives P independent of y.

At the outer interface, the pressure balances the surface tension force. Since pressure does not change with y, at the inner interface the secondary fluid exerts a normal stress exactly equal to the normal stress due to surface tension of the outer interface. Since $\zeta_2 = \zeta_1$, the normal stress on the primary fluid is same as the normal stress exerted by a single interface of surface tension = $\sigma_1 + \sigma_2$, and the core closes with boundary conditions identical to single jet. In fact the dispersion equation obtained is identical to that of a single jet with $\sigma = \sigma_1 + \sigma_2$ and the growth rate $s_0\varepsilon^0$ (Eq. 1.46) is of the single jet form.

Since the growth rate for the stretching mode goes as ε^0 and that for the squeezing mode goes as $\varepsilon^{1/2}$, the stretching mode will dominate for thin films. Numerical results show that this is true even for finite O(1) film thickness.

Another limiting case of a compound jet is for $a \to \infty$, a single jet in an infinite fluid (Tomotika (1935)). We have solved the dispersion equation for this case numerically. The squeezing mode disappears since its k-domain of instability (k<

1/a) vanishes, i.e., $k_\sigma \rightarrow 0$ as $a \rightarrow \infty$. The stretching mode reaches a limit. The solution becomes independent of the surface tension ratio ($\gamma=\sigma_2/\sigma_1$), since the outer interface recedes to infinity.

APPENDIX I

The functions a_{mn} given below are those appearing in eqs. (1.25) and (1.26)

$$a_{11} = s - (1-k^2)\frac{kI_1(k)}{sI_0(k)}\left[1 + \frac{I_1(k)\{K_0(ka)I_0(k) - I_0(ka)K_0(k)\}}{G(k)I_0(ka)I_0(k)}\right] \tag{1.48}$$

$$a_{12} = \frac{-kI_1(k)\gamma(1-\frac{1}{a^2})}{sI_0(k)I_0(ka)}\left[I_0(k) + \frac{I_1(k)(1-\frac{1}{\beta})\{K_0(ka)I_0(k) - I_0(ka)K_0(k)\}}{G(k)I_0(ka)}\right] \tag{1.49}$$

$$a_{21} = -\frac{1}{\beta as}\frac{(1-k^2)I_1(k)}{G(k)I_0(ka)I_0(k)} \tag{1.50}$$

$$a_{22} = s - \gamma(\frac{1}{a^2} - k^2)\frac{k}{\beta s}\left[\frac{I_1(ka)}{I_0(ka)} + (1-\frac{1}{\beta})\frac{I_1(k)}{I_0^2(ka)G(k)ka}\right] \tag{1.51}$$

$$G(k) = -(1-\frac{1}{\beta})\left[\frac{I_1(k)K_0(ka) + K_1(k)I_0(ka)}{I_0(ka)}\right] + \frac{1}{kI_0(k)} \tag{1.52}$$

II.II TEMPORAL ANALYSIS OF A VISCOUS COMPOUND JET

II.II.I Formulation of the Linear Stability

A doubly infinite thread of a fluid of density ρ_1 and viscosity μ_1 is surrounded by a coaxial annulus of an immiscible fluid of density ρ_2 and of viscosity μ_2. Both fluids are assumed incompressible. In the base state there is no flow, and the interfaces are cylindrical and concentric with inner and outer radii R_1 and R_2. The tensions of the inner and outer interfaces are σ_1 and σ_2, respectively (Fig. 2.1 pg. 73). In the stationary base state the pressure distribution is given by:

$$P_2^{[o]} = \gamma/a \; ; \; P_1^{[o]} = 1 + \gamma/a \tag{2.1}$$

where $P_i^{[o]}$ denotes the base state nondimensional pressure of region i (i=1 is the core, i=2 is the annular domain and the superscript [0] denotes the base state), pressure is scaled with the capillary pressure $[\sigma_1/R_1]$), $a = R_2/R_1$ and $\gamma = \sigma_2/\sigma_1$.

We now define an initial condition for the formulation of the temporal linear stability analysis. We assume that at t=0, the cylindrical interfacial geometry of the base state is perturbed by an axisymmetric disturbance with scale δ (<<1). We locate a cylindrical coordinate system (r,θ,z) where the z axis coincides with the core axis in the base state. For axisymmetric disturbances at the inner and/or outer interfaces, the interfacial locus is specified nondimensionally as $r=f_1(z,t)$ and $r=f_2(z,t)$, (lengths are scaled with R_1 and time by $[[\rho_1 R_1^3]/\sigma_1]^{1/2}$) and the initial condition is specified as: $f_1(z,t=0) = 1 + \zeta_{1,0}(z)\,\delta$ and $f_2(z,t=0) = a + \zeta_{2,0}(z)\,\delta$. The initial velocities in the core and the annular region are assumed to be zero. The initial interfacial disturbances cause hydrodynamic flow and interfacial motion for t>0. Since the fluid is assumed incompressible and the motion is axisymmetric, the nondimensional components of velocity (u_i and w_i in the r and z directions, respectively), can be described in terms of a (nondimensional) stream function $\Psi_i(r,z)$:

$$u_i = \frac{1}{r}\frac{\partial \Psi_i}{\partial z};\quad w_i = -\frac{1}{r}\frac{\partial \Psi_i}{\partial r} \qquad (2.2)$$

Here, velocities are scaled as $\sqrt{(\sigma_1/\rho_1 R_1)}$ and the stream function by $[R_1^2\sqrt{(\sigma_1/\rho_1 R_1)}]$. The stream function and interfacial deflections can be expanded in δ:

$$f_1(z,t) = 1 + \zeta_1^{[1]}(z,t)\,\delta + O(\delta^2) \qquad (2.3)$$

$$f_2(z,t) = a + \zeta_2^{[1]}(z,t)\,\delta + O(\delta^2) \qquad (2.4)$$

$$[\Psi_i(r,z,t),\ P_i(r,z,t)] = [\Psi_i^{[1]}(r,z,t)\delta,\ P_i^{[0]} + P_i^{[1]}(r,z,t)\delta] + O(\delta^2) \qquad (2.5)$$

where the superscript [1] denotes the order of the expansion in δ, and the evolution in time of the first order quantities define the linear stability.

Substituting the expansion for the stream function into the Navier Stokes equation for the stream function, and retaining the first order in δ terms, results in a linear differential equation for $\Psi_i^{[1]}(r,z,t)$. Fourier transforming in z (with wave number k) and Laplace transforming in time (with parameter s) yields the following equation in r:

$$D\left(D-\frac{J^{1/2}d_i s}{m_i}\right)\Psi_i(r,k,s)=0$$

$$D=\frac{d^2}{dr^2}-\frac{1}{r}\frac{d}{dr}-k^2 \tag{2.6}$$

The dimensionless parameters introduced in (2.6) are: $J=\rho_1\sigma_1R_1/\mu_1^2$, $m_1=1$, $m_2 = m = \mu_2/\mu_1$, $d_2=d=\rho_2/\rho_1$ and $d_1=1$. The variable $\Psi_i(r,k,s)$ denotes the Fourier-Laplace transform of the first order stream function (the superscript [1] has been dropped for clarity). The transforms of the stream function and the interfacial deformations (to be used in the boundary conditions below) are defined as:

$$\begin{bmatrix}\Psi_i(r,k,s)\\ \zeta_i(k,s)\end{bmatrix}=\int_{-\infty}^{\infty}\left[\int_0^{\infty}\begin{bmatrix}\Psi_i(r,z,t)\\ \zeta_i(z,t)\end{bmatrix}e^{-st}dt\right]e^{-ikz}dk \tag{2.7}$$

The linearized first order in δ, boundary conditions in dimensionless form in the Fourier-Laplace domain are:

(a) at r =0, the velocity is bounded:

$$\Psi_1<\infty, \tag{2.8}$$

$$\frac{d\Psi_1}{dr}<\infty; \tag{2.9}$$

(b) at r=1, the velocity is continuous, the tangential and shear stresses balance and the kinematic condition relates the interfacial deflection to the radial velocity:

$$\Psi_1=\Psi_2, \tag{2.10}$$

$$\frac{d\Psi_1}{dr}=\frac{d\Psi_2}{dr}, \tag{2.11}$$

$$m[D\Psi_2 + 2k^2\Psi_2] = [D\Psi_1 + 2k^2\Psi_1], \tag{2.12}$$

$$\begin{aligned} &\frac{m}{ikr}\frac{d}{dr}[(D - sJ^{1/2}\frac{d}{m})\Psi_2] + 2mik\frac{d}{dr}[\frac{1}{r}\Psi_2] - \\ &\frac{1}{ikr}\frac{d}{dr}[(D - sJ^{1/2})\Psi_1] - 2ik\frac{d}{dr}[\frac{1}{r}\Psi_1] = [k^2 - 1]\zeta_1, \end{aligned} \tag{2.13}$$

$$\zeta_1 = \frac{ikJ^{1/2}\Psi_1}{rs} + \frac{\zeta_{1.0}}{s}; \tag{2.14}$$

(c) at r=a, the tangential stress is equal to zero, the normal stress balances the capillary force and the kinematic condition relates the interfacial deflection of the outer interface to the radial velocity there.

$$D\Psi_2 + 2k^2\Psi_2 = 0, \tag{2.15}$$

$$\frac{m}{ikr}\frac{d}{dr}[(D - sJ^{1/2}\frac{d}{m})\Psi_2] + 2mik\frac{d}{dr}[\frac{1}{r}\Psi_2] = -\gamma[k^2 - \frac{1}{a^2}]\Psi_2, \tag{2.16}$$

$$\zeta_2 = \frac{ikJ^{1/2}\Psi_2}{as} + \frac{\zeta_{2.0}}{s}; \tag{2.17}$$

In the above, $\zeta_{i.0}$ denotes the Fourier transform of the initial deflections $\zeta_{i.0}(z)$.

The general solution of (2.6) is

$$\Psi_i(r) = A_i rI_1(kr) + B_i rK_1(kr) + D_i rI_1(\beta_i r) + E_i rK_1(\beta_i r) \tag{2.18}$$

where I_1 and K_1 are the modified Bessel function of order 1, and A_i, B_i, C_i, D_i are the constants of integration, which can depend on the wave number k and $\beta_i^2 = k^2 + sJ^{1/2}d_i/m_i$ for i=1,2. Substituting the general solution into the boundary conditions leads to the implicit matrix equation A(s,k)**x** =**b** for the growth rate s(k). A(s,k) is a 8*8 matrix (see Appendix).

$$\mathbf{b}^t = [0,0,0,0,0,0,\frac{\zeta_{1.0}}{s},\frac{\zeta_{2.0}}{s}] \tag{2.19}$$

$$\mathbf{x}^t = [A_1,B_1,C_1,D_1,A_2,C_2,\zeta_1,\zeta_2] \tag{2.20}$$

If A is non-singular, $\mathbf{x}(k,s)=A^{-1}(k,s)\mathbf{b}(k)$. This, in combination with eq(2.18) gives the solution in the Fourier-Laplace domain. The inversion into the real space-time domain is performed in the appendix.

At long time the solution depends on the maximum growth rate of the fastest growing mode. Thus, we look at the growth rates, s(k), of all the modes as a function of the wave number (k) and other system parameters to locate the maximum. We also study the effect of the system parameters on the maximum growth rate. The growth rates $s_n(k)$ are the zeroes of the dispersion equation det(A(k,s))=0. The subscript n in the growth rate denotes the nth mode. This is an implicit dispersion equation for the growth rate $s_n(k)$ as a function of the wave number. Since the dispersion equation is transcendental, there may be an infinite number roots for a given k; we examine only the unstable roots, because the stable roots decay and do not contribute at long times.

The equation det(A(k,s))=0 is an implicit equation to determine the growth rate s as a function of m, d, a, J and k. In general, when all the forces are important the equation does not simplify and has to be solved numerically. Long wave results (see Section II.II.II.1) show that there are 3 modes whose growth rates go to zero as $k \to 0$. These represent three modes of the system. There are other solutions of the dispersion equation but they are all stable. Two of these modes are unstable, i.e., the real part of the growth rate is positive, and the third is stable. The growth rate of the two growing modes as a function of the wave number is shown in figure 2.2. The growth rate of the first mode is real and positive for $k < 1$, i.e., this mode is unstable to all waves with wavelength greater than the undisturbed core circumference. The second mode has a real and positive growth rate for $k < 1/a$, implying that it is unstable to all disturbances with wavelength greater than the undisturbed outer circumference of the annulus. The third mode has a negative real part and so is stable to all waves. It is real for some range of wave numbers and then becomes complex.

A single jet is unstable to all axisymmetric disturbances with wavelength greater than it's circumference because the surface potential energy is decreased when such perturbation superimposes on the cylindrical jet. Thus, in a compound jet, for the disturbances with wavelength greater than the outer circumference of annulus, the surface potential energies of both interfaces decrease, making the system unstable; for disturbances having wavelengths smaller than the core circumference, the surface energy of both the interfaces decrease, resulting in the decay of the disturbances or stability to such disturbances. Finally, for waves with wavelength greater than the core's circumference but less than the annulus' circumference the surface potential energy of the inner interface decreases while that of outer interface increases. The amplitude ratio determines whether the configuration possesses more energy than the initial condition of no flow. If it does, the configuration is unstable; otherwise it is stable. In general, a system is unstable if disturbances of at least one wavelength grow. As such, our system is unstable to the capillary instability.

After calculating the growth rate and substituting into the dispersion equation, one finds the amplitude ratio in the Fourier-Laplace domain, i.e., $\tilde{\hat{\zeta}}_2 / \tilde{\hat{\zeta}}_1$. The growing mode whose growth rate goes to zero at k=1/a has a real and negative amplitude ratio for $0 < k < 1/a$. This implies the two interfaces grow out of phase and thus squeeze the film fluid; hence the name squeezing mode. The other growing mode, whose growth rate goes to zero at k=1, has a real and positive amplitude ratio for $0<k<1$. This implies the two interfaces grow in phase, i.e., the film stretches; hence, the stretching mode. Figure (2.3) shows the stretching and squeezing modes respectively. At k=1/a , the circumferential curvature of the outer interface balances the longitudinal curvature. Since the growth rate of the squeezing mode goes to zero at k=1/a, it is necessary that the forces due to surface tension balance on the inner surface as well. The only way, this is possible, if $k \neq 1$, is if $\zeta_1 = 0$. So, $\zeta_2/\zeta_1 = \infty$. Similarly for the stretching mode at k=1, $\zeta_2/\zeta_1 = 0$.

II.II.II Asymptotic Results

II.II.II.1 Long Waves ($k \to 0$)

Since capillarity destabilizes cylindrical threads to interfacial waves longer than the circumference of the undisturbed interface, it is interesting to examine the long wave dynamics of the compound thread by finding the asymptotic expressions for the growth rate as $k \to 0$ with ε fixed. This long wave limit implies the length scales in the axial direction are much longer than the length scales in the radial direction, for both the core and the annulus.

We assume regular expansions of s and Ψ_i in k , i.e. ,

$$s = s^{(1)}k + s^{(2)}k^2 + O(k^3); \qquad (2.21)$$

$$\Psi_i = \Psi_i^{(0)} + \Psi_i^{(1)}k + \Psi_i^{(2)}k^2 + O(k^3); \qquad (2.22)$$

Substituting these into the governing equation and boundary conditions and solving the leading order problem in k, we get the following solutions to the growth rate:

$$s = \pm\sqrt{\frac{1+a\gamma}{2(a^2d-d+1)}}k + O(k^2) \qquad (2.23)$$

$$s = \frac{\gamma J^{1/2}}{16m\,a^3(1+\gamma a)}(4a^4\ln(a) + (m-3)a^4 + 2(2-m)a^2 + m - 1)k^2 + O(k^3) \qquad (2.24)$$

These solutions represent 3 modes. Two of them are growing and the third is decaying. The asymptotic limits (k→0) of the two growing modes are compared with the numerical solutions in figure 2.2.

Another way of getting these asymptotic results is by separating the modified Bessel functions K_0 into their logarithmic and the algebraic parts: $K_n(z)=g(z) + (-1)^{n+1}\ln(z/2)\ I_n(z)$, where g(z) is real. By multiplying Column 1 of the matrix A by ln(ka/2) and subtracting it from Column 2 one can eliminate the ln(k) terms in the expansion of K_n. Similarly, by multiplying Column 3 by $\beta_2 a$ and subtracting from Column 4, one can eliminate the remaining ln(k) terms in the determinant. Thus, it is consistent to assume, as above, a regular expansions of ψ_i and s in k. If one expands the remaining terms in the determinant in k (using the symbolic algebraic operations in Mathematica for instance), the determinant gives the same roots as obtained above.

As k →0, the growth rate of all the unstable modes should also go to zero because k=0 implies a uniform radial expansion or contraction of the jet. However in either case there is no axial pressure gradient $\partial p/\partial z$ and thus there is no force to drive the instability.

In the squeezing mode, $s \sim k^2$. The growth rate is independent of density of the two fluids (see eqn 2.24) because inertia does not contribute to leading order and the viscous forces balance pressure in each fluid. The pressure in the film is $O(k^0)$ to balance surface tension at the outer interface. This creates O(k) axial pressure gradient in the film which drives an O(k) axial flow. This causes an $O(k^2)$ radial velocity from continuity and an O(k) shear in the film. Continuity of velocities and stresses at the inner interface drive an O(k) axial velocity, an $O(k^2)$ radial velocity, an O(k) shear and an $O(k^0)$ pressure and normal stress in the core. At the inner interface, pressure balances the surface tension and does not involve inertia. The normal stress in the film and the core only is simply the pressure because velocities are of higher order and the leading order pressure is uniform across the cross-section. The amplitude ratio, ζ_2/ζ_1 has a k^0 order contribution which is $-1/\gamma$.

In stretching mode, the growth rate is linear in k as k→0 and does depend on the fluids' densities. That is, inertia contributes to leading order. The pressure in the film is $O(k^0)$ to balance surface tension at the outer interface. This creates an $O(k^0)$ axial velocity which is independent of radial position. From continuity, there is an O(k) radial velocity. The boundary conditions at the inner interface create velocities and stresses in the core of the same order as in the film. The axial velocities are independent of radial position in both the core and the film. Thus, there is no shear in either the film or the core to leading order and the growth rate is independent of the viscosities of the primary and secondary fluids; see eqn 2.23. Since to leading order the axial velocities are independent of r , the radial velocities must be linear in r to satisfy continuity. The flow then is an axial stretching that causes a radial displacement. This implies that the deflections at the interfaces are in phase and also proportional to r, i.e., $\zeta_2/\zeta_1=R_2/R_1 = a$.

In the long wave limit, the stable, third mode becomes a mirror image of the stretching mode, i.e., the velocities and amplitudes associated with this mode are identical to those in stretching mode, but this mode decays at the same rate that the stretching mode grows. The asymptotic results match those in figure 2.2 obtained numerically. There are other solutions to the dispersion equation for which the growth rate does not go to zero as $k\rightarrow0$. In these modes, in the long wave limit, there is no axial pressure gradient $\partial p/\partial z$ to leading order and inertia balances viscous forces. Thus, the fluid decelerates and the growth rate is negative, implying stability.

II.II.II.2 Thin films ($\varepsilon\rightarrow0$)

If the film is thin with respect to the undisturbed core radius R_1, it is convenient to define a parameter $\varepsilon = (R_2-R_1)/R_1 = a-1$, the dimensionless film thickness, which is small compared with one. The dimensionless radial length scale in the film is O(ε) while the film's dimensionless axial scales and all dimensionless core length scales remain O(1). As a result, the radial derivatives in the film are relatively large, i.e., O(1/ε). In order to rescale the rapid radial variation in the film we stretch the radial length scale via the change of variables: y-derivatives in the annulus are O(1). One can expand the solutions in powers of ε and match core and annulus solutions in orders of ε.

$$y \equiv \frac{r-1}{\varepsilon} \tag{2.25}$$

To determine which scalings of s in ε will be appropriate, one can guess that these scales persist even in the long wave regime. As such one expands the three long wave asymptotic results in powers of ε to extract these scales analytically. For the three modes, respectively, one gets

$$s = \frac{J^{1/2}\gamma}{4(1+\gamma)}\varepsilon^2 k^2 + O(\varepsilon^3) \tag{2.26}$$

$$s = \pm\sqrt{\frac{1\mp\gamma}{2}}\,\varepsilon^0 k + O(\varepsilon) \tag{2.27}$$

Two of the roots scale as ε^0 and one root scales as ε^2. For each mode, we then substitute regular expansions for s and Ψ_i into the differential equation and the boundary conditions and solve the leading order problem in ε.

As a means of checking our results we expand these expressions for s in the long wave limit of k→0. These results are identical to equation (2.26) and (2.27), i.e., those obtained by taking the limit ε→0 of the long wave results.

(i) Stretching Mode

For the ε^0 mode, assume the regular expansions of s and ψ_i in ε,

$$s = s_0 + s_1\varepsilon + s_2\varepsilon^2 + O(\varepsilon^3) \tag{2.28}$$

$$\Psi_i = \Psi_i^{[0]} + \Psi_i^{[1]}\varepsilon + \Psi_i^{[0]}\varepsilon^2 + O(\varepsilon^3) \tag{2.29}$$

The leading order problem gives an implicit equation for s_0. The solution is,

$$(k^2-1)k(1+\gamma)I_1(k)I_1(\beta) - 4k^3\beta I_1(k)(I_0(\beta) - \frac{I_1(\beta)}{\beta}) + 2k^2(I_0(k) - \frac{I_1(k)}{k})(s_0+2k^2)I_1(\beta) + J^{1/2}s_0 I_0(k)I_1(\beta)(J^{1/2}s_0+2k^2) = 0 \tag{2.30}$$

where

$$\beta = \sqrt{k^2 + J^{1/2}s_0} \tag{2.31}$$

Corresponding to this solution, the leading order for Ψ_1 and Ψ_2 become

$$\Psi_1^{[0]} = ((1+2\frac{k^2}{J^{1/2}s_0})\frac{1}{I_1(k)}r I_1(kr) - 2\frac{k^2}{J^{1/2}s_0 I_1(\beta)}r I_1(\beta r))A \tag{2.32}$$

$$\Psi_2^{[0]} = A \tag{2.33}$$

where A is a constant that can depend on k.

In the stretching mode, $s \sim \varepsilon^0$. Figure (2.5) shows the asymptotic limit of the stretching mode as $\varepsilon \to 0$. In the film, the normal stress $(-p+(2/\sqrt{J})\partial u/\partial r)$ is $O(\varepsilon^0)$ to balance the surface tension and is independent of the radial position. In the stretching mode the inner and the outer interfaces grow in phase, i.e., the curvatures are in the same direction. Thus, to balance the O(1) film stress, it's necessary to have O(1) pressure in the core. O(1) core pressure drives O(1) radial and axial velocities in the core. This drives an O(ε^0) axial and radial flows in the film which are independent of y. The O(1) shear stress in film has to be independent of y because there is no inertia or pressure to balance the leading order viscous force O(1/ε) that would arise if the O(1) shear stress would vary with y. But this O(1) shear stress has to be zero at the outer interface (gas-liquid), thus, the film has no shear stress to order one. Thus, the O(1) axial velocity in the film has to be independent of y. The leading order radial velocity (O(1)) also has to be independent of y to satisfy continuity. At the outer interface, normal stress supports the surface tension. Since the normal stress does not change with y, the secondary fluid exerts a normal stress at the inner interface equal to the normal stress due to surface tension of the outer interface. Since $\zeta_2 = \zeta_1$, the normal stress on the primary fluid is equal to the normal stress exerted by a single interface of surface tension $\sigma_1 + \sigma_2$. The shear stress on the primary fluid is zero since there is no shear in the film. Thus the core closes with boundary conditions identical to those for a single jet. The dispersion equation (eq 2.30) is identical to that for a single jet (2.34) with $\sigma_1 + \sigma_2$ ($1+\gamma$ in dimensionless form) in (2.30) replaced by σ_1 (1 in dimensionless form) in (2.34)

$$\begin{aligned} &J(k^2-1)k\, I_1(k)\, I_1(\beta) - 4k^3 \beta\, I_1(k)\left(I_0(\beta) - \frac{I_1(\beta)}{\beta}\right) \\ &+ 2k^2\left(I_0(k) - \frac{I_1(k)}{k}\right)(s+2k^2)\, I_1(\beta) + s\, I_0(k)\, I_1(\beta)(s+2k^2) = 0 \end{aligned} \tag{2.34}$$

(ii) Squeezing Mode

For the ε^2 mode, assume the regular expansions,

$$s = s_2\varepsilon^2 + O(\varepsilon^3) \tag{2.35}$$

$$\Psi_i = \Psi_i^{[0]} + \Psi_i^{[1]}\varepsilon + O(\varepsilon^2) \tag{2.36}$$

In this case one can solve for the leading order growth rate s_2 explicitly.

Where

$$s_2 = J^{1/2} k \frac{(1-k^2)}{2I_1(k)} F_1(k) \frac{\gamma}{1+\gamma} \tag{2.37}$$

$$F_1(k) = -k \frac{I_0^2(k)}{I_1(k)} + k I_1(k) + 2I_0(k)) \tag{2.38}$$

The leading orders for ψ_1 and ψ_2 are

$$\Psi_1^{[1]} = B[\frac{I_0(k)}{I_1(k)} F_1(k) r I_1(kr) - \frac{1}{F_1(k)} r^2 I_0(kr)] \tag{2.39}$$

$$\Psi_2^{[2]} = B[\frac{2I_1(k)s_2}{\sqrt{J}(k^2-1)k\gamma F_1(k)} + y] \tag{2.40}$$

where B is a constant that depends on k.

The squeezing mode squeezes fluid out of the film. Since the viscous resistance increases with decreasing film thickness , the growth rate should decrease. As shown earlier, asymptotic analysis reveals that for the squeezing mode, $s \sim \varepsilon^2$, i.e., s/ε^2 approaches a limiting value as $\varepsilon \to 0$ (see figure 2.5). Let us first consider the film scales. The pressure is $O(\varepsilon^0)$ to support the surface tension and this drives a axial flow of order ε^2 .

$$\frac{\partial P}{\partial z} \approx \varepsilon^0 \approx \frac{1}{\varepsilon^2} \frac{\partial^2 w}{\partial y^2} \tag{2.41}$$

The $O(\varepsilon^2)$ axial velocity drives an order ε^3 radial flow from continuity. This causes an $O(\varepsilon)$ shear stress.

$$\frac{\partial w}{\partial r} = \frac{1}{\varepsilon}\frac{\partial w}{\partial y} = O(\varepsilon). \tag{2.42}$$

This $O(\varepsilon)$ shear in the film causes shear in the core to the same order. Hence, the velocities and pressure in the core are also order ε. The order ε axial velocity in the core entrains by continuity at the inner interface an $O(\varepsilon)$ axial velocity in the film. $O(\varepsilon)$ axial flow drives $O(\varepsilon^2)$ radial velocity in the film. But this $O(\varepsilon)$ axial velocity is shear free. The radial velocity in the core is $O(\varepsilon)$ but this vanishes at the inner interface because the film's radial velocity is $O(\varepsilon^2)$. The kinematic condition requires the growth rate to be $O(\varepsilon^2)$,

In the film, the normal stress is simply the pressure because the velocity gradients do not contribute to leading order. Note that the film pressure is independent of y and is equal to the capillary pressure due to the deformed outer interface. The pressure in the core is $O(\varepsilon)$. Thus, it does not contribute to the normal stress at the inner interface and the film pressure is balanced by the capillary pressure of the inner interface. This implies that the capillary force exerted by the inner and the outer interface balance each other. So, $\gamma_2(1/a^2-k^2)\zeta_2 = -\gamma_1(1-k^2)\zeta_1$ or $\zeta_2/\zeta_1 = -1/\gamma + O(\varepsilon)$. In the squeezing mode, the film and the core problems do not decouple.

Since the growth rate for the stretching mode goes as ε^0 and that for the squeezing mode goes as ε^2, it is clear that for thin films the growth rate for the stretching mode would be higher than that for the squeezing mode.

II.II.II.3 Thick films ($a \to \infty$)

Another limiting case of a compound jet is when the radii ratio $a \to \infty$. The result should be a single jet in an infinite medium (Tomotika 1935). We solved the dispersion equation for this case numerically. In this limit, the squeezing mode disappears because it unstable if $k < 1/a$ and, as $a \to \infty$, $k_{cr} \to 0$ (fig 2.6). Also, the maximum growth rate for the squeezing mode goes to zero as $a \to \infty$ (fig 2.6). The Tomotika solution matches the stretching mode solution as $a \sim 10$ (fig 2.7). The growth rate for the stretching mode becomes independent of the surface tension ratio as the outer interface recedes to infinity.

II.II.III Numerical Results for Order One Film Thickness

The fastest growing wave determines the evolution of the compound thread. Therefore, it is important to find the characteristics of the fastest growing waves associated with each mode and to determine which of the two modes will dominate for a given choice of parameters. The important system parameters are the viscosity ratio m , the surface tension ratio γ and the density ratio d. The fastest growing wave is characterized by the wave number k_m, it's growth rate s_m and the amplitude ratio amp_m. The maximum growth rate s_m determines the breakup time for the jet, k_m determines the volume of the compound drops at breakup and amp_m determines the phase angle between the deflection of the two interfaces, which qualitatively determines the breakup configuration. Although breakup is a strongly non-linear phenomenon, for the single jet, the breakup time and volume of the drops correlate very closely to those determined by the linear analysis.

II.II.III.1 Effect of the viscosity ratio

Increasing the viscosity of the secondary fluid increases the viscous resistance and thus leads to a decrease in the growth rate (figure 2.8a). The decrease is more pronounced in the squeezing mode because there is more fluid motion due to squeezing of fluid. For the entire range of m, the growth rate of the stretching mode is higher so the linear analysis predicts formation of compound drops. The size of the drops can be changed by manipulating m as there is a significant decrease in k_m with increase in m for the stretching mode (figure 2.8b). With increase in m, k_m decreases for the squeezing mode too, but since it is not the dominant mode, this decrease is unlikely to be observed in experiments. A decrease in k_m results in larger drops.

An increase in m results in decrease in both the core and the film velocities. Thus, the amplitude, ratio which is the ratio of the radial velocities at the two interfaces, does not change significantly (figure 2.8c).

If we let the viscosity ratio m approach zero, i.e., $\mu_2 \rightarrow 0$ and then let J approach infinity, i.e., $\mu_1 \rightarrow 0$, the dispersion equation for the viscous compound fiber reduces to the inviscid dispersion equation.

II.II.III.2 Effect of the surface tension ratio

The surface tension forces are independent of the film thickness. So, the variation in s_m, k_m and amp_m with a change in γ for finite film thickness should be qualitatively similar to that in thin films.

In the thin film limit, the growth rate $s(\gamma)$, and hence $s_m(\gamma)$, for the squeezing mode is inversely proportional to $1 + 1/\gamma$. We observe the same trend for $\varepsilon \sim 1$ as shown in figure 9a. In the squeezing mode, the growth rate increases with an increase in γ for any k due to an increase in the driving force.

In thin film limit, the stretching mode is like a single jet with dimensionless surface tension, $1+\gamma$. Thus, the growth rate is a function of $1+\gamma$. The same holds true for finite film thickness (figure 2.9a). In the stretching mode, the growth rate increases with an increase in γ for $k<1/a$ and decreases for $1/a<k<1$. The reason for this is because an increase in γ results in an increase in the net force exerted by the outer interface, which is de-stabilizing if $k<1/a$ and stabilizing otherwise. Thus if $k_m>1/a$, s_m will decrease with an increase in γ and the reverse will happen if $k_m<1/a$. In figure 2.9b, $k_m > 1/a$ (=0.5), for $\gamma<1$. In this range, s_m decreases (figure 2.8a) although the decrease is not evident in the figure. If $\gamma>1$, $k_m>1/a$, hence s_m increases with increase in γ. The growth rate of the stretching mode is higher than that of the squeezing mode for the entire range of γ, so it is the dominant mode.

As $\varepsilon\rightarrow 0$, the amplitude ratio for the stretching and the squeezing mode were 1 and $-1/\gamma$, respectively. When $\varepsilon\sim 1$, amp_m for the squeezing mode follows $-1/\gamma$ closely and amp_m for the stretching mode is close to 1 for the entire range of γ(figure 2.9c).

Figure 2.9b shows the variation of k_m with γ for the stretching and the squeezing modes. There is a significant decrease in k_m with increase in γ for the stretching mode which affords the possibility of manipulating the drop size at breakup. In squeezing mode, k_m increases with γ but since, it is not the dominant mode this decrease is unlikely to be observed in experiments.

II.II.III.3 Effect of the density ratio

An increase in the film density increases the inertia and, since the driving force does not increase, the growth rate goes down. In squeezing mode, there is more fluid motion, so its decrease in growth rate is more appreciable. (figure 2.10a). An increase in the film's density will decrease the velocity in both the primary and the secondary fluids; so, there is not a significant change in the amplitude ratio for either mode. It decreases for the stretching mode with increase in d and the squeezing mode follows the opposite trend (figure 2.10c). In figure 2.10b, k_m for the squeezing mode decreases slightly with an increase in d and k_m for the stretching mode follows an interesting trend: it has a maxima at d ~ 1.

Thus, for all parameters values that we have scanned, the stretching mode is always the dominant mode, which can lead to the breakup of the compound jet into compound drops. An appropriate choice of the fluid properties allows one to tailor the break up time and drop size.

III. COMPARISON WITH EXPERIMENT

The theory developed in this paper predicts the breakup of a compound thread resulting in the formation of compound drops and gives the linear theory's estimate of the breakup lengths and of the drop sizes at breakup. Hertz and Hermanrud (1983) have done experiments with a compound jet generated using a single nozzle assembly and filmed as the jet moved in the axial direction. In a reference frame moving with the jet velocity, the jet is like a thread. So, we compare their experimental results with the theoretical predictions. The primary fluid in their experiment was a water soluble ink and the secondary fluid was a silicone oil. The physical parameters were: $\sigma_2 = 20\times10^{-3}$ N/m, $\sigma_1 = 50\times10^{-3}$ N/m, $\mu_2 = \mu_1 = 2$ cp, $\rho_2 = \rho_1 = 1000$ kg/m^3, $R_1 = 75\times10^{-6}$m, $R_2 = 150\times10^{-6}$ m, V=1.98m/s. So, $\gamma=0.4$, d=1, m=1, J=937.

Their observations include the formation of compound drops and pictures of the compound jet as it comes out of the orifice.. From the pictures it is possible to measure the wavelength(s) of the disturbances. The wave number measured from figure 5 from Hertz & Hermanrud (1983) is 0.64 for the first wave. The wave number changes in the axial direction and the average is 0.6. Fig(2.11) shows the predictions based on the temporal analyses. The maxima in the inviscid temporal growth rate is at k=0.66 and that in the viscous growth rate is at k=0.62. Sanz & Meseguer (1985) compared the results of the same experiment with their theoretical predictions based on the one dimensional temporal model. Their prediction for the wave number was 0.7.

At long times if breakup has yet not occurred and the system is still in the linear regime, the dominant mode, i.e., the mode with the highest growth rate, is the observable one. But at short times, other modes also contribute and this may explain why the observed wavelength of the jet changes along the axial direction.

IV. DISCUSSION AND CONCLUSIONS

The compound thread is unstable due to capillarity. We have solved its temporal hydrodynamic stability using transform techniques, and find two unstable modes. In one, a stretching mode, the interfaces grow in phase and in the second, a squeezing mode, they grow out of phase. The stretching and the squeezing modes are unstable for waves longer than the outer and the inner circumferences, respectively.

In the stretching mode, extrapolating the growth beyond the linear regime will result in the breakup of the core leading to drops of primary fluid in the secondary fluid. If the system continues to follow its pre-breakup dynamics, further non-linear stretching growth will finally cause rupture of film to form compound drops. In the squeezing mode when extrapolating the linear dynamics, either the film or the core can break first depending on the film thickness. In experiments, both modes grow and the one with the higher growth rate will dominate; it will become the observable mode at long times if the system is still in the linear regime. The growth rate of the stretching mode appears to be always higher, and so it dominates the long time, linear regime and presumably the breakup dynamics. On the other hand, the squeezing mode can cause breakup for very thin films. To see this note that, for film breakup in the stretching mode, $|\zeta_2|+|\zeta_1| \sim\varepsilon$ and for the film breakup in squeezing mode, $|\zeta_2-\zeta_1| \sim\varepsilon$. For the core to break in either mode, $|\zeta_1|\sim1$. If the film is not thin, the stretching mode dominates and results in the formation of drops of the primary (core) fluid in the secondary (annular) fluid. If the linear dynamics persist the instability results in compound drops.

In the thin film limit, the squeezing mode's growth rate goes to zero as ε^2 in the viscous and as $\varepsilon^{1/2}$ in the compound jet. In this limit, the stretching mode becomes a single jet solution with surface tension equal to the sum of the two interfacial tensions. If the initial disturbance is broad band in k (as noise), the system selects the wave number (k_m) with the maximum growth rate (s_m). Changes in jet parameters shift k_m and s_m, thus affording the possibility of manipulating the breakup size and breakup length.

For an inviscid compound jet if the two interfaces are initially exactly out of phase, with the amplitude ratio for the squeezing mode, the compound jet continues to grow in the squeezing mode. But in general all the modes are present in the initial condition and so it is reasonable to expect the stretching mode to dominate. The formation of compound drops, which is consistent with stretching mode dominance was observed by Hertz and Hermanrud (1983). Our predictions of the k_m compare well with their experiments.

Control over the breakup time and drop size is very important in applications. In some of the applications of compound jets such as coaxial extrusion of polymer fibers, it is desirable to have a stable jet. In such applications the growth rate needs to be low enough so that the time scales of breakup are smaller than the time scales of solidification of the polymers. Some of the physical properties of the polymers may have to be tailored to get the desired s_m. A proper analysis, though, would require a stability analysis of a compound jet with visco-elastic fluids. Luckily, such an analysis will not be very different from the one performed here since this problem has no base flow. In other applications such as ink-jet printing, it is desired to break the jet into drops of a fixed, uniform size. This can again be achieved by manipulating some of the physical properties of either the primary or the secondary fluids or by tailoring the interfacial surface tensions as shown in the previous section.

APPENDIX II

In the Fourier-Laplace domain the solution to equation (2.6) is,

$$\Psi_i(r) = A_i r I_1(kr) + B_i r K_1(kr) + D_i r I_1(\beta_i r) + E_i r K_1(\beta_i r) \qquad (2.43)$$

$$x^t = [A_1, B_1, C_1, D_1, A_2, C_2, \varsigma_1, \varsigma_2] \qquad (2.44)$$

$$b^t = [0,0,0,0,0,0,\frac{\hat{\varsigma}_{1.0}}{s},\frac{\hat{\varsigma}_{2.0}}{s}] \qquad (2.45)$$

$$x(k,s) = A^{-1}(k,s)b(k) \qquad (2.46)$$

A is the following 8*8 matrix:

$$\begin{matrix}
0 & 0 & 0 & 0 & I_1(k) & I_1(\beta_1) & -\sqrt{J}s & 0 \\
I_1(ka) & K_1(ka) & I_1(\beta_2 a) & K_1(\beta_2 a) & 0 & 0 & 0 & -\sqrt{J}s \\
I_1(k) & K_1(k) & I_1(\beta_2) & K_1(\beta_2) & 0 & 0 & -\sqrt{J}s & 0 \\
kI_0(k) & -kK_0(k) & \beta_2 I_0(\beta_2) & -\beta_2 K_0(\beta_2) & -kI_0(k) & -\beta_1 I_0(\beta_1) & 0 & 0 \\
\begin{array}{c} -d\sqrt{J}sI_0(ka)+ \\ -2mk^2 I_1'(ka) \end{array} & \begin{array}{c} d\sqrt{J}sK_0(ka)+ \\ -2mk^2 K_1'(ka) \end{array} & -2m\beta_2 I_1'(\beta_2 a) & -2m\beta_2 K_1'(\beta_2 a) & 0 & 0 & 0 & Jk(1-\frac{k^2}{a^2}) \\
\begin{array}{c} d\sqrt{J}sI_0(k)+ \\ 2mk^2 I_1'(k) \end{array} & \begin{array}{c} -d\sqrt{J}sK_0(k)+ \\ 2mk^2 K_1'(k) \end{array} & 2m\beta_2 I_1'(\beta_2) & 2m\beta_2 K_1'(\beta_2) & \begin{array}{c} -\sqrt{J}sI_0(k)+ \\ -2k^2 I_1'(k) \end{array} & -2\beta_1 I_1'(\beta_1) & Jk(1-k^2) & 0 \\
2k^2 I_1(ka) & 2k^2 K_1(ka) & I_1(\beta_2 a)(\beta_2^2+k^2) & K_1(\beta_2 a)(\beta_2^2+k^2) & 0 & 0 & 0 & 0 \\
2mk^2 I_1(k) & 2mk^2 K_1(k) & mI_1(\beta_2)(\beta_2^2+k^2) & mK_1(\beta_2)(\beta_2^2+k^2) & -2k^2 I_1(k) & -I_1(\beta_1)(\beta_1^2+k^2) & 0 & 0
\end{matrix}$$

(2.47)

If C_{ij} is the cofactor of $A_{ji}(k,s)$, using the cofactor expansion of $A^{-1}(k,s)$ in (2.46), one gets,

$$x(k,s) = \frac{C(k,s)b(k)}{|A(k,s)|} \qquad (2.48)$$

Using **b**(k) from (2.45), in (2.48), the ith (i=1,...,8) component $x_i(k,s)$ of $\mathbf{x}_i(k,s)$ is,

$$x_i(k,s) = \frac{C_i7\,\hat{\varsigma}_{1.0} + C_i8\,\hat{\varsigma}_{2.0}}{s\,|A(k,s)|}\; i = 1,8 \qquad (2.49)$$

In particular,

$$\hat{\zeta}_1(k,s) = \frac{\hat{\zeta}_{1.0}\, C_{77}(k,s) + \hat{\zeta}_{2.0}\, C_{78}(k,s)}{s\,|\,A(k,s)\,|} \tag{2.50}$$

$$\hat{\zeta}_2(k,s) = \frac{\hat{\zeta}_{1.0}\, C_{87}(k,s) + \hat{\zeta}_{2.0}\, C_{88}(k,s)}{s\,|\,A(k,s)\,|} \tag{2.51}$$

One needs to invert (2.49)-(2.51) to get the solution in the space-time domain.

We begin by inverting the Laplace transform.

$$\hat{\zeta}_i(k,t) = \frac{1}{2\pi i} \int_{p(k)-i\infty}^{p(k)+i\infty} \hat{\zeta}_i(k,s)\, e^{st}\, ds \tag{2.52}$$

where p(k) is real and larger than the largest real part of any singularity of the integrand of (2.52) for that value of k. To perform the line integration, we appeal to the residue theorem. Thus, for a given k, we need to find the poles and branch cuts of $\hat{\zeta}_i(k,s)$ in the s plane. The poles of the integrand in (2.52) can arise from the roots of the dispersion equation, i.e., det(A)=0 or s=0 or when the components of the cofactor matrix diverges. Since the cofactors involve products of the matrix elements, the cofactors can diverge only if some of the terms of the matrix become infinite. For a given $k \neq 0$, this can happen only when β_2 becomes 0, i.e., $s=-mk^2/dJ^{1/2}$. But as $\beta_2 \to 0$, asymptotic analysis using $K_0(\beta_2) \sim \ln(\beta_2)$, $K_1(\beta_2) \sim 1/\beta_2$, $I_0(\beta_2) \sim \beta_2^0$ and $I_1(\beta_2) \sim \beta_2$ shows that C_{ij} and det(A) stay finite. Similarly k=0 is not a pole for any arbitrary s. Thus the only poles of the integrand are those for which det(A)=0 or s=0. If s=0, the system is stable so we need not consider this pole. That the integrand involves $\beta_i=\mathrm{sqrt}(k^2+sJ^{1/2}m_i/d_i)$ would seem to indicate it has branch cuts, However, since β_i only appears in the entire functions $I_0(\beta_i)$, $I_1(\beta_i)/\beta_i$, $K_0(\beta_i)$, $K_1(\beta_i)/\beta_i$ in det(A), this turns out not to be the case. Thus, to evaluate the Laplace inverse, one needs to consider only the poles introduced by the dispersion equation for a given k. Let us denote these poles by $s_n(k)$. Assume that all the poles are simple:

$$\zeta_1(k,t) = \sum_n \frac{\zeta_{1.0} C_{77}(k,s_n) + \zeta_{2.0} C_{78}(k,s_n)}{s \frac{\partial |A(k,s)|}{\partial s}\Big|_{k,s_n}} e^{s_n t} \tag{2.53}$$

A similar expression can be written for ζ_2. Now we perform the Fourier inversion.

To accomplish the inversion, one needs to know the initial conditions, i.e., $\tilde{\zeta}_{1.0}$, $\tilde{\zeta}_{2.0}$. Let us first consider the initial disturbances to be periodic. Without the loss of generality, we assume the initial disturbances to be a single harmonics. A periodic function can be represented as a sum of sines and cosines using Fourier series expansion and the response of the linear system to such a disturbance is simply the sum of the responses to each harmonic.

Thus,

$$\tilde{\zeta}_{1.0} = G e^{(k_{1.0} z)} ; \tilde{\zeta}_{2.0} = H e^{(k_{2.0} z)} \tag{2.54}$$

Thus,

$$\hat{\zeta}_{1.0} = 2\pi G \delta(k - k_{1.0}) ; \hat{\zeta}_{2.0} = 2\pi H \delta(k - k_{2.0}) \tag{2.55}$$

Using these in eq(2.53) we get,

$$\hat{\zeta}_1 = 2\pi \sum_n [G C_{77} \delta(k - k_{1.0}) + H C_{78} \delta(k - k_{2.0})] \frac{e^{s_n t}}{s \frac{\partial |A|}{\partial s} \Big|_{k,s_n}}] \tag{2.56}$$

Fourier inversion yields

$$\zeta_1 = \sum_n \Big[GC_{77}(k_{1,0}, s_n(k_{1,0})) \frac{e^{ik_{1,0}z + s_n(k_{1,0})t}}{s \frac{\partial |A|}{\partial s} \Big|_{k_{1,0}, s_n(k_{1,0})}} + HC_{78}(k_{2,0}, s_n(k_{2,0})) \frac{e^{ik_{2,0}z + s_n(k_{2,0})t}}{s \frac{\partial |A|}{\partial s} \Big|_{k_{2,0}, s_n(k_{2,0})}} \Big] \quad (2.57)$$

Similarly,

$$\zeta_2 = \sum_n \Big[GC_{87}(k_{1,0}, s_n(k_{1,0})) \frac{e^{ik_{1,0}z + s_n(k_{1,0})t}}{s \frac{\partial |A|}{\partial s} \Big|_{k_{1,0}, s_n(k_{1,0})}} + HC_{88}(k_{2,0}, s_n(k_{2,0})) \frac{e^{ik_{2,0}z + s_n(k_{2,0})t}}{s \frac{\partial |A|}{\partial s} \Big|_{k_{2,0}, s_n(k_{2,0})}} \Big] \quad (2.58)$$

Thus the response is of form,

$$\zeta_1 = \sum_{k_0} \sum_n \mathrm{coeff}(k_0, s_n(k_0))\, e^{ik_0 z + s_0 t} \quad (2.59)$$

where k_0 are the poles of the initial conditions. At long time the solution would be dominated by the fastest growing mode. This result is in agreement with the normal mode analysis.

Thus as long time the response goes as $\exp(s_m t)$, where s_m is the maximum growth rate of the fastest growing mode.

If the initial disturbances are smooth and decay at $\pm\infty$, the Fourier transform of the initial disturbances will not have any pole on the real k axis. Since the disturbances grow as $e^{ikz+s(k)t}$, one can use the method of steepest descent to evaluate the long time asymptotic response.

$$\zeta_1(z,t) = \frac{1}{2\pi}\int_{-\infty}^{\infty}\sum_n \frac{\hat{\zeta}_{1,0}C_{77}(k,s_n) + \hat{\zeta}_{2,0}C_{78}(k,s_n)}{s\frac{\partial\,|\,A(k,s)\,|}{\partial s}\Big|_{k,s_n}} e^{ikz+s_n(k)t}\,dk \tag{2.60}$$

At long times, the integrand goes to zero if $s_r<0$. The stretching contributes to the integral for $-1<k<1$ and the squeezing mode contribute for $-1/a<k<1/a$. All the other modes decay at long times. Thus,

$$\zeta_1(z,t) = \frac{1}{2\pi}\sum_n \int_{-k_{c,n}}^{k_{c,n}} \frac{\hat{\zeta}_{1,0}C_{77}(k,s_n) + \hat{\zeta}_{2,0}C_{78}(k,s_n)}{s\frac{\partial\,|\,A(k,s)\,|}{\partial s}\Big|_{k,s_n}} e^{ikz+s_n(k)t}\,dk \tag{2.61}$$

where $k_{c,n}=1, 1/a$ for the stretching and the squeezing modes, respectively and $n=1$ (stretching),2(squeezing). Now we change the variable of integration from k to s. $\partial|A|/\partial s = -dk/ds^{*}\partial|A|/\partial k$. Using this in eq(2.61) gives,

$$\zeta_1(z,t) = -\frac{1}{2\pi}\sum_n \left[\int_{s(-k_{c,n})}^{0} + \int_{0}^{s(k_{c,n})}\right] \frac{\hat{\zeta}_{1,0}C_{77}(k,s_n) + \hat{\zeta}_{2,0}C_{78}(k,s_n)}{s\frac{\partial\,|\,A(k,s)\,|}{\partial k}\Big|_{k,s_n}} e^{ikz+s_n(k)t}\,ds \tag{2.62}$$

The growth rates, $s_n(k)$, for $k>0$ are shown in figure(2.2). By manipulating the matrix A, it is shown that det(A(k,s))=det(A(-k,s) if k and s are real. Thus $s(-k)=s(k)$. The growth rates go to zero at $k=k_{c,n}$ and then increase to some maximum value s_m, at $k=k_m$. The growth rates then decrease to go to zero at $k=0$. The path of integration in (2.62) which in the k plane is from $-k_{c,n}$ to $+k_{c,n}$ is shown in figure (2.12a). It lies on the real s line because s(k) is purely real for $-k_{c,n}<k<k_{c,n}$. The path goes from $s=0$ to $s=s_m$ and then comes back to $s=0$. This corresponds to $-k_{c,n}<k<0$. The path is the same for $0<k<k_{c,n}$. Thus, the integral in (2.62) becomes a branch cut integral along this path. At long times, the dominant

contribution to the integral comes from an O(1/t) region around $s=s_m$. Substituting $u=s_m - s$, the integral in (2.62) can be written as,

$$\zeta_1(z,t) = -\frac{1}{2\pi} e^{s_m t} \sum_n \int \frac{\hat{\zeta}_{1.0} C_{77}(k_n(u),u) + \hat{\zeta}_{2.0} C_{78}(k_n(u),u)}{(s_m - u) \frac{\partial |A(k,u)|}{\partial k} \Big|_{k_n(u),u}} e^{ik_n(u)z} e^{-ut} du \qquad (2.63)$$

where the integral has to be carried for both the branches of $k=k(s)$, i.e., $-k_{c,n}<k<0$ and $0<k<k_{c,n}$. We first perform the integration for $0<k<k_{c,n}$.

The integrand in (2.63) is of form $f(u)e^{-ut}$ and $t\to\infty$. Let $f(k,s)=\det(A(k,s))$.

Expanding $f(s,k)$ around the maxima, one gets,

$$\begin{aligned} f(s,k) &= f(s_m,k_m) + (k-k_m)f_k + (s-s_m)f_s + \frac{(s-s_m)^2}{2} f_{ss} \\ &+ \frac{(s-s_m)(k-k_m)}{2} f_{sk} + \frac{(k-k_m)^2}{2} f_{kk} + \ldots\ldots \end{aligned} \qquad (2.64)$$

where f_k, f_s, f_{kk}, f_{ss} denote the partial derivatives evaluated at the maxima.

$$f(s,k) = f(s_m,k_m) = f_k = 0 \qquad (2.65)$$

Thus, around the maxima,

$$(k-k_m) = \pm\sqrt{\frac{2f_s}{f_{kk}}}\sqrt{(s_m - s)} + O(s_m - s) = \pm\sqrt{\frac{2f_s}{f_{kk}}}\sqrt{u} + O(u) \qquad (2.66)$$

where (-) corresponds to above the branch cut and (+) below.

Also, at u=0, ds/dk=0 because s has a maximum as u=0. Thus,

$$\frac{\partial f}{\partial k} = -\frac{ds}{dk}\frac{\partial f}{\partial s} = 0 \quad \text{at } u=0 \qquad (2.67)$$

$$\frac{\partial f}{\partial k} = \frac{\partial^2 f}{\partial k^2}\Big|_{k=k_m}(k - k_m) + O((k - k_m)^2) \qquad (2.68)$$

Expanding the integrand in (2.63) around u=0 and using (2.64)- (2.68), to leading order, one gets,

$$\zeta_1(z,t) = -\frac{1}{2\pi}e^{s_m t}\sum_n \frac{\hat{\zeta}_{1.0}C_{77} + \hat{\zeta}_{2.0}C_{78}}{s_m\sqrt{2 f_{kk} f_s}}\Big|_{k_{m.n},u=0} e^{ik_{m.n}z}\int \pm\frac{1}{\sqrt{u}}e^{-ut}du \qquad (2.69)$$

The integration path is above and below the branch cut as shown in fig 2.12b. The branch cut integration can be performed using the method of steepest descent. As t→∞, the leading contribution to the integral comes from the region of O(1/t) around u=0. Substituting z=ut in (2.69), one gets,

$$\zeta_1(z,t) = -\frac{1}{2\pi}\frac{e^{s_m t}}{\sqrt{t}}\sum_n \frac{\hat{\zeta}_{1.0}C_{77} + \hat{\zeta}_{2.0}C_{78}}{s_m\sqrt{2 f_{kk} f_s}}\Big|_{k_{m.n},u=0} e^{ik_{m.n}z}\int \pm\frac{1}{\sqrt{z}}e^{-z}dz \qquad (2.70)$$

where the branch cut for z extends from 0 t0 ∞.

The contribution to the integral $1/\sqrt{z}\, e^{-z}$ from the path around z=0 is zero. Thus the integral in (2.70) reduces to,

$$\int_{\infty}^{0}\frac{1}{-\sqrt{z}}e^{-z}dz + \int_{0}^{\infty}\frac{1}{\sqrt{z}}e^{-z}dz = 2\int_{0}^{\infty}\frac{1}{\sqrt{z}}e^{-z}dz = 2\sqrt{\pi} \qquad (2.71)$$

Using this in (2.70), one gets, and performing the integration for k<0, one gets,

$$\zeta_1(z,t) = \sqrt{\pi}\sum_n \begin{matrix} 2\dfrac{e^{s_m}}{\sqrt{t}}\Big[e^{ik_m z}\dfrac{\zeta_{1.0}(k_m, s_m)C_{77}(k_m, s_m) + \zeta_{2.0}C_{78}(k_m, s_m)}{s_m\sqrt{-2 f_s f_{kk}(s_m, k_m)}} + \\ e^{-ik_m z}\dfrac{\zeta_{1.0}(-k_m, s_m)C_{78}(k_m, s_m) + \zeta_{2.0}C_{78}(-k_m, s_m)}{s_m\sqrt{-2 f_s f_{kk}(s_m, -k_m)}}\Big] \end{matrix} \qquad (2.72)$$

Similarly,

$$\zeta_2(z,t)=\sqrt{\pi}\sum_n \begin{array}{l} 2\dfrac{e^{s_m}}{\sqrt{t}}\Big[e^{ik_m z}\dfrac{\zeta_{1.0}(k_m,s_m)C_{87}(k_m,s_m)+\zeta_{2.0}C_{87}(k_m,s_m)}{s_m\sqrt{-2f_s f_{kk}(s_m,k_m)}}+ \\ \qquad e^{-ik_m z}\dfrac{\zeta_{1.0}(-k_m,s_m)C_{87}(k_m,s_m)+\zeta_{2.0}C_{88}(-k_m,s_m)}{s_m\sqrt{-2f_s f_{kk}(s_m,-k_m)}}\Big] \end{array} \tag{2.73}$$

Thus, the long time solution depends on the maxima of the growth rate and goes as $\exp(s_m t)/\sqrt{t}$. This result differs from the normal mode result because of the $\sqrt{t}$ in the denominator. But the exponential dependence stays same. Thus, one needs to evaluate the maximum growth rate to look at the long time behavior.

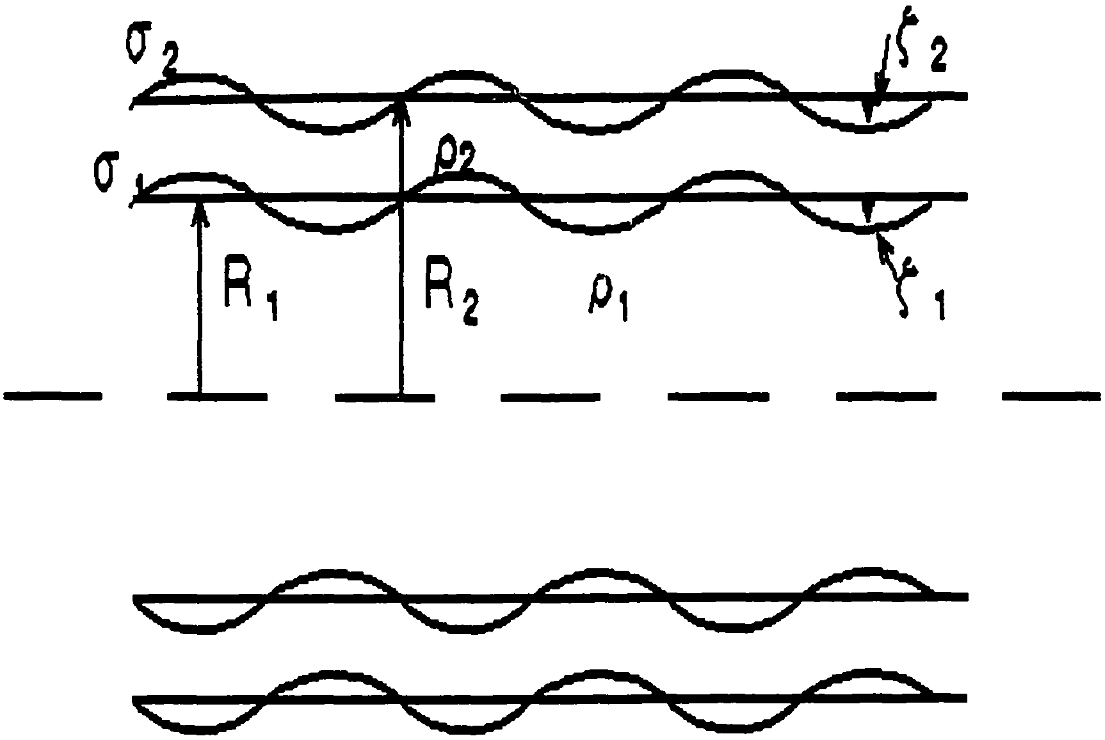

Figure 1.1. Geometry of the compound jet

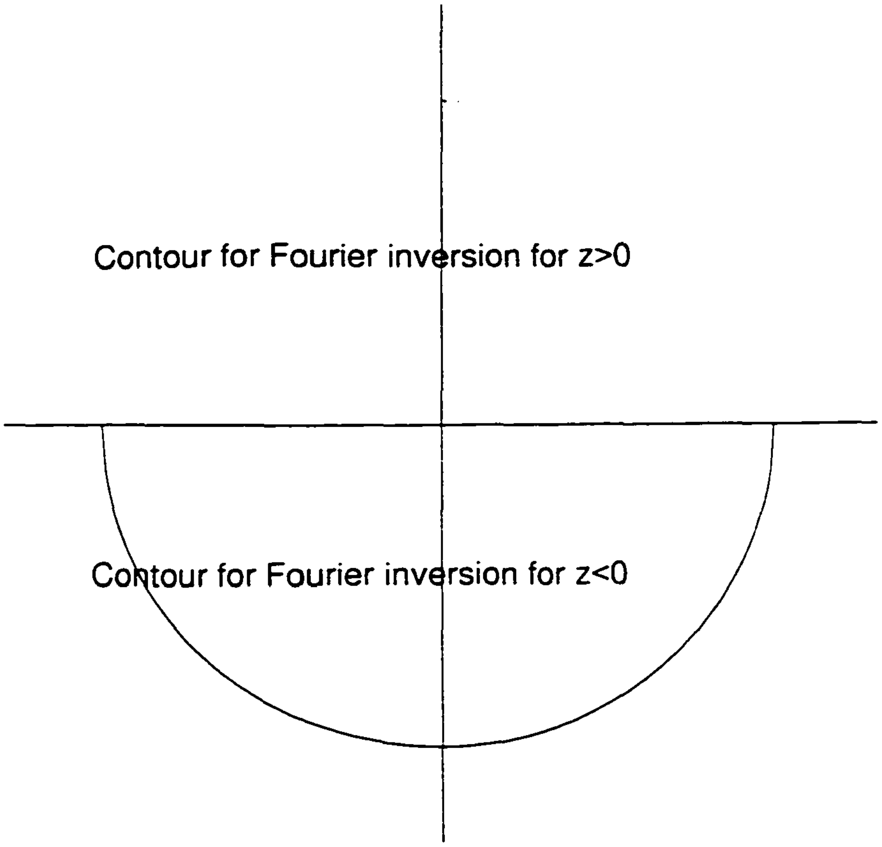

Figure 1.2. Contours for Fourier Inversion

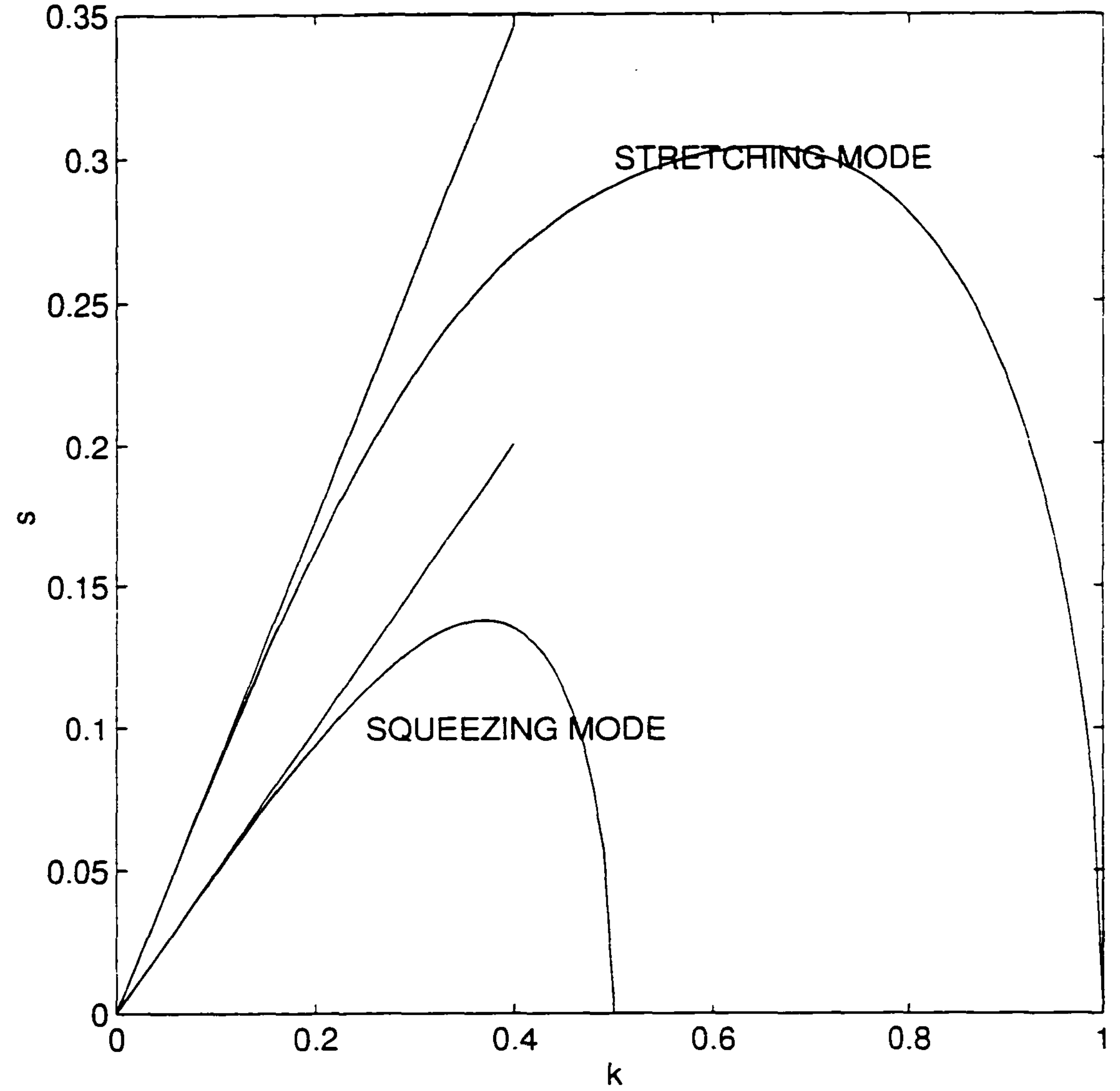

Figure 1.3. Growth rate, s_r, of the strtching and the squeezing modes as a function of wave number. $\beta=1$, $\gamma=2$, $a=2$

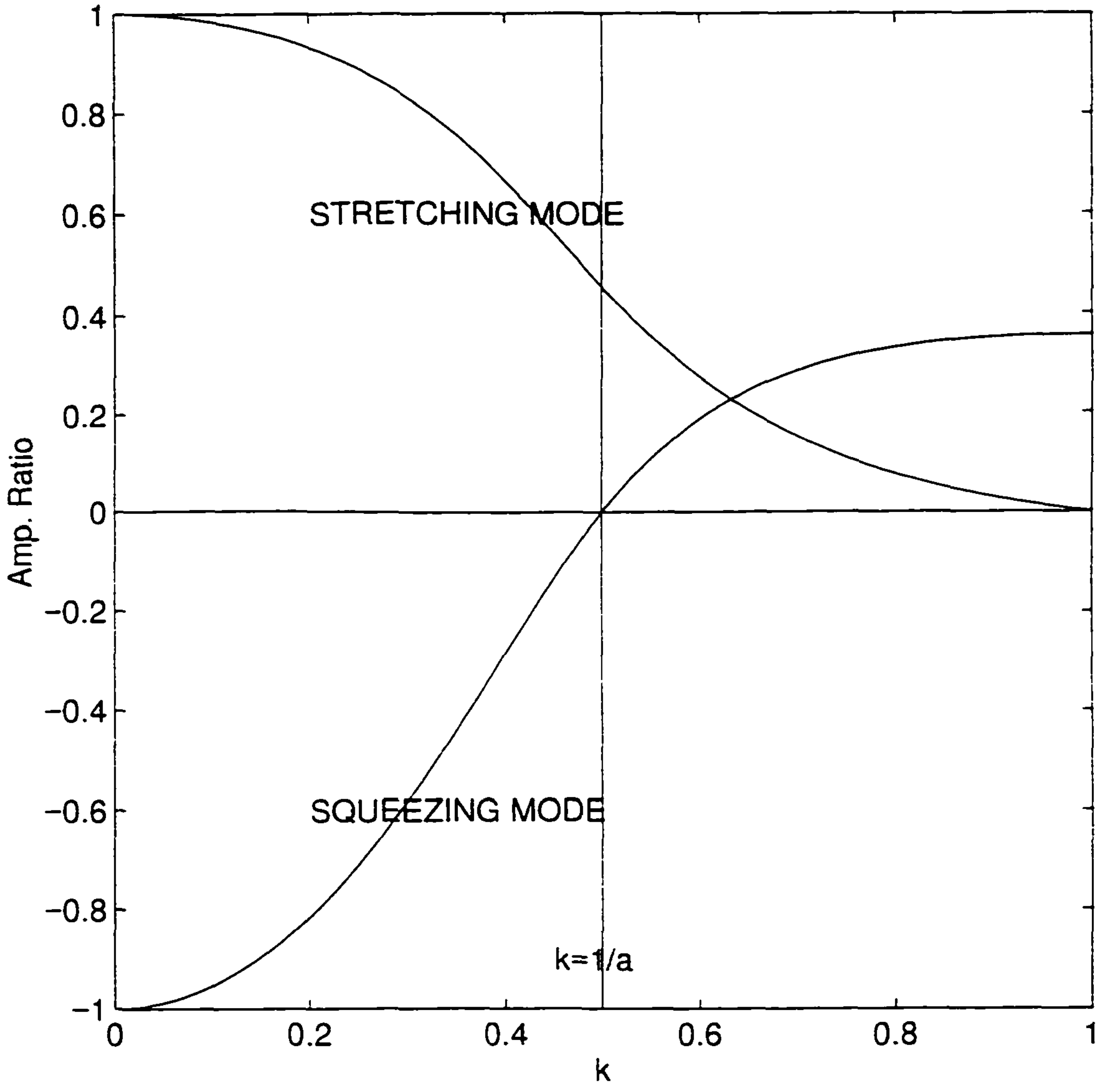

Figure 1.4. Amplitude ratio, $\tilde{\zeta}_2 / \tilde{\zeta}_1$ for the Stretching and the Squeezing modes as a function of the wave number. $\beta=1$, $\gamma=2$, a=2

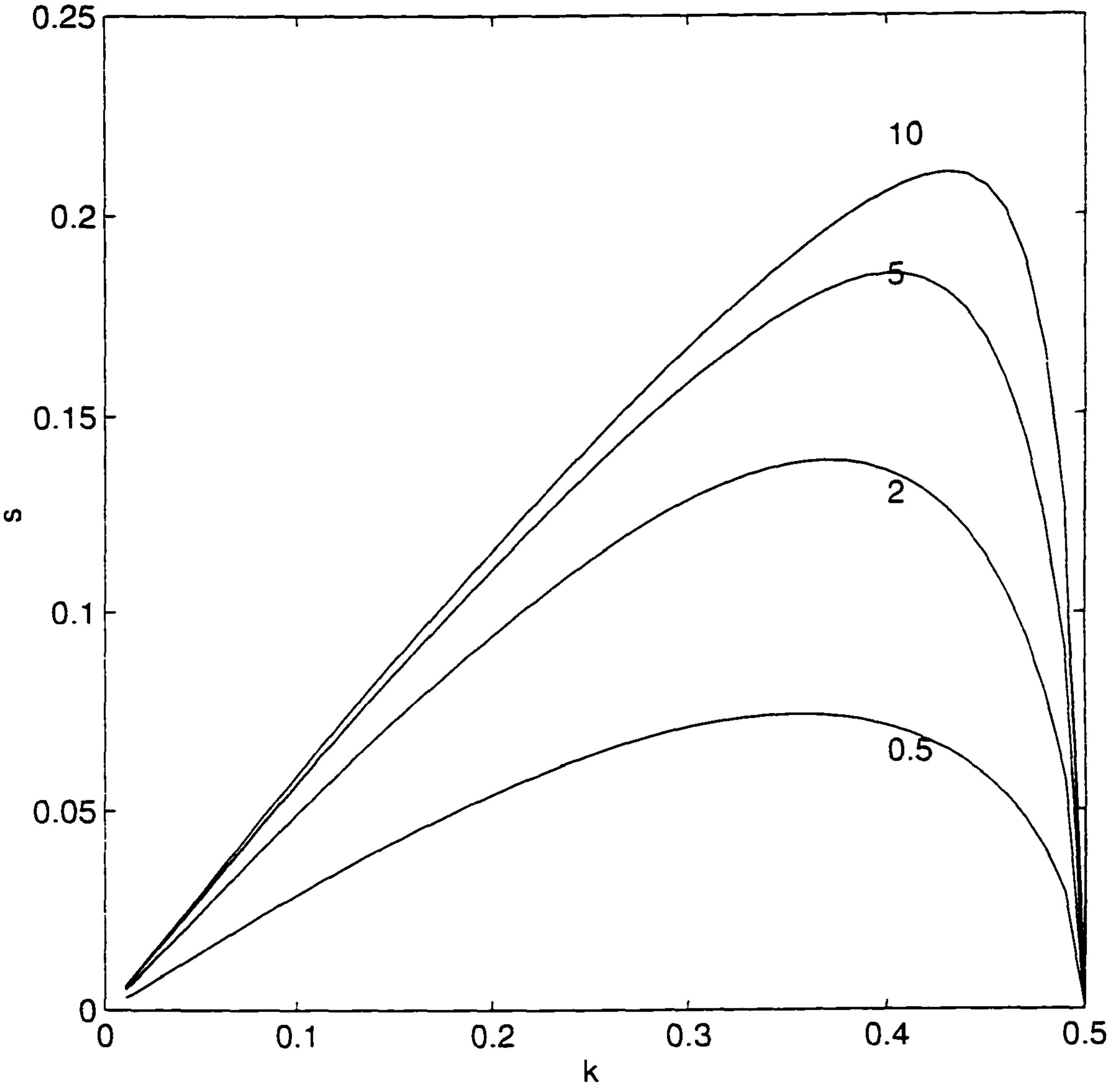

Figure 1.5. Effect of the surface tension ratio (γ) on the growth rate of the squeezing mode. The numbers on the curves denote the values of γ. β=1, a=2.

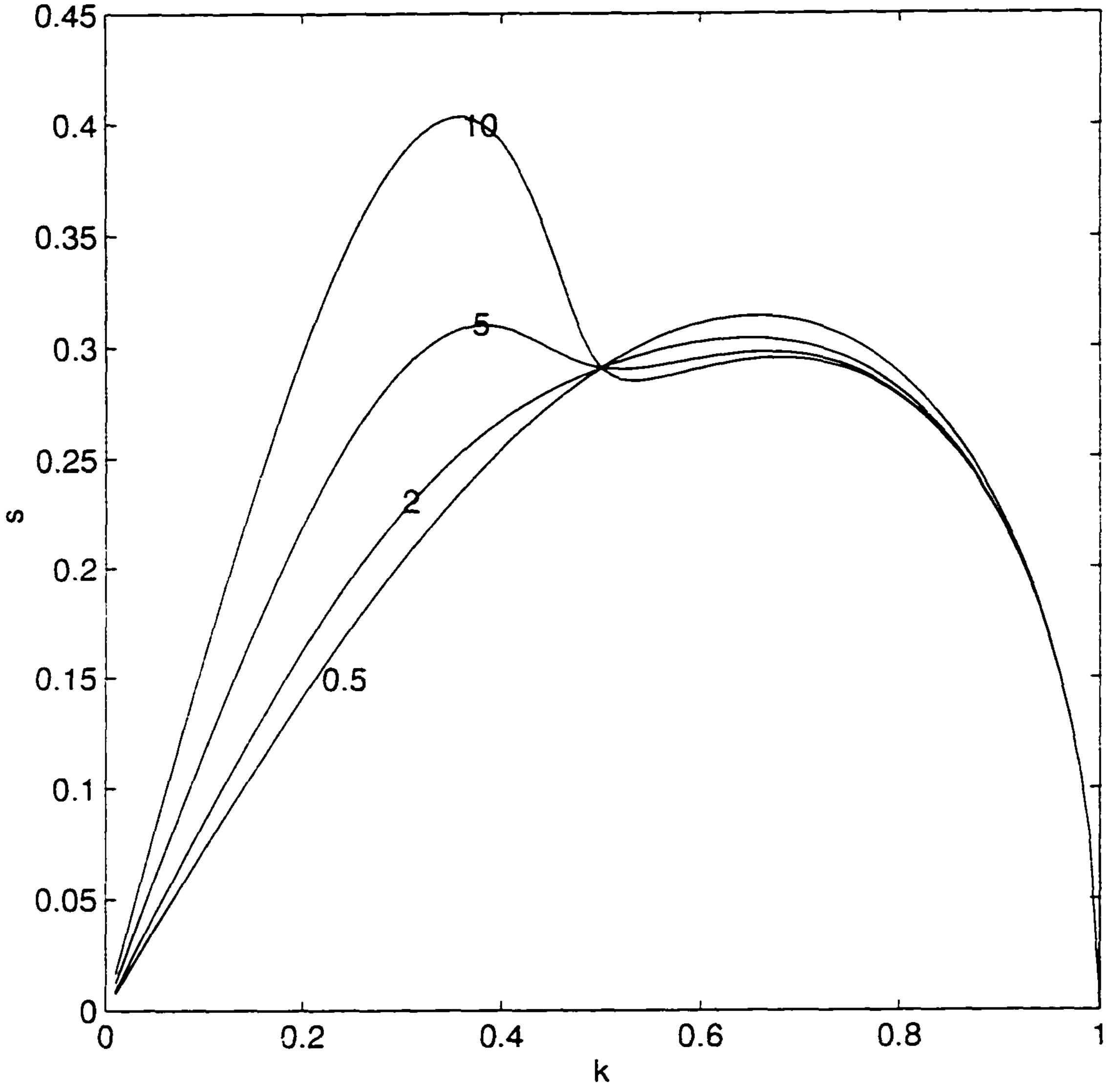

Figure 1.6. Effect of the surface tension ratio (γ) on the growth rate of the stretching mode. The numbers on the curves denote the values of γ. $\beta=1$, $a=2$.

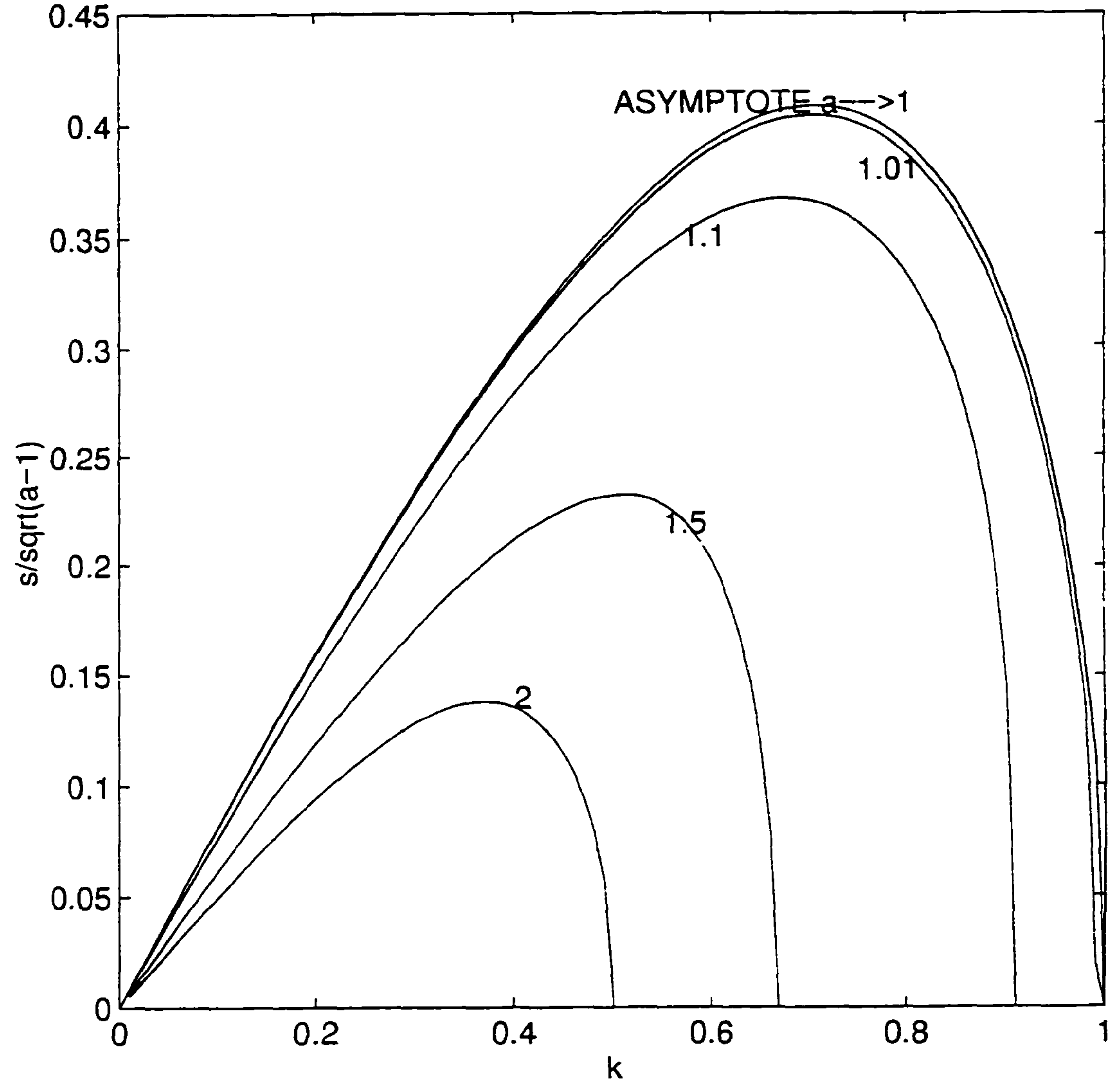

Figure 1.7. Effect of the radii ratio (a) on the growth rate of the squeezing mode. The numbers on the curves denote the values of a. β=1, γ=2.

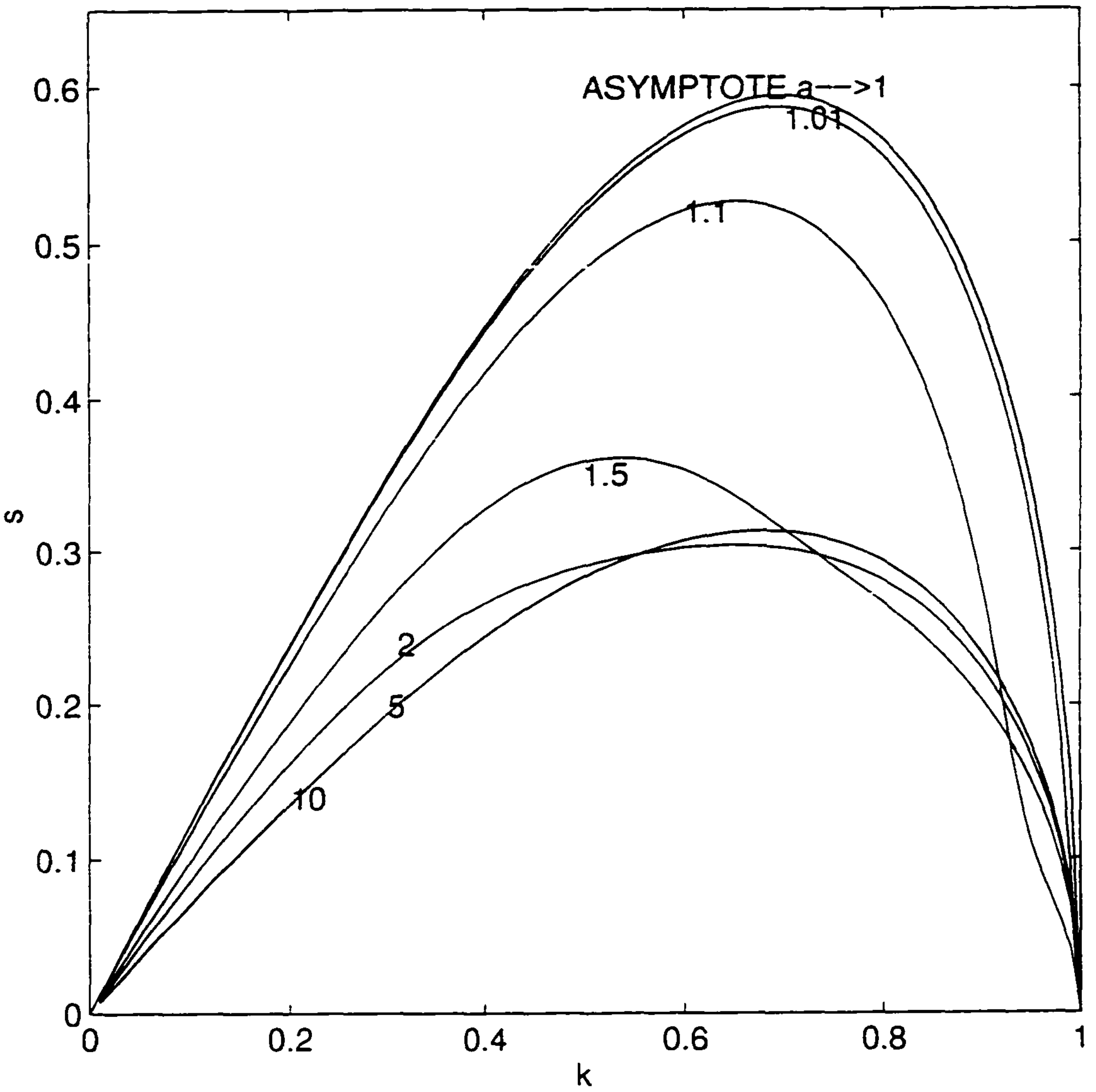

Figure 1.8. Thin film limit and a→∞ limit for the stretching for the stretching mode. The numbers on the curves denote the values of a. $\beta=1, \gamma=2$.

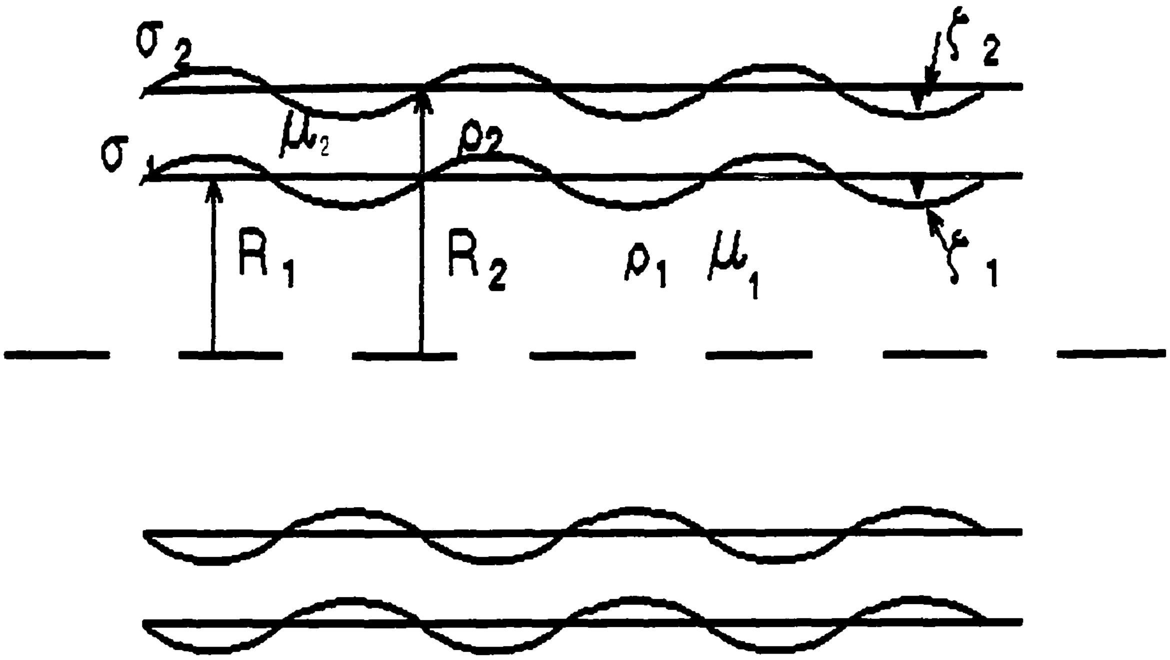

Figure 2.1 Geometry of the viscous ccmpound jet

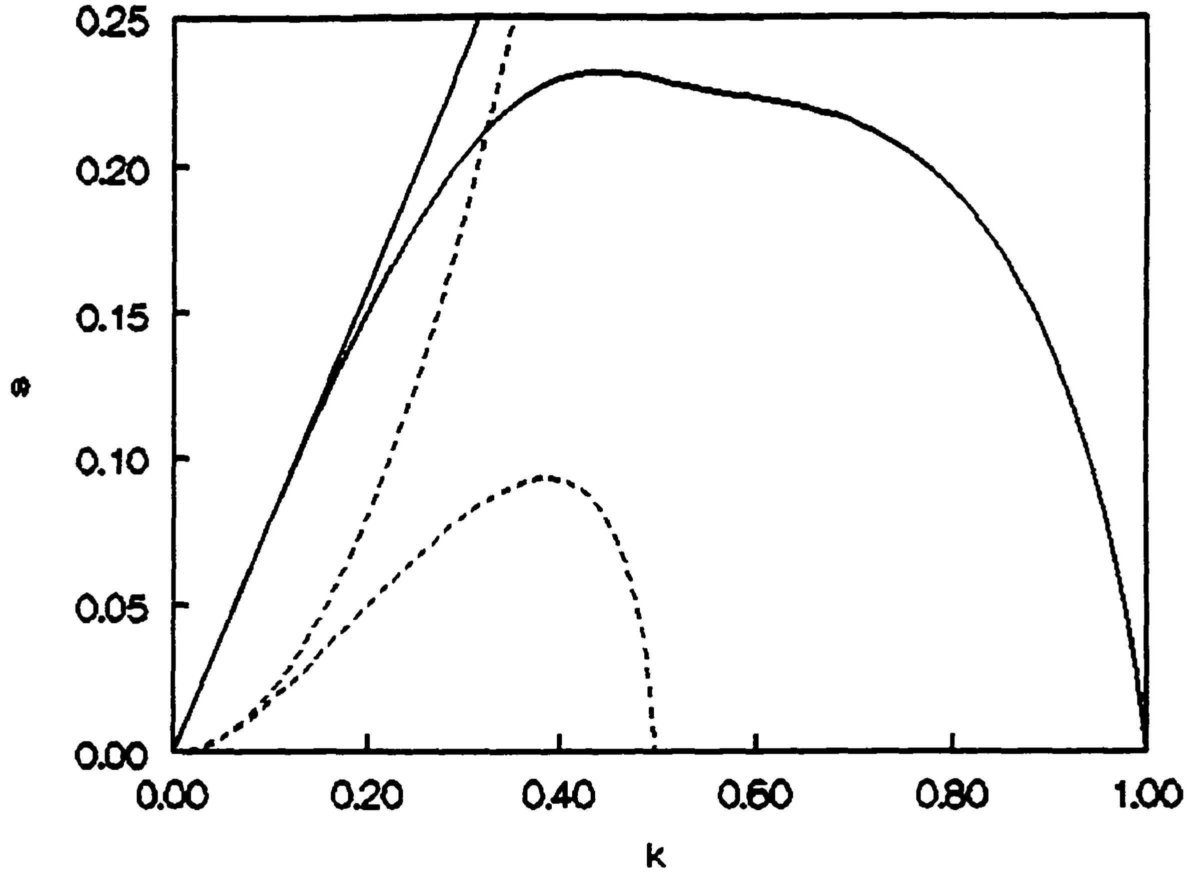

Figure 2.2 The two growing temporal modes. a=2, d=1,γ=2, m=l, J=1000 ________ (stretching), -------- (squeezing)

TWO TEMPORAL UNSTABLE MODES

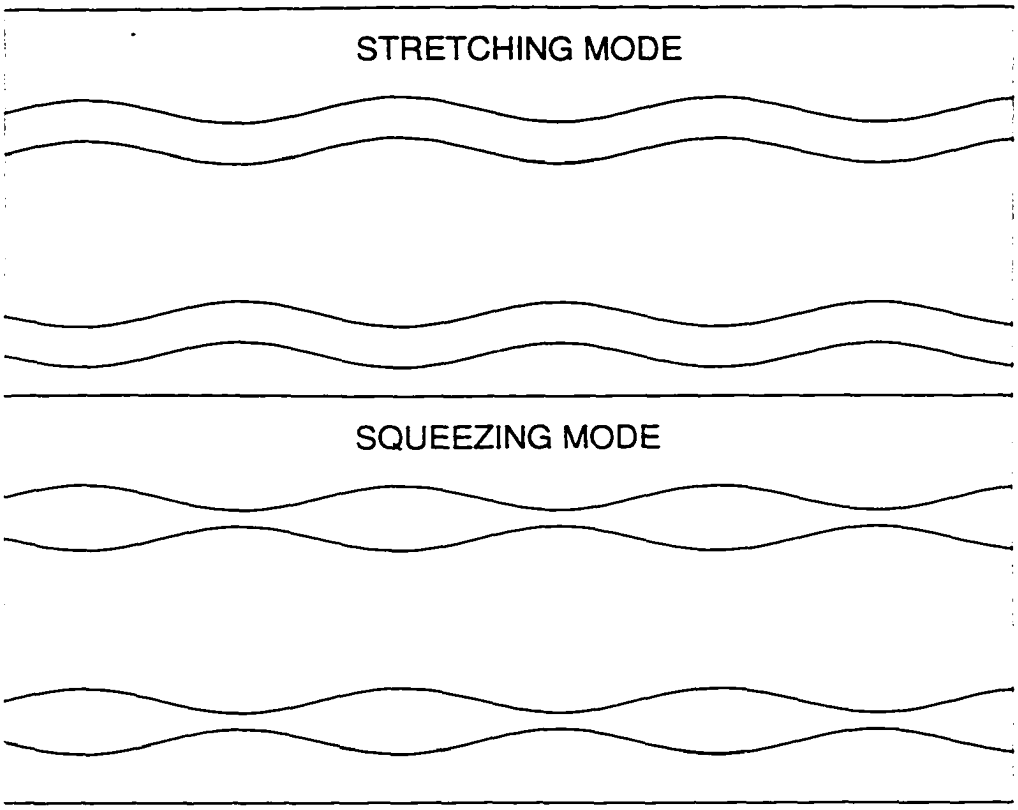

Figure 2.3 The stretching and the squeezing modes

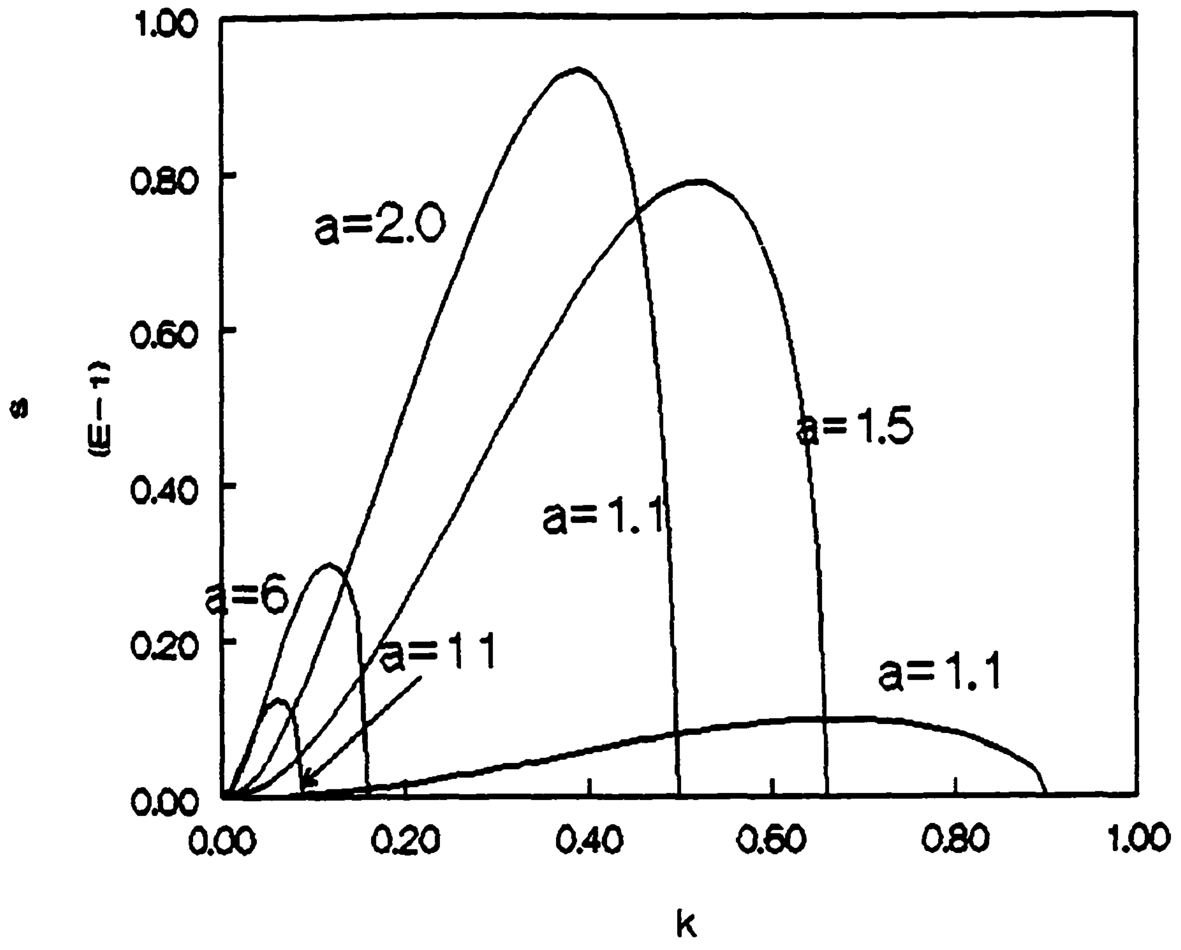

Figure 2.4 Thin film (ε→0) limit for the squeezing mode.
d=l, γ=2, m=l, J=l 000

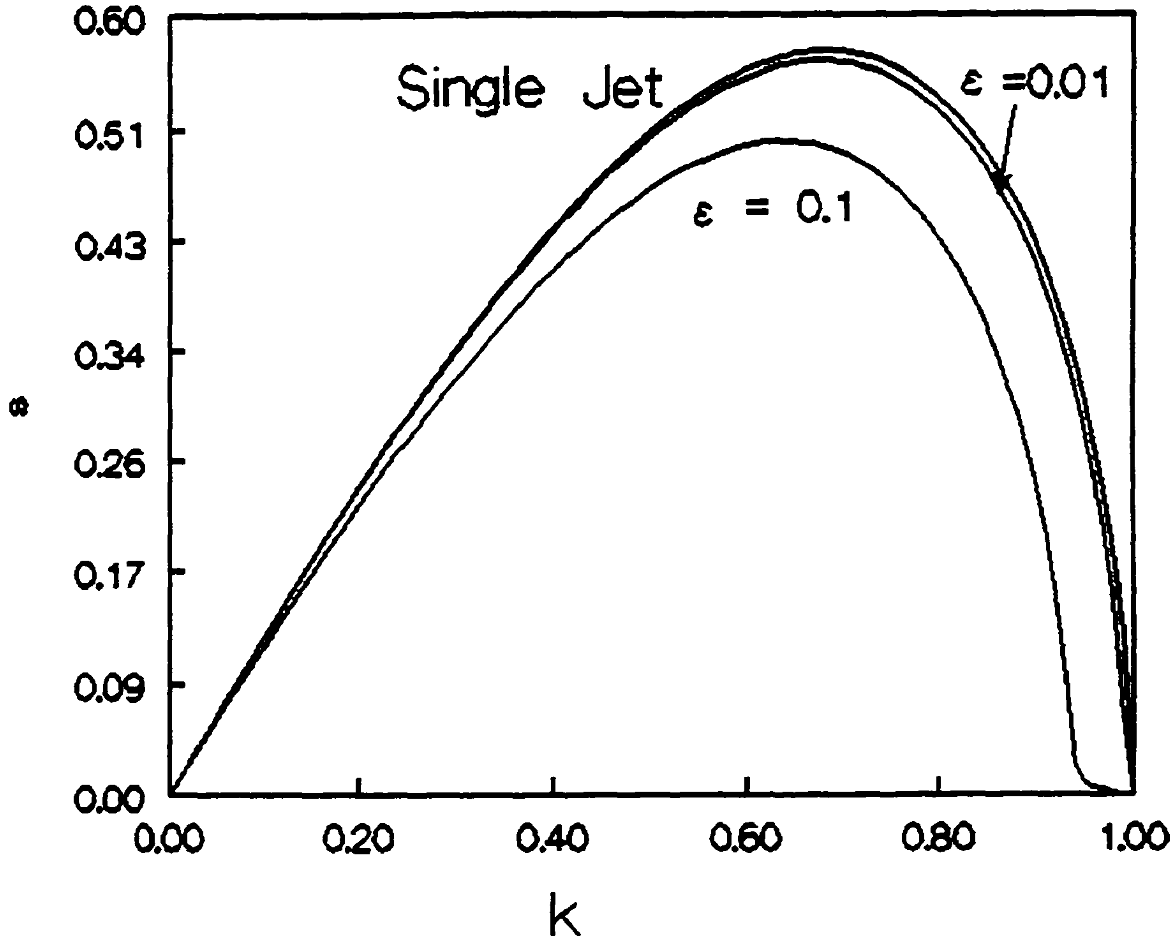

Figure 2.5 Thin film (ε→0) limit for the stretching mode.
d=l, γ=2, m=l, J=1000

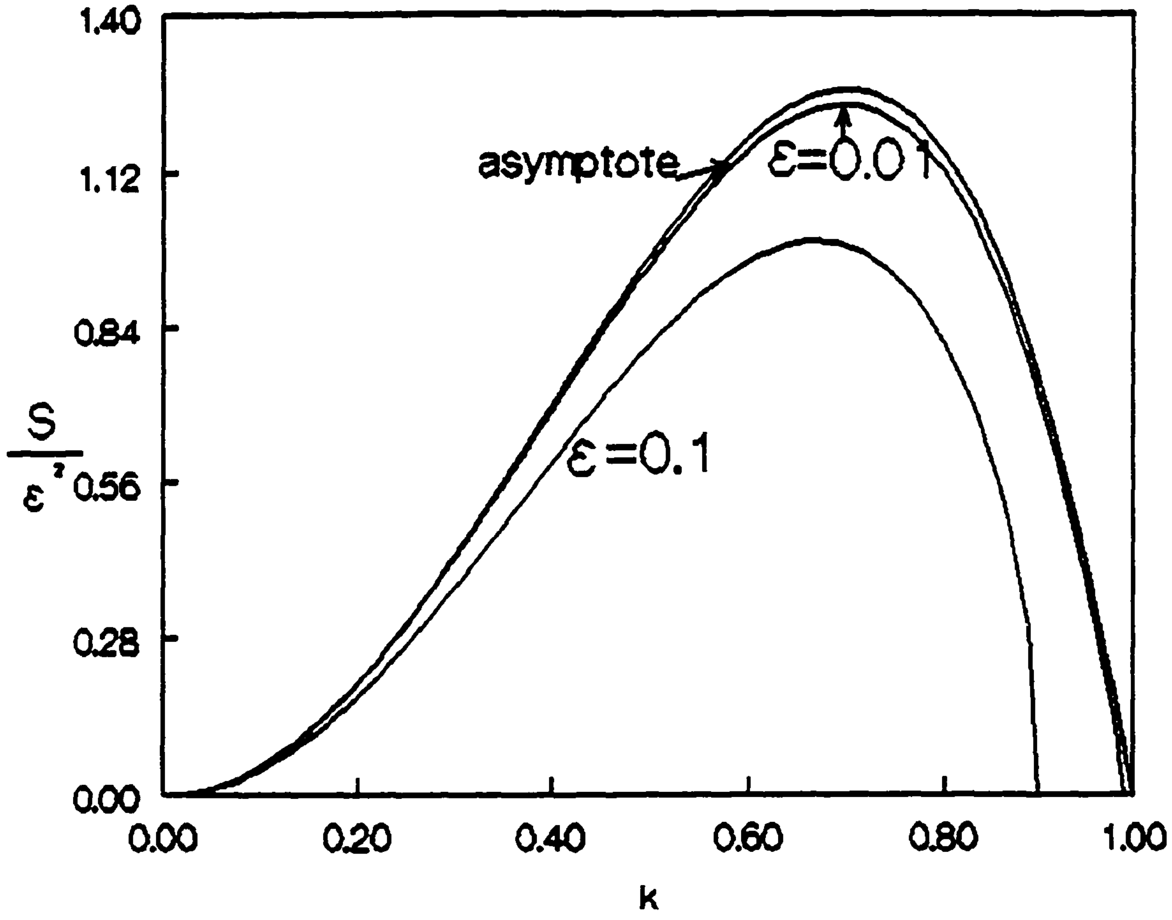

Figure 2.6 a→∞, limit for the squeezing mode.
d=l, γ=2, m=1, J=l 000

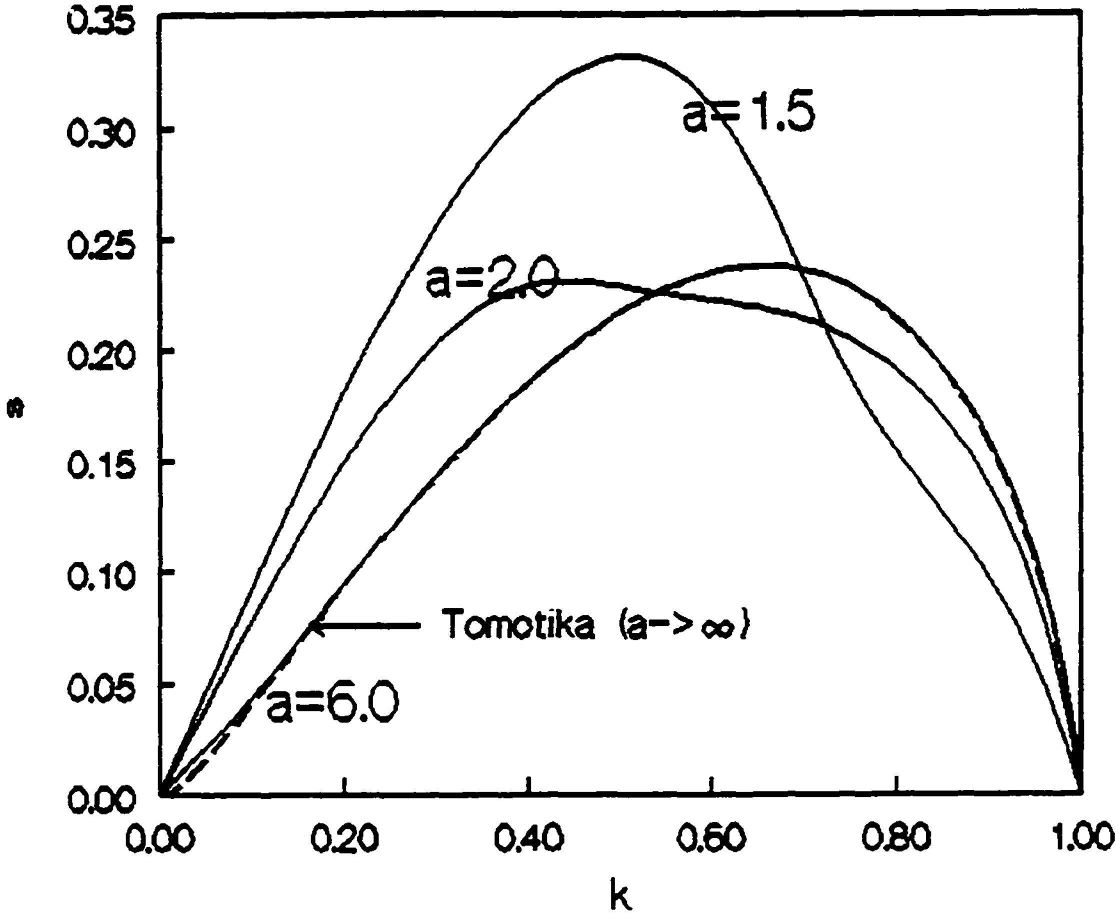

Figure 2.7 a→∞ limit for the stretching mode.
d=l, γ=2, m=1, J=l 000

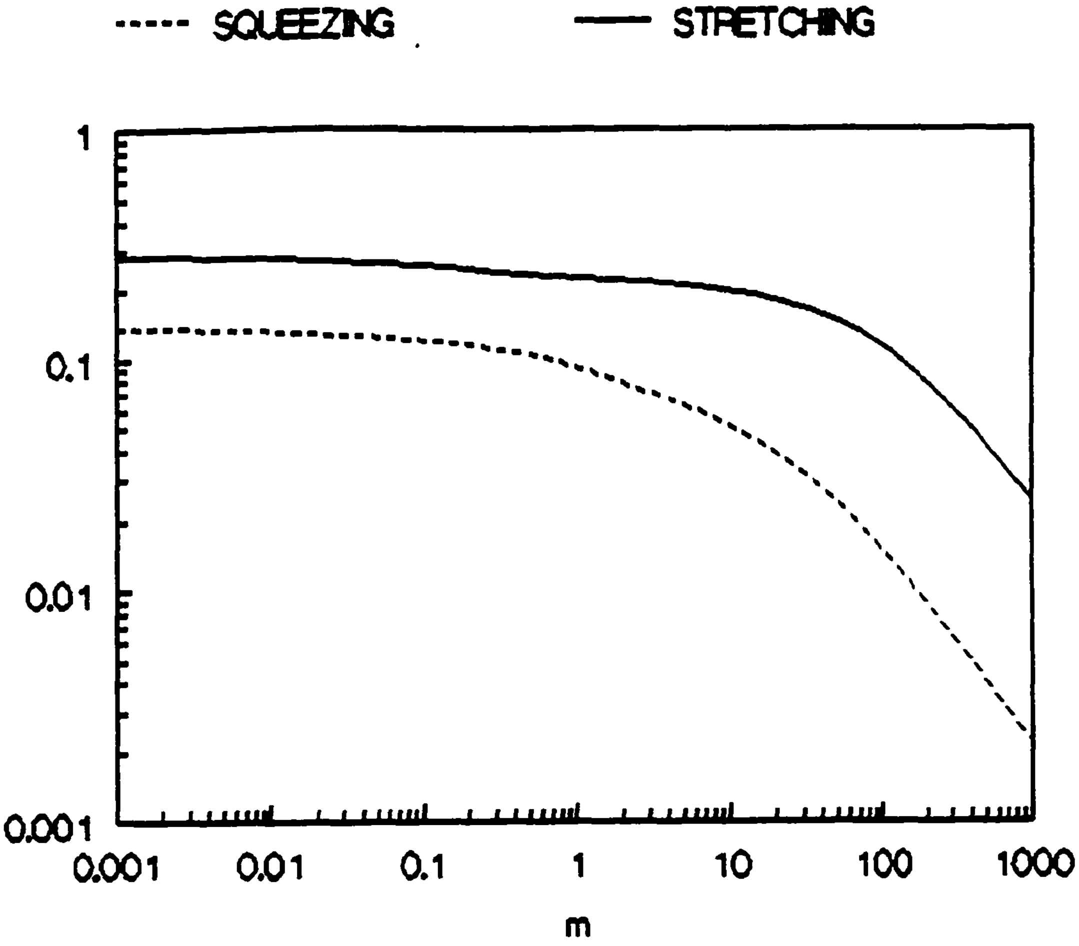

Figure 2.8a Effect of the viscosity ratio (m) on s_m. d=1,a=2, γ=2, J=1000
_______ (stretching), ------- (squeezing)

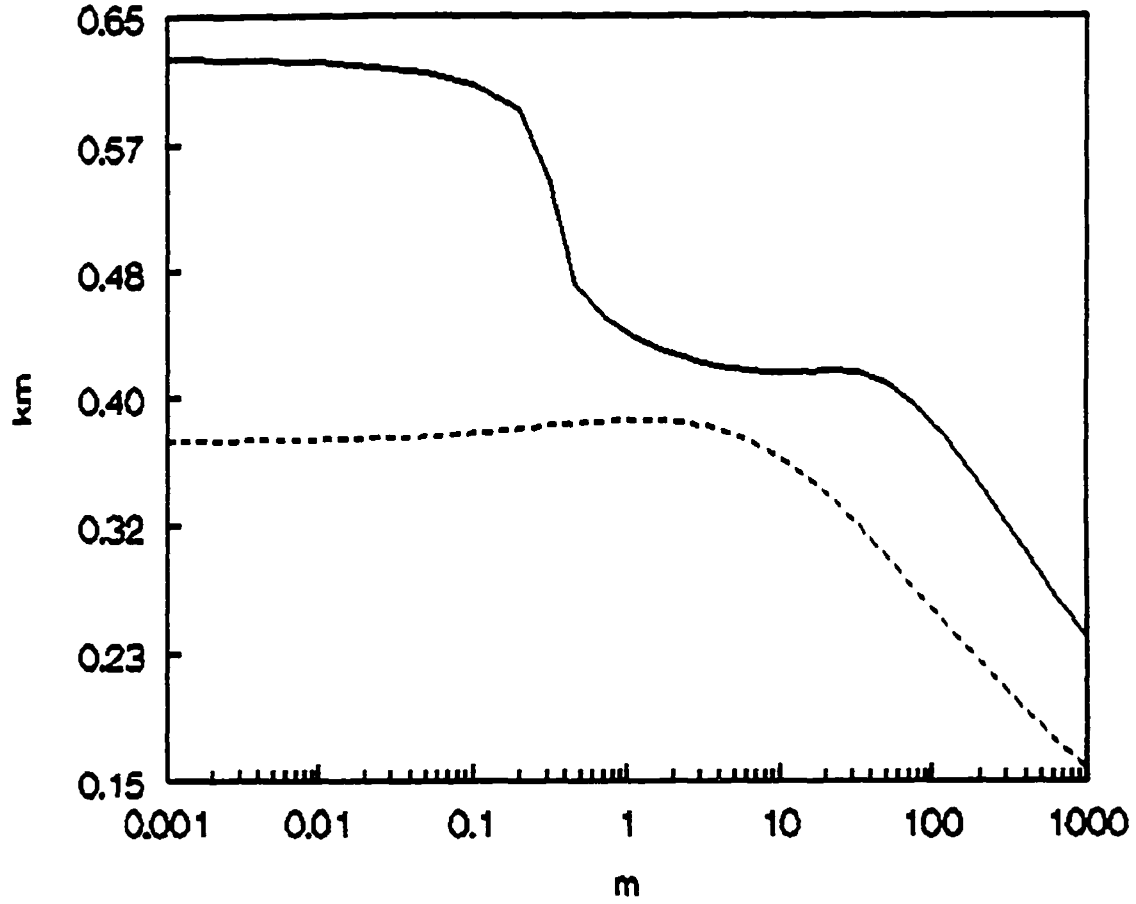

Figure 2.8b Effect of the viscosity ratio (m) on k_m. d=1,a=2, γ=2, J=1000
_______ (stretching), -------- (squeezing)

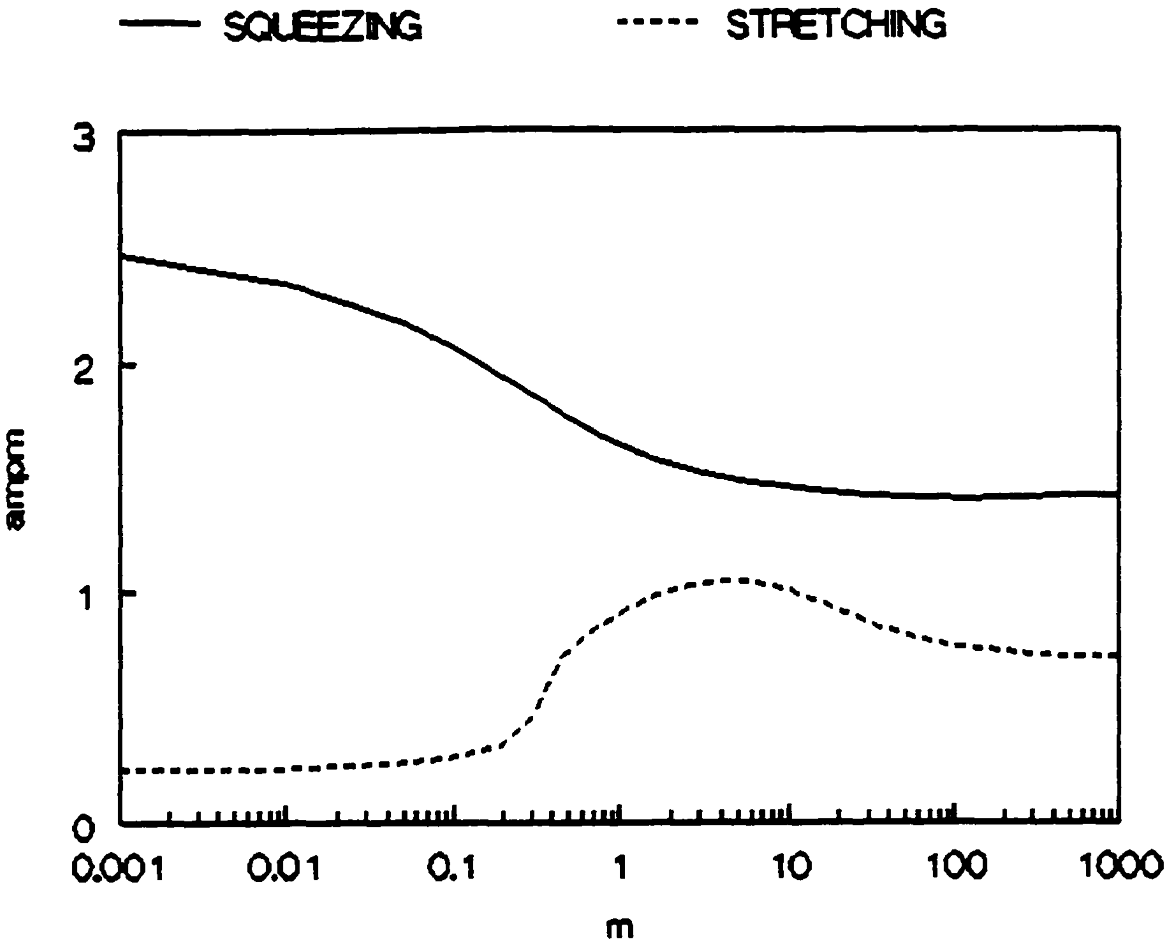

Figure 2.8c Effect of the viscosity ratio (m) on amp_m. d=1,a=2, γ=2, J=1000
_______ (stretching), -------- (squeezing)

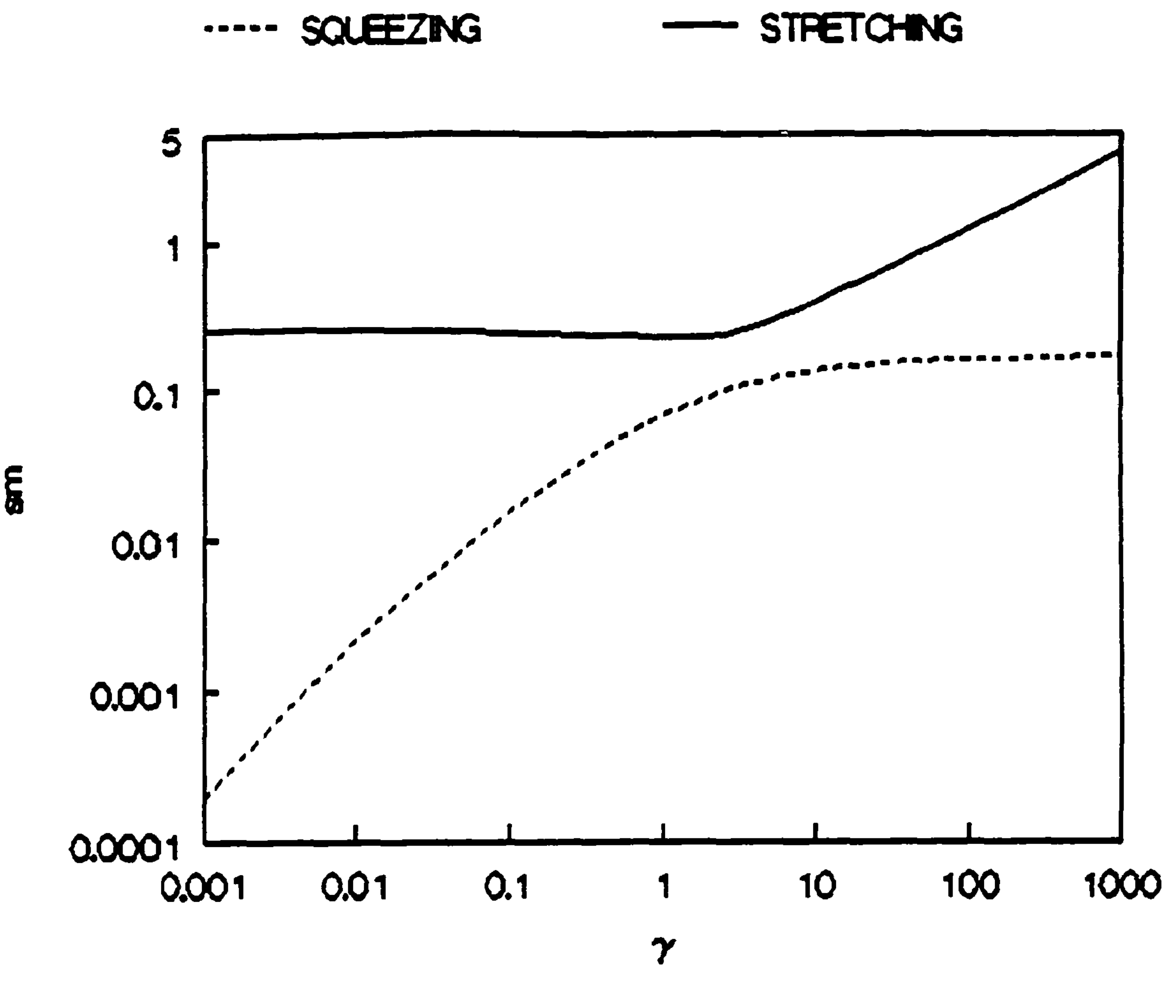

Figure 2.9a Effect of the surface tension ratio (γ) on s_m. d=1,a=2,m=1, J=1000
_______ (stretching), -------- (squeezing)

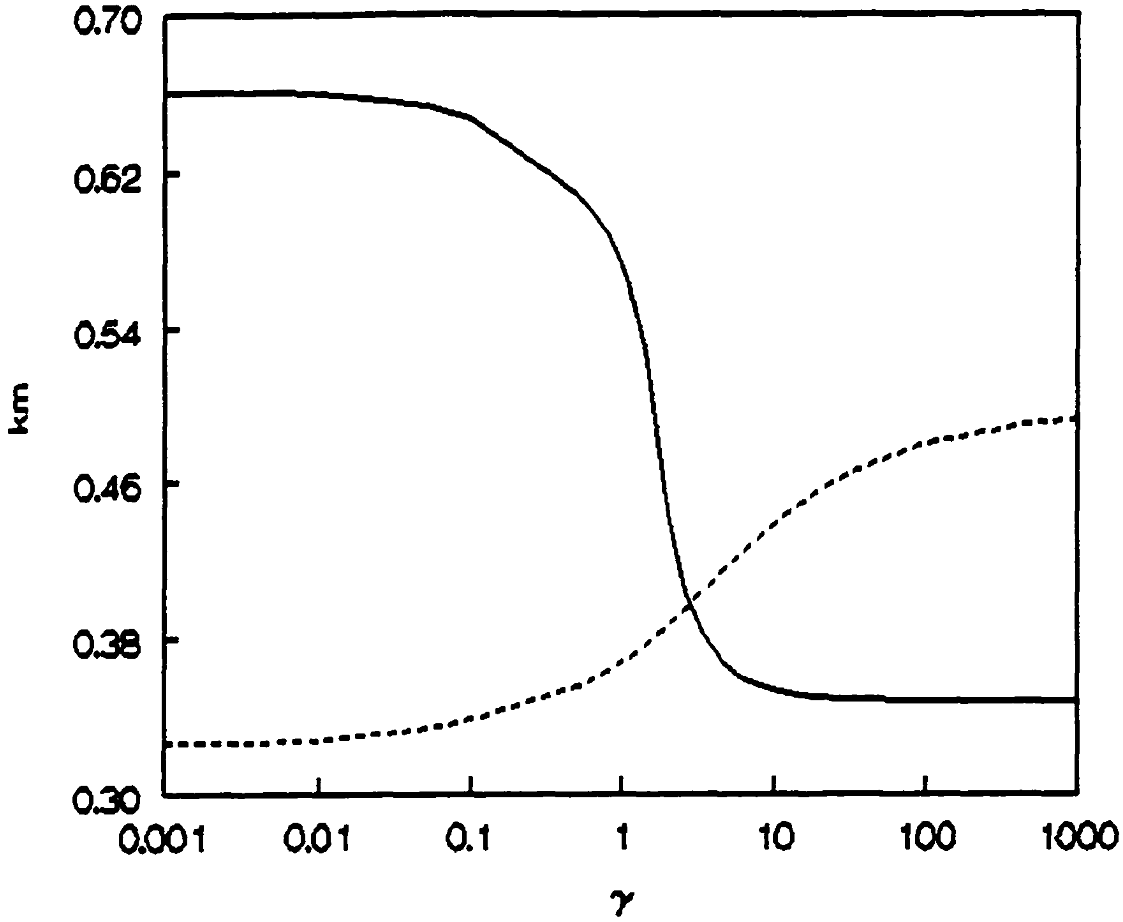

Figure 2.9b Effect of the surface tension ratio (γ) on k_m. d=1,a=2,m=1, J=1000
_______ (stretching), ------- (squeezing)

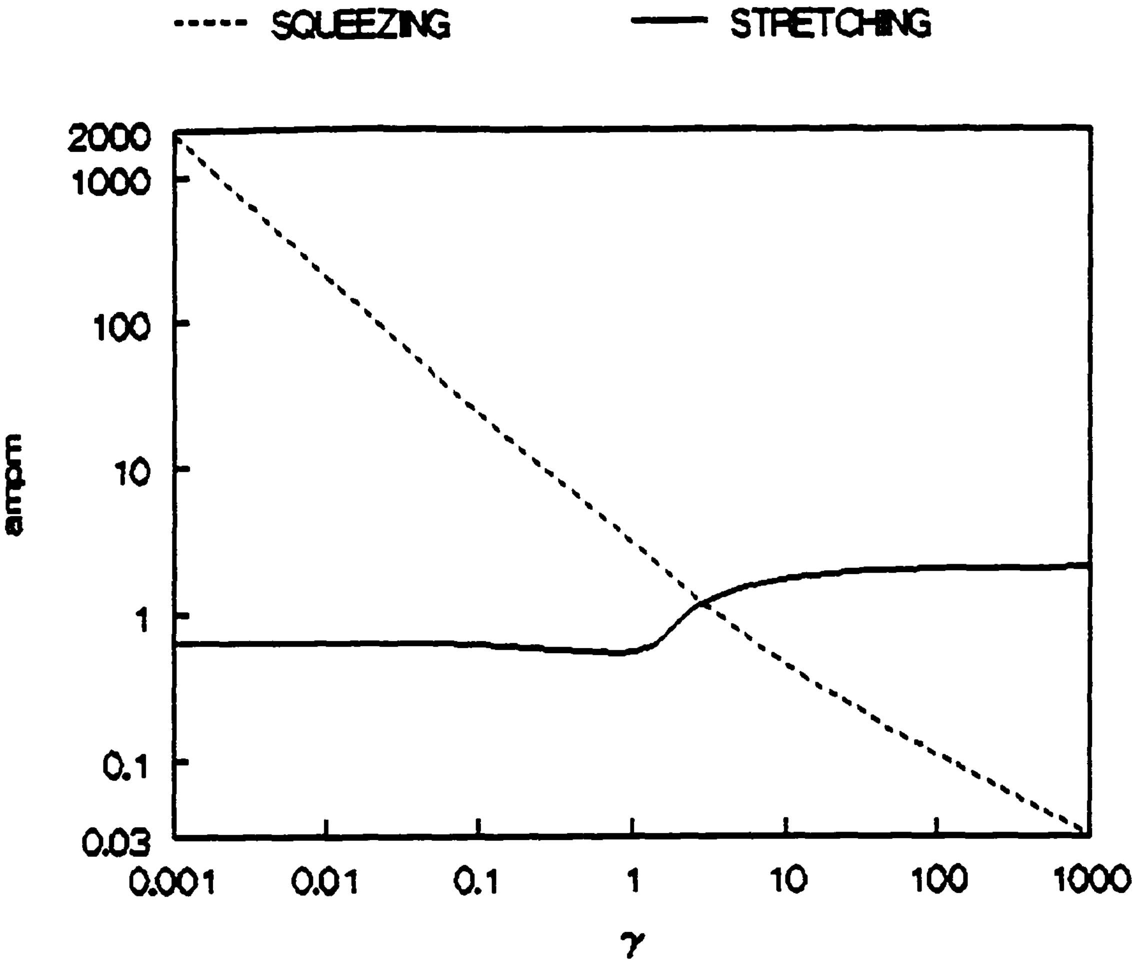

Figure 2.9c Effect of the surface tension ratio (γ) on amp_m. d=1,a=2, m=1, J=1000 _______ (stretching), -------- (squeezing)

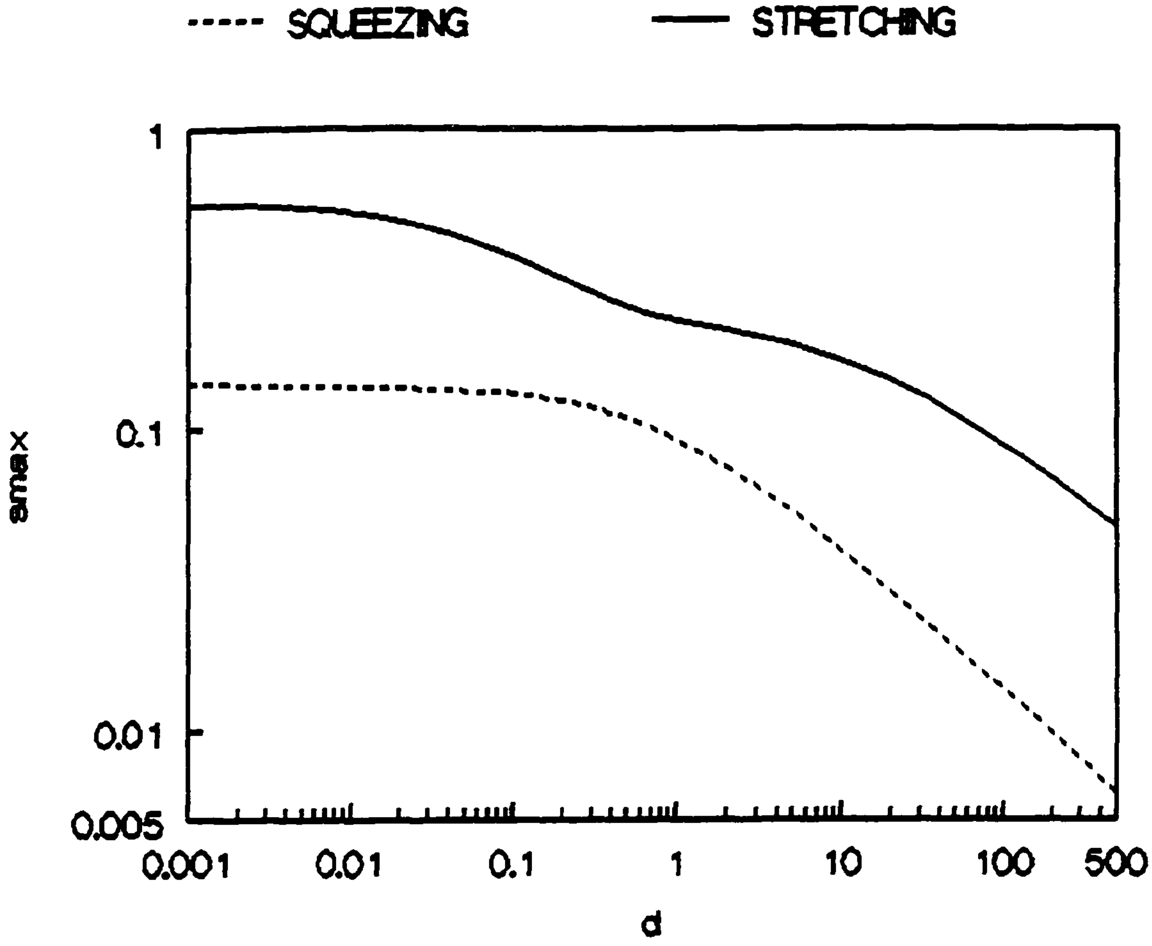

Figure 2.10a Effect of the density ratio (d) on s_m. m=1,a=2, γ=2, J=1000
________ (stretching), -------- (squeezing)

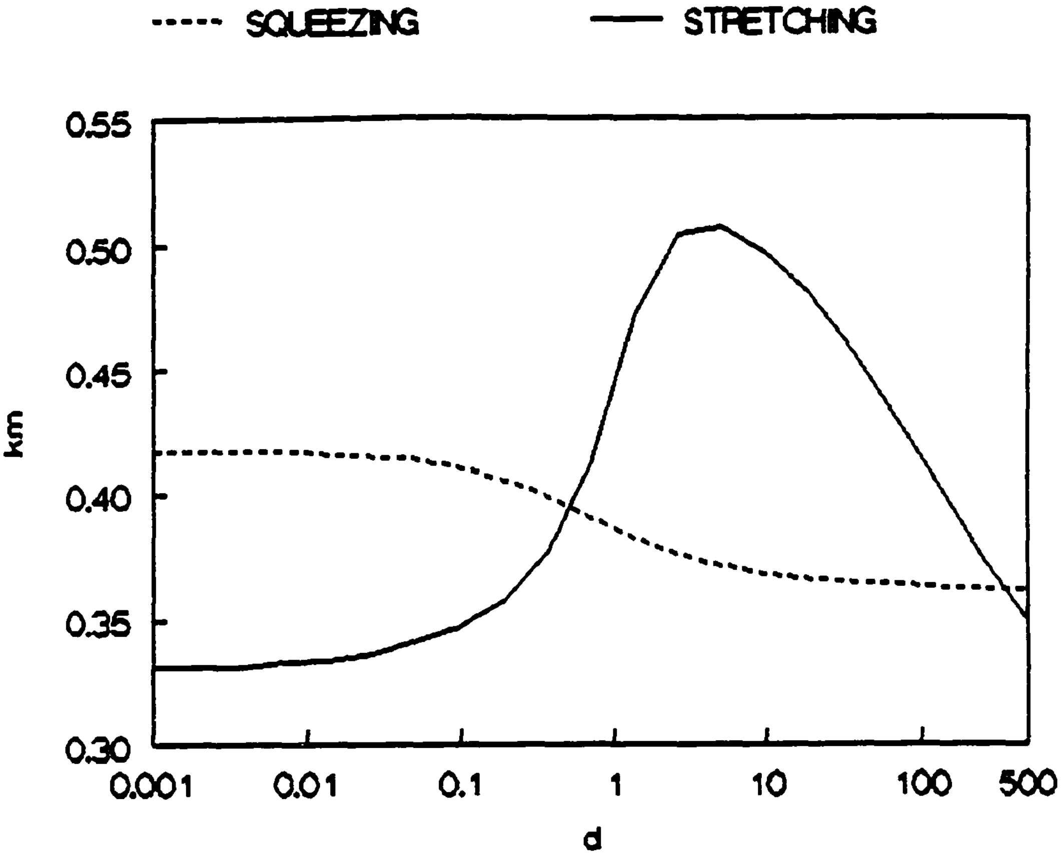

Figure 2.10b Effect of the density ratio (d) on k_m. m=1,a=2, γ=2, J=1000

________ (stretching), --------- (squeezing)

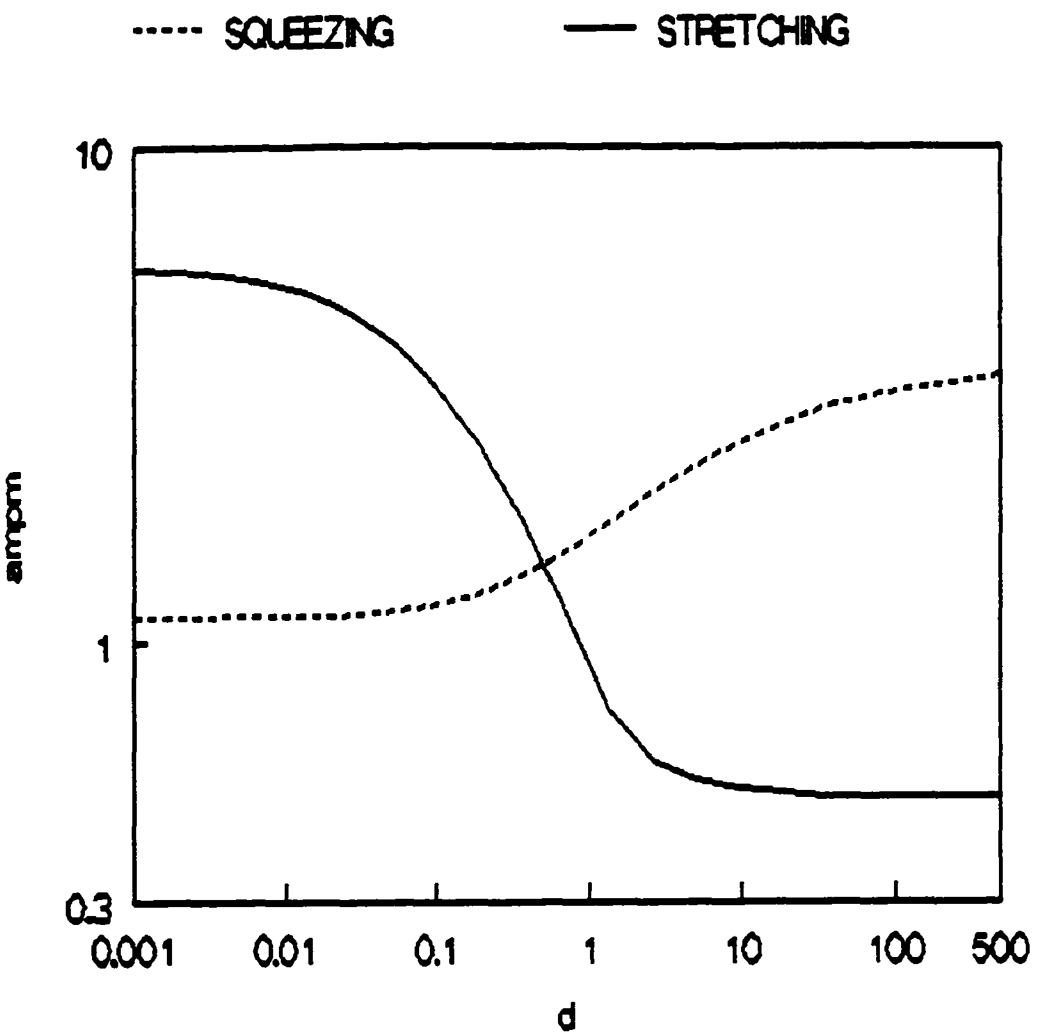

Figure 2.10c Effect of the density ratio (d) on amp_m. m=1,a=2, γ=2, J=1000
_______ (stretching), -------- (squeezing)

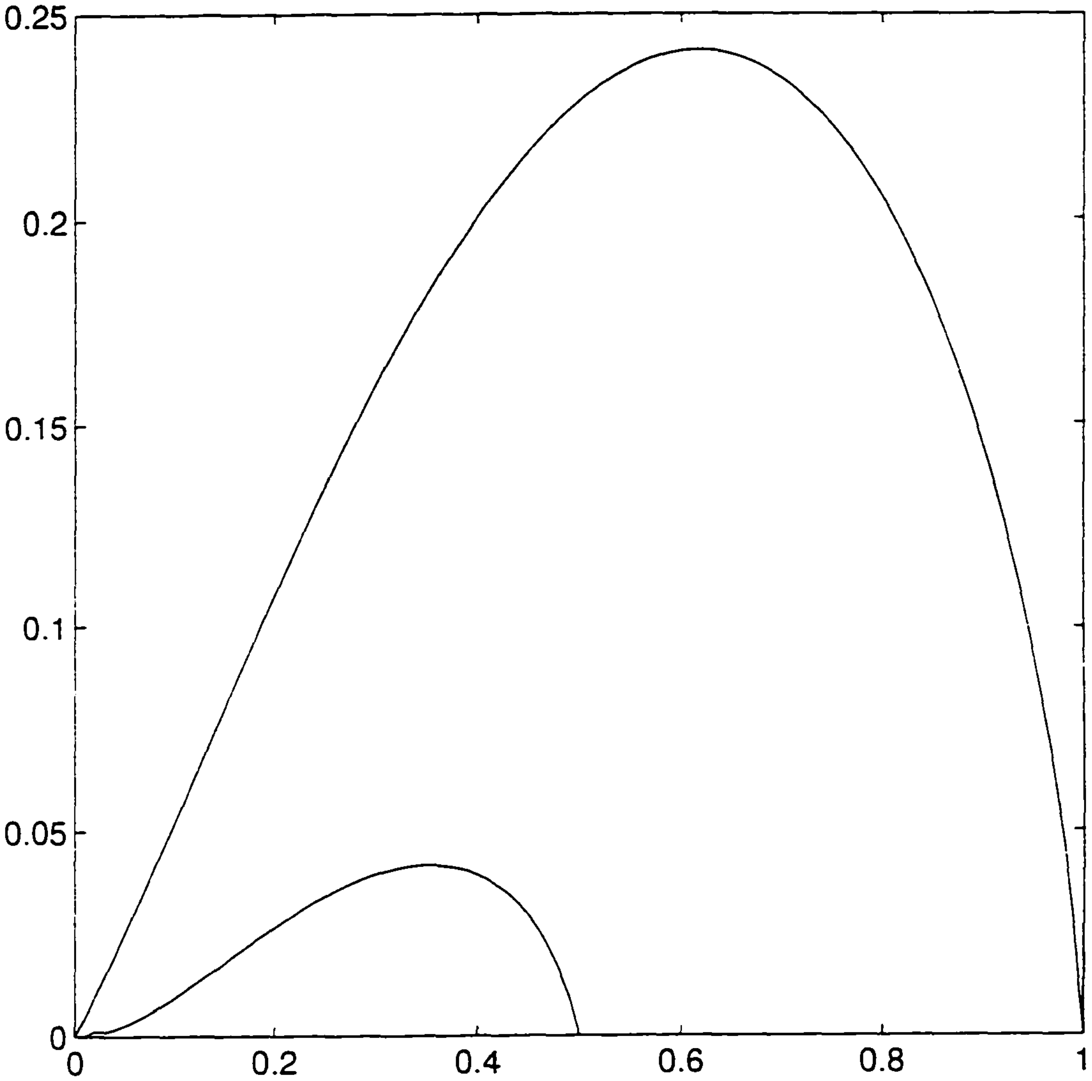

Figure 2.11 Comparison with experiment. γ=0.4, a=2, d=1, J=937

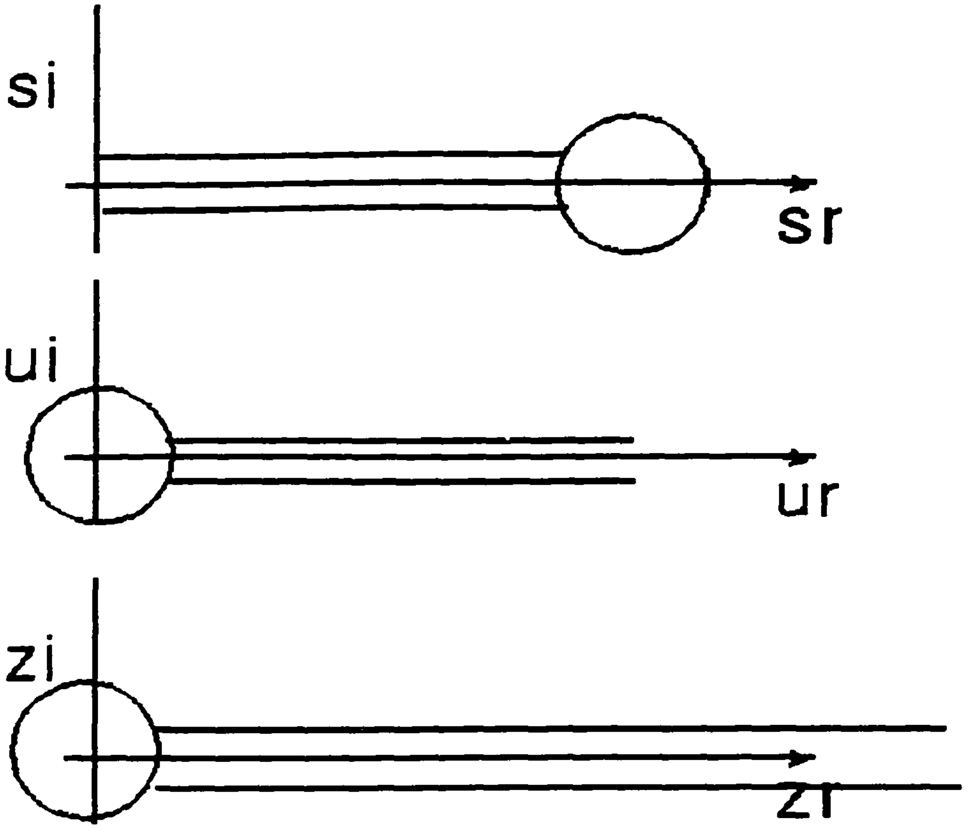

Figure 2.12 Branch cut contour in the s, u, z plane

CHAPTER 3

SPATIAL ANALYSIS OF AN INVISCID COMPOUND JET

I. INTRODUCTION

Most technological applications of jets involve liquid coming out of an orifice as a cylindrical column and breaking downstream. The disturbances which cause the jet breakup are either intentionally introduced at the orifice tip or are picked up due to the friction as the liquid exits the nozzle. Thus the disturbances are caused due to a spatially fixed source and these disturbances grow downstream and cause breakup. The appropriate frame to analyze this problem is the convective or the spatial instability.

In this chapter. we analyze the spatial instability of an inviscid compound jet. As mentioned earlier, Keller et. al. (1973), showed for a single jet. the equivalence of the spatial and the temporal analyses. However. they point out that the spatial root that merges with the temporal solution is not the fastest growing spatial root. They hypothesized that the faster growing modes have a very long wavelength and the finite length of the jet prevents the manifestation of these modes. We first check the validity of this hypothesis and show that the modes which Keller considered to be the fastest growing are actually evanescent modes, i.e.. they should not be included in the inversion and hence do not contribute to the instability. We further resort to asymptotic analysis to verify that compound jet behaves in a similar manner. i.e., the spatial modes merge into the temporal modes at high jet velocities. The spatial analysis of an inviscid single jet predicts that it becomes absolutely unstable below a critical Weber number of approximately 3.2. One would expect the compound jet to do likewise. We reduce the Weber number in our analysis of the compound jet to see if we obtain a 'pinch' type of singularity that gives rise to an exponential growth in time, i.e., the absolute instability. The existence of the absolute instability can be detected either in the k plane by locating the pinch singularity or in the s plane by cusp formation. We use both the mappings to detect the absolute instability and verify that they are equivalent. We show that the compound jet is absolutely unstable below a critical Weber number that is a function of the system parameters.

This is the first attempt in literature to analyze the spatial instability of a compound jet. We solve the problem in the Fourier Laplace domain and invert the solution to space time domain. We follow Briggs and first invert the Fourier transform followed by the Laplace transform. We compare the results of the spatial analysis to those of the temporal analysis that we obtained earlier in Chapter II. We also compare our theoretical predictions to available experimental data in literature.

II.Formulation of the linear stability theory

II.1 Governing equations and boundary conditions

A doubly infinite jet of an inviscid fluid A. of density ρ_1 is surrounded by a coaxial annulus of an immiscible inviscid fluid B. of density ρ_2 (figure 1). Choose a cylindrical coordinate system (r, θ, z), whose z axis is coincident with the fluid cylinder's axis. The compound jet is moving in a vacuum with a uniform velocity in the positive z direction. The undeflected inner interface is $r=R_1$ and the outer interface is $r=R_2$. The interfacial surface tensions are σ_1 and σ_2, respectively.

The equations of motion and continuity in dimensionless form are

$$\beta_i \frac{D v_i}{D t} = -\nabla P_i + F_i(r,t)\delta(z - z_0) \qquad (1)$$

$$\nabla . v_i = 0 \qquad (2)$$

(i =1,2)

where in fluid i, P_i is the pressure, $\mathbf{v}_i$ is the velocity vector and $\mathbf{F}_i$ is a source of disturbance. In the governing equations and the boundary conditions, we non-dimensionalize lengths by $[R_1]$, time by $[(\sigma_1/r_1R_1^3)^{-1/2}]$, pressure by the surface tension pressure $[\sigma_1/R_1]$ and velocity by $[(\sigma_1/r_1R_1)^{1/2}]$. The dimensionless parameters are $a=R_2/R_1$, $\gamma=\sigma_2/\sigma_1$, $\beta_2=\beta=\rho_2/\rho_1$ and $\beta_1=1$. The interfaces are denoted by $r=h_i(z,t)$. Define the mean curvature H_i of interface i (i=1,2) by,

$$2H_i = -\frac{1}{h_i(1+h_i'^2)^{\frac{1}{2}}} + \frac{h_i''}{(1+h_i'^2)^{\frac{3}{2}}} \qquad (3)$$

Aside from the centerline condition ($\mathbf{v}_i$,P finite at r=0), the boundary (the jump in normal stress and the continuity of velocity) and kinematic conditions in dimensionless form are:

$$[[n.v]]_i = 0 \quad \text{at} \quad r = h_i(z,t) \quad i=1,2 \qquad (4)$$

$$[[P]]_i = 2H\gamma \text{ at } r = h_i(z,t) \quad i = 1,2 \qquad (5)$$

$$[\frac{\partial}{\partial t} + v_i.\nabla](r - h_i) = 0 \text{ at } r = h_i(z,t) \quad i = 1,2 \qquad (6)$$

In the base state there is no forcing disturbance in the bulk and the interfaces are undeflected. Let u and w denote the radial and axial velocities, respectively. Any solution of the form, w=F(r), where F is completely arbitrary, satisfies the base state equations (1)-(6) exactly. Since we are interested in capillary driven instabilities, we restrict the analysis to the solution in which w=constant=V in the same in both the core and the annulus. With this assignment, there is no slip at the interface, thereby preventing the Kelvin Helmoltz type of instability. Thus, we concentrate on the base state:

$$u_i^0 = 0,\ w_i^0 = V \quad i = 1,2 \tag{7}$$

$$P_2^0 = \frac{\gamma}{a},\ P_1^0 = 1 + \frac{\gamma}{a} \tag{8}$$

If a small (~ λ), axisymmetric disturbance is introduced into the jet. the disturbances to the velocities and the interface from the base state are also of order λ. For i=1.2. we have

$$P_i(r,z,t) = P^0 + P_{i1}(r,z,t)\lambda + O(\lambda^2) \tag{9}$$

$$v_i(r,z,t) = (0,V) + v_{i1}(r,z,t)\lambda + O(\lambda^2) \tag{10}$$

$$h_1(z,t) = 1 + \zeta_1(z,t)\lambda + O(\lambda^2) \tag{11}$$

$$h_2(z,t) = a + \zeta_2(z,t)\lambda + O(\lambda^2) \tag{12}$$

Substituting these in the governing equations. one gets the leading order equation for the perturbation quantities.

$$\beta\left(\frac{\partial v_i}{\partial t} + V\frac{\partial v_i}{\partial z}\right) = -\nabla P_i + F(r,t)\delta(z - z_0) \tag{13}$$

$$\nabla . v_i = 0 \tag{14}$$

where we delete subscript 1 for simplicity. We choose the origin to coincide with the location of source; thus z_0=0.

II.2 Transformation to Fourier Laplace domain

We shall now take the Fourier Laplace transform of the equations.

Define the transforms as

$$\hat{f}(k) = \int_{-\infty}^{\infty} f(z)e^{-ikz}dz \tag{15}$$

$$\tilde{f}(s) = \int_{0}^{\infty} f(t)e^{-st}dt \tag{16}$$

The spatial instability derives from spatial disturbances that are localized in space. These disturbances can either grow or decay in place or they can convect with the jet. These disturbances can either arise in the bulk of the fluid (as we have assumed) or at either of the interfaces. In the latter case, the disturbance would enter the normal stress condition instead of the governing equations and would only change the form of the inhomogeneity (e.g, eq(25) below). As we shall see, the general results below on convective and absolute instabilities would still be valid.

We solve the spatial problem in the stationary coordinate (lab) frame because the location of the onset of absolute instability depends on the observer. The lab frame is the most appropriate choice for observing the jet while conducting experiments.

Since the fluids are incompressible we can define a stream function i by

$$u = -\frac{1}{r}\frac{d\psi}{dz};w = \frac{1}{r}\frac{d\psi}{dr} \tag{17}$$

Substituting the stream function into the equations of motion (eq(13)), eliminating the pressure and then taking Fourier-Laplace transform, we get,

$$\left(r\frac{d}{dr}\frac{1}{r}\frac{d}{dr} - k^2\right)\tilde{\hat{\Psi}} = \frac{r}{\beta_i(s + ikv)}\left[\frac{d(\tilde{\hat{F}}_{i,z}(r,s)}{dr} - ik\tilde{F}_{i,r}(r,s)\right] = E_i(r,s,k) \tag{18}$$

where $F_{i,z}$ and $F_{i,r}$ are the z and r components of $\mathbf{F}_i$. Assume that the source is separable, i.e.,

$$F_i(r,t) = H_i(r)T(t) \tag{19}$$

Thus

$$E_i = \frac{M_i(r,k)}{s+ikV}\tilde{T}(s);\quad M_i(r,k) = \frac{r}{\beta}\left[\frac{dH_{iz}}{dr} - ikH_{ir}\right] \tag{20}$$

The solution to Eq. (18) is,

$$\tilde{\tilde{\Psi}} = R_i r I_1(kr) + Q_i r K_1(kr) + \tilde{\tilde{\Psi}}_{i,p} \tag{21}$$

$$\tilde{\tilde{\Psi}}_{i,p} = r\frac{\tilde{T}}{s+ikv}\left[I_1(kr)\int K_1(kr)E_i dr + K_1(kr)\int I_1(kr)E_i dr\right] = \frac{\tilde{T}}{s+ikv}Z_{i,p}(r,k) \tag{22}$$

R_i, Q_i are integration constants that are functions of k and s, and (22) defines $Z_{i,p}(r,k)$. Note that the only pole of $Z_{i,p}$ in the k plane is k=0.

The boundary conditions are the same as in the temporal problem. Upon substituting the above solution in the boundary conditions, we get the matrix equation $A_s(s,k)\mathbf{x}=\mathbf{b}(s,k)$, where A_s is the same 5*5 matrix as in the temporal problem except that s has to be replaced by s+ikV, i.e., $A_s(k,s)=A(k,s+ikV)$

$$A_s(k,s) = \begin{pmatrix} I_1(k) & -\dfrac{I_1(k)}{\beta} & \dfrac{K_1(k)}{\beta} & 0 & 0 \\ \dfrac{kI_1(k)}{s} & 0 & 0 & s+ikv & 0 \\ 0 & \dfrac{kI_1(ka)}{(s+ikv)\beta} & \dfrac{-kK_1(ka)}{(s+ikv)\beta} & 0 & s+ikv \\ 0 & I_0(ka) & K_0(ka) & 0 & \gamma(\dfrac{1}{a^2}-k^2) \\ I_0(k) & -I_0(k) & -K_0(k) & (1-k^2) & 0 \end{pmatrix} \tag{23}$$

$$\tilde{x} = \left[R_1 \bar{s}, \beta R_2 \bar{s}, -\beta Q_2 \bar{s}, -i\tilde{\zeta}_1, -i\tilde{\zeta}_2 \right] \quad ; \quad \bar{s} = s + ikv \tag{24}$$

The reason for this is that A_s derives from the substitution of the homogeneous solution of the transformed equations into the boundary conditions. Both of these are the same for the temporal and the spatial formulations, except that. in the temporal formulation the reference frame moves with the jet. The particular solution and/or the initial conditions contribute to **b**, which here becomes,

$$\begin{aligned} b^i = \frac{\tilde{T}}{s+ikV} c^i = \frac{\tilde{T}}{s+ikv} [& s(Z_{2.p} - Z_{1.p}\big|_{r=1}), \quad -k\, Z_{1.p}\big|_{r=1}, \quad -k \frac{Z_{2.p}}{r}\Big|_{r=a}, \\ & \bar{s}\left(\frac{-\beta\bar{s}}{ka}\frac{dZ_{2.p}}{dr} - \frac{H_{2.z}}{k}\Big|_{r=a}\right), \bar{s}\left(-\frac{\bar{s}}{k}\frac{dZ_{1.p}}{dr} - \frac{H_{1.z}}{k} + \beta\frac{\bar{s}}{k}\frac{dZ_{2.p}}{dr} - \frac{H_{2.z}}{k}\Big|_{r=1}\right] \end{aligned} \tag{25}$$

When $A_s(s.k)$ is non-singular, the solution in the Fourier-Laplace domain is $\tilde{x}=A_s^{-1}(s.k)\mathbf{b}(s.k)$

II.3 Inversion to real space time domain

The inverse of the combination of **x** with eq(21) gives the solution in the space-time domain. Since the only dependent variables of interest in **x** are ζ_1 and ζ_2 . one can in principle reduce A_s to a 2*2 before inversion. Since we only perform this inversion in principle. we omit this calculation.

We first invert the Fourier transform:

$$\begin{aligned} x(z,t) = \frac{1}{4\pi^2 i}\int_{c-i\infty}^{c+i\infty} e^{st}\left[\int_{\infty}^{\infty} \tilde{x}\,(k,s)\,e^{ikz}dk\right]ds = \\ \frac{1}{4\pi^2 i}\int_{c-i\infty}^{c+i\infty} \tilde{T}(s)\,e^{st}\left[\int_{\infty}^{\infty} \frac{A_s^{-1}(k,s)c(k,s)}{s+ikv}e^{ikz}dk\right]ds \end{aligned} \tag{26}$$

Again to obtain the space-time domain solution, one can evaluate both line integrals involved using the method of residues with an appropriate choice of contours (figure 2). However, because the initial disturbance can be arbitrary, stability analysis focuses, rather, only on the form of the solution, i.e., whether for some disturbance it can grow in space and time.

If D_{mn} is the cofactor of $A_{s,nm}$, the cofactor expansion of $A_s^{-1}(k,s)$ in (48) gives,

$$\tilde{x}(z,s) = \frac{1}{2\pi}\int_{-\infty}^{\infty} A_s^{-1}(k,s)b(k,s)\,e^{ikz}\,dk = \tilde{T}\int_{-\infty}^{\infty} \frac{D(k,s)c(k,s)}{(s+ikv)|A_s(k,s)|}e^{ikz}\,dk \tag{27}$$

$$|A_s(k,s)| = \det[A_s(k,s)] \tag{28}$$

For each s along the Laplace contour, the poles of the function in the k plane will arise from the roots of the dispersion equation, from the poles of D(k,s)**c**(k,s) and from k such that s+ikv=0. The poles of D(k,s)**c**(k,s) occur when any of the components of either of the matrices becomes singular. This happens in the k plane for k=0. As k→0, the pressure gradients, i.e., dP/dz, dP/dr vanish: so there is no driving force to accelerate the fluid and the growth rate goes to zero.

If the integrand in (27) has only simple poles, the residue theorem gives

$$\tilde{x}(z,s) = i\tilde{T}(s)\sum_{n}\lim_{k\to k_n}\left[(k-k_n)\frac{D(k,s)c(k,s)}{(s+ikV)|A_s(k,s)|}\right]e^{ik_nz} = \tilde{T}(s)\phi(s,z) \tag{29}$$

Since we are interested in the stability of the system rather than in its precise evolution from a specific initial condition, we do not need to calculate the residues. It suffices to investigate the transform inversions by examining the poles in the s plane and the corresponding poles in the k plane.

To invert the Laplace integral we choose the Bromwich contour whose vertical line (s_r=c) lies to the right of all singularities of $\tilde{x}(z,s)$. The singularities of $\tilde{x}(z,s)$ can arise either from $\tilde{T}(s)$ or from $\phi(s,z)$. One may take the source to be periodic in time. For example if the source introduces a sinusoidal disturbance, $T=\sin(\omega t)$, $\tilde{T}=1/(s^2+w^2)$ and the poles are $s=\pm i\omega$. To search for the poles of $\phi(s,z)$, we hold the real part of s ($s=s_r+i\, s_i$) fixed and vary the imaginary part. We do this for all values of $0<s_r<c$. For $z>0$, choose the upper contour in fig(2) to invert the Fourier integral. As s changes along the line s_r=c, the poles in the k plane which arise from the zeroes of the dispersion equation move in the k plane. The residues are continuous functions of s; so $\phi(s,z)$, which is simply the sum of all the residues in the upper half k-plane, is continuous. However, if a pole in the k plane crosses the real k axis in the process of traversing the s_r=constant line, the pole no longer lies inside the Fourier inverse contour and does not contribute to the Fourier inverse at that value of s. This situation would lead to a discontinuity in $\phi(s,z)$. Since, by hypothesis, the line s_r=c lies to the right of all singularities in the s plane, the poles do not cross the real k line for s_r=c since this would create a singularity in $\tilde{x}(z,s)$.

As we reduce c, i.e., move the Bromwich contour to left, the poles in the k plane may start crossing the real k line and lead to singularities. Following Briggs (1964), one can remove these singularities by defining the analytic continuation of ϕ which is the integral along a contour deformed (see figure 3) in a manner so as to continue including or excluding pole that cross the $k=k_r$ line due to motion along the s_r=constant line when $s_r<c$. But, if two poles coming from different sides of the real k line merge, we would want to deform the contour so as to keep one of the poles (A) but not include the other (B) in its interior, as in the left part of figure 4, for $z>0$. This is clearly not possible and gives rise to a second order pole of the dispersion equation in the k-plane and a non-removable singularity inside the Bromwich contour. We call this a "pinch" type singularity since it is caused due to pinching (merging) of roots in the k-plane. If s_r at such a singular point is greater than zero, its residue generates an absolute instability. Note that if the double root arises due to the merging of two roots inside or outside the Fourier inversion contour, it is not a pinch pole and gives only a finite contribution to the inversion.

Recall that a periodic source introduces purely imaginary singularities in the s plane. So, in the absence of a pinch singularity with a positive real part, the source's poles will cause the system to oscillate in time with the same frequency as the source. If the pinch pole exists in the k plane for $s=s_r+i\,s_i$ and $s_r>0$, the system grows in time, i.e., it is absolutely unstable. Since the pinch type pole is a double or higher root in k of the dispersion equation.

$$f_s(k_0,s_0) = 0, \frac{\partial f_s}{\partial k}(k_0,s_0) = 0 \quad \text{where} \quad f_s(k,s) = \det(A_s(k,s)) \tag{30}$$

$$f_s(k,s) = 0 \Rightarrow \frac{\partial f_s}{\partial k} = -\frac{\partial f_s}{\partial s}\frac{ds}{dk} \quad \text{if} \quad \frac{\partial f_s}{\partial s}(k_0,s_0) \neq 0 \tag{31}$$

We note that this is a not a sufficient condition for this kind of absolute instability. Thus,

$$\frac{ds}{dk} = -\frac{\dfrac{\partial f_s}{\partial k}}{\dfrac{\partial f_s}{\partial s}} = 0 \quad \text{at} \quad (k,s) = (k_0,s_0) \tag{32}$$

If an explicit solution of the dispersion equation for the growth rate exists and if the pole in the s plane is simple, one can use (32) to find the multiple double roots and calculate the corresponding growth rates there. To conclude that the system is absolutely unstable, one must still verify that the double pole arises as the coalescence of a pole that lies outside with one that lies inside the Fourier contour when s lies on the s plane Bromwich contour.

If the system is not absolutely unstable, the sign of the imaginary parts of the poles inside the deformed contour in the k-plane control the growth or decay of the disturbance in the longitudinal (z) direction. If the imaginary part of k is negative. there is growth for $z>0$. So growth can arise only when poles are in the upper half k plane for large s_r and they cross into the lower half of the plane upon reducing s_r within $0<s_r<c$.

Before proceeding to the Results section. we note some interesting characteristics of the system's dispersion equation that will be useful in following its roots. For example.

$$f_s(s,k) = -[f_s(s^*,-k^*)]^* = [f_s(-s^*,k^*)]^* \qquad (33)$$

where * denotes complex conjugate. So if $f_s(s,k)=0$. then $f_s(s^*,-k^*)=0$ as well and one need only consider solutions of the dispersion equation in the right half k plane.

From eq. (33) If s is purely imaginary ($s=is_i$), as it is at the source generated singularities.

$$f_s(is_i,k^*) = [f_s(is_i,k)]^* \qquad (34)$$

i.e., the solution in the upper half k plane is a mirror image of the solution in the lower half k plane when $s_r=0$.

III. RESULTS AND DISCUSSION

III.1 Convective Instability

We investigate for a given velocity and jet parameters, what the response of the system will be to a disturbance that is sinusoidal in time and of known frequency. As discussed, the source generates 2 poles $\pm i\omega$ in the s-plane. If the system is not absolutely unstable the response will be sinusoidal in time with the same frequency as that of the source. It will grow or decay spatially depending on the poles in the k plane that correspond to $\pm i\omega$. The non-zero poles in the k plane arise either from the dispersion equation or when $(s+ikV)=0$. Let us first consider the poles arising from the dispersion equation. Consider only the poles corresponding to $s=i\ s_i=-i\omega$, since the poles for $s=+i\omega$ are their reflections about the imaginary k line. We obtain the roots of the dispersion equation for large s_r so that none of the roots lie on the real k axis and follow them as s_r decreases. Let us explain: We know that the growth rate for the spatial modes is given by, $s+ikV=g(k)$, where $g(k)$ is the temporal growth rate obtained by solving the dispersion equation, $W(k)s^4+X(k)s^2+Y(k)=0$. From the temporal results, $g(k)$ is real for k real in the region of instability. When the poles cross the real k axis, k is purely real and $s+ikV$ is real at well. This gives $s_i=-ik_rV$ and s_r corresponds to the temporal growth for the real k_r. Thus if s_r is greater than the maximum temporal growth rate, there can be no pole crossing the real k axis as we vary s_i. Thus the value of c in the Bromwich contour should be greater than the maximum temporal growth rate.

As discussed, since a pole's crossing the real k axis leads to a discontinuity in the integrand for the Laplace inversion, we introduce the analytic continuation of the integral that we identify as the Fourier inverse when s lies along vertical line of the Bromwich contour. Following Briggs (1964), we continue this to include s values for s_r less than or equal to the critical values corresponding to k_r- axis crossover, as in the formulation section to search for the s-plane singularities. Figure 5 shows two of the poles "1" and "2" of the dispersion equation in the k plane. Each curve is a mapping of the fixed s_r line onto the k-plane through the dispersion relation. (Arrows on the curves in fig 5 and other subsequent figures of poles in the k plane show the direction of increasing ω). For large s_r, root 1 lies in the upper and root 2 lies in the lower half k-plane. On reducing s_r, root 1 moves down and root 2 moves up. If these poles were to merge at some $s_r>0$, the jet would be absolutely unstable. But for V=2, the roots do not merge. They intersect in the k plane but the value of s_i at those intersections is different for the two roots; so, these intersections do not represent a double root. They arise because s(k) is a multi-valued function. At $s_r=0$, a part of root 1 lies in the lower half k plane and this represents a spatially unstable wave for z>0. Root 2 is evanescent for z>0 because it is not inside the contour for Fourier inversion. It is stable for z<0 because it lies inside the contour but has negative k_i implying stability for z<0. Fig 6 shows similar plots for roots 3 and 4. Both the roots lie in the upper half k plane for large s_r. On reducing s_r, root 3 moves down and crosses into the lower k plane and hence represents an spatially unstable mode for z>0. Root 4 moves down too, but it just touches the real k axis at $s_r=0$. Thus it is a neutrally stable mode for z>0. Root 3 does not merge with any evanescent root and thus the jet has no absolute instability. Fig 7 shows the plots for root 5, which lies in the upper half plane for large s_r. Like root 3, it moves down on reducing s_r but just touches the real k axis for $s_r=0$.

The pole for $s+ikV=0$ lies in the upper half plane for large s_r and hits the real k axis for $s_r=0$. This also represents a neutral mode for $z>0$. Note that for $s+ikV=0$, the dispersion equation, i.e., $f_s(-ikV,k)=f(0,k)=0$ has only neutrally stable roots.

Thus, roots 1 and 3 are unstable for $z>0$. The cut-off Strouhal number ($|s_i|/V$) above which the modes are stable is about 1 and 1/a for the primary and the secondary modes respectively. The exact values depend on the jet velocity. Leib and Goldstein (1986) found similar results for a single inviscid jet. The growth rate of root 1 is larger; henceforth we refer to it as the primary mode and to the root 3 as the secondary mode. Each mode has a maximum $k_{i,max}$ in its spatial growth rate. In response to a broad band disturbance, the system will at long times (if it is still in the linear regime) select the frequency which gives the highest growth rate.

The spatial growth rates k_i are strong functions of the jet velocity and increase as the jet velocity decreases. Figures 8 and 9 show the wave number k_r vs the driving frequency $s_i=\pm\omega$ for the primary and secondary modes respectively. At high velocities, for each mode, $k_r=-s_i/V$ for $|s_i|<V/\alpha$ ($\alpha=1$ for the primary mode; $\alpha=a$ for the secondary mode). For $s_i > V/a$, there is a sudden change in the slope. For high velocities, $k_r=-s_i/V$ implies the disturbances just convect in the +z direction. It is reasonable to suspect that they will grow with a rate that depends on their wavelengths, as in temporal instability. Let $\tau:=z/V$ be the Lagrangian time spent by an element of fluid since crossing the origin. Its spatial growth is given by e^{ikz} and its temporal growth by e^{st}, vis.,

$$e^{ikz} = e^{ik_r z-k_i z} = e^{ik_r z-k_i V\tau} \tag{35}$$

The wave number in both the temporal and the spatial analysis is k_r. Thus, at high velocities we guess that the spatial growth rate $-ik_i(s_i)V$ equals the temporal growth rate $s(k_r(s_i))$. We now show this is indeed asymptotically the case.

Recall, the solution to the spatial dispersion equation can be expressed as. $s+ikV=g(k)$. If V is large and $s=-i\omega$, let us define a real variable $\eta=\omega/V$. Thus the dispersion equation becomes,

$$-i\eta V+ikV=g(k)_{.}\Rightarrow i\eta+ik=\frac{g(k)}{V} \tag{36}$$

To leading order in 1/V, the asymptotic solution of (36) is,

$$k=\eta-i\frac{g(\eta)}{V} \tag{37}$$

To leading order, the wavelength is simply that of the convected disturbance, i.e., $k_r=\eta=\omega/V$ and $-k_i=g(\eta)/V=g(k_r)/V$. Thus, $-k_iV=g(k_r)=s(\text{temporal})$.

Figures 10 and 11 show $-k_iV$ vs k_r for the primary and secondary modes respectively. At high velocities, the curves merge into the temporal solution of s vs k as predicted by the asymptotic analysis (eq 37). This implies the disturbances grow as they convect and so the Lagrangian motion in z direction is equivalent to an infinite jet progressing in time. Though the spatial analysis is more pertinent to the problem of free flowing jets, the temporal problem will give the same predictions as the spatial if the velocity of the jet is sufficiently high. Since the single jet is a limiting case of the compound jet, this result is true for the single jet as well. This and the surprising range of validity of the linear theory in general are the reasons why predictions on drop size based on the temporal model agree well with experiments. Also, in experiments the jet is actually semi-infinite. But since the doubly infinite jet is stable in the negative direction, it is reasonable to model the semi-infinite jet as a doubly infinite jet.

III.2 ABSOLUTE INSTABILITY

If the velocity of the jet is not very large, there is some dispersion as the disturbance gets convected along the jet, and the more appropriate spatial analysis gives more accurate predictions.

If the jet velocity becomes smaller than a critical value, the jet becomes absolutely unstable, i.e., any disturbance will grow in space as well as in time. The onset of an absolute instability is determined by the merging of the growing and evanescent roots as explained. Fig 18 shows the movement of the evanescent root, i.e., root 2, and the growing secondary root on reducing s_r for V=1.7. For s_r=0.005, the roots did not merge. At some s_r between 0.005 and 0, the curves merge and then split to give a topologically different configuration at s_r=0 than what was obtained at V=2 (fig 5-8). This merging results in an absolute instability. Thus to determine if the jet is absolutely unstable, one needs to map the locations of the poles in the k plane for s along the s_r=0 line and look at the topology. At V=1.7, the primary mode does not yet merge with an evanescent root in the lower k plane and thus is only convectively unstable. On further reducing the jet velocity, the primary mode also undergoes such a merge to contribute another root which grows in time. But, the critical velocity for the primary mode is lower than that of the secondary mode. In an experiment it would be desirable to stay above the critical velocity of the secondary mode in order to maintain a jet that is only convectively unstable. At

$V=0$, the merger for either mode takes place on the real k axis at $k=k_r$ and $s=g(k_r)$. The k_r for the primary and the secondary modes correspond to the k at which the temporal growth rate ($s=g(k)$) is maximum for the stretching and the squeezing mode, respectively. This happens because at $V=0$, the spatial dispersion equation, i.e., $f_s(s,k)=f(s+ikV,k)$ reduces to the temporal form. Also, the required condition for absolute instability, $ds/dk=0$, is same as the condition for the maxima in $s=s(k)$.

The critical velocity for the jet is a function of all the system parameters. For our system, an explicit solution of $s=g(k)-ikV$ exists. A necessary condition for the onset of an absolute instability is $ds/dk=\partial s_r/\partial k_r+i\partial s_i/\partial k_r=0$. The root can be found numerically or graphically by plotting lines of constant k_i in the s plane and looking for a cusp formation. At the cusp, both s_i and s_r reach a local extremum ($\partial s_r/\partial k_r=\partial s_i/\partial k_r=0$) as functions of k_r and $ds/dk=0$. This method is shown in fig(13) for the secondary mode. It agrees with the one followed earlier because the frequency at the cusp formation is the same as the frequency at the merging of the secondary and the evanescent modes.

To locate the critical velocity, we solve the equation, $ds/dk=g'(k)-iV=0$, to obtain the V at which the real part of s at absolute instability becomes 0. Above this velocity, s_r at the merger of the roots in the k plane is negative and hence the jet is not absolutely unstable. Fig 14 shows the plot of s_r at the merger and V. From the plot, the critical velocity $V_c=1.77$ for a jet with $\beta=1$, $\gamma=2$ and $a=2$.

IV COMPARISON WITH EXPERIMENT

Hertz and Hermanrud(1983) did some experiments with compound jet. They took pictures of the jet as it moves in the axial direction. We compared their experimental results with the temporal predictions in Chapter II. The spatial model is the appropriate one to analyze their results. Here we compare the predictions of the inviscid spatial analysis to the experimental results and also compare the theoretical predictions of the three models that we used in our analyses, inviscid temporal. inviscid spatial and the viscous temporal.

As mentioned in Chapter II, the wave number measured from figure 5 from Hertz and Hermanrud (1983) is 0.64 for the first wave. The wave number changes in the axial direction and the average is 0.6. In this experiment there was no specific frequency disturbance imposed, so the system selects the dominant wave, i.e., the wave with the maximum growth rate. Fig(15) shows the predictions based on the temporal and the spatial analyses. The spatial analysis predicts that the jet is convectively unstable. The velocity is large but not large enough for the temporal and spatial growth rates to overlap. The maxima in the temporal growth rate is at k=0.66 and in the spatial growth rate occurs at k=0.677, which are both in very good agreement with the experimental findings. Sanz & Meseguer (1985) compared the results of the same experiment with their theoretical predictions based on the one dimensional temporal model. Their prediction for the wave number was 0.7.

V. CONCLUSIONS

A compound jet is unstable due to capillarity. We have solved the problem of the hydrodynamic instability for a compound jet both temporally (Chapter II) and spatially in a unified approach using the transform formulation. The difference between the temporal and the spatial instability lies in the origin of the disturbance. If the instability is initiated by a disturbance in the initial condition, the situation is one of temporal instability and if the disturbances originate from a localized spatial source, the instability is spatial. The spatial solution is more appropriate for the present problem since the source of disturbance is usually located at the tip of an orifice from which the compound jet emerges. At very high jet velocities, the disturbances grow spatially, but there is no dispersion and the results of the spatial instability agree with those of the temporal instability. At velocities below a critical value which is a function of the jet parameters the jet becomes absolutely unstable.

The spatial analysis predicts that the inviscid compound jet is always unstable for $z>0$. There are two unstable modes, the primary and the secondary. The growth rate of the primary mode is higher. The primary and the secondary modes are unstable below critical Strouhal numbers that are close to 1 and $1/a$, respectively. The exact values depend on the Weber number. The axial growth rate of both the modes increases with a decrease in the jet velocity. The critical velocity below which the jet is absolutely unstable is different for the two modes. At high velocities, the primary and the secondary modes merge into the stretching and the squeezing modes of the temporal analyses, respectively. The breakup size and length can be controlled by manipulating the frequency of the source. If no specific frequency is present in the source, i.e., the disturbance has a wide range of frequencies, the one with the highest axial growth will dominate at long lengths if the linear theory still applies. At short lengths, all the frequencies will contribute and this will result in a variation of the observed wavelength along the axial direction.

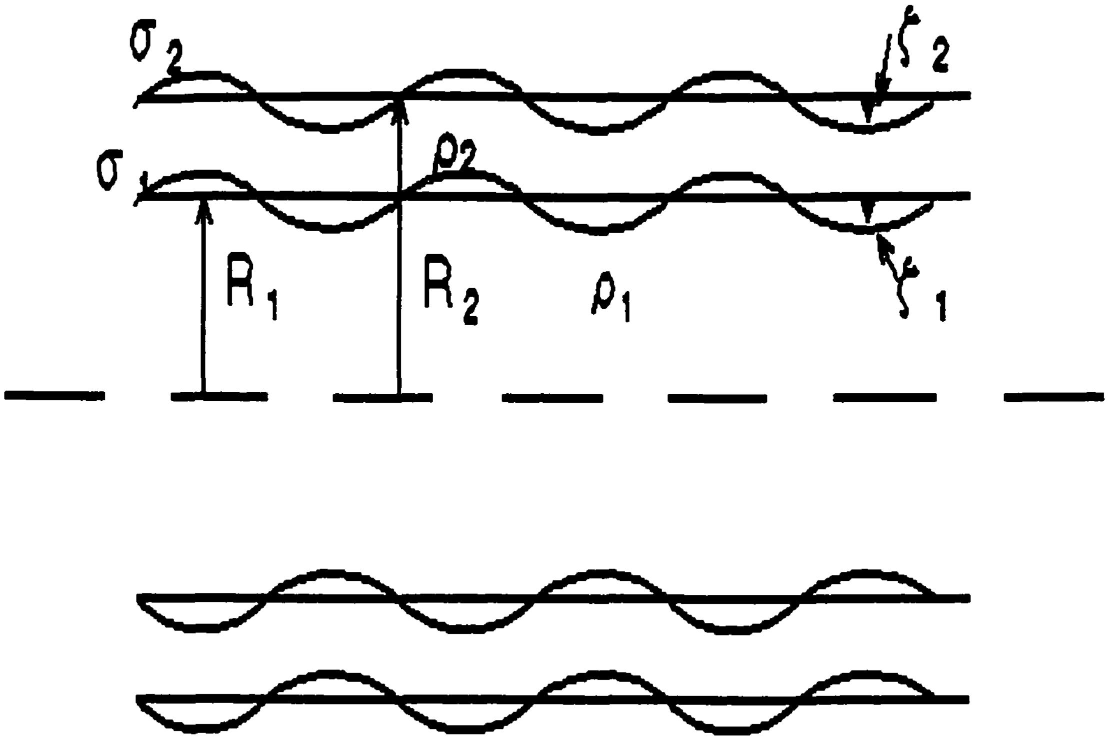

Figure1 Geometry of the inviscid com pound jet

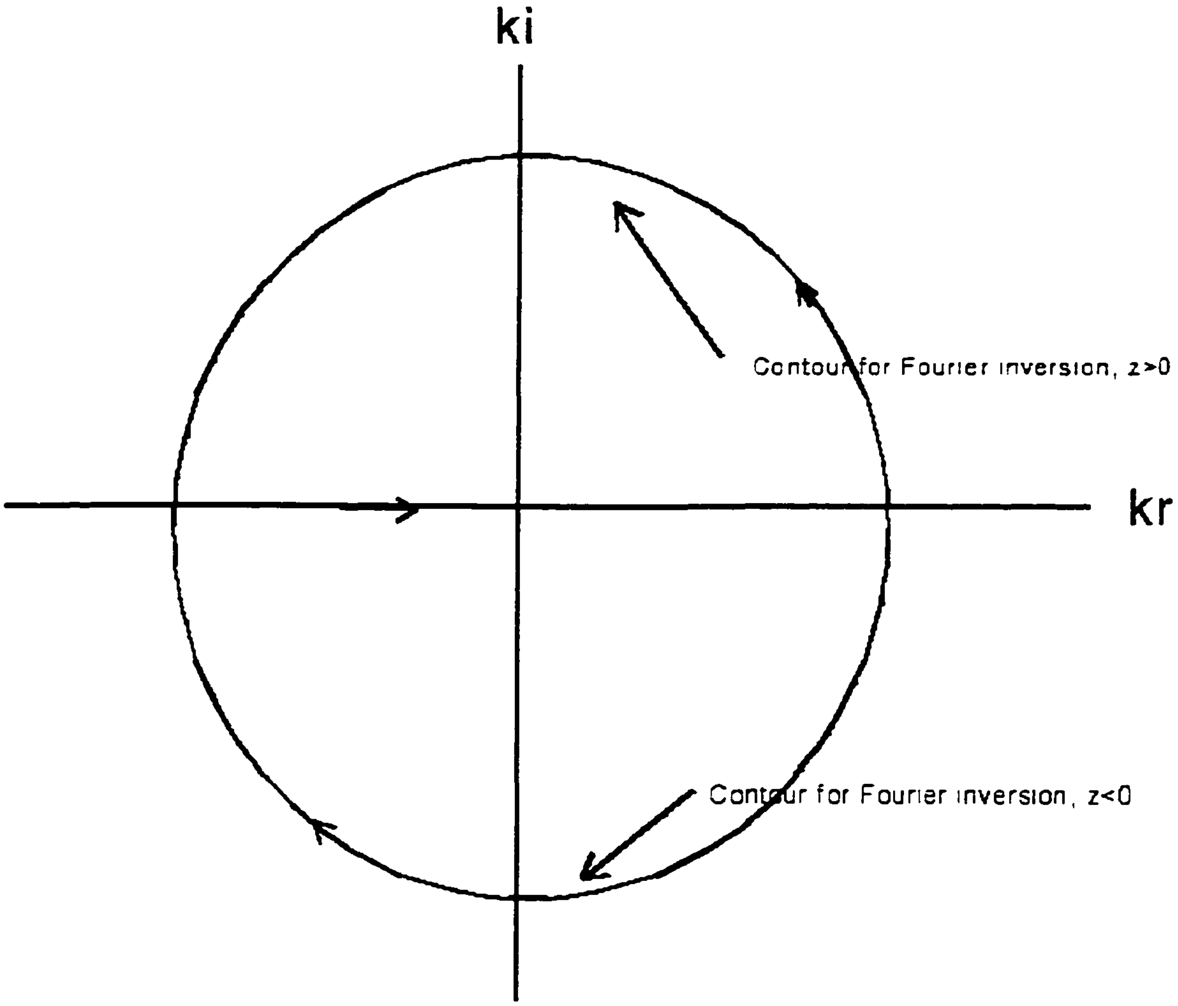

Figure 2 Contour for the Fourier inversion

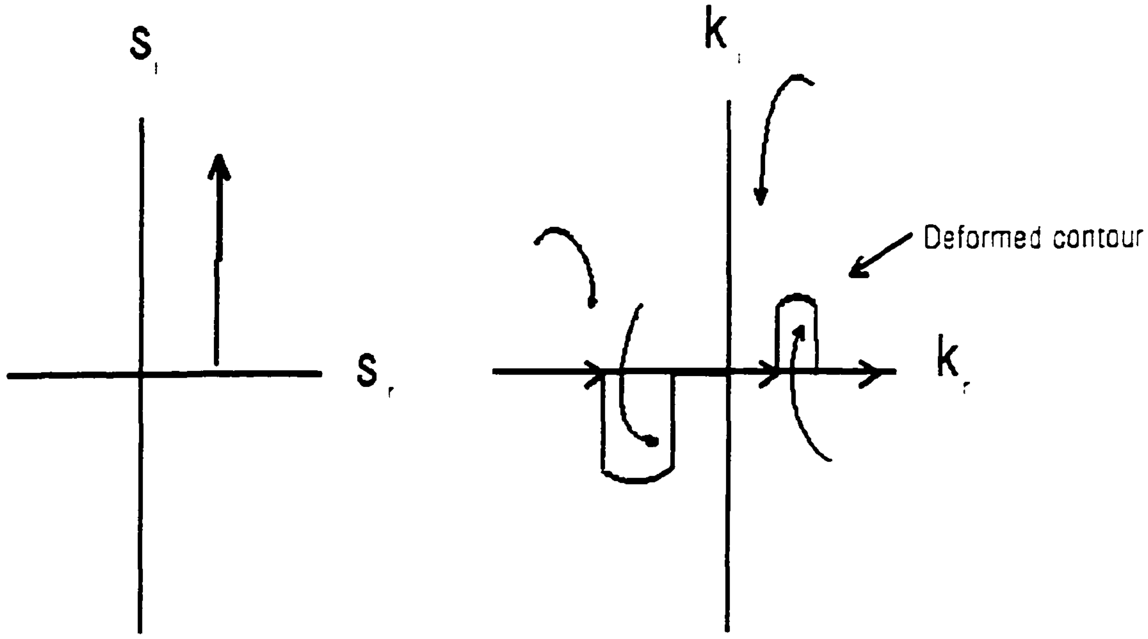

Movement of poles in k plane
due to motion of s in s plane

Figure 3 Motion of roots k(s) in the k plane due to motion of s in the s plane (convective instability)

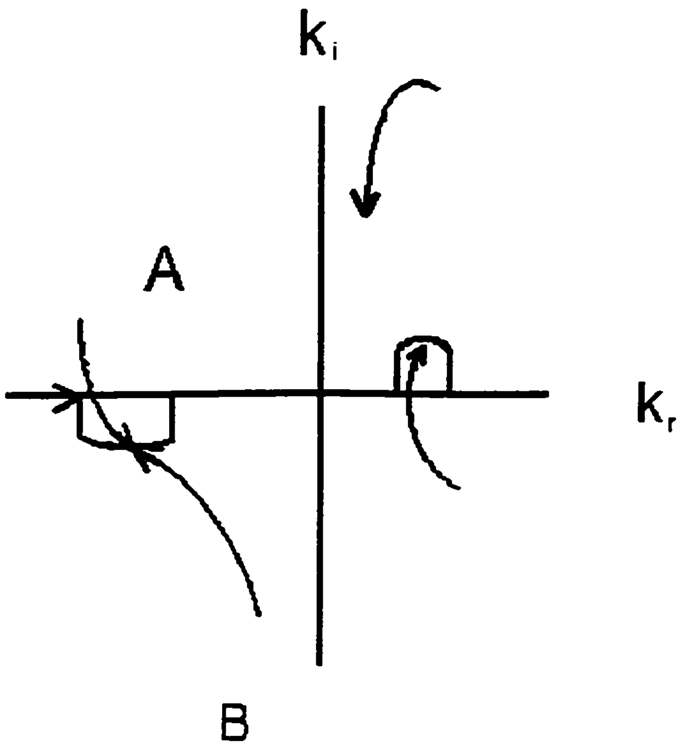

Origin of Absolute instability

Figure 4 Merging of roots in the k plane leading to absolute instability

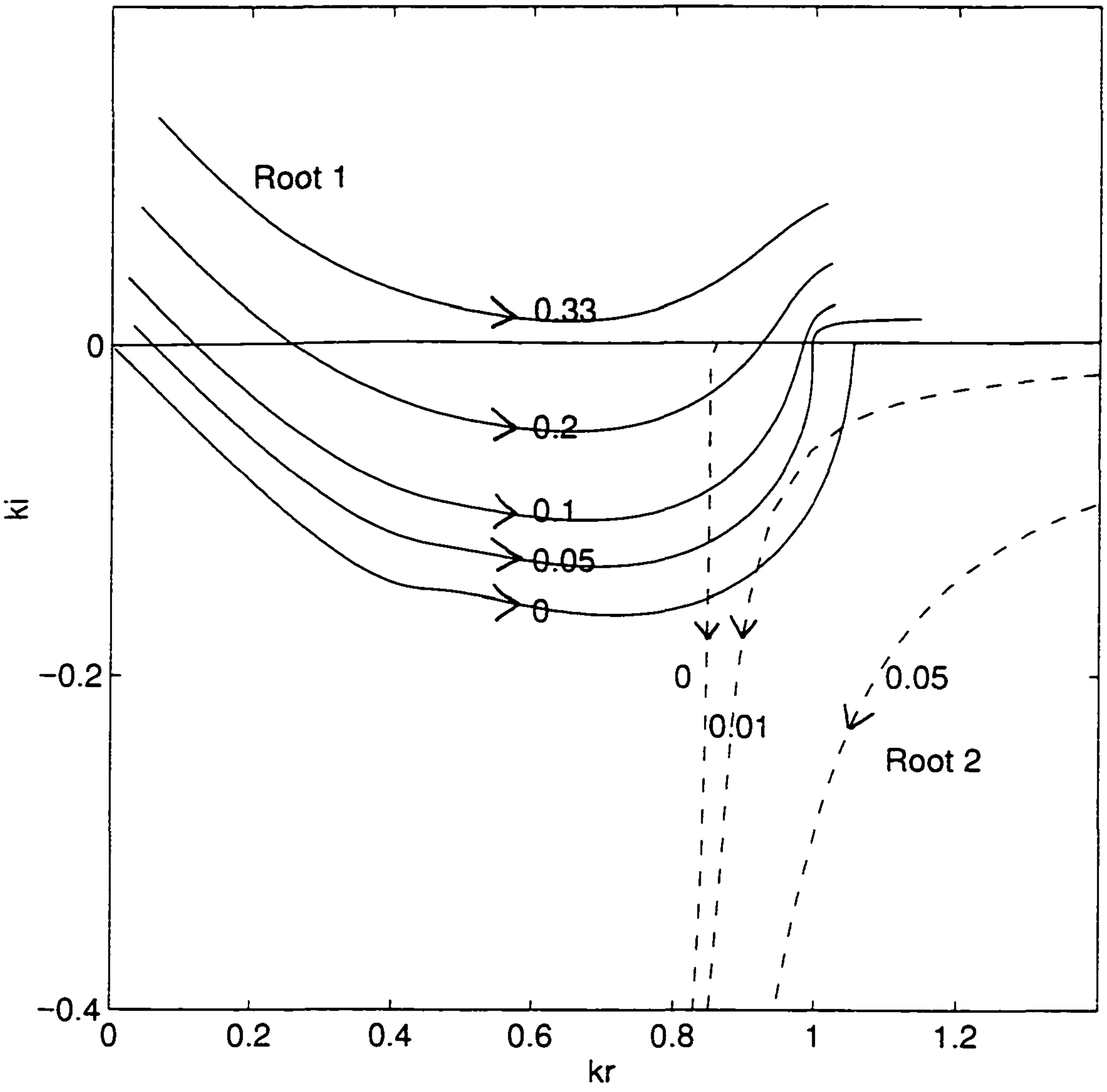

Figure 5. Mapping of constant s_r lines in the k-plane for the spatial roots 1 and 2. $s=s_r-i\omega$. Arrows show the direction of increasing ω. The numbers on the curves denote the values of s_r. $\beta=l,\gamma=2,a=2,V=2$

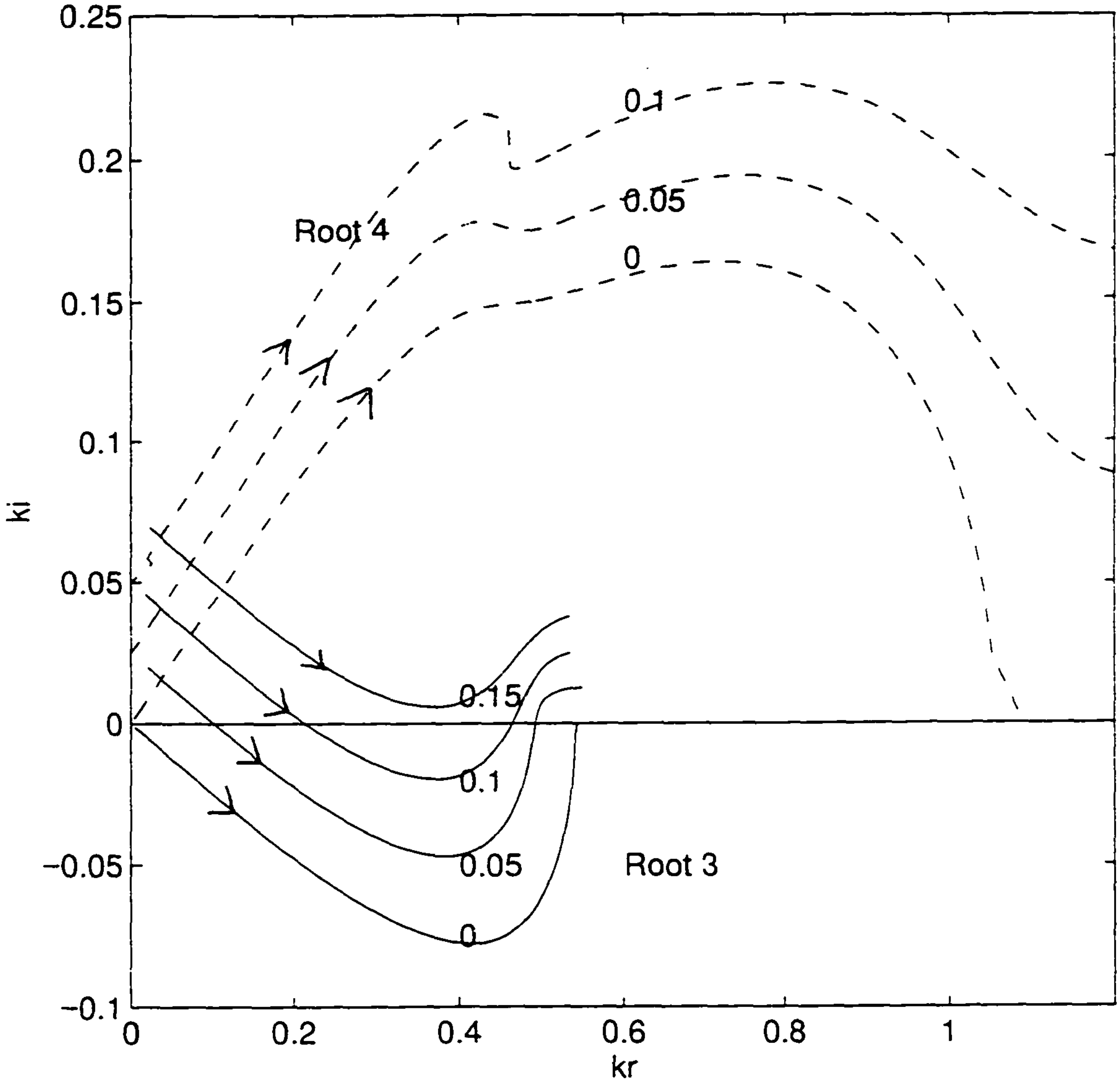

Figure 6. Mapping of constant s_r lines in the k-plane for the spatial roots 3 and 4. $s=s_r-i\omega$. Arrows show the direction of increasing ω. The numbers on the curves denote the values of s_r. $\beta=1,\gamma=2,a=2,V=2$

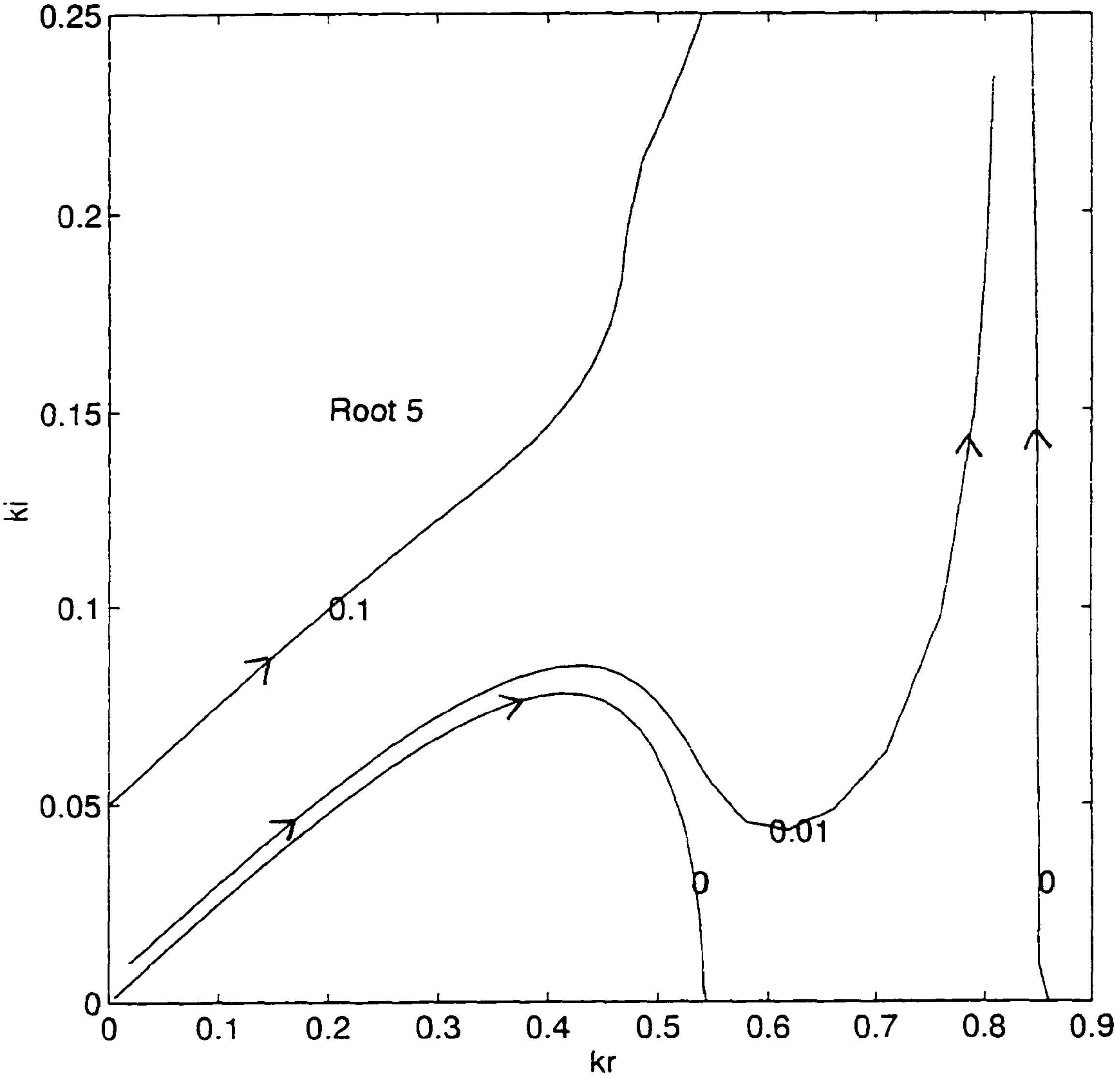

Figure 7. Mapping of constant s_r lines in the k-plane for the spatial mode 5. $s=s_r-i\omega$. Arrows show the direction of increasing ω. The numbers on the curves denote the values of s_r. $\beta=l,\gamma=2,a=2,V=2$

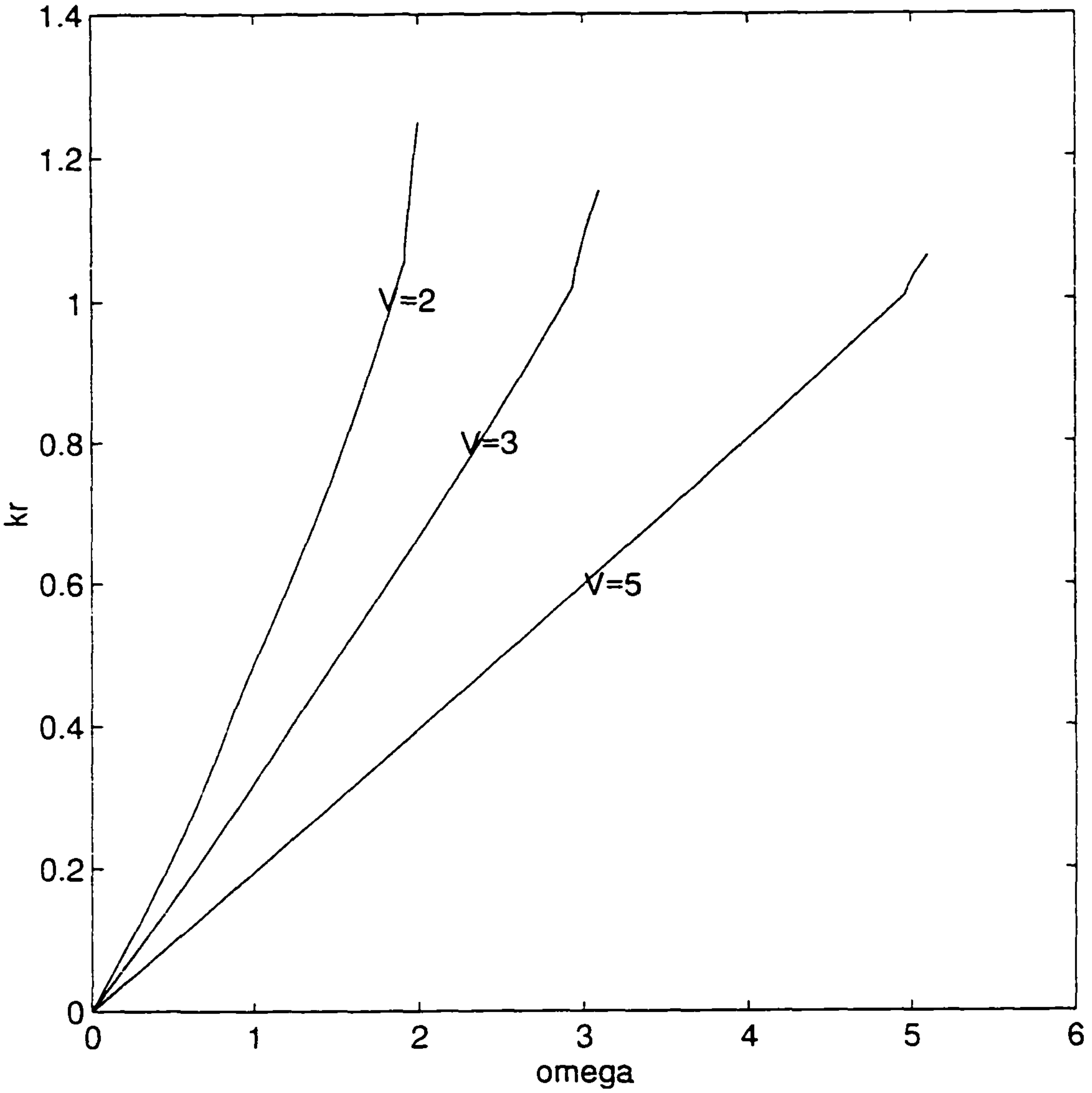

Figure 8. k_r-ω plot for the primary spatial mode (Root 1) at different velocities. β=1 ,γ=2,a=2

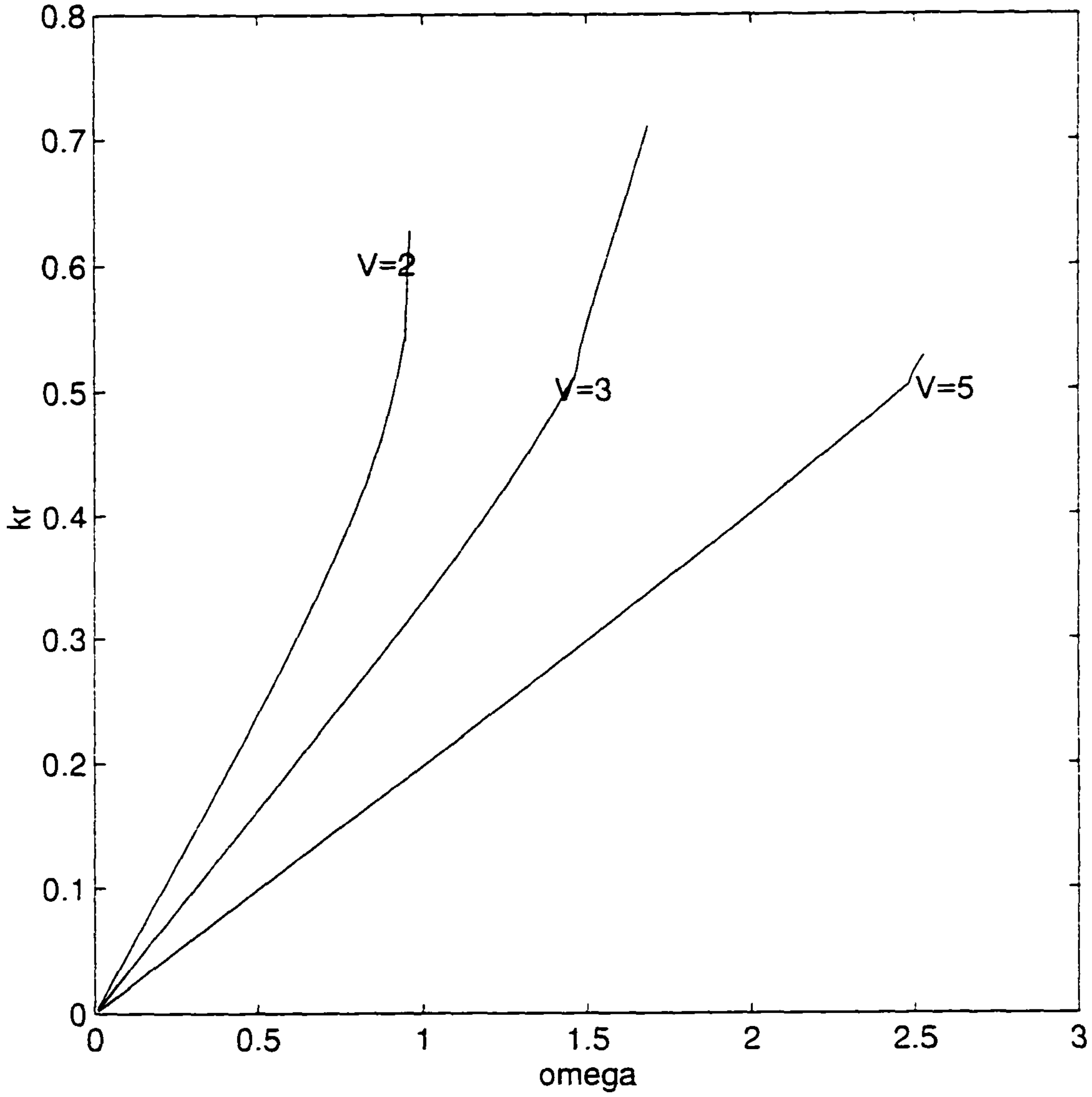

Figure 9. k_r-ω plot for the secondary spatial mode (Root 3) at different velocities. β=1 ,γ=2,a=2

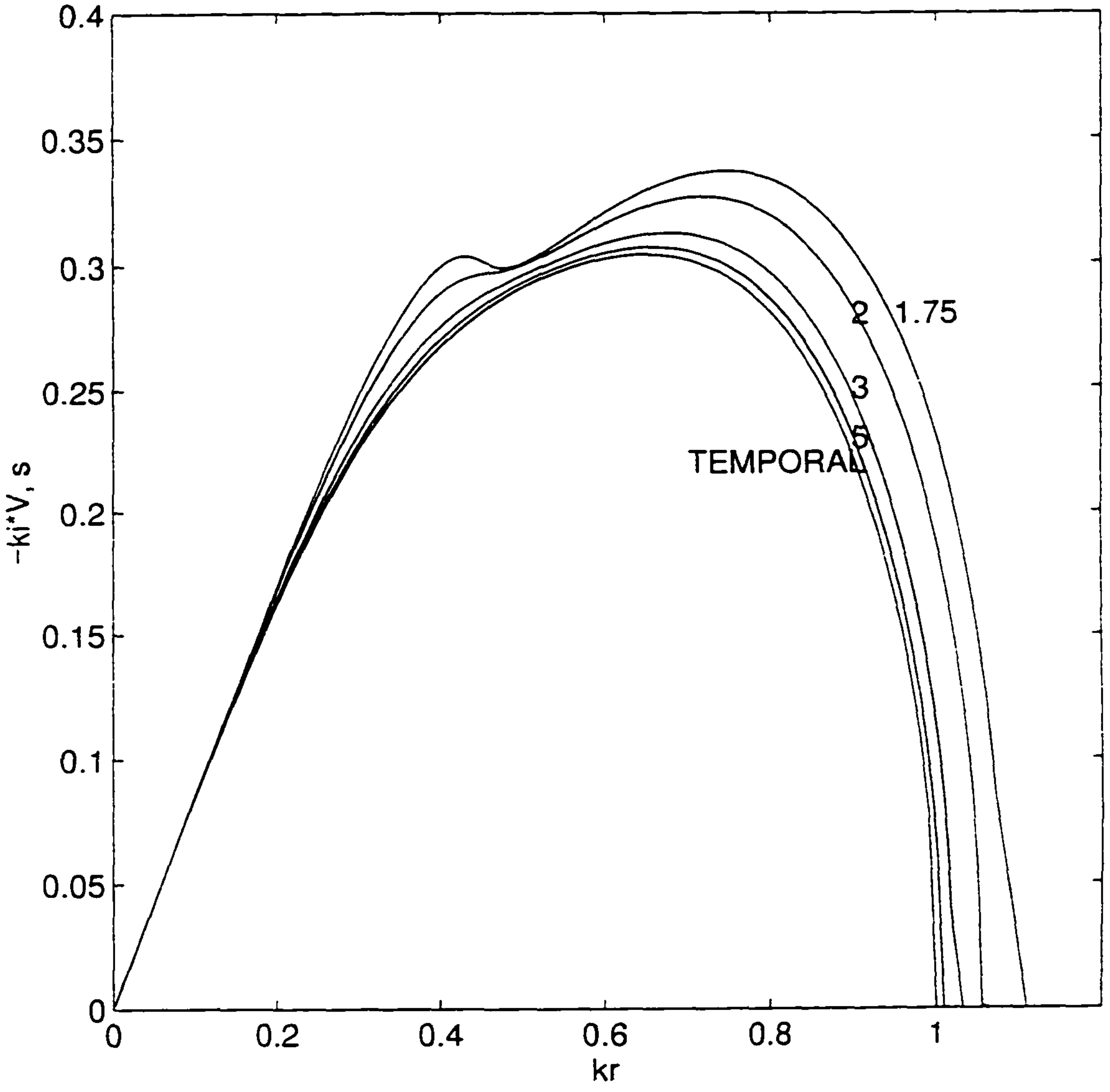

Figure 10. Effect of the jet velocity on spatial growth rates for the primary mode and its comparison with the temporal growth rate for the stretching mode. The numbers on the curves denote the values of V. β=l,γ=2,a=2

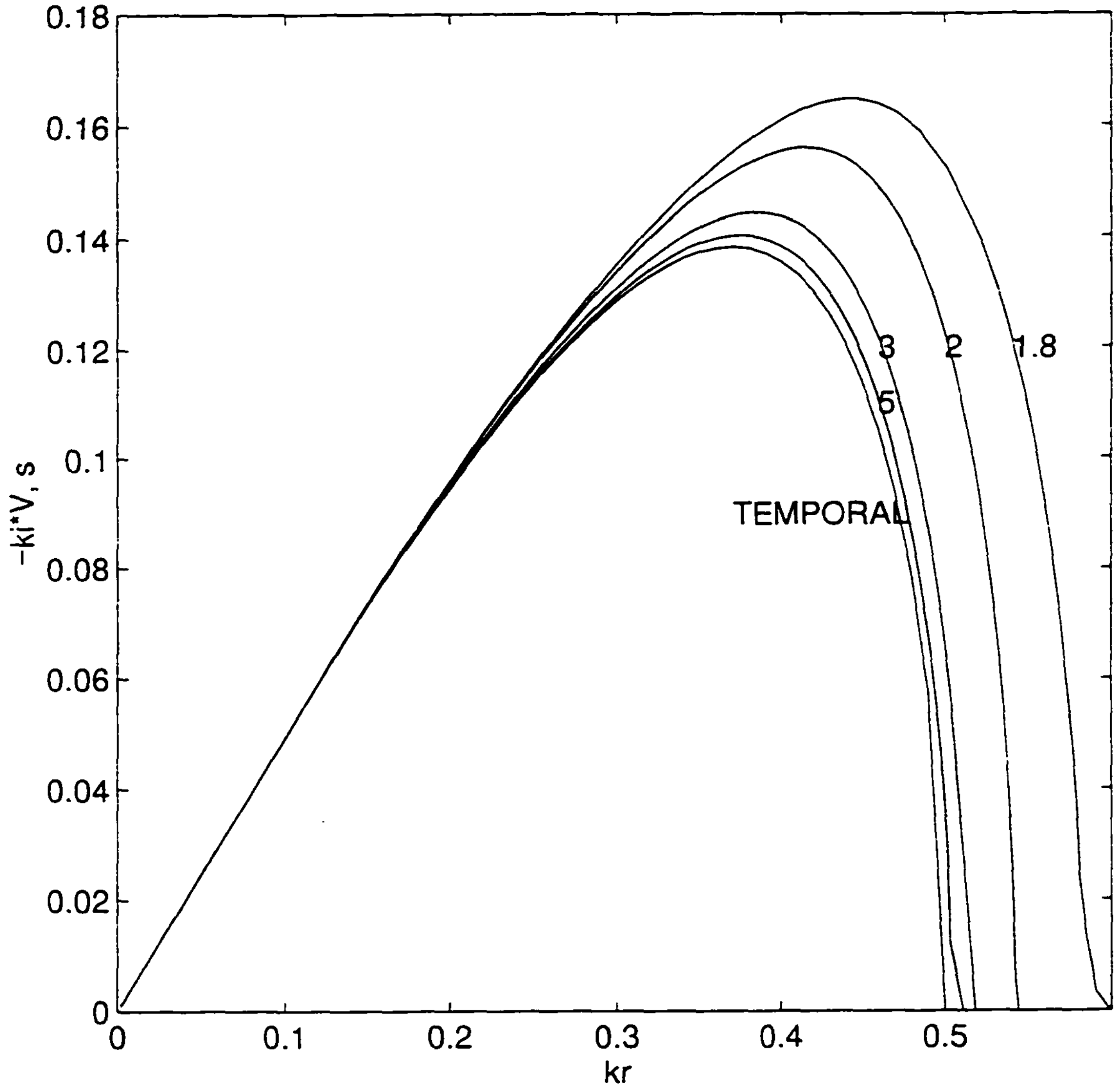

Figure 11. Effect of the jet velocity on spatial growth rates for the secondary mode and its comparison with the temporal growth rate for the squeezing mode. The numbers on the curves denote the values of V. β=l,γ=2,a=2

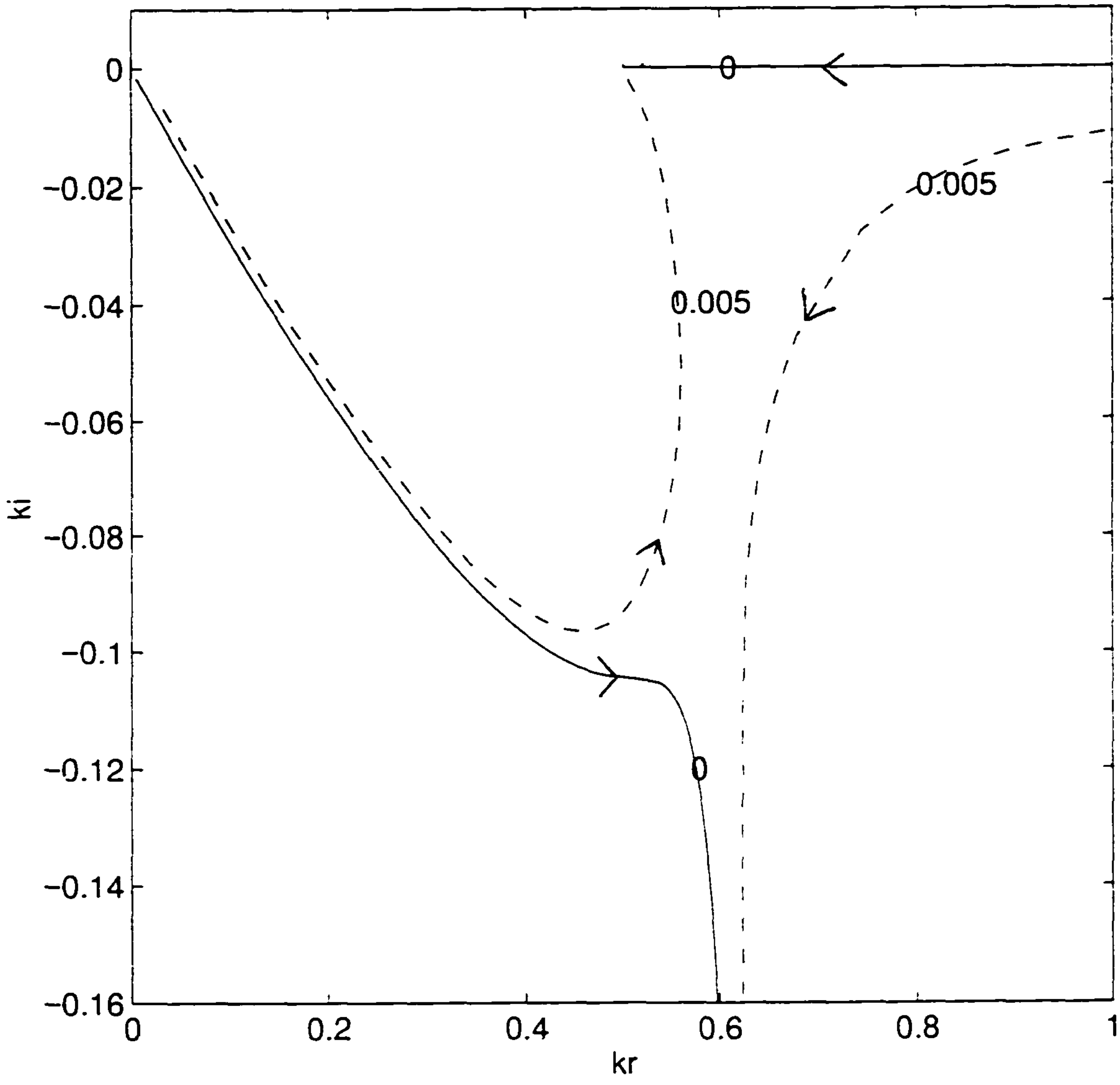

Figure 12 Merging of secondary and evanescent roots causing absolute instability. The numbers on the curves denote the values of s_r. β=1,γ2,a=2,V=1.7

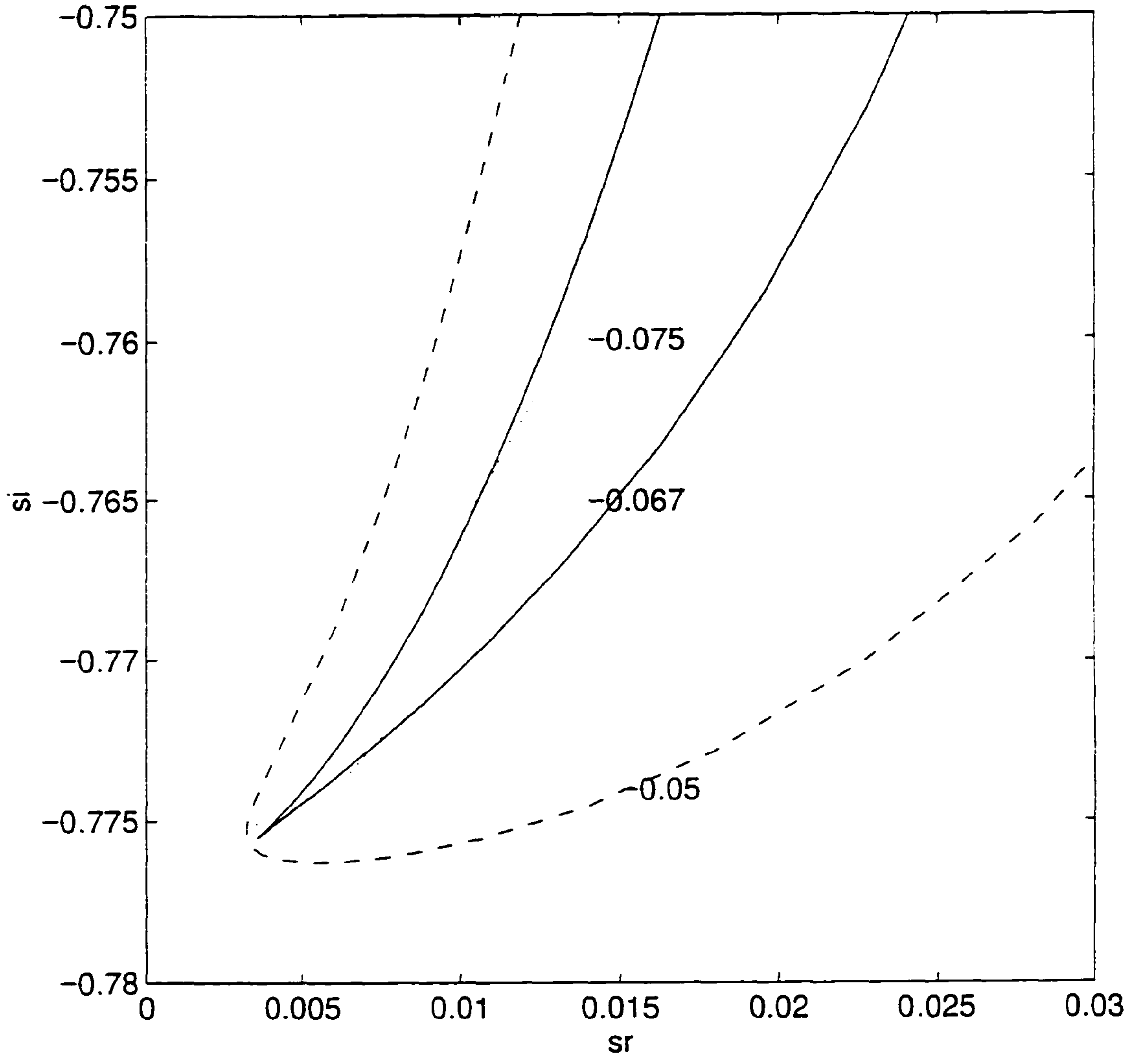

Figure 13 Cusp formation in s-plane implying ds/dk=0. The curves are mapping of constant k_i lines in the s plane. The numbers on the curves denote the values of k_i $\beta=1,\gamma=2,a=2,V=1$ ·7

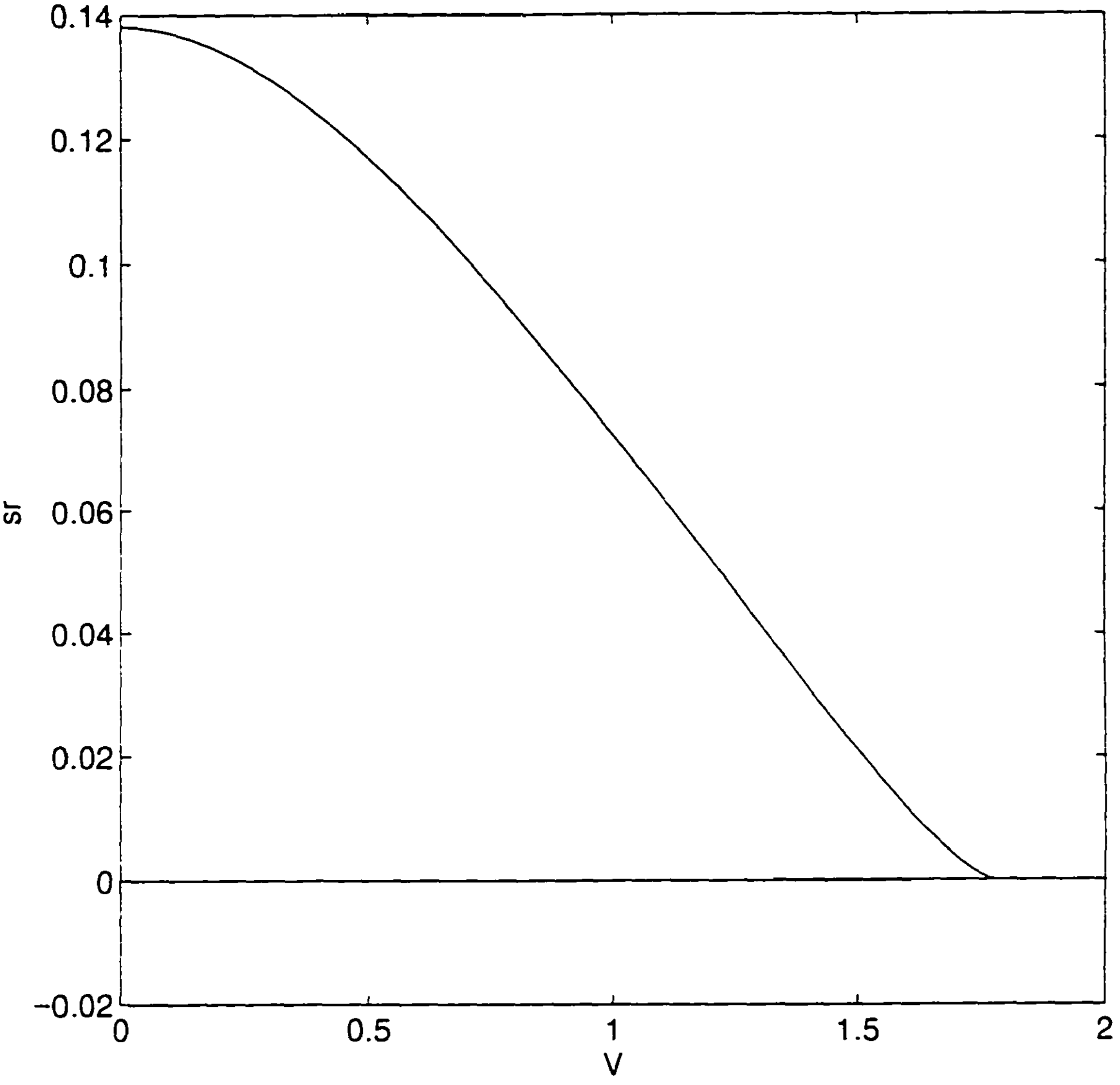

Figure 14 Variation in s_r at absolute instability with V. $\beta=1,\gamma=2,a=2$

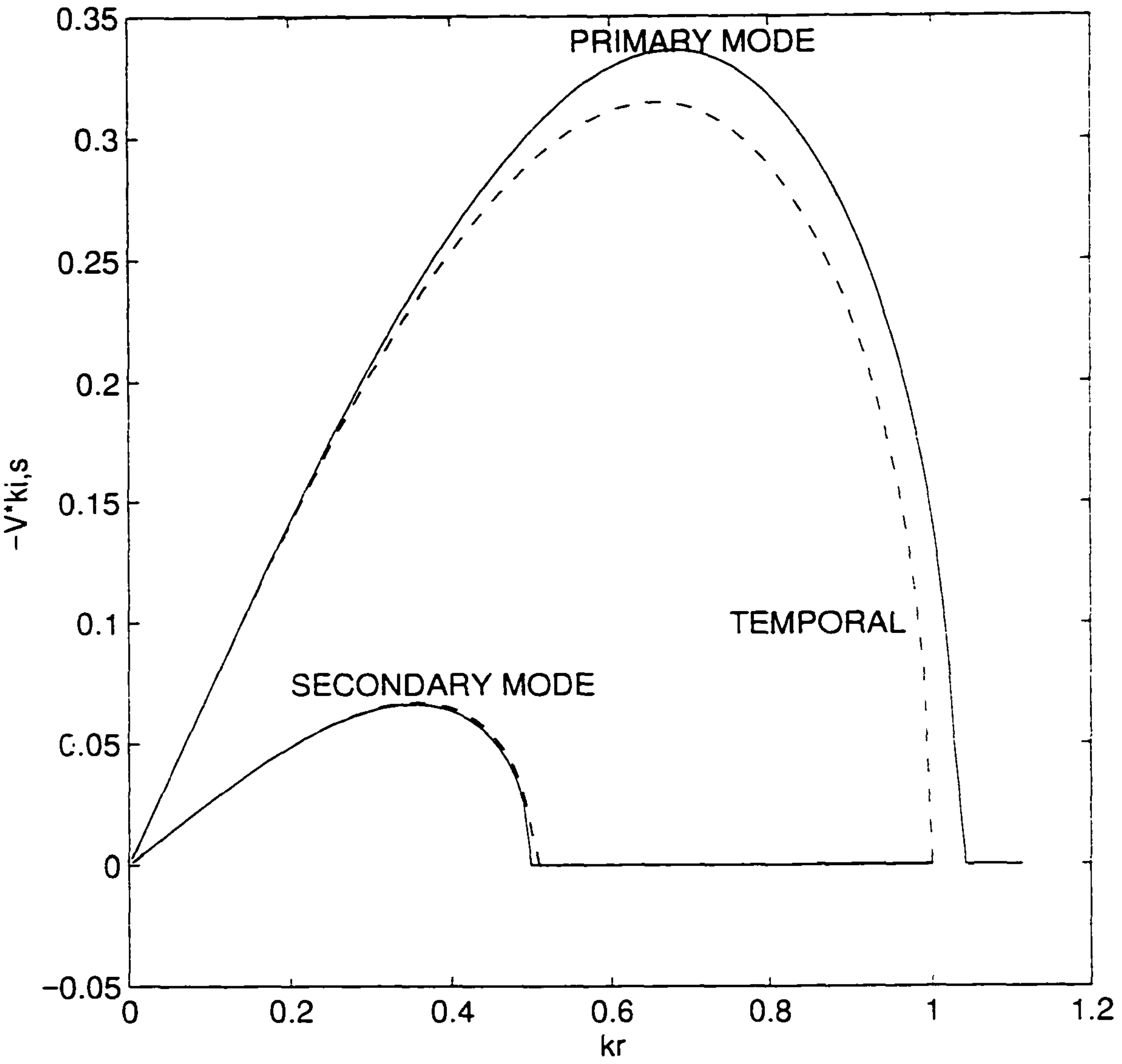

Figure 15 Comparison of the predictions of the temporal and the spatial theories with experiment performed by Hertz & Hermanrud. $\beta=1$,$\gamma=0.4$,$a=2$,$V=2.426$

CHAPTER 4

ABSOLUTE INSTABILITY OF AN INVISCID COMPOUND JET

(1) INTRODUCTION

Spatial analysis of an inviscid single jet (Leib and Goldstein 1986) shows that it becomes absolutely unstable below a critical Weber number of 3.2. This implies that any disturbance imposed on the jet grows exponentially in time, everywhere. Since capillarity drives the instability in both the single and the compound jets, it is expected that a compound jet will also become absolutely unstable below a critical Weber number.

Chauhan et. al. (Chauhan et al. 1996) provided the first insight into the spatial analysis of the compound jet in the absence of gravity. They showed that there are again two spatially growing modes and, as in the single jet at high Weber numbers, these merge with the temporal results. One (primary) mode is unstable for ω/v from 0 to approximately 1 and the other (secondary) from 0 to approximately 1/a. However, for finite velocities, these modes are no longer purely stretching or squeezing. The wave length and growth rate of the convective instability are functions of surface tension, thickness and density ratios.

The questions that remain are: 1. At what critical values of the Weber number does a compound jet become absolutely unstable? 2. How does this critical Weber number V_{crit} depend on these system parameters? We focus primarily on the effect of the surface tension ratio γ. 3. How does the dominant absolute growth rate and wave length vary with the Weber number below V_{crit}?

These unresolved issues are important from the standpoint of application. A separate issue is: 4. Does the compound jet lend itself to easy observability of the absolute instability? (In fact, the manifestation of absolute instability in jet problems is debatable.) A necessary condition for being able to distinguish the absolute from the convective instability is to be able to discern instability characteristics, e.g., growth rate, wave length, dispersion, that may differ between the two. Clearly such measurements require the convective instability to break the jet sufficiently far, i.e., at least a few jet radii ($k_i a<<1$), from the nozzle. For the single jet of water in air, the critical velocity is low and, since k_i typically scales with $s_r(k_r)/V$, $k_i a$ turns out to be order 1. Thus it is interesting to investigate whether the absolute instability of the compound jet more readily lends itself to observation than that of the single jet.

Section II formulates the linear stability problem and describes the mechanics of finding V_{crit}, the growth rates and wave lengths for the absolute instability from the roots of the dispersion equation. Section III carries out these calculations and the effect of γ on them. The subsequent section uses these results to identify conditions best suited for the observation of absolute instability.

II Formulation of the linear stability theory

II.IGoverning equations and boundary conditions

A doubly infinite jet of an incompressible, inviscid fluid A, of density ρ_1 is surrounded by a coaxial annulus of an immiscible incompressible, inviscid fluid

B, of density ρ_2 (figure 1). Choose a cylindrical coordinate system (r, θ, z), whose z axis is coincident with the fluid cylinder's axis. The compound jet is moving in a vacuum with a uniform velocity in the positive z direction. The undeflected inner interface is $r=R_1$ and the outer interface is $r=R_2$. The interfacial surface tensions are σ_1 and σ_2, respectively.

The equations of motion and continuity in dimensionless form are

$$\nabla \bullet \mathbf{v}_i = 0 \qquad (i=1.2) \tag{1}$$

$$\beta_i \frac{D\mathbf{v}_i}{Dt} = -\nabla P_i \qquad (i=1.2) \tag{2}$$

where in fluid i, P_i is the pressure and $\mathbf{v}_i$ is the velocity vector. In the governing equations and the boundary conditions, we non-dimensionalize lengths by $[R_1]$, time by $[(\sigma_1/\rho_1 R_1^3)^{-1/2}]$, pressure by the surface tension pressure $[\sigma_1/R_1]$ and velocity by $[(\sigma_1/\rho_1 R_1)^{1/2}]$. The dimensionless parameters are $a=R_2/R_1$, $\gamma=\sigma_2/\sigma_1$, $\beta_2=\beta=\rho_2/\rho_1$ and $\beta_1=1$. The interfaces are denoted by $r=h_i(z,t)$ $(i=1.2)$. Define the mean curvature H_i of interface i $(i=1.2)$ by,

$$2H_i = -\frac{1}{h_i(1+h_i'^2)^{\frac{1}{2}}} + \frac{h_i''}{(1+h_i'^2)^{\frac{3}{2}}}$$

(3)

Aside from the centerline condition ($\mathbf{v}_1$, P finite at r=0), the boundary (the jump in normal stress and the continuity of velocity) and kinematic conditions in dimensionless form are:

$$[[P]]_i = 2H\gamma_i + F_i(t)\delta(z - z_o) \quad \text{at } r = h_i(z,t) \quad i = 1,2 \tag{4}$$

$$[\frac{\partial}{\partial t} + \mathbf{v}_i \bullet \nabla](r - h_i) = 0 \quad \text{at } r = h_i(z,t) \quad i = 1,2 \tag{5}$$

$$[[\mathbf{n} \bullet \mathbf{v}]]_1 = 0 \quad \text{at } r = h_1(z,t) \tag{6}$$

where $[[\;]]_i$ denotes the difference between inside and outside of interface i. **n** is the outward unit vector normal to the interface and $F_i(t)$ is the temporal forcing in the pressure applied on surface i at $z=z_0$. Below, we take $z_0=0$, i.e.. the source's position defines the origin.

In the base state there is no forcing, and the interfaces are undeflected. Let u and w denote the radial and axial velocities, respectively. Any velocity solution of the form, u=0, $w=\Phi(r)$, where Φ is twice differentiable, but otherwise completely arbitrary, satisfies the base state equations (1)-(6) exactly. Since we are interested in capillary driven instabilities, we restrict the analysis to solutions in which w=constant=V in both the core and the annulus. With this assignment, there is no slip at the interface, thereby preventing the Kelvin Helmoltz type of instability. Thus, we concentrate on the base state (superscript "o"):

$$u_i^{(o)} = 0, \; w_i^{(o)} = V \quad i = 1,2 \tag{7}$$

$$P_2^{(o)} = \frac{\gamma}{a}, P_1^{(o)} = 1 + \frac{\gamma}{a} \tag{8}$$

If a small ($\sim \lambda$), axisymmetric disturbance is introduced into the jet at the nozzle tip, the disturbances to the velocities and the interface from the base state are also of order λ. For i=1,2, we have

$$\begin{aligned} u_i(r,z,t) &= u_i^{(1)}(r,z,t)\lambda + O(\lambda^2) \\ w_i(r,z,t) &= V + w_i^{(1)}(r,z,t)\lambda + O(\lambda^2) \end{aligned} \tag{9}$$

$$h_1(z,t) = 1 + \zeta_1^{(1)}(z,t)\lambda + O(\lambda^2) \tag{10}$$

$$h_2(z,t) = a + \zeta_2^{(1)}(z,t)\lambda + O(\lambda^2) \tag{11}$$

$$P_i(r,z,t) = P_i^{(o)} + P_i^{(1)}(r,z,t)\lambda + O(\lambda^2) \tag{12}$$

Substituting these in the governing equations, one gets the leading order equation for the perturbation quantities,

$$\beta_i\left(\frac{\partial \mathbf{v}_i}{\partial t} + V\frac{\partial \mathbf{v}_i}{\partial z}\right) = -\nabla P_i \qquad (i=1,2) \tag{13}$$

$$\nabla\bullet\mathbf{v}=0 \qquad (i=1,2) \tag{14}$$

where we delete superscript 1 denoting the perturbation order. Taking the divergence of the momentum balance and using the equation of continuity, we get

$$\nabla^2 P_i = 0 \tag{15}$$

II.II Transformation to the Fourier-Laplace domain

Defining the Laplace and Fourier transforms as

$$\hat{g}(s,k) = \int_{-\infty}^{\infty} e^{-ikz}\{\int_{0}^{\infty} e^{-st}\, g(t,z)dt\}dz \tag{16}$$

In the transformed domain, equation (15) becomes:

$$[\frac{d^2}{dr^2}+\frac{1}{r}\frac{d}{dr}-k^2]P_i(r,k,s)=0 \tag{17}$$

where we delete ^ , so P_i (r,k,s) is the pressure in the Fourier-Laplace domain. The general solution of (17) is,

$$P_i=A_iI_0(kr)+B_iK_0(kr) \tag{18}$$

where I_o and K_0 are the modified Bessel functions of order 0 and A_i, B_i are constants of integration which can be functions of k and s but not of r.

The boundary and kinematic conditions (4-6) in dimensionless form in the Fourier-Laplace domain are:

$$P_2=-\gamma(\frac{1}{a^2}-k^2)\zeta_2+F_2(s) \quad \text{at } r=a: \tag{19}$$

$$P_1-P_2=-(1-k^2)\zeta_1+F_2(s) \quad \text{at } \quad r=1: \tag{20}$$

$$u_1=s\zeta_1 \text{ at } r=1; \tag{21}$$

$$u_1=u_2 \quad \text{at} \quad r=1: \tag{22}$$

$$u_2=s\zeta_2 \text{ at } r=a; \tag{23}$$

The velocity and pressure are finite at r=0.

Using (13) to get $u_i(r,k,s)$, and substituting for u_i and P in (19)-(23) yields A(k,s)**x**=**b**(k,s), where

$$b^t=[0.0,0.F_1,F_2]$$

(24)

$$x^t = [A_1, A_2, B_2, \zeta_1, \zeta_2]; \tag{25}$$

$$A(k,s) = \begin{pmatrix} I_1(k) & -\dfrac{I_1(k)}{\beta} & \dfrac{K_1(k)}{\beta} & 0 & 0 \\ \dfrac{kI_1(k)}{s+ikV} & 0 & 0 & s+ikV & 0 \\ 0 & \dfrac{kI_1(ka)}{(s+ikV)\beta} & \dfrac{-kK_1(ka)}{(s+ikV)\beta} & 0 & s+ikV \\ 0 & I_0(ka) & K_0(ka) & 0 & \gamma(\dfrac{1}{a^2}-k^2) \\ I_0(k) & -I_0(k) & -K_0(k) & (1-k^2) & 0 \end{pmatrix} \tag{26}$$

The solution of this system of 5 equations for ζ_1 and ζ_2 is.

$$\zeta_1 = \frac{1}{|A|}[C_{44}F_2 + C_{45}F_1] \tag{27}$$

$$\zeta_2 = \frac{1}{|A|}[C_{54}F_2 + C_{55}F_1] \tag{28}$$

where $|A|$ is the determinant of the matrix A whose mnth element is a_{nm}, with corresponding cofactor C_{mn}. Let us consider a situation in which $F_1=0$ and $F_2(t)=Fe^{i\omega t}$, i.e., a periodic disturbance in the film's pressure introduced at z=0.

II.III Inversion to space time domain

To get the solution in the time and space domain, one must invert the solution from the Fourier-Laplace domain, i.e.,

$$\zeta_i(z,t) = \frac{1}{4\pi^2 i}\int_{-\infty}^{\infty} e^{ikz}\left[\int_{c-i\infty}^{c+i\infty} \zeta_i(k,s)e^{st}ds\right]dk \qquad (29)$$

where c(k) is a real number that lies to the right of all singularities of ζ in the s plane for each k. We perform both of these integrals as contour integrations in the complex plane and thus their evaluations involve determining and following the poles of the integrands. Although we leave the details of the inversions for the appendix, we make a few operational notes for the discussion below.

The absolute instability arises from the merger (to form higher order poles) at $s_r>0$ of k-plane poles that for large s_r have k_i of opposite signs. Thus the calculations in the next section focus on following the locations/motions of these poles in the k-plane as s_r changes, and carefully tracks the merge points back to large $s_r>0$. Since the outer integrand consists of a sum of residues of the inner integral, that outer inversion requires a contour integration for each of these residues, and each may require a separate contour. These latter contours Γ (in the k-plane) do not lead to absolute instability if it is possible to choose Γ with corresponding s values everywhere having negative real parts.

III RESULTS AND DISCUSSION

III.I MERGING PATTERNS IN THE k PLANE (Origin of absolute instability)

The implicit function theorem allows one to solve $|A(k.s(k))|=0$ for s(k) if ds/dk?0. The absolute instability results from merging to form a higher order root of two k-plane roots i.e., where $\partial|A(k.s)|/\partial k=0$ as well, which lie in the opposite halves of the k plane for large s_r. Since $d|A(k.s(k))|/dk$ is zero along the manifold

$|A(k,s(k))|=0$, either $\partial|A(k,s)|/\partial s=0$ or $ds/dk=0$. By numerical investigation, we never find $\partial|A(k,s)|/\partial s=0$ and $|A(k,s(k))|=0$ at the same point; thus $ds/dk=0$ at a second order pole. The condition $ds/dk=0$ is clearly necessary for absolute instability, but not sufficient because one must still follow these roots in the k plane fcr large s_r. Solution of these equations locates the mergings.

In order to determine for how large an s_r one must continue the roots in the k plane, note that at the points at which a root crosses the real k axis, the dispersion equation takes the form, $s_n+ikV=g_n(k)$; here $g_n(k)$ is the temporal growth rate of the n^{th} mode. Chauhan *et al* (Chauhan et al. 1996) use the form of the dispersion equation which is explicit in s to show that the temporal growth is either purely real or purely imaginary for k real. Thus, if s_r is greater than the maximum temporal growth rate ($\max(g_n(k))$) for the corresponding mode, there can be no solution to $s_n=g_n(k)-ikV$ and k(s) cannot intersect real k axis. For each mode, this is then the maximum s_r to continue the k-plane roots.

Our first goal is to locate the critical velocity at a fixed γ. Then by examining the detailed merging patterns we investigate how the growth rate of the absolute instability varies with velocity at constant γ. Finally, we construct the marginal curve for critical velocity as a function of γ. In each of the Figs. 2-8 below, we plot curves which represent the solutions of the dispersion equation for values of $s=s_r-i\omega$, $\omega>0$ (see below), i.e., the images of vertical lines in the s-plane. The curves/roots labeled [1], [2] lie in the upper, and those labeled [3], [4] lie in the lower half k plane at large s_r. On reducing s_r [1], [2] move down and [3], [4] move up and can result in intersections where $\partial|A(k,s)|/\partial k=0$. Upon further reducing s_r, the topology of the continuous branches of the image of the s-plane vertical lines changes and only parts of these continuous branches derive from branches [1] or [2]. To keep track of the section of each branch which continues to the upper half k plane for large s_r, we denote the frequencies (the parameter along the branch curve) for which the root moves to the upper half k plane by ω_u and write the interval of ω_u in curly brackets { }. For example, since the entire root [1] is in the upper half k plane for large s_r, we write [1] $\{\omega_u>0\}$. Similarly, the entire root [3] moves to the lower half for large s_r; hence [3]$\{\omega_u=\phi\}$, where ϕ is the null set. The condition for absolute instability implies that ω at the intersection, ω_a, should belong to ω_u for precisely one of the intersecting roots.

By examining the matrix in equation (26), one can show that the dispersion equation $f(s,k)=|A|=0$ satisfies the symmetries $f(s,k,V)=f(s^*,k^*,-V)^*$ and $f(s,k)=-[f(s^*,-k^*)]^*=[f(-s^*,k^*)]^*$, where * denotes complex conjugate. Thus if $f(s_r+i\omega,k_r+ik_i)=0$, then $f(s_r-i\omega,-k_r+ik_i)=0$, or for a given s_r the solution for $s_i=-\omega$ is a mirror image of $s_i=\omega$ about the imaginary k axis. This symmetry permits us to only inspect $\omega>0$, i.e., $s_i<0$. Also, if $s_r=0$, $s^*=-s$. Hence if $f(i\omega,k_r+ik_i)=0$, then $f(i\omega,k_r-ik_i)=0$, or for purely imaginary s the solutions in the upper and lower half k planes are mirror images.

Figs. (2) and (3) show three roots of the dispersion equation in the k plane for V=2.0 with the value of s_r labeling the curves and with ω parametrizing then, where $s=s_r-i\omega$. The direction of the arrows on the curves in these and all the subsequent figures shows the direction of increasing ω. In addition, in these and subsequent figures (2)-(8), a=2, γ=2 and β=1. At V=2 there is no merging of roots (and a curve Γ, such that, s_r on the curve is everywhere negative. exists). The intersections in the k plane of modes [1] and [3] are not mergings because they correspond to different s values. They arise because k(s) is multivalued. There is a different curve Γ for each mode. Modes [1] and [3] are shown in figure 2.1 and modes [2] and [3] in figure 2.2. Upon decreasing s_r mode [1] and [2] move down and mode [3] moves up. Modes [1] and [2] lie inside the contour for the k-plane integration, but at s_r=0, lie in the lower half k-plane (see appendix), i.e.. k_i is negative for these modes: thus they contribute residues that grow spatially. At s_r=0, modes [1] and [2] join the real k axis, to the right of critical values that, as mentioned earlier, are close to, but not equal to 1/a and 1. respectively. Mode [3] is an evanascent mode, i.e., it does not contribute to instability because it lies outside the contour for the Fourier inversion. There is another evanascent mode which will contribute to absolute instability at lower velocities. We call this mode [4] and will show it in later figures. Modes [1] and [2] lie below or on the real k axis for s_r=0 and hence these modes are convectively unstable and lead to axial growth. As noted in the introduction, the critical values of k_r for these modes are approximately equal to, but only at V=0 are they exactly equal to, 1 and 1/a. The spatial growth rates $-k_i$ of each mode change with frequency, with a maximum $k_{i,max}$ for each mode i.=1,2. For all frequencies the spatial growth rate of mode [1] is the higher.

On reducing the velocity to 1.75 (see Fig. 4), [2] merges with evanescent root [3] at (s,k)=(0.0008-0.8055 i, 0.6077-0.041 i). On further reducing s_r, the curves split to form [23] and [32], which are plotted for s_r=0. Clearly, in the region between [23] and [32], for any k, there is at least one solution s(k) for which s_r>0. Thus, we choose Γ (not shown) such that between curves [23] and [32] it is the mapping of $s_i=s_{i,m}=-0.8055$. As explained in the appendix, this contributes exponential growth in time which is the absolute instability. Root [1] appears in the figure to illustrate that it has not merged with any evanescent roots.

On further reducing the velocity, more modes becomes absolutely unstable, i.e., either the curve Γ has to pass through two or more regions where $s_r(k)>0$ or one must construct different Γ curves for each of the two convectively unstable modes and they both have to pass through regions of s_r>0.

Fig (5) shows the mergings at V=1.50. At (s,k)=(0.0211-0.6624 i, 0.5415-0.1001 i), roots [2]$\{\omega_u>0\}$ and [3]$\{\omega_u=\phi\}$ merge. It represents absolute instability i.e.. ω_a belongs to ω_u for root [2] only. On further reducing s_r, the merger splits to form roots [23]$\{\omega_u<0.6624)$ and [32]$\{\omega_u>0.6624\}$. The part of [32] for $\omega>0.6624$ was in the upper half k and the rest was in the lower half k plane for large s_r. The next intersection takes place between [23] $\{\omega_u<0.6624\}$ and [1] $\{\omega_u>0\}$ at (s,k)=(0.0044-0.6887 i, 0.4665-0.2177 i). This also causes absolute instability because ω_a=0.6887 belongs to ω_u for [1] mode only. (If ω_a at this second intersection were less than that for the first intersection, ω_a would belong to ω_u for both roots and hence the merger would not cause absolute instability.) This merger then splits upon reducing s_r to form [123] and [231].

Figs (6) shows the mergings at V=1.3. The first merger takes place at (s,k)=(0.0486-0.5964i,0.4562-0.2233i) between root [1]$\{\omega_u>0\}$ and root [3]$\{\omega_u=\phi\}$. It represents absolute instability because $\omega_c=0.5964$ belongs to ω_u for mode [1] only. On reducing s_r these roots split to form [13]$\{\omega_u<0.5964\}$ and [31]$\{\omega_u>0.5964\}$. The next merger takes place between [31]$\{\omega_u>0.5964\}$ and [2]$\{\omega_u>0\}$ at (s,k)=(0.0418-0.5579,0.5058-0.1041). Thus it also causes absolute instability because $\omega_a=0.5579$ belongs to ω_u for [2] only. After splitting these roots form [231]$\{0<\omega_u<0.5579, \omega_u>0.5964\}$ and [32]$\{\omega_u>0.5579\}$. On reducing s_r further, at (s,k)=(0.0173-1.1237i,1.2142-0.2244i), [231] $\{0<\omega_u<0.5579, \omega_u>0.5964\}$ intersects with [4]$\{\omega_u=\phi\}$. For this merger $\omega_a=1.1237$ belongs to ω_u for mode [231] only. Thus, this merger is also absolutely unstable. After the merger the roots split into [2314] $\{0<\omega_u<0.5579, 0.5964<\omega_u<1.1237\}$ and [4231] $\{\omega_u>1.1237\}$.

Fig(7) is the plot of the roots in the k plane for V=1. There are three mergings at V=1 and each one is again absolutely unstable. The first one is between [1]$\{\omega_u>0\}$ and root [3]$\{\omega_u=\phi\}$ at (s,k)=(0.1152-0.4625i,0.4367-0.2181i). It represents absolute instability because $\omega_a=0.4625$ belongs to ω_u only for mode [1]. On reducing s_r these roots split to form [13]$\{\omega_u<0.4625\}$ and [31]$\{\omega_u>0.4625\}$. This merger is similar to the one at V=1.3 but the next one is different. It takes place between [31]$\{\omega_u>0.4625\}$ and [4]$\{\omega_u=\phi\}$ at (s,k)=(0.1016-0.4712i,1.0049-0.2190i). It also causes absolute instability because $\omega_a=0.4712$ belongs to ω_u for only [31]. After splitting these roots form, [41]$\{\omega_u>0.4712\}$ and [314]{

$0.4625<\omega_u<0.4712\}$. On reducing s_r further, the third merging occurs at $(s,k)=(0.0724-0.4122i, 0.4676-0.0988i)$ between $[314]\{0.4625<\omega_u<0.4712\}$ and $[2]\{\omega_u>0\}$. $\omega_a=0.4122$ belongs to ω_u for mode [2] only. Thus, this merger is also absolutely unstable. After the merger the roots split into $[2314]\ \{0<\omega_u<0.4122, 0.4625<\omega_u<0.4712\}$ and $[3142]\{\omega_u>0.4122\}$.

Fig(8) shows the mergings at V=0.5. The first merging is between $[1]\{\omega_u>0\}$ and root $[4]\{\omega_u=\phi\}$ at $(s,k)=(0.2389-0.3511i, 0.7798-0.2235i)$. It represents absolute instability because $\omega_a=0.3511$ belongs to ω_u for mode [1] only. On reducing s_r these roots split to form $[14]\{\omega_u<0.3511\}$ and $[41]\{\omega_u>0.3511\}$. The next merger takes place between $[41]\{\omega_u<0.3511\}$ and $[3]\{\omega_u=\phi\}$ at $(s,k)=(0.2159-0.2488i, 0.4254-0.1801i)$. It also causes absolute instability because $\omega_a=0.2488$ belongs to ω_u for [41] only. After splitting these roots form $[413]\{0.2488<\omega_u<0.3511\}$ and $[341]\{\omega_u<0.2488\}$. On reducing s_r further, the third merging happens at $(s,k)=(0.1169-0.1925i, 0.4103-0.0746i)$ between $[413]\{0.2488<\omega_u<0.3511\}$ and $[2]\{\omega_u>0\}$. $\omega_a=0.1925$ belongs to ω_u for mode [2] only. Thus, this merger is also absolutely unstable. After the merger the roots split into $[4132]\ \{\omega_u<0.1925\}$ and $[2413]\{<0\omega_u<0.1925, 0.2488<\omega_u<0.3511\}$.

At V=0.1 (not shown) the first merger is similar to that at V=0.5. There the second merger is between $[41]\{\omega_u=\phi\}$ and $[3]\{\omega_u<\omega_{a.1}\}$, where $\omega_{a.1}$ is the frequency at the first merger. This second merger is absolutely unstable if the frequency at merger $\omega_{a.2}$ lies in the range of ω_u for [13], i.e., $\omega_{a.2}<\omega_{a.1}$. But in region V, this is not true and hence the second merger in this region does not cause absolute instability. The third merger in region V is between [2]$\{\omega_u>0\}$ and [413]$\{\omega_{a1}<\omega_u<\omega_{a2}\}$ which becomes a null set $\{\phi\}$ in region V. Thus the last intersection between [2]$\{\omega_u>0\}$ and [412]$\{\phi\}$ is absolutely unstable.

At V=0 the merging pattern is the same as at V=0.1. What is unique, however, is that the two mergings (the first and the third) which give rise to absolute instability, i.e., which take place for $s_r>0$, take place on the real k axis. Recall $s_n+ik_nV=g(k_n)$. At V=0 and k real, $s=g(k_n)$, which is simply the equation for the temporal roots. As noted in the Introduction, the temporal roots are purely real when unstable. The merging of roots requires, in addition, ds/dk= d(g(k))/dk=0, which is just the condition for the maximum of the temporal growth rate.

From this catalog of merging patterns one can construct a phase diagram (Figs. 9 and 10, plots of the simultaneous solutions of $|A(k,s)|=0$ and ds/dk=0 having $s_r\geq 0$) which synthesizes the change in the order (upon reduction of s_r) of the merging patterns and thereby gives the dominant absolute growth rate as a function of the non-dimensional velocity V. The demarcations in the figures are the values of V at which the order of the merging patterns change and they identify the first four regions. The discussion above describes the patterns for each of these regions. Region V is distinguished from region IV not for this reason, but rather because in region V, the second merging is no longer absolutely unstable. As Figure 10 shows, this demarcation is the value of V at which the s_i values for the first and second mergings are equal: that is, at this point, the second merging changes from being between root [3] and the root-[1]-

part of [41] to being between root [3] and the root-[4]-part of [41]. Note that the three curves in Fig. 9 all intersect the s_r=0 axis. The second intersection is a transverse one, while the first and third intersect at finite V values and remain on the V axis for all higher values of V. The reason for this is that for V greater than these intersection values (where the curves no longer represent absolute instability (s_r>0)), there is nevertheless always a merging of roots of the dispersion equation for s_r=0. From Figures 11 and 12, plots of the wave length k_r and the axial growth rate k_i of each of the three root intersection curves from Fig. 9 and 10, one can see this. From Fig. 12, the k_i values corresponding to the s_r=0 V values are clearly zero. In addition, Fig. 11 shows that the k_r values corresponding to the s_r=0 V values are greater than approximately 1 and 1/a. the cutoff k_r values for each mode that divide convectively growing (k_i<0) from decaying waves.

Certain regularities in these figures are apparent. As a result of the aforementioned symmetries of f(s.k.V), the curves in Figs. 9 and 11 are symmetric and those in Figs. 10 and 12 are anti-symmetric (V<0 not shown in Fig. 10) about V=0. These symmetries imply that the region z>0 for a jet traveling in a positive z direction behaves in an identical manner to the region z<0 for a jet moving with the same speed in the negative z. In addition, Fig. 9 indicates that the two absolutely unstable mergings have zero slope at V=0 whereas the root that is not absolutely unstable has a (symmetric) cusp there. The reason for this behavior, as we now show, is because k is purely real for the absolutely unstable mergings and complex for the other. To see this, recall that the solution of the dispersion equation, a biquadratic in $s+ikV$, takes the form $s+ikV=g(k)$. If one considers $s=s(k(V),V)$, then the condition for merging becomes $\partial s/\partial k=0$. Begin by taking $\frac{ds}{dV}=\frac{\partial s}{\partial V}+\frac{\partial s}{\partial k}\frac{dk}{dV}$. Note that the partial with respect to V of the dispersion equation gives $\frac{\partial s}{\partial V}=-ik$. Inserting this and the condition for merging into the total derivative gives the following component equations: $\frac{ds_r}{dV}=k_i$ and $\frac{ds_i}{dV}=-k_r$. Thus, for mergings on the real k axis at $V=0$, $ds_r/dV=0$ while for the merging that takes place off the axis for $V=0$, it is non-zero.

The outer envelope in Figure 9 defines the dominant growth rate of the absolute instability. Clearly its slope is discontinuous due to different mergings dominating in different regions. Consequently, at the boundaries of these regions, the dominant wave length k_r and axial growth k_i can change discontinuously as one switches from one branch of Fig. 9 to another at a region boundary crossing. See Figs. 11 and 12. It is important to stress here that the merging patterns displayed in Figures 9 and 10 as well as this outer envelope are strong functions of the system parameters, e.g., a and γ, and must therefore be calculated for each specific case.

These discontinuities of k_r and k_i in the dominant mode below the critical Weber number are unique to the compound jet relative to the single jet. Let us compare these results to the single jet's. The single jet's dispersion equation is simply $(s+ikV)^2=k^2(1-k^2)I_1(k)/I_0(k)$ and Figure 13 shows the only merging pattern below the critical V=1.8. Correspondingly, there is only one dominant mode (and no discontinuity in k_r or in k_i), which Fig. 14 displays in terms of what we have called a phase diagram, i.e., s_r vs V. Again, above the critical value of V the mergings exist for $s_r=0$. i.e., the curve in Fig. 14 continues along the V axis, and lie on the real k axis, i.e.. $k_i=0$ (figure 15) to the right of the k_r of the convectively growing waves, i.e., k_r is greater than one which is the approximate cutoff for the convective waves (figure 16) The symmetries in velocity shown above for the compound jet are true for the single jet also. The slope of s_r vs. V goes to zero at V=0 and s_i goes to zero too at V=0 (figure 17).

III.II MERGING PATTERNS IN THE s PLANE

The origin of absolute instability lies in the merging of roots in the k plane to yield a double root. At the double root ds/dk=0 (see appendix). Since the dispersion equation is explicit in s=s(k), it is useful to transform this merging to the s plane. Hence, we make plots of constant k_i in the s plane. There are four solutions to the dispersion equation for a given k, thus, there are 4 modes in the s plane. We show one of these for V=1.71 in fig(18). The three curves are plots for k_i of -0.02, -0.0629, -0.1 The middle curve has a cusp at s=.0029-0.7815i. The k corresponding to this cusp is. 0.5952-0.0629i. This is exactly the point of the merger of two roots in the k plane. The cusp formation implies, $ds_i/dk_r=ds_r/dk_r=0$. {k_i is constant along these curves and cusp formation implies that both s_r and s_i have reached local extrema}. The mapping s(k) is analytic thus the above conditions imply ds/dk=0. It is possible to follow the roots in the s plane to detect the onset of absolute instability. However, ds/dk=0 is only a necessary and not a sufficient condition for absolute instability. The necessary condition is that the roots that merge in the k plane must lie in the opposite halves for large s_r. Plots of constant k_r also show the cusp formation for the same reason {ds/dk=0}. (figure 19) Infact, a mapping of any curve passing through the point of merger, in the s plane through the dispersion equation results in the cusp formation. To ensure that the cusp represents absolute instability, one can pass through the critical point along some arbitrary path and cross the real k axis {ex a line inclined at some angle to the real k axis}. If the real s at the critical point is a minimum and on varying k_i along the line, one exceeds the maximum temporal growth rate s_r in both directions then the merging is absolutely unstable because this ensures that the points that merge lie in opposite k halves for s_r larger than the maximum temporal growth rate. This is shown in fig 20. The straight line in the figure shows the maximum temporal growth. We choose a line in the k plane passing through the critical point (0.5952-0.0629i) and with a slope of -1. Fig 20 shows the plot of real s corresponding to points on this line and the k_i on this line. There is a cusp formation at the critical point and the s_r at the cusp is a minimum. On either side of the critical point s_r increases and crosses the maximum s_r corresponding to this mode which is 0.1381. Thus this merger is absolutely unstable. The same result was earlier obtained by analyzing the merging patterns in the k plane.

III.III EFFECT OF THE SURFACE TENSION RATIO ON THE CRITICAL V

As remarked, the merging patterns above change significantly with a change in system parameters β,γ and a. Because the instability is driven by surface tension, the most important of these is the surface tension ratio, γ. Fig. 21 shows the effect of the surface tension ratio on the critical Weber number of the compound jet. As with changing V, different modes become dominant in different ranges of γ and this leads to the discontinuities in slope of the critical velocity at $\gamma=0.3$ and 1.3. Moreover, the values of the critical Weber number go significantly above and below the critical V=1.8 for the single jet.

III.IV CONDITIONS NECESSARY FOR EXPERIMENTAL MANIFESTATION of the ABSOLUTE INSTABILITY

Despite a growing literature on the theoretical possibility of the absolute instability in jets of a single fluid, this type of instability has not been observed experimentally. Below we investigate the reason for this difficulty and argue that these difficulties are far less constraining for the compound jet. Thus the compound jet should be much more conducive to such observations.

When absolute instability sets in below the critical velocity, the theory predicts that waves with wave length $1/k_{ra}$ characteristic of the absolute instability will grow in time everywhere along the jet with growth rate $1/s_{ra}$. In contrast, the convective instability, which is present both above and below this critical velocity, grows spatially with a spatial growth rate $1/k_i$. This k_i is a function of the applied frequency ω and has a maximum k_{imax} for a particular frequency. In principle, in order to observe the absolute instability, it is necessary that the convective instability not break the jet too close to the nozzle ($1/k_{ic}>>1$, k_{ic} non-dimensional) and that the absolute instability be slow enough to allow the jet to first form convectively ($1/s_{ra}>>1/(k_{ia}V)$). This latter criterion is easy to satisfy. since the growth rate s_{ra} of the absolute instability at the critical velocity is zero. and increases continuously below V_{crit} (Fig. 9). The scenario envisioned is for the jet to form clearly and initially break convectively with wave number k_{rmax} . Then. on a slower time scale $1/s_{ra}$ the wave number k_{ra} takes over everywhere and the jet breaks with this wave number everywhere (excluding effects close to the nozzle) due to the absolute instability. (Note that the absolute instability also has a convective part which could. in principle contribute to the character of the absolute-instability-dominated part of the break up. However. in these jet problems. k_{ia} turns out to be very close to zero.)

For the single-fluid jet at the critical value V_{crit} =1.775. $-k_{imax}$=0.2425. which. when accounting for the nozzle effects may not allow a long enough jet to discern break-up everywhere in its domain. In contrast, in the compound jet. the value of $-k_{imax}$ is a function of the system parameters. and (Fig. 22) a choice of fluids with a surface tension ratio larger than one can easily give $-k_{imax}$ below 0.15. In addition, Fig. 21 shows that although the convectively unstable waves travel essentially with the jet velocity. the absolutely unstable waves grow significantly slower. Unfortunately, according to Fig. 23, the wave length of the absolutely unstable waves at high γ does not distinguish itself significantly from the convective wave length. However, if the lower γ values do indeed yield a long enough jet, then these two wave lengths will be significantly different, with the absolute waves being significantly shorter (about half) than the convective waves.

Note that Figures 21 and 23 display curves that are only piecewise continuous. Just as in the Fig. 9 where they led to curves with piecewise continuous slopes, changes in γ change the values at which the curves of root mergings cross the $s_r=0$ axis. At particular values of the surface tension ratio, the particular curve (the "dominant" one) that crosses for highest velocity, thereby determining V_{crit}, can change and thus change the characteristics observable characteristics there.

IV CONCLUSIONS

In addition to being convectively unstable at all velocities, the inviscid compound jet is also absolutely unstable below a critical velocity. This critical velocity is a function of the jet parameters the ratios of densities, surface tensions and radii of the two interfaces. We focus on the surface tension ratio and find that the critical velocity can be either less than or greater than the value 1.775 for the single jet with the same radius and density of the inner fluid and a surface tension equal to the fluid-fluid tension of the compound jet. At V=0, the absolute instability recovers the maximum growth rate of the standard temporal analysis.

The absolute instability arises from certain roots of the dispersion equation that have multiplicity greater than one. In the compound jet there are at least three such roots and for sufficiently low velocities one or more of these has positive temporal growth rate s_r. As one varies the system parameters, say γ, the root that attains positive s_r for the largest velocity (thereby determining V_{crit}) can change. This change leads to discontinuities in the wave length and wave speed of the absolute instability at criticality. At different values of V at fixed γ, there may be multiple non-simple roots with positive s_r, and the one with the largest positive s_r will dominate. This leads to a plot of the growth rate as a function of the non-dimensional jet velocity V whose slope is only piecewise continuous. These discontinuities are absent in the single fluid jet.

We have determined that a compound jet with surface tension ratio γ greater than one should lead to a jet that is susceptible to break up by the convective instability at longer non-dimensional distances from the jet nozzle than the single-fluid jet. This should facilitate the observation of the absolute instability for non-dimensional jet velocities just below criticality, a task which has thus far proven elusive for the single-fluid jet.

V APPENDIX

The solution in the Fourier-Laplace domain is given as,

$$\zeta_i(z,t) = \frac{1}{4\pi^2 i}\int_{-\infty}^{\infty} e^{ikz}\left[\int_{c-i\infty}^{c+i\infty} \zeta_i(s,k)e^{st}ds\right]dk \qquad (30)$$

where

$$\zeta_1 = \frac{1}{|a_{mn}|}[C_{44}F_2 + C_{45}F_1] \tag{31}$$

$$\zeta_2 = \frac{1}{|a_{mn}|}[C_{54}F_2 + C_{55}F_1]$$

(32)

$$F_1 = 0 : F_2(t) = e^{i\omega t} \rightarrow F_2(s) = \frac{1}{s - i\omega} \tag{33}$$

The solution has to be inverted to space-time domain. Because the solution for s(k) is explicit we first perform the Laplace inversion. The Laplace inversion can be done by converting the line integral to a Bromwich contour integral and using the residue theorem to evaluate the integral. The residues have to be calculated at all the poles of ζ in the s plane for a given k. From eq (32) the poles in the s plane arise from those of F_1 , F_2 or when det(A)= $|A|$ =0 or when any of the terms C_{mn} is singular or some combination of these. The terms of the matrix C stay finite in the s plane except when s+ikV=0. If s+ikV=0. C_{mn} diverges as 1/(s+ikV) and det(A) diverges as $1/(s+ikV)^2$. Thus s=-ikV is not a pole of ζ(k.s). The poles that contribute to instability arise from the roots of f(k.s)=det(A)=0 and from the poles of F_i. f(k.s)=0 is the dispersion equation of the system. For a given k. the poles $\{s_n(k)\}$ in the s plane are the roots of the dispersion equation. The dispersion equation gives 4 roots for each k. i.e.. n=1..4. The Laplace inverse gives.

$$\zeta_1(k,t) = \left[\sum_{n=1}^{4} \frac{C_{44}(k,s_n(k))}{\frac{\partial |A|}{\partial s}\Big|_{k,s_n(k)}} \frac{1}{s_n(k) - i\omega} e^{s_n(k)t} + \frac{C_{44}(k,i\omega)}{|A|_{k,i\varpi}} e^{i\varpi t}\right] = \qquad (34)$$

$$[\zeta_1(k,t)^{[1]} + \zeta_1(k,t)^{[2]}]$$

One can write a similar expression for ζ_2. The above expression is for any given k and is also valid in case two roots of the dispersion equation merge resulting in a second order or higher order pole and also when k is such that det(A(k,iω)=0 in which case the dispersion equation has a root at the pole of the source and thus the integrand in (34) has a higher order pole. At higher order poles the sum of the residues in (34) results in the residue corresponding to the higher order pole. Let us show this for the case when $k=k^*$ is such that the dispersion equation has a first order zero at $s_n(k)=i\omega$ for $n=1$, i.e., $s_1(k^*)= i\omega$ and $\det(A(k^*, i\omega)=0$.

$$\zeta_1(k,t)^{[1]} + \zeta_1(k,t)^{[2]} = \sum_{n=1}^{3} \frac{C_{44}(k,s_n(k))}{\frac{\partial |A|}{\partial s}\Big|_{k,s_n(k)}} \frac{1}{s_n(k) - i\omega} e^{s_n(k)t} +$$

$$\frac{C_{44}(k,s_1(k))}{\frac{\partial |A|}{\partial s}\Big|_{k,s_1(k)}} \frac{1}{s_1(k) - i\omega} e^{s_1(k)t} - \frac{C_{44}(k,i\omega)}{|A|_{k,i\varpi}} e^{i\varpi t} \qquad (35)$$

$$\zeta_1(k^*,t)^{[1]} + \zeta_1(k^*,t)^{[2]} = \lim k \to k^* (\zeta_1(k,t)^{[1]} + \zeta_1(k,t)^{[2]}) \qquad (36)$$

Expanding $s_1(k)$ and det(A) around k^*, one gets.

$$s_1(k) = i\omega + \frac{d(s_1(k)}{dk}\Big|_{k^*} (k-k^*) + O(k-k^*)^2;$$

$$|A|(k,i\omega) = \frac{d|A(k,i\omega)|}{dk}\Big|_{k^*} (k-k^*) + O(k-k^*)^2 \qquad (37)$$

Also, if (k,s) solve the dispersion equation,

$$d|A| = 0 = \frac{\partial |A|}{\partial k} dk + \frac{\partial |A|}{\partial s} ds \Rightarrow \frac{ds}{dk} = -\frac{\partial |A|}{\partial k} / \frac{\partial |A|}{\partial s} \tag{38}$$

Using (35) - (38) in (34) one gets,

$$\zeta_1(k^*, t)^{[1]} + \zeta_1(k^*, t)^{[2]} = \sum_{n=1}^{3} \frac{C_{44}(k^*, s_n(k^*))}{\frac{\partial |A|}{\partial s}\Big|_{k^*, s_n(k^*)}} \frac{1}{s_n(k^*) - i\omega} e^{s_n(k^*)t} + \Xi$$

$$\Xi = \lim k \to k^* \{C_{44}(k, i\omega) \frac{(ds/dk)}{-\frac{\partial |A|}{\partial k}} [\frac{k - k^*}{s_1(k) - i\omega}] \frac{1}{k - k^*} \Big|_{k, i\omega} e^{is_1(k)t} - \frac{C_{44}(k, i\omega)}{|A|_{k, i\varpi}} e^{i\varpi t}\}$$

$$= \lim k \to k^* C_{44}(k, i\omega) \frac{1}{k - k^*} \frac{1}{\frac{\partial |A|}{\partial k}} [-1 + \{1 + \frac{\partial^2 |A|}{\partial k^2} / \frac{\partial |A|}{\partial k}(k - k^*) + O(k - k^*)^2\}^{-1}]$$

$$= -C_{44}(k^*, i\omega) \frac{\frac{\partial^2 |A|}{\partial k^2}}{(\frac{\partial |A|}{\partial k})^2} \Big|_{k^*, i\omega} = -C_{44}(k^*, i\omega) \frac{\frac{\partial^2 |A|}{\partial s^2}(-\frac{ds}{dk})^2}{(\frac{\partial |A|}{\partial s})^2(-\frac{ds}{dk})^2} \Big|_{k^*, i\omega} = -C_{44}(k^*, i\omega) \frac{\frac{\partial^2 |A|}{\partial s^2}}{(\frac{\partial |A|}{\partial s})^2} \Big|_{k^*, i\omega} \tag{39}$$

which is exactly the residue at the second order pole $s=i\omega$ for $k^*=k_1(i\omega)$.

We now perform the Fourier inversion.

$$\zeta_1(z, t) = \frac{1}{2\pi} \int_{-\infty}^{\infty} \zeta_1(z, t) e^{ikz} dk \tag{40}$$

For the Fourier inverse to exist, the Fourier transform should have no non-integrable singularities on the real k axis. However the dispersion equation does yield real k solutions for certain values of ω, in particular $k=0$ for $\omega=0$. These points are singular for both $\zeta_1^{[1]}(k,t) + \zeta_1^{[2]}(k,t)$ but $\zeta_1^{[1]}(k,t) + \zeta_1^{[2]}(k,t)$ is finite at these points. Thus, $\zeta_1^{[1]}(k,t) + \zeta_1^{[2]}(k,t)$ has no singularity in the entire k plane, in particular on the real k line and thus the Fourier inverse exists.

$$\zeta_1(k,t)^{[1]} + \zeta_1(k,t)^{[2]} = \sum \frac{C_{44}(k, s_n(k))}{\frac{\partial |A|}{\partial s}\Big|_{k, s_n(k)}} \frac{1}{s_n(k) - i\omega} e^{s_n(k)t} + \frac{C_{44}(k, i\omega)}{|A|_{k, i\varpi}} e^{i\varpi t} \qquad (41)$$

First, we invert the second term in eq(34), i.e., $\zeta_1(k,t)^{[2]}$. The inversion can be performed by closing the Fourier contour in the upper half plane and then using the residue theorem to evaluate the contour integral (fig 24).

$$\zeta_1(z,t)^{[2]} = \frac{1}{2\pi} \int_{-\infty}^{\infty} \frac{C_{55}(k, i\omega)}{|A|_{k, i\omega}} e^{i\varpi t} e^{ikz} dk = i \sum \frac{\bar{C}_{55}}{\frac{\partial |A|}{\partial k}} \Big|_{k(i\varpi), i\varpi} e^{ik(i\varpi)z + i\varpi t} \qquad (42)$$

where the residues are calculated at all the poles of the dispersion equation in the upper half k plane for $s=i\omega$. The dispersion equation is transcedental in k, thus $k(i\omega)$ has an infinite solutions. The contribution from this inversion will decay in the z direction ($k_i>0$) and hence will not contribute to spatial instability.

To invert the first term in (34), i.e., $\zeta_1(k,t)^{[1]}$ we cannot choose the contour that we chose to invert $\zeta_1(k,t)^{[2]}$ because as $|k|\rightarrow\infty, s_r \sim |k|^{3/2}$, hence the integrand in the inversion goes to infinity on the contour $\{|k|\rightarrow\infty;\ k_r>0\}$. Since the integrand goes as $\exp(s_n t)$, we wish to close the Fourier contour via a curve Γ on which the $s_r(k)$, i.e., the real part of the solution of the dispersion equation is negative, so that the contribution to the contour integral from this curve (of order $\exp(ikz+st)$) decays to zero at long times. Hence the Fourier inverse becomes equal to the sum of the residues which grow axially ($k_i<0$). Fig(25) shows the curve Γ chosen to close the contour in one instance. Note that if the dispersion equation has more than one mode, i.e., the Laplace inverse has more than one term, as is the case in this problem, we may need to choose a separate Γ for each mode. The singularities of $\zeta_i(k,t)^{[1]}$ occur at $k=k(i\omega)$. Thus,

$$\zeta_i(z,t)^{[1]} = \frac{1}{2\pi}\int_{-\infty}^{\infty} \zeta_i(k,t)^{[1]} e^{ikz}\, dk = \pm i \sum \mathrm{Resides}(k(i\omega), i\omega)$$

$$\mathrm{Residue} = \lim k \to k(i\omega) \frac{C_{55}}{\dfrac{\partial |A|}{\partial s}} \frac{k - k(i\omega)}{s_n(k) - i\omega} \Big|_{k, s_n(k)}\; e^{ikz + s_n(k)t} \tag{43}$$

$$= \frac{C_{55}}{\dfrac{\partial |A|}{\partial s}} \frac{dk}{ds} \Big|_{k(i\omega), i\omega}\; e^{ik(i\varpi)z + i\varpi t} = -\frac{C_{55}}{\dfrac{\partial |A|}{\partial k}} \Big|_{k(i\omega), i\omega}\; e^{ik(i\varpi)z + i\varpi t}$$

where the residues are calculated at all the roots of the dispersion equation that lie inside the contour and the sign in front depends on whether the curve Γ is located in the upper half or the lower half k plane. The residues grow axially if Γ lies and surrounds singularities in the lower k plane and give the convectively unstable solution for $z>0$. The condition for being able to find such a curve Γ is that there is no double root in the k plane formed by merging of two single roots which lie in the opposite k halves (upper and lower) for large s_r.

Upon lowering s_r a merger of two first order roots which for large s_r lie in opposite (upper and lower) halves for large s_r results in a double root. a curve Γ such that $s_r(k)<0$ on Γ, does not exist (fig 26). The line integral along Γ has to be evaluated and a portion of it lies along k such that $s_r(k) >0$ and so gives rise to a contribution that grows in time for all z, i.e., an absolute instability. To evaluate the asymptotic response one chooses Γ such that one has to pass through the minimum possible value of s_r along Γ as shown in fig(26). This curve is the solution of $\det(A(k,s_r+ i\, s_{ic}))=0$ where $s_{i,a}$ is s_i at the double root, i.e., $ds/dk=0$, for the intersection which gives rise to the absolute instability. Let Γ1 be the part of Γ in the region where $s_r>0$. Let the rest of Γ be Γ2. Let us denote the real k line from $-\infty$ to ∞ by C. Thus.

$$\bar{\zeta}_i^{[1]}(z,t)=\frac{1}{2\pi}\Big[\int_{\Gamma1+\Gamma2+C}\bar{\zeta}_i^{[1]}(k,t)\,e^{ikz}\,dk-\int_{\Gamma1+\Gamma2}\bar{\zeta}_i^{[1]}(k,t)\,e^{ikz}\,dk\Big] \tag{44}$$

Using residue theorem.

$$\int_{\Gamma1+\Gamma2+C}\bar{\zeta}_i^{[1]}(k,t)\,e^{ikz}\,dk=2\pi i\sum\frac{C_{55}}{\frac{\partial|A|}{\partial s}}\frac{ds}{dk}e^{ik(i\varpi)z+i\varpi t} \tag{45}$$

$$\int_{\Gamma2}\bar{\zeta}_i^{[1]}e^{ikz}dk=\int_{\Gamma2}\frac{C_{55}}{\frac{\partial|A|}{\partial s}}\frac{1}{s(k)-i\omega}e^{ikz+s(k)t}dk\rightarrow 0\ \text{as}\ \mathrm{Re}(s(k))<0\ \text{on}\ \Gamma2 \tag{46}$$

The curve Γ1 is the mapping of $s_i=s_{i,a}$. The parameter on the curve is s_r which goes from 0 (point A in figure) to $s_{r,a}$ (point B in figure) and then back to 0 (point C). To evaluate the integral on Γ1, we transform the variable from k to s(k). s(k) is a multivalued function. we choose the branch corresponding to the mode [1]. On transforming to the s_1 domain, the integral along Γ_1 becomes.

$$\int_{\Gamma3}\frac{C_{55}}{\frac{\partial|A|}{\partial k}}\frac{1}{s_1-i\omega}e^{ik(s_1)z+s_1t}ds_1 \tag{47}$$

where Γ3 is the branch cut as shown in fig(27a). Thus, the merger of the roots in the k plane results in branch cuts in the s plane which we didn't consider while performing the Laplace inverse. We now evaluate the contribution from this branch cut. At point B' ($s=s_a$) in the figure (27a) which corresponds to B in the k plane, ds/dk=0 and $\partial|A|/\partial k=0$. Thus, one can use Watson's lemma to evaluate the integral in the long time limit. The contribution to the integral from the circular path around B^i is zero because we shall show later that the integrand behaves as $(s-s_a)^{-1/2}$ near B^i ($s=s_a$ at B^i) thus the integral around the circular path is of the order $(s-s_a)(s-s_a)^{-1/2}=(s-s_a)^{1/2}$ which goes to zero. At long times. the dominant contribution to the integral comes from the region O(1/t) around the maxima. Let $f(s,k)=|A(s.k)|$. Expanding f(s.k) around the maxima. one gets.

$$\begin{aligned} f(s,k) &= f(s_a,k_a) + (k-k_a)f_k + (s-s_a)f_s + \frac{(s-s_a)^2}{2}f_{ss} \\ &+ \frac{(s-s_a)(k-k_a)}{2}f_{sk} + \frac{(k-k_a)^2}{2}f_{kk} + \ldots\ldots \end{aligned} \tag{48}$$

where f_k, f_s, f_{kk}, f_{ss} denote the partial derivatives evaluated at the maxima.

$$f(s,k) = f(s_a,k_a) = f_k = 0 \tag{49}$$

Thus, around the maxima.

where (-) corresponds to above the branch cut and (+) below.

Also. at u=0, ds/dk=0 because s has a maximum at u=0. Thus.

$$(k-k_a) = +-\sqrt{\frac{2f_s}{f_{kk}}}\sqrt{(s_a-s)} + O(s_a-s) = +-\sqrt{\frac{2f_s}{f_{kk}}}\sqrt{u} + O(u) \tag{50}$$

$$\frac{\partial f}{\partial k} = -\frac{ds}{dk}\frac{\partial f}{\partial s} = 0 \quad \text{at } u=0 \tag{51}$$

$$\frac{\partial f}{\partial k} = \frac{\partial^2 f}{\partial k^2}\Big|_{k_m}(k-k_m) + O((k-k_m)^2) \tag{52}$$

Expanding the integrand in (47) around u=0 and using (21)- (25), to leading order. one gets,

$$\frac{C_{55}(k_a, s_a)e^{ik_a z+s_a t}}{\sqrt{2f_s f_{kk}}}\frac{1}{s_a - i\omega}\int \pm \frac{e^{(s-s_a)t}}{\sqrt{(s_a - s)}}ds \tag{53}$$

The integration path is above and below the branch cut as shown in fig 27(b) and where (-) corresponds to above the branch cut and (+) below. The branch cut integration can be performed using the method of steepest descent. As $t \rightarrow \infty$, the leading contribution to the integral comes from the region of O(1/t) around u=0. Substituting z=ut in (53), one gets.

$$\int \pm \frac{e^{(s-s_a)t}}{\sqrt{(s_a - s)}}ds = \frac{1}{\sqrt{t}}\int \pm \frac{e^{-z}}{\sqrt{z}}dz \tag{54}$$

where the branch cut for z extends from 0 t0 ∞. The contribution to the integral $1/\sqrt{z}\, e^{-z}$ from the path around z=0 is zero. Thus the integral in (54) reduces to.

$$\int_{\infty}^{0} \frac{1}{-\sqrt{z}} e^{-z}dz + \int_{0}^{\infty} \frac{1}{\sqrt{z}} e^{-z}dz = 2\int_{0}^{\infty} \frac{1}{\sqrt{z}} e^{-z}dz = 2\sqrt{\pi} \tag{55}$$

The integral in (53) becomes.

$$\frac{C_{55}(k_a, s_a)e^{ik_a z+s_a t}}{\sqrt{2f_s f_{kk}}}\frac{1}{s_a - i\omega}\frac{1}{\sqrt{t}} \tag{56}$$

Substituting (46), (56) in (44), we get.

$$\zeta_1 = -i\sum \frac{C_{55}}{f_k}\Big|_{k_n(i\omega),i\omega} e^{ik_n(i\omega)z - i\omega t} - \frac{1}{2\pi}\frac{C_{55}(k_a, s_a)e^{ik_a z+s_a t}}{\sqrt{2f_s f_{kk}}}\frac{1}{s_a - i\omega}\frac{1}{\sqrt{t}} \tag{57}$$

The first term represents the convective instability and the second term represents absolute instability.

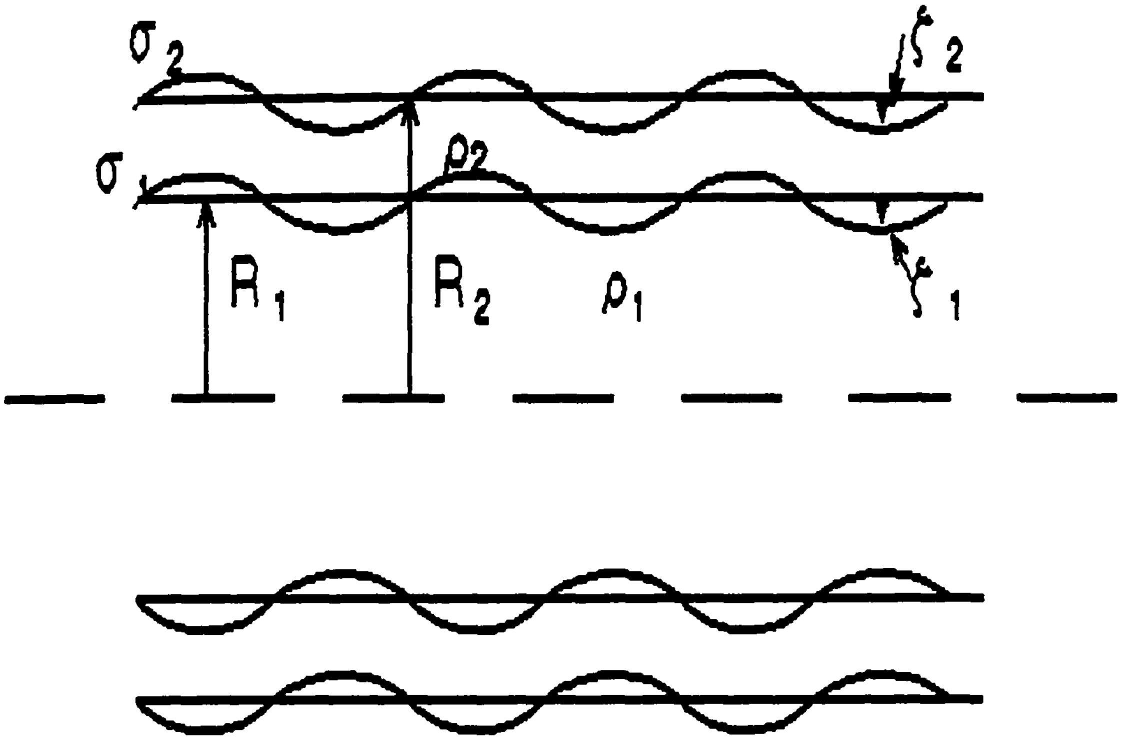

Figure 1 Compound jet geometry

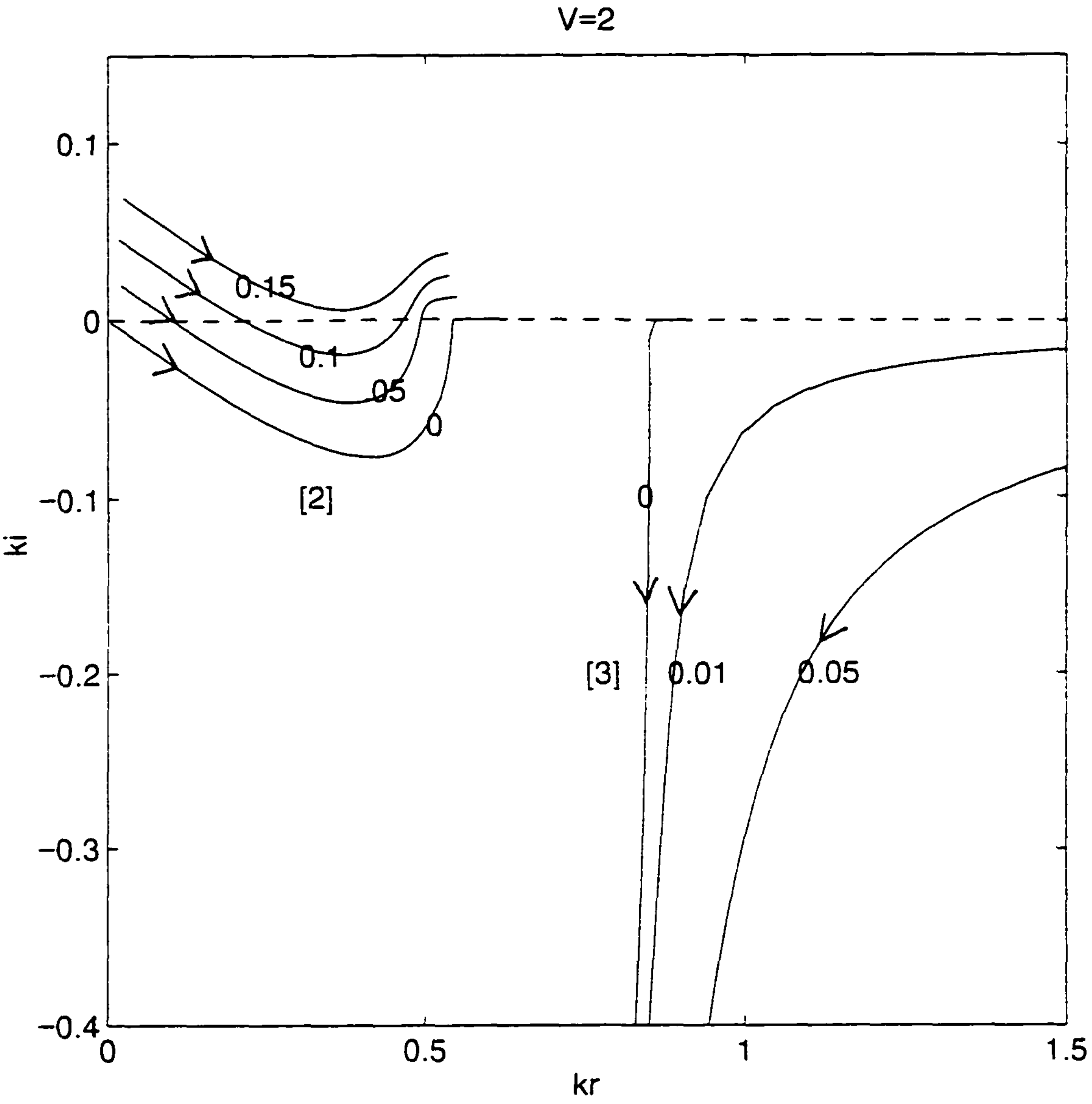

Figure 2 Mapping of constant s_r lines in the k-plane for the spatial roots [2] and [3]. $s=s_r-i\omega$. Arrows show the direction of increasing ω. The numbers on the curves denote the values of s_r. $\beta=1,\gamma=2,a=2,V=2$

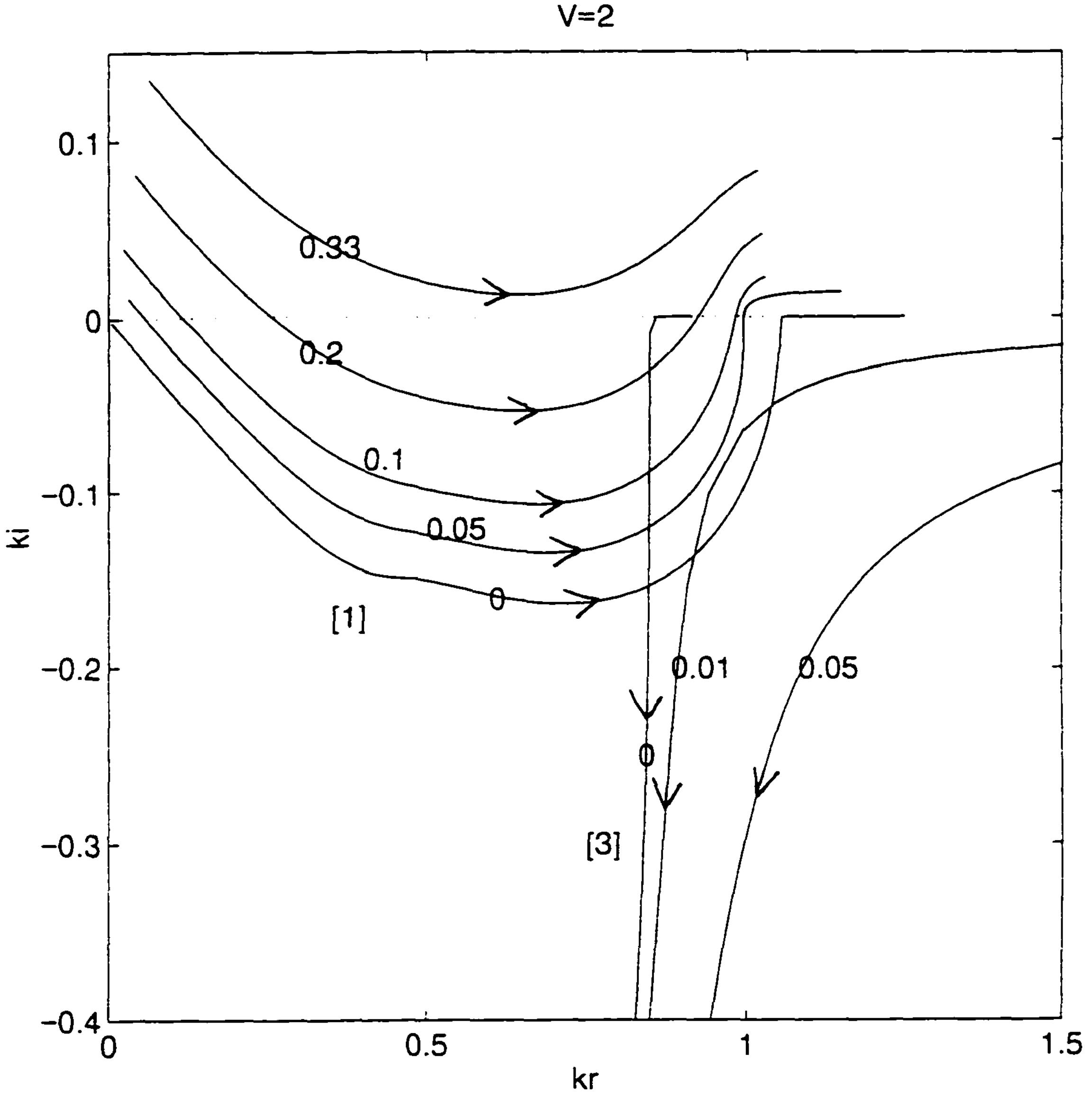

Figure 3 Mapping of constant s_r lines in the k-plane for the spatial roots [1] and [3]. $s=s_r-i\omega$. Arrows show the direction of increasing ω. The numbers on the curves denote the values of s_r. $\beta=1,\gamma=2,a=2,V=2$

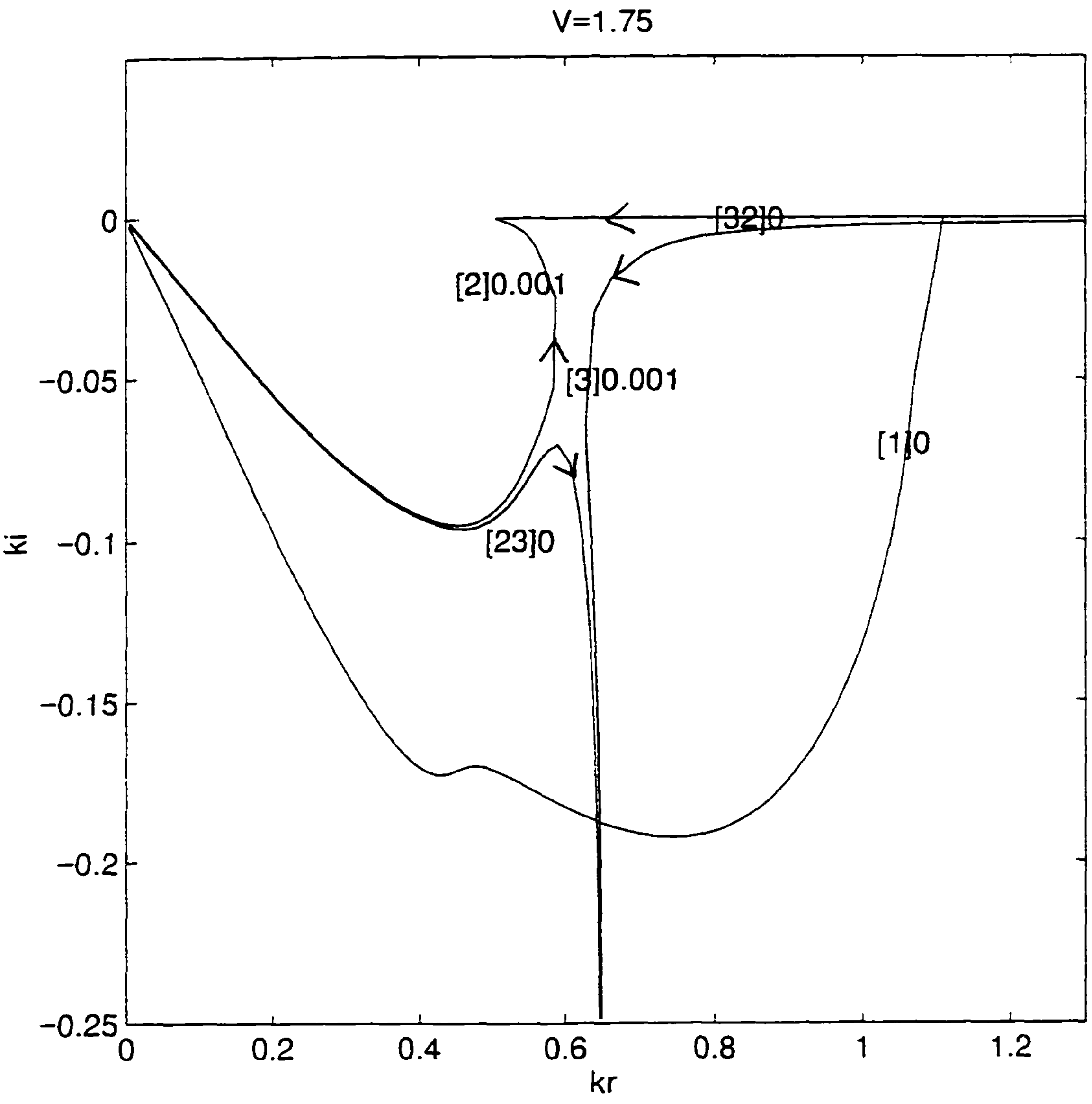

Figure 4 Merging patterns in the k plane. $s=s_r-i\omega$. Arrows show the direction of increasing ω. The numbers on the curves denote the values of s_r. $\beta=1,\gamma=2,a=2,V=1.75$

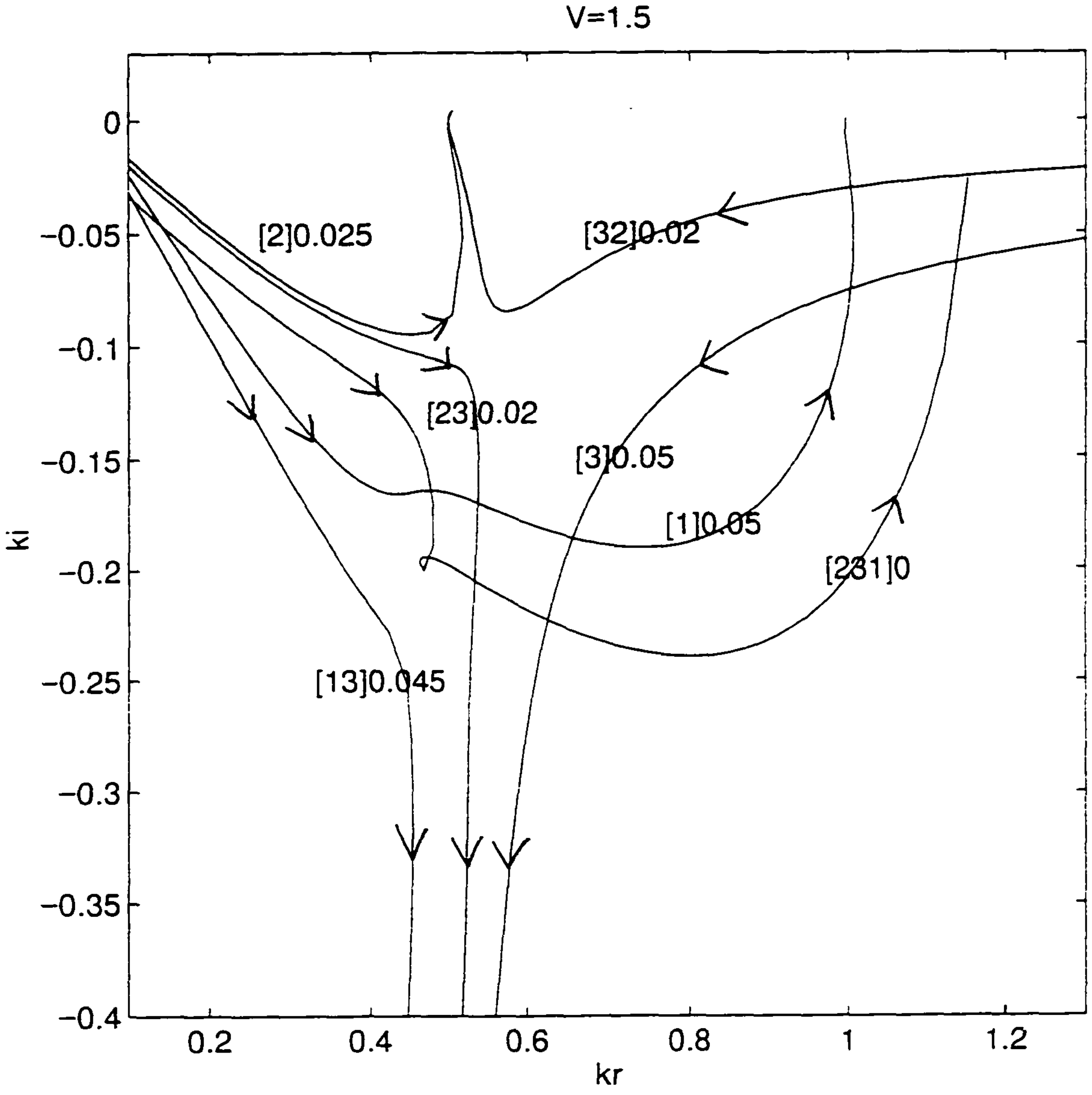

Figure 5 Merging patterns in the k plane in Region I. $s=s_r-i\omega$. Arrows show the direction of increasing ω. The numbers on the curves denote the values of s_r. $\beta=1, \gamma=2, a=2, V=1.5$

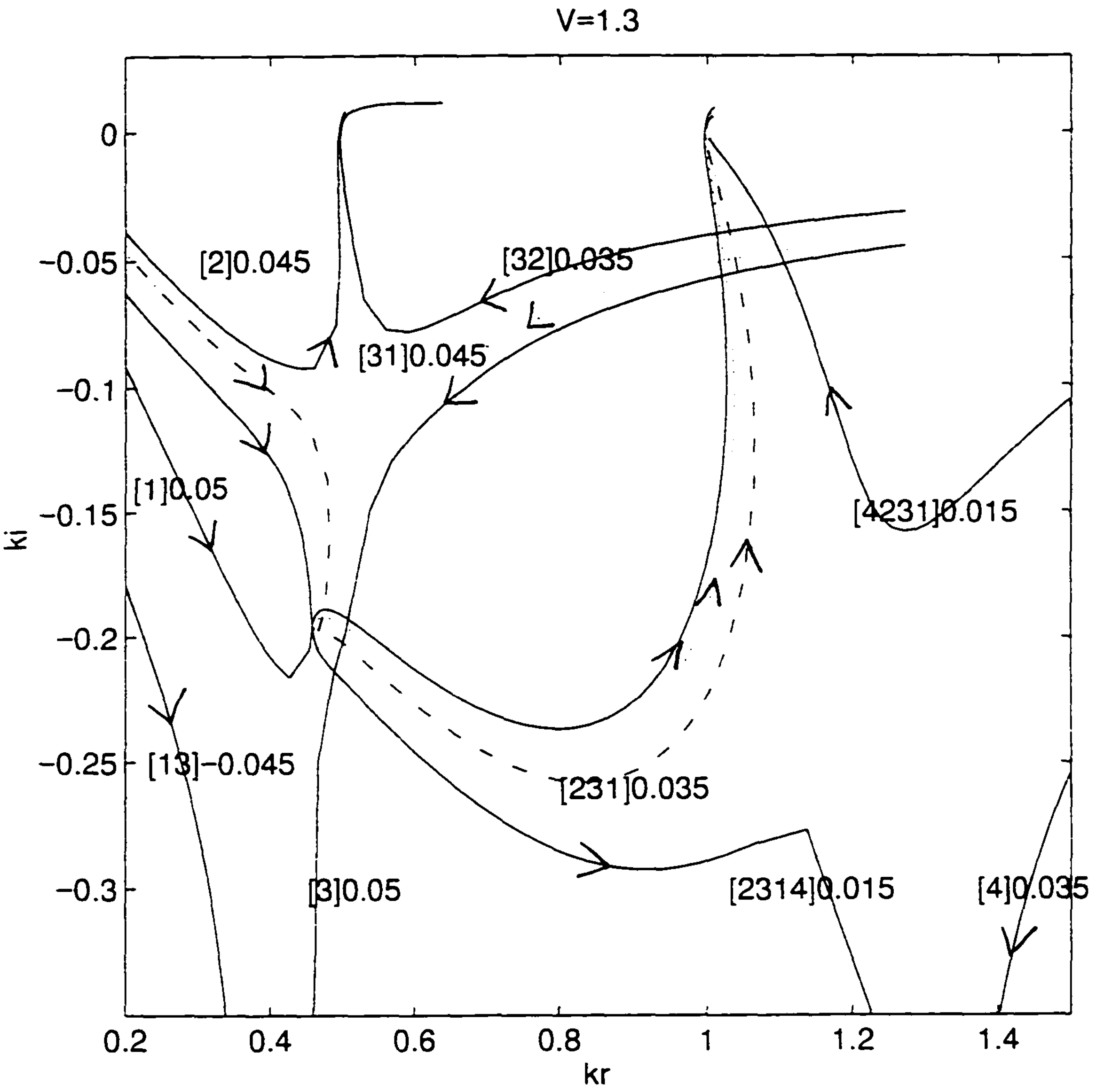

Figure 6 Merging patterns in the k plane in Region II. $s=s_r-i\omega$. Arrows show the direction of increasing ω. The numbers on the curves denote the values of s_r. $\beta=1,\gamma=2,a=2,V=1.3$

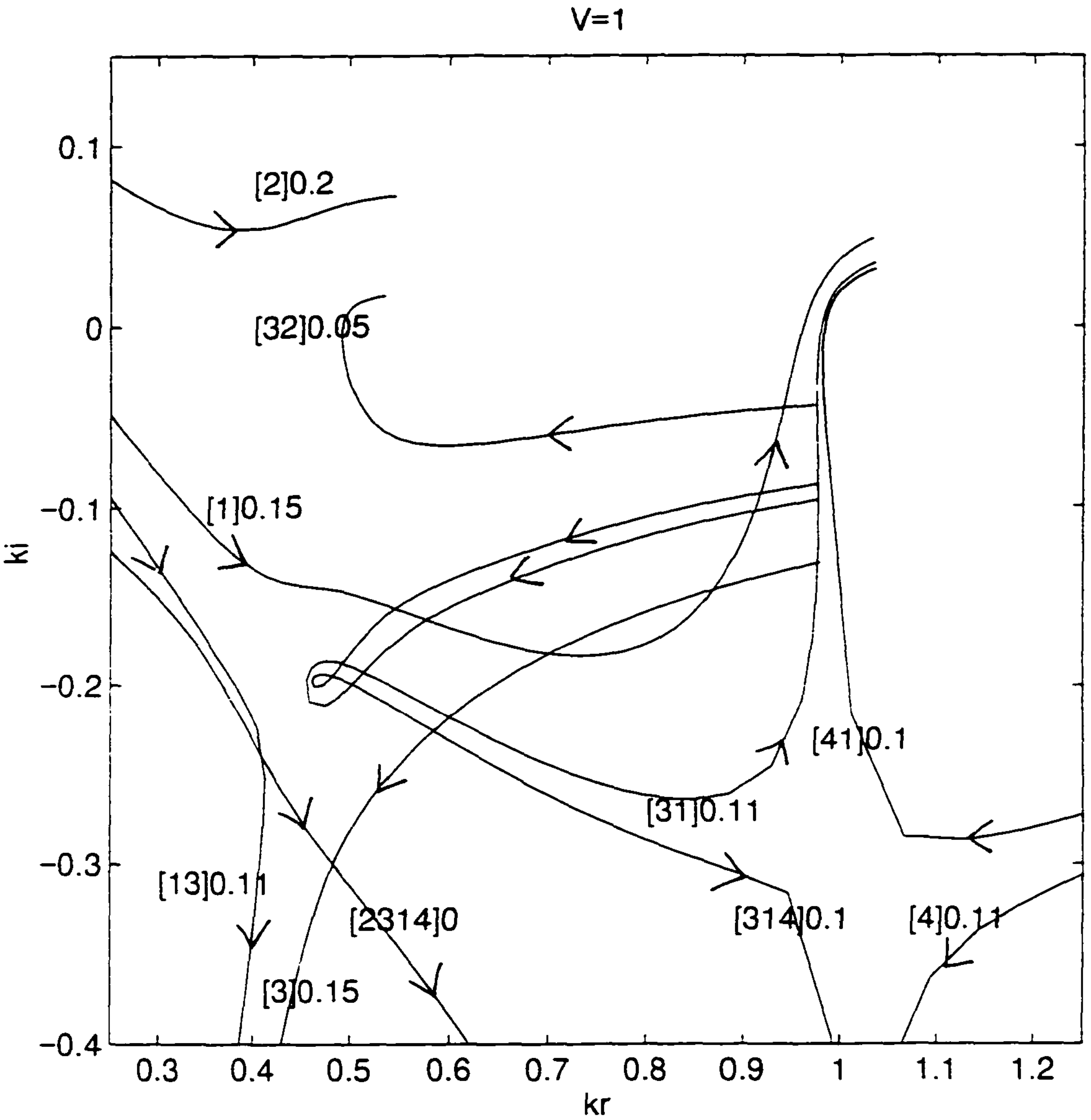

Figure 7 Merging patterns in the k plane in Region III. $s=s_r-i\omega$. Arrows show the direction of increasing ω. The numbers on the curves denote the values of s_r. $\beta=1,\gamma=2,a=2,V=1$

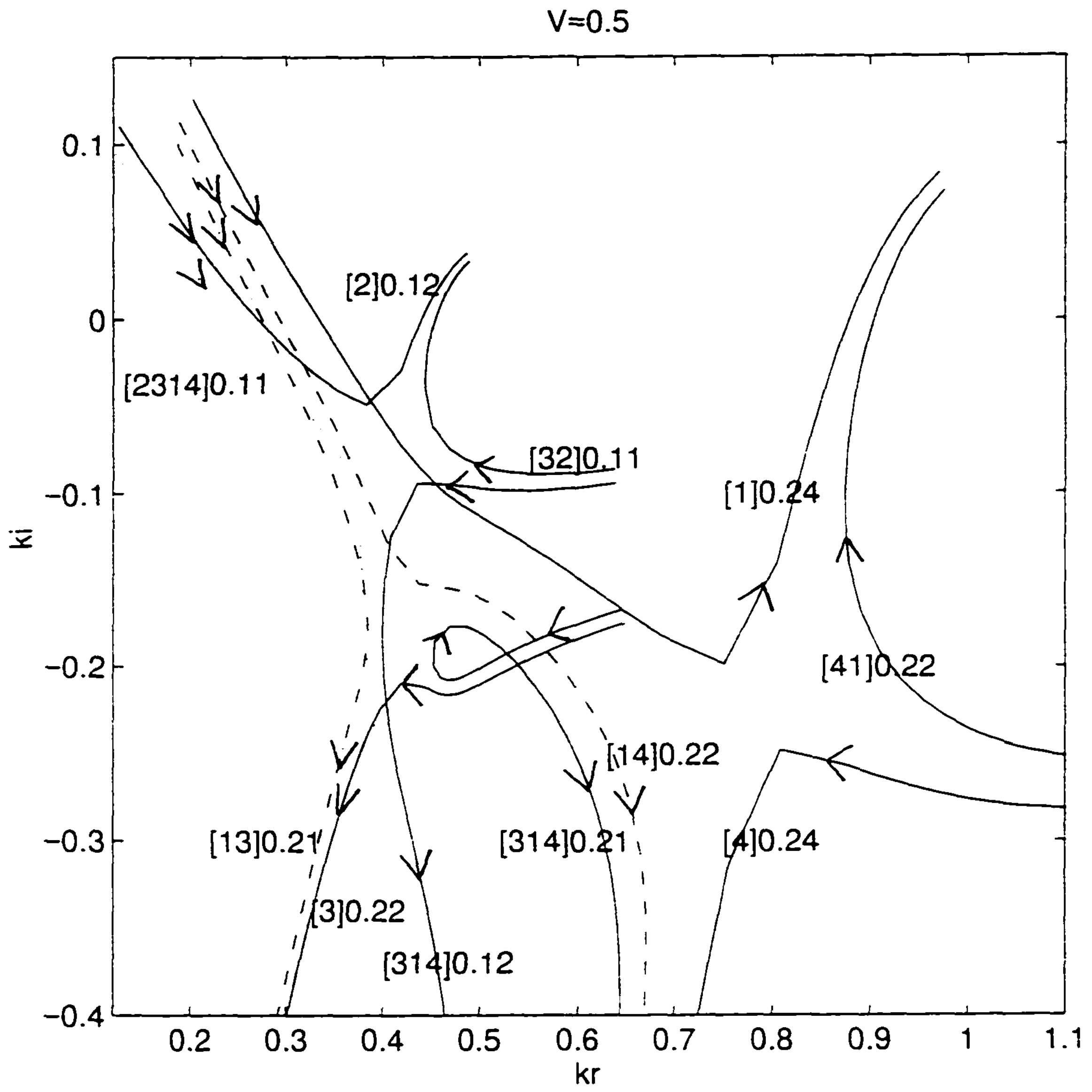

Figure 8 Merging patterns in the k plane in Region IV. $s=s_r-i\omega$. Arrows show the direction of increasing ω. The numbers on the curves denote the values of s_r. $\beta=1,\gamma=2,a=2,V=0.5$

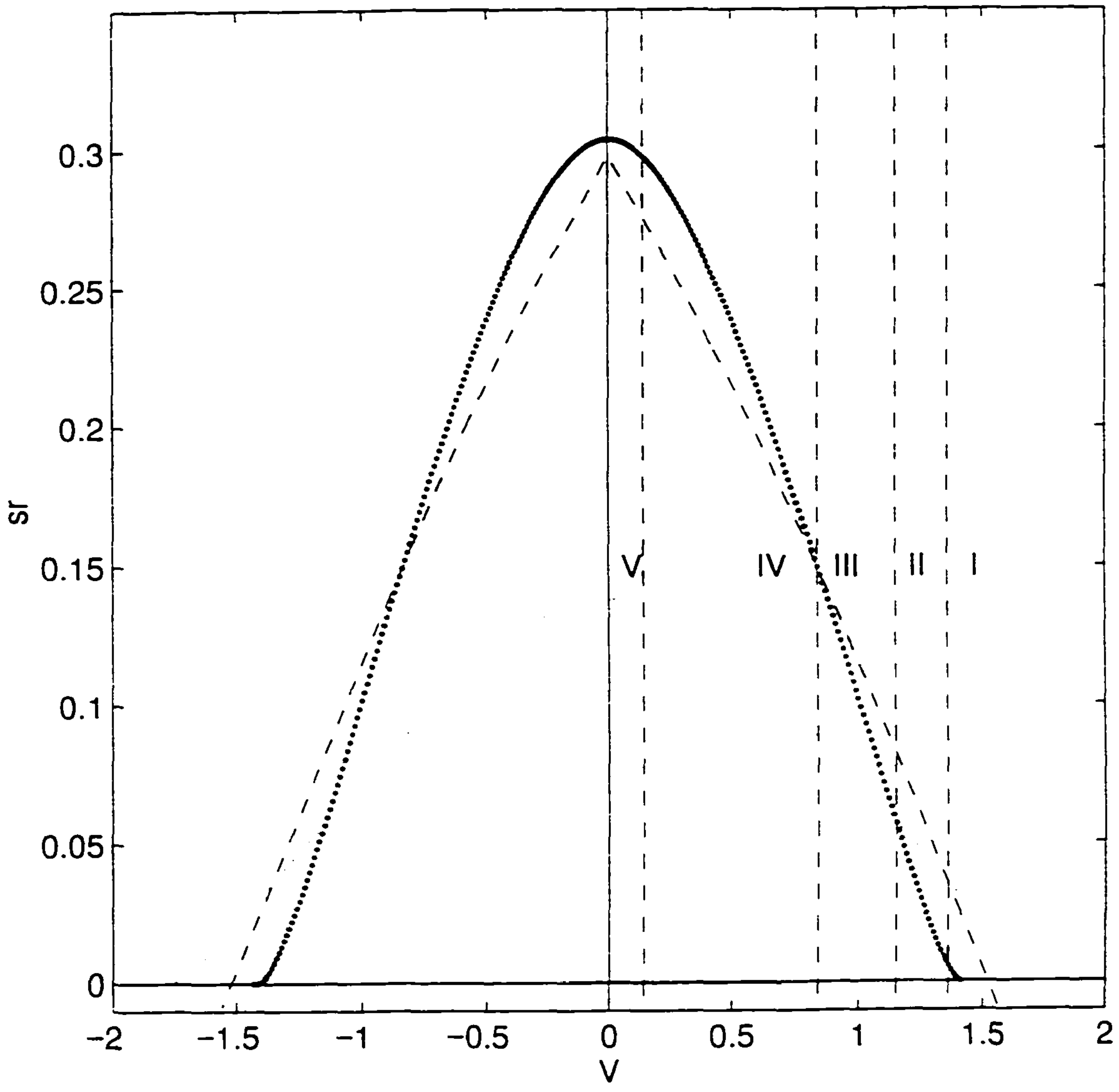

Figure 9 s_r at absolute instability for the three absolutely unstable modes in the 5 regions. $\beta=1, \gamma=2, a=2$

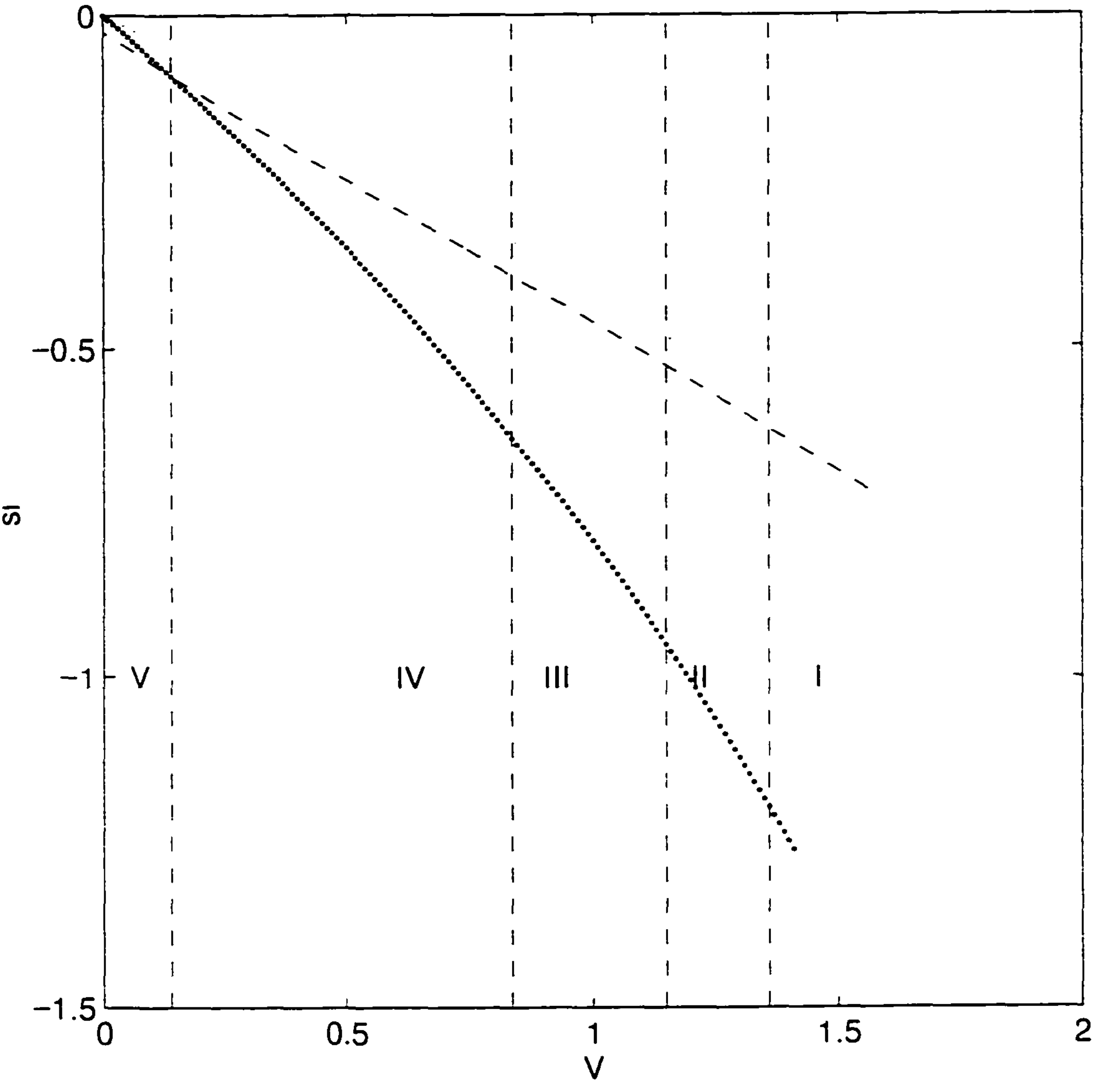

Figure 10 s_i at absolute instability for the three absolutely unstable modes in the 5 regions. $\beta=1, \gamma=2, a=2$

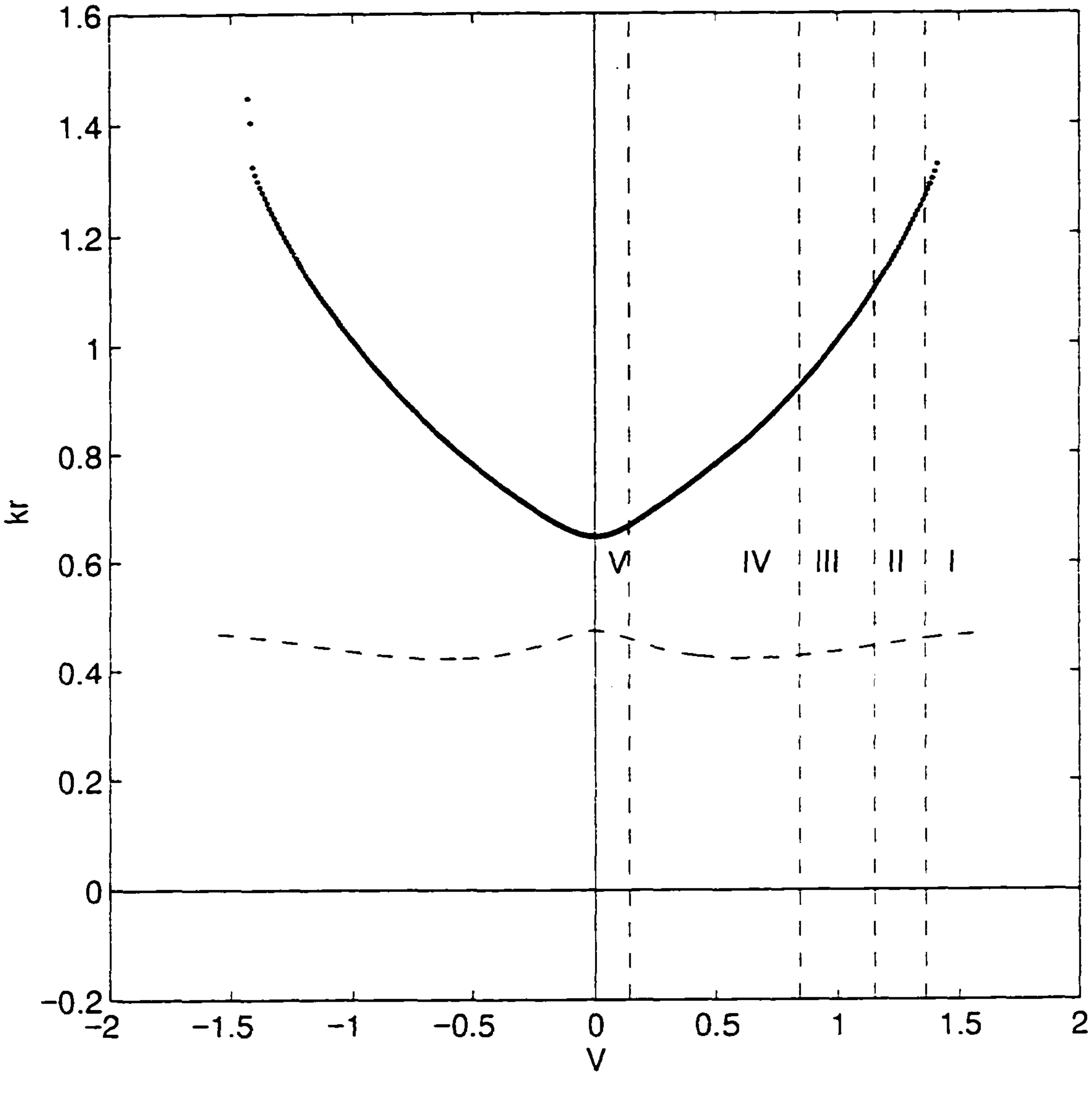

Figure 11 k_r at absolute instability for the three absolutely unstable modes in the 5 regions. $\beta=1, \gamma=2, a=2$

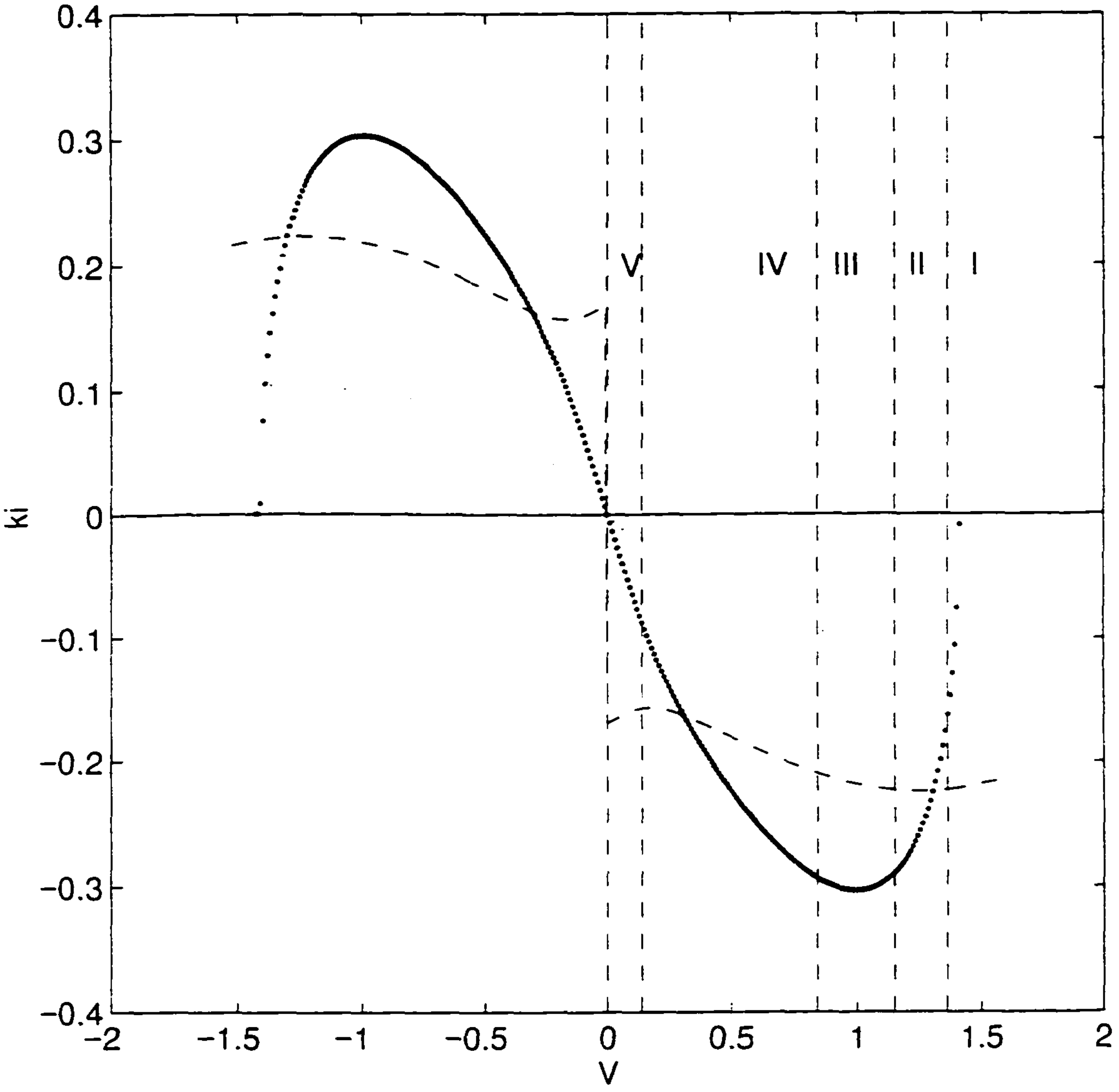

Figure 12 k_i at absolute instability for the three absolutely unstable modes in the 5 regions. $\beta=1,\gamma=2,a=2$

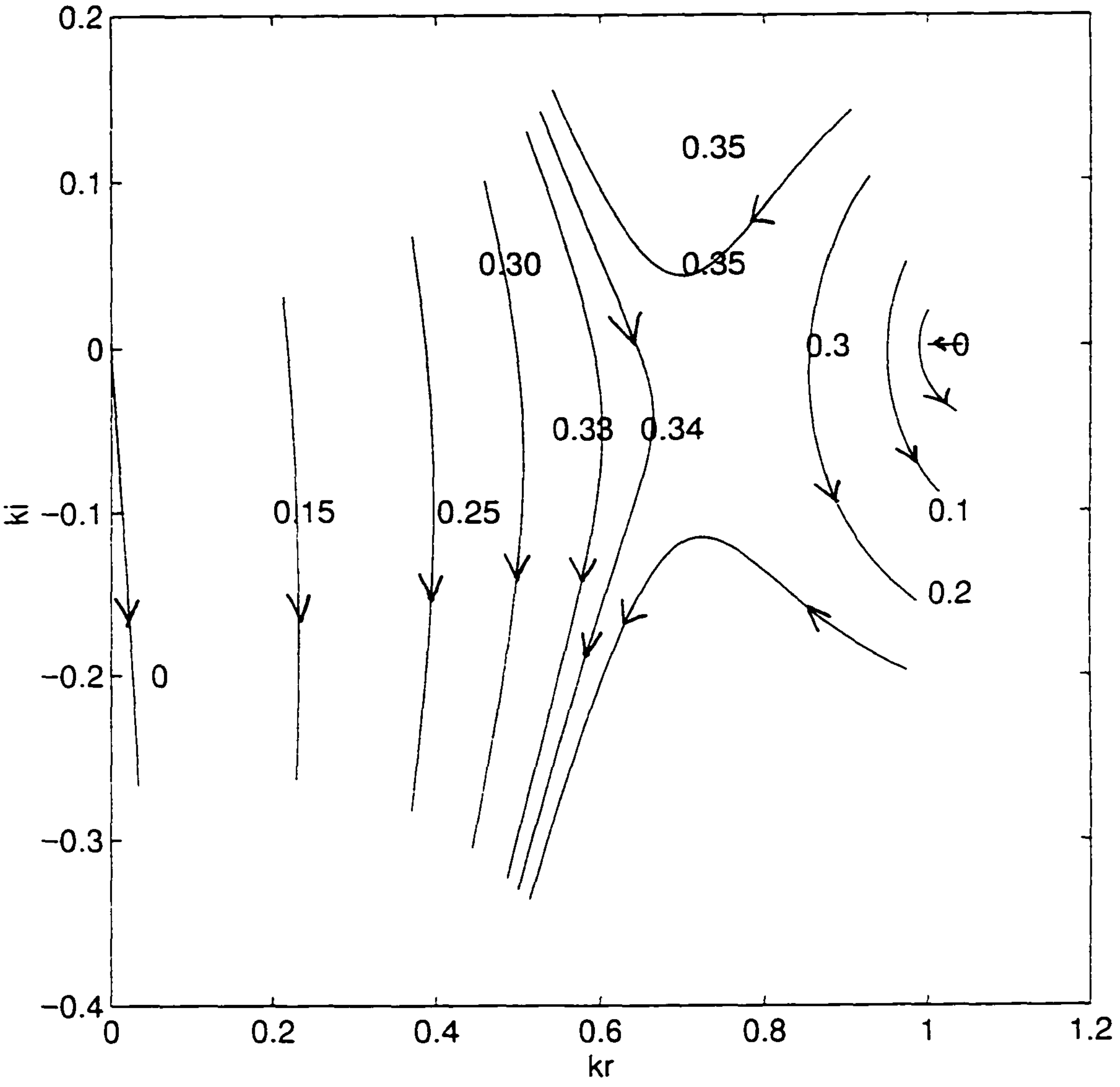

Figure 13 Merging patterns in the k plane for a single jet

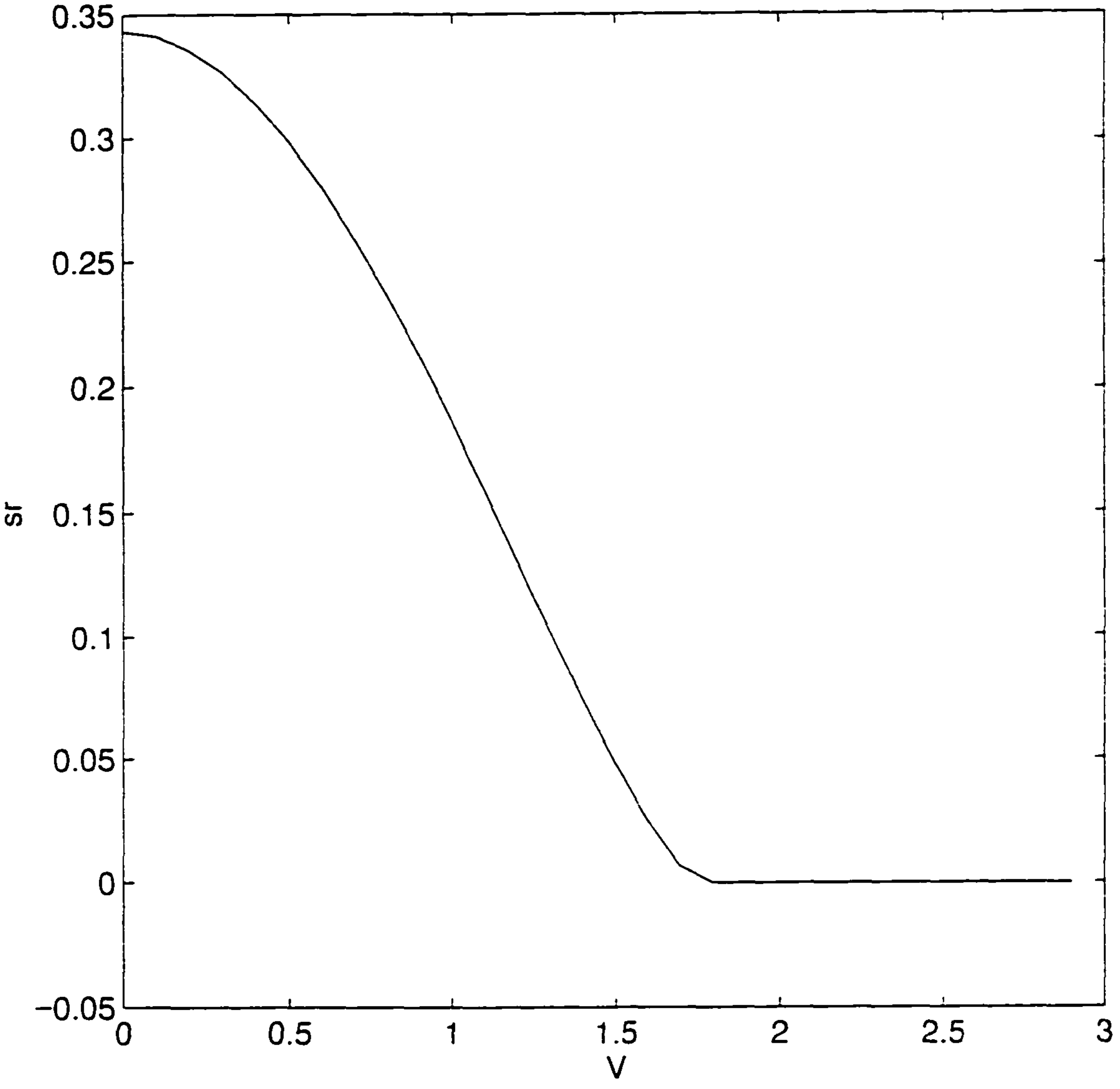

Figure 14 s_r of the absolutely unstable waves as a function of jet velocity for a single

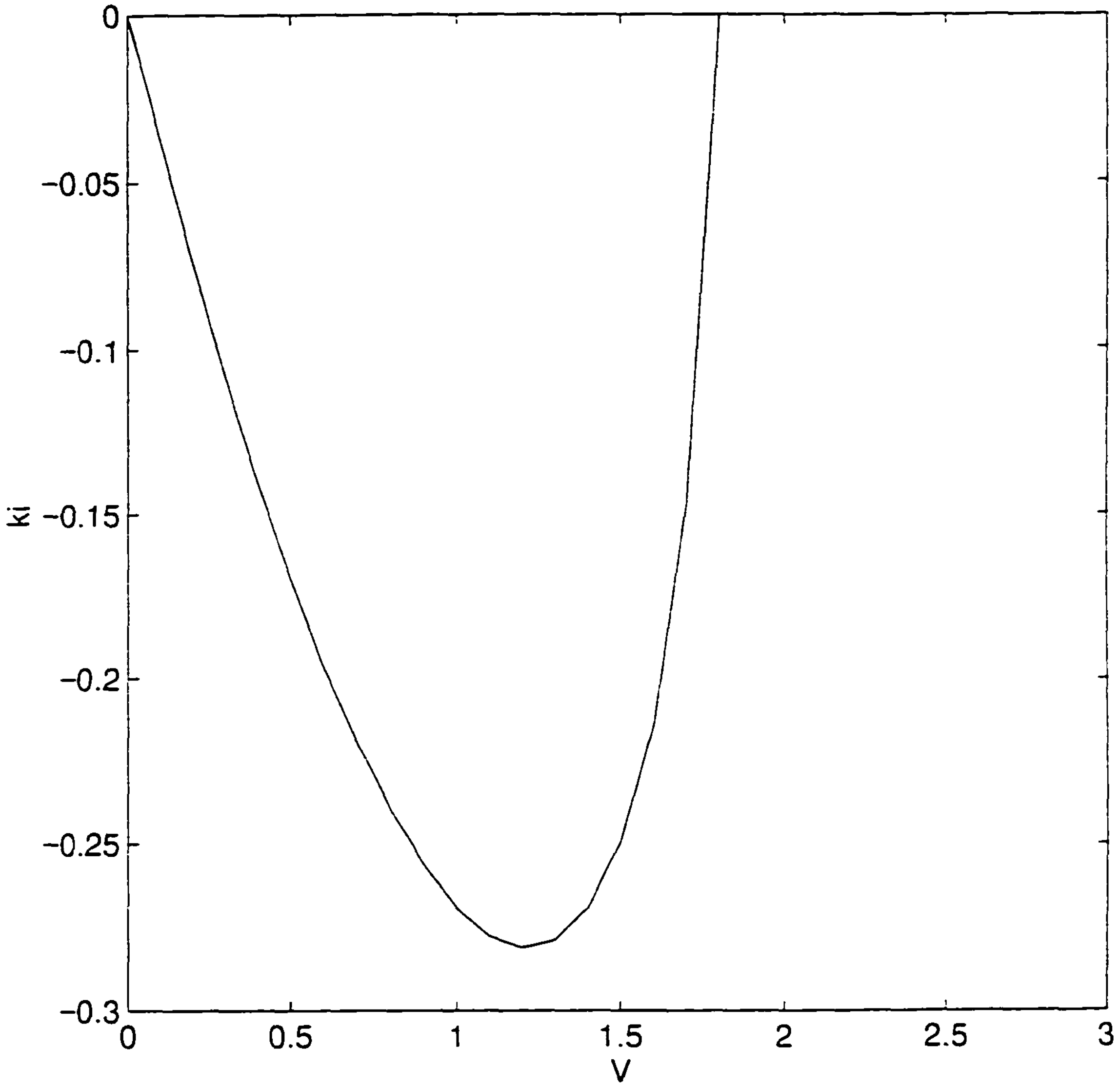

Figure 15 k_i of the absolutely unstable waves as a function of jet velocity for a single jet

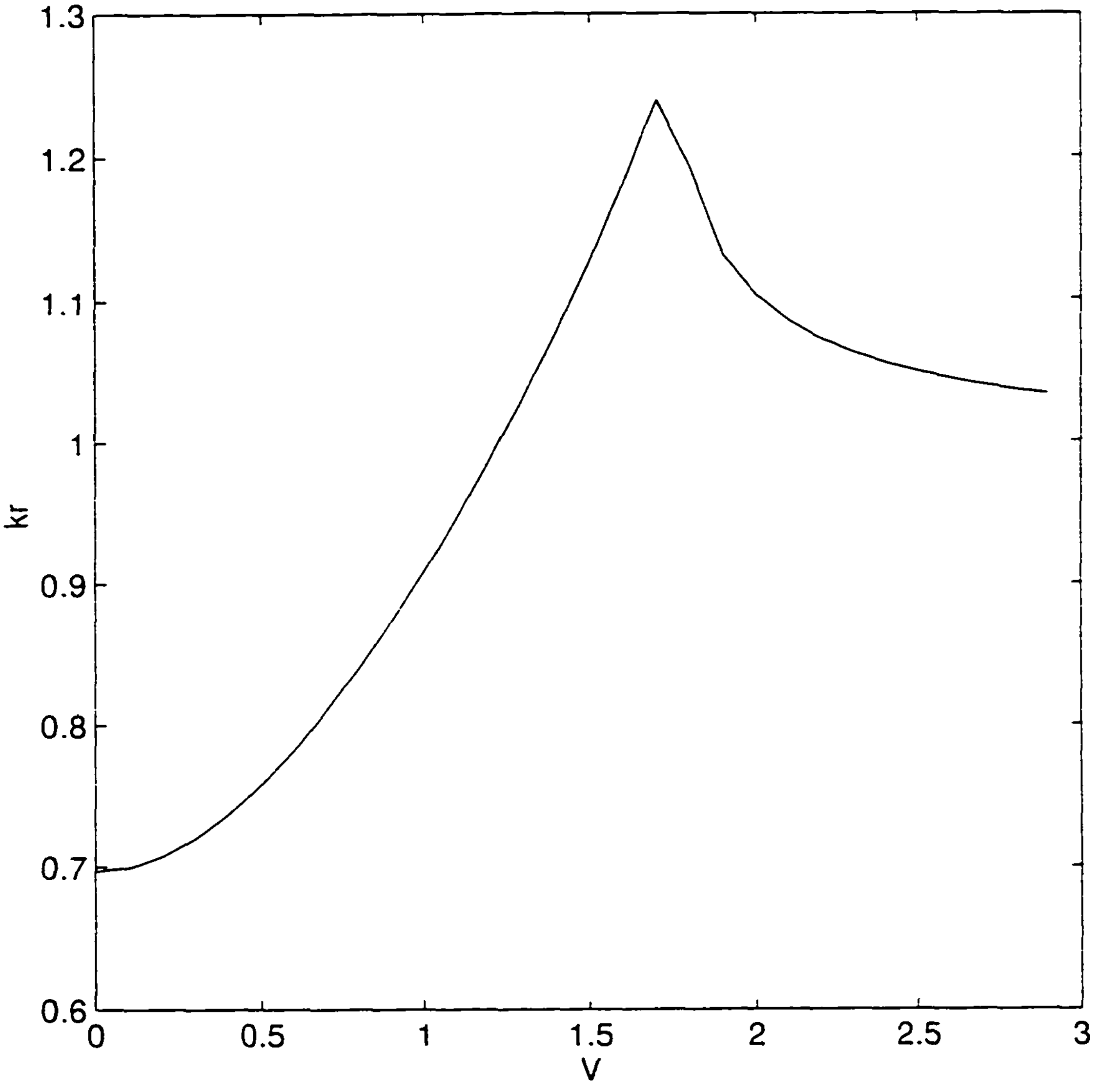

Figure 16 k_r of the absolutely unstable waves as a function of jet velocity for a single

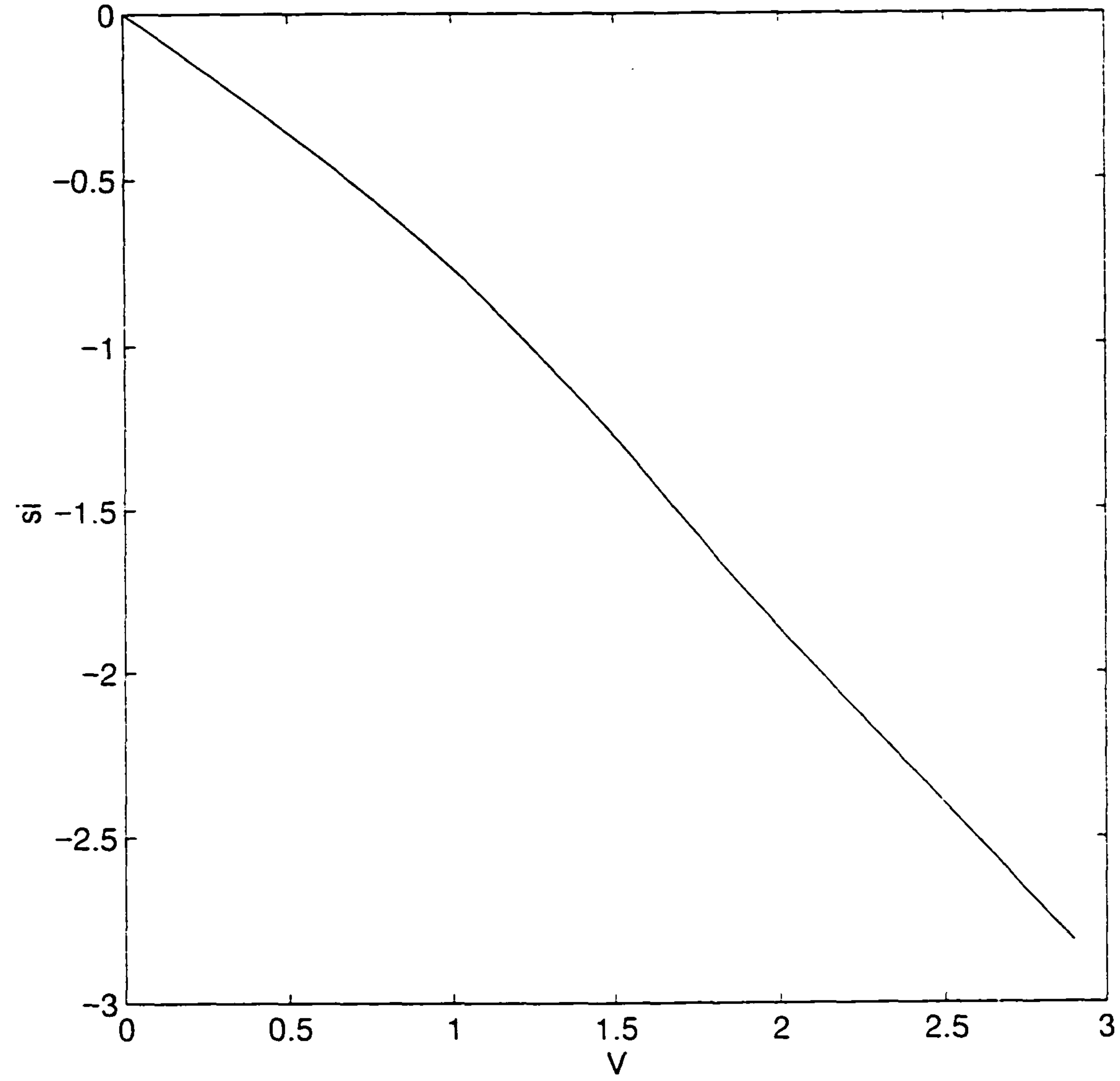

Figure 17 s_i of the absolutely unstable waves as a function of jet velocity for a single jet

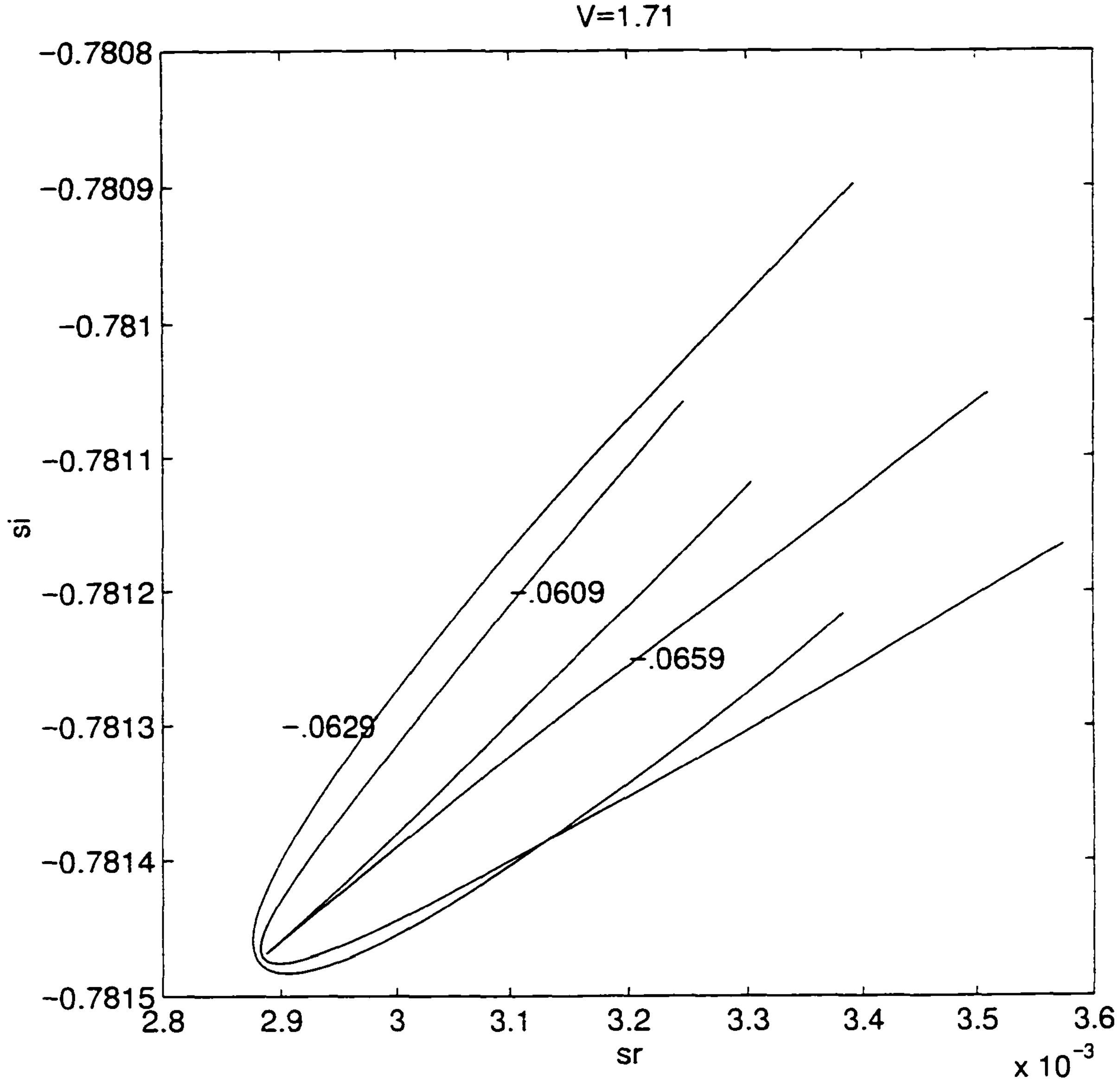

Figure 18 Formation of cusp in the s plane signifying ds/dk=0 (plots of constant k_i)

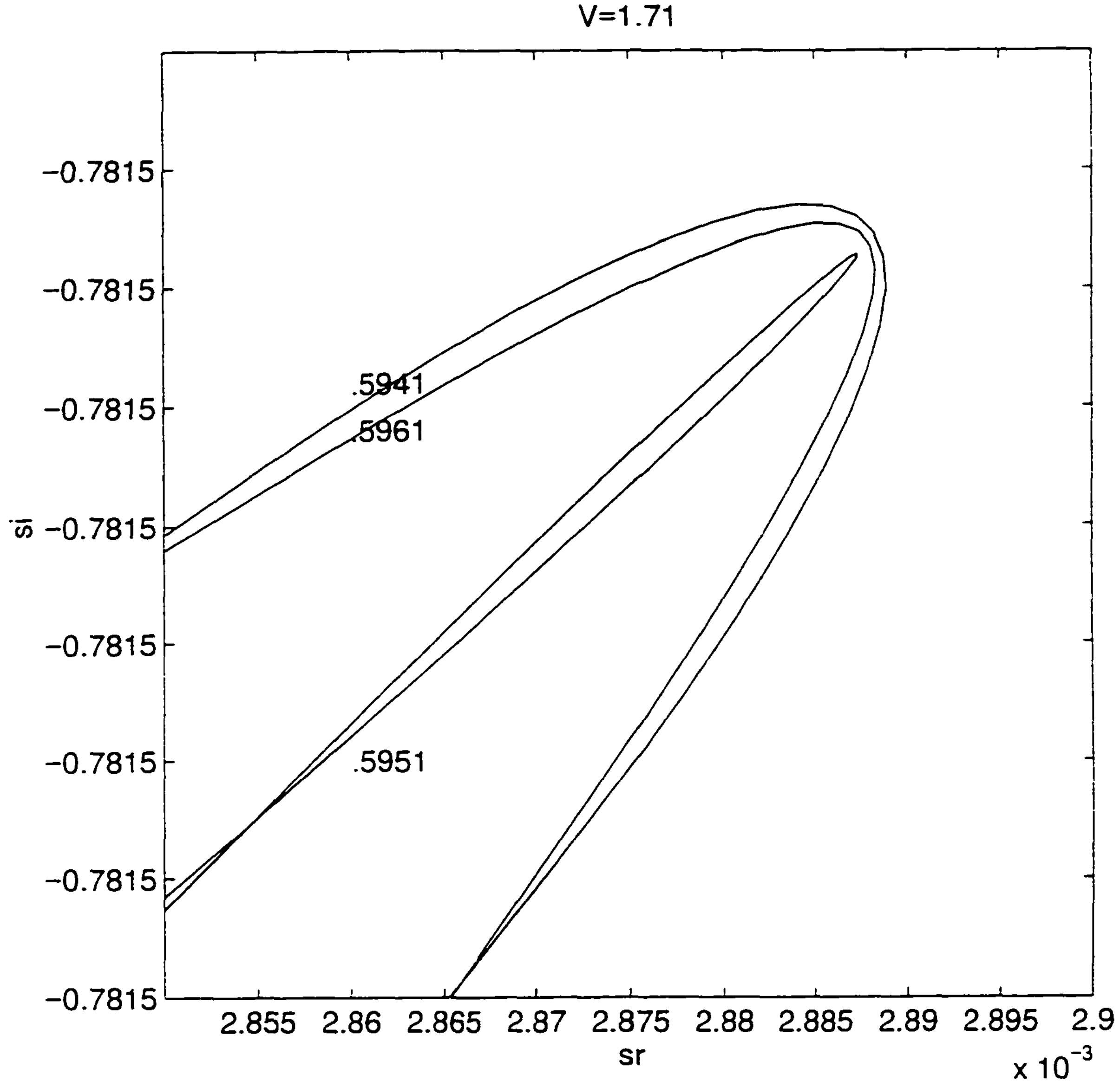

Figure 19 Formation of cusp in the s plane signifying ds/dk=0 (plots of constant k_r)

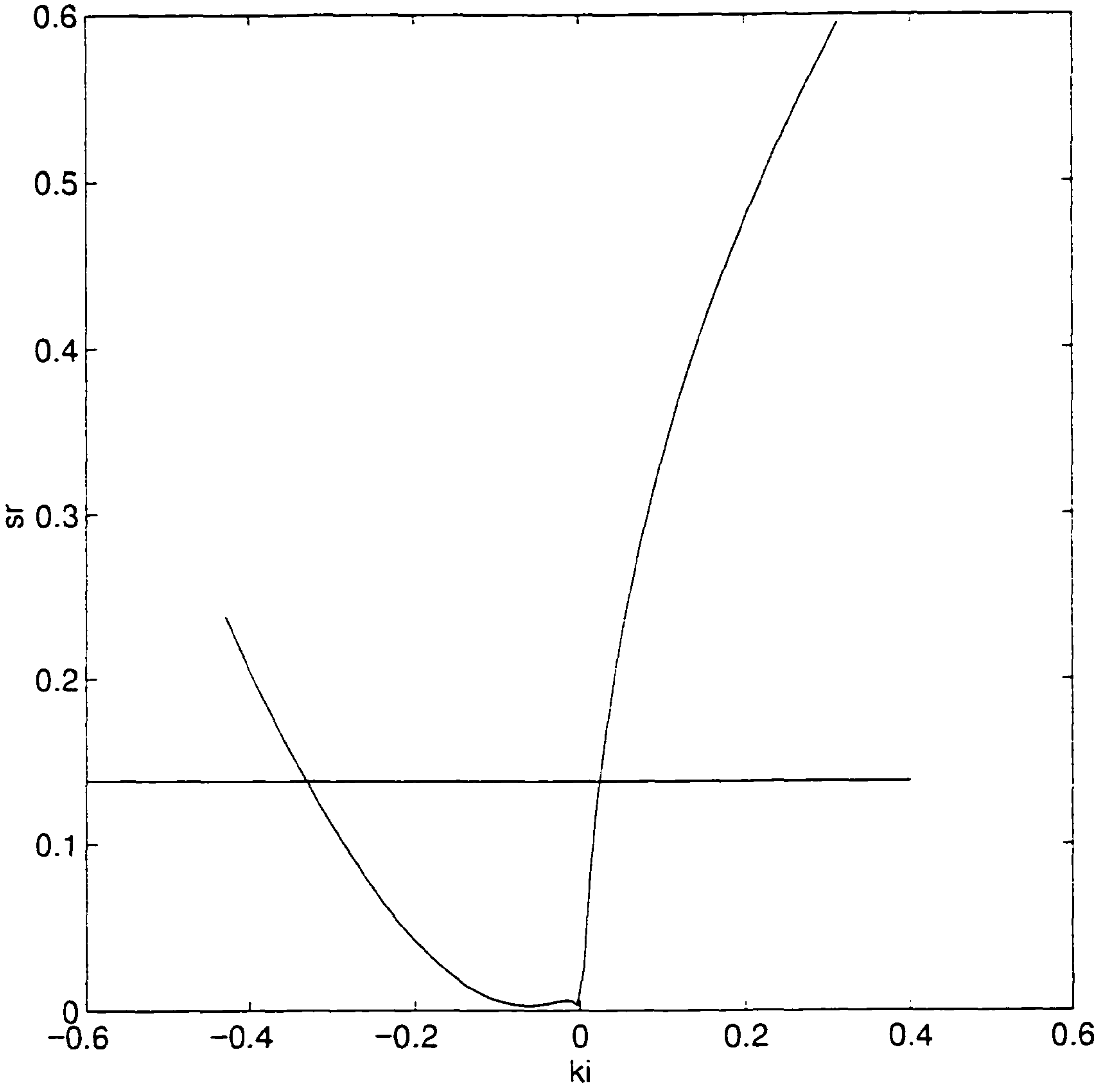

Figure 20 Plot of s_r vs. k_i along a line passing through the cusp in the k plane to determine whether the cusp represents absolute instability

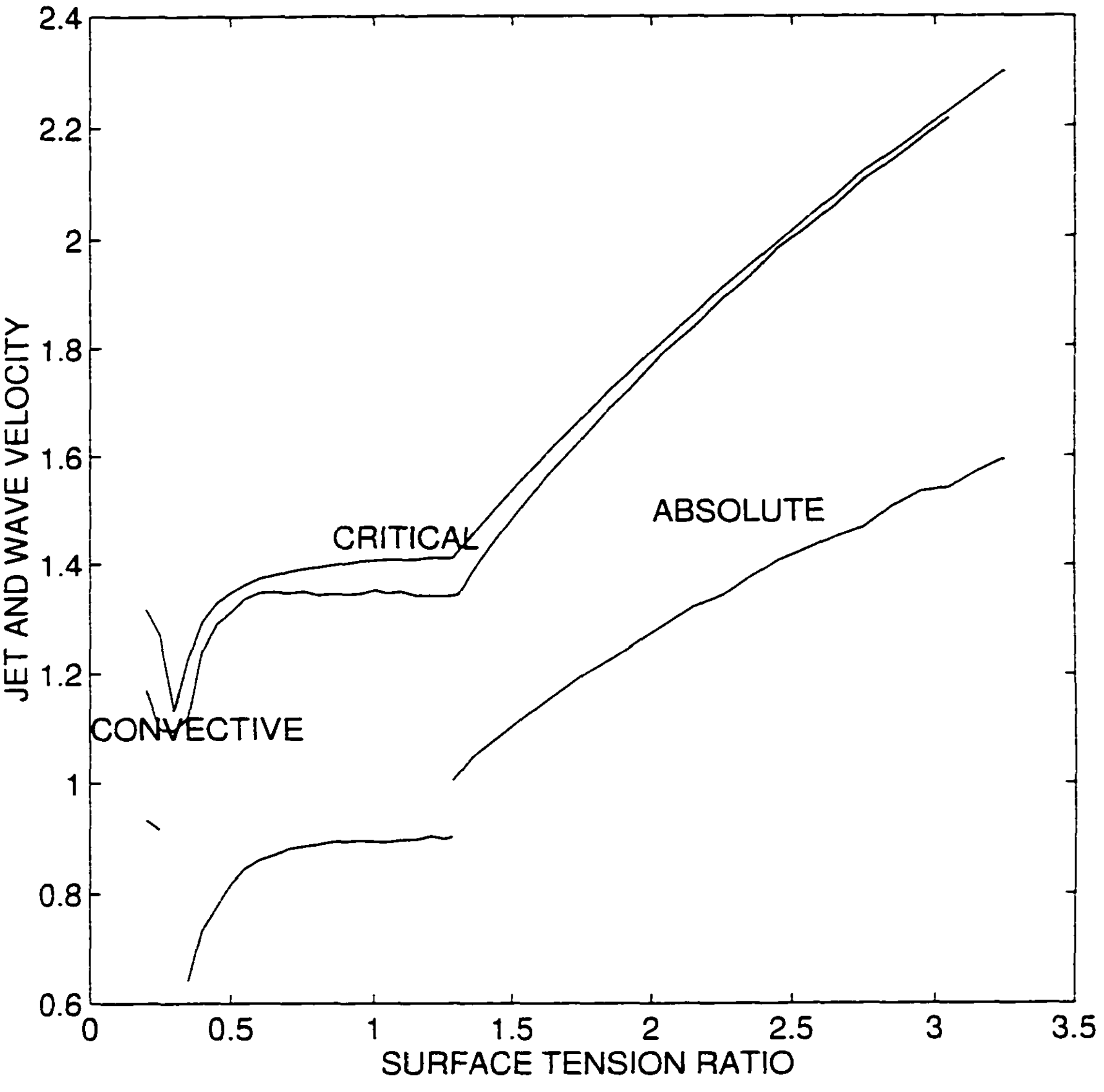

Figure 21 The critical jet velocity, and the phase velocities of the fastest growing convective waves and the absolutely unstable waves at the critical jet velocity as a function of the surface tension ratio (γ). β=1,a=2

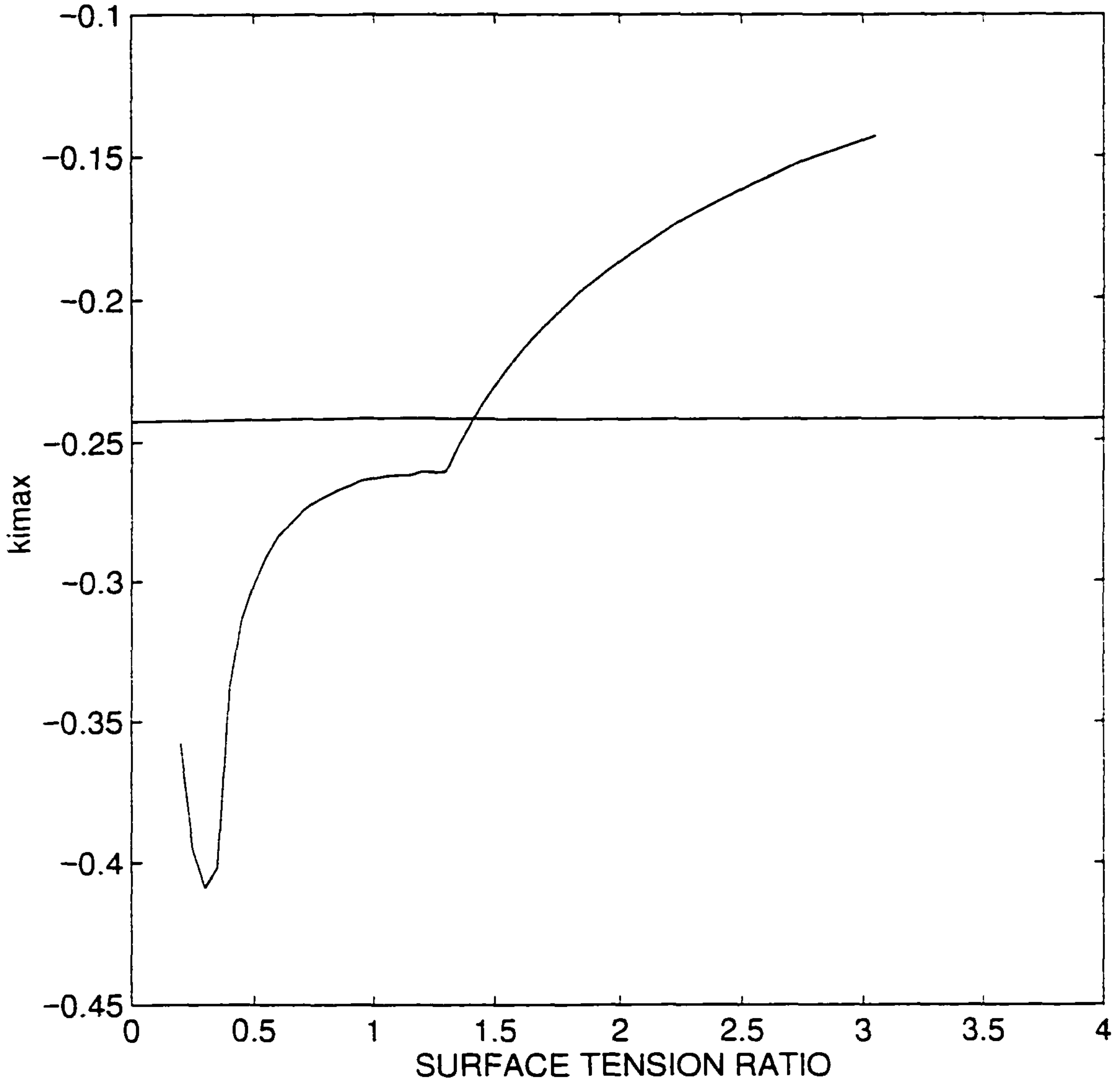

Figure 22 The spatial growth rate (k_i) of the fastest growing convective wave as a function of the surface tension ratio (γ). β=l,a=2. The straight line shows the growthrate of the fastest growing convective wave for an inviscid single jet

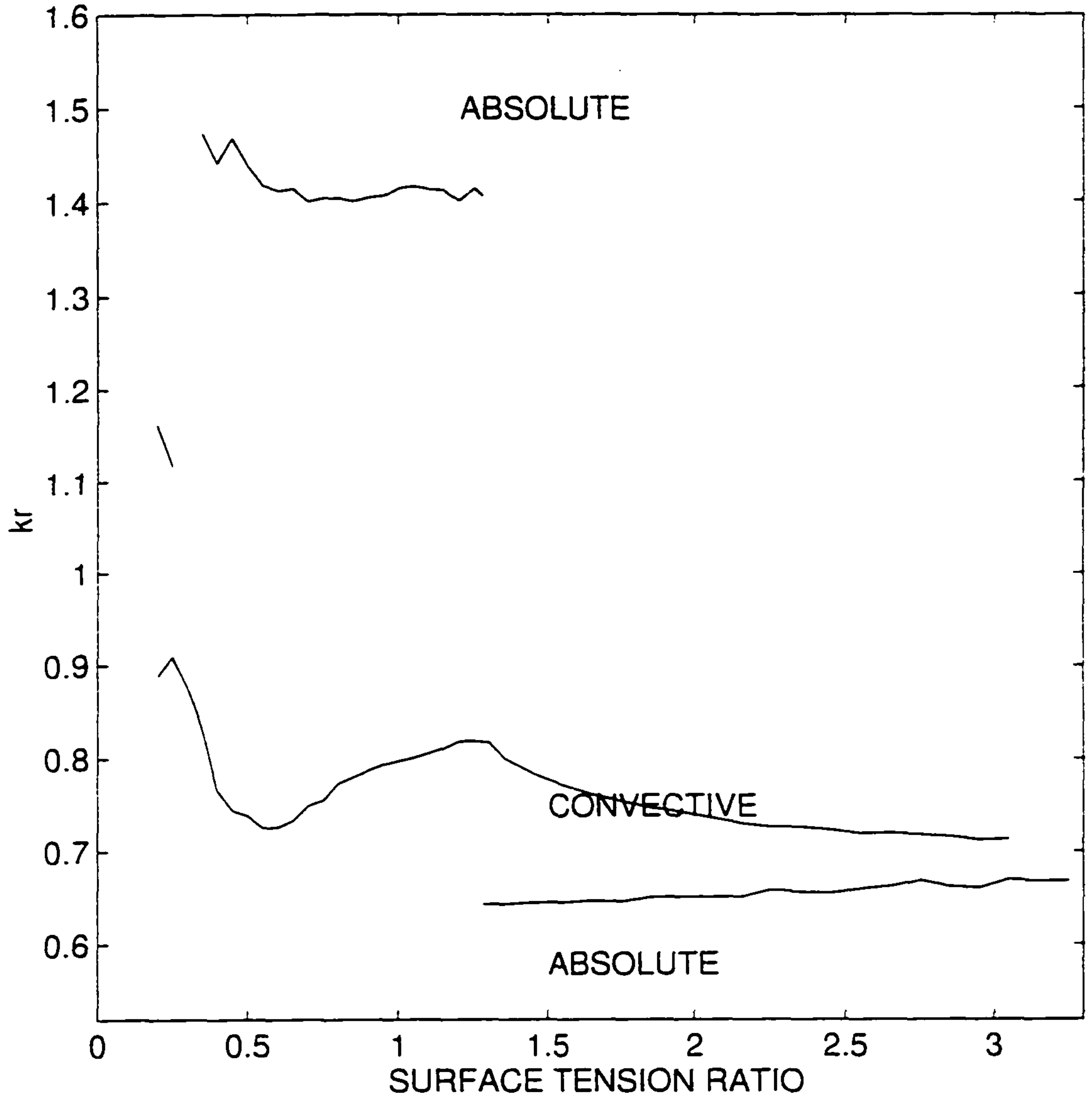

Figure 23 The wavenumber k_r of the fastest growing convective wave and the k_r of the absolutely unstable waves at critical velocity as a function of the surface tension ratio (γ). β=1,a=2.

]

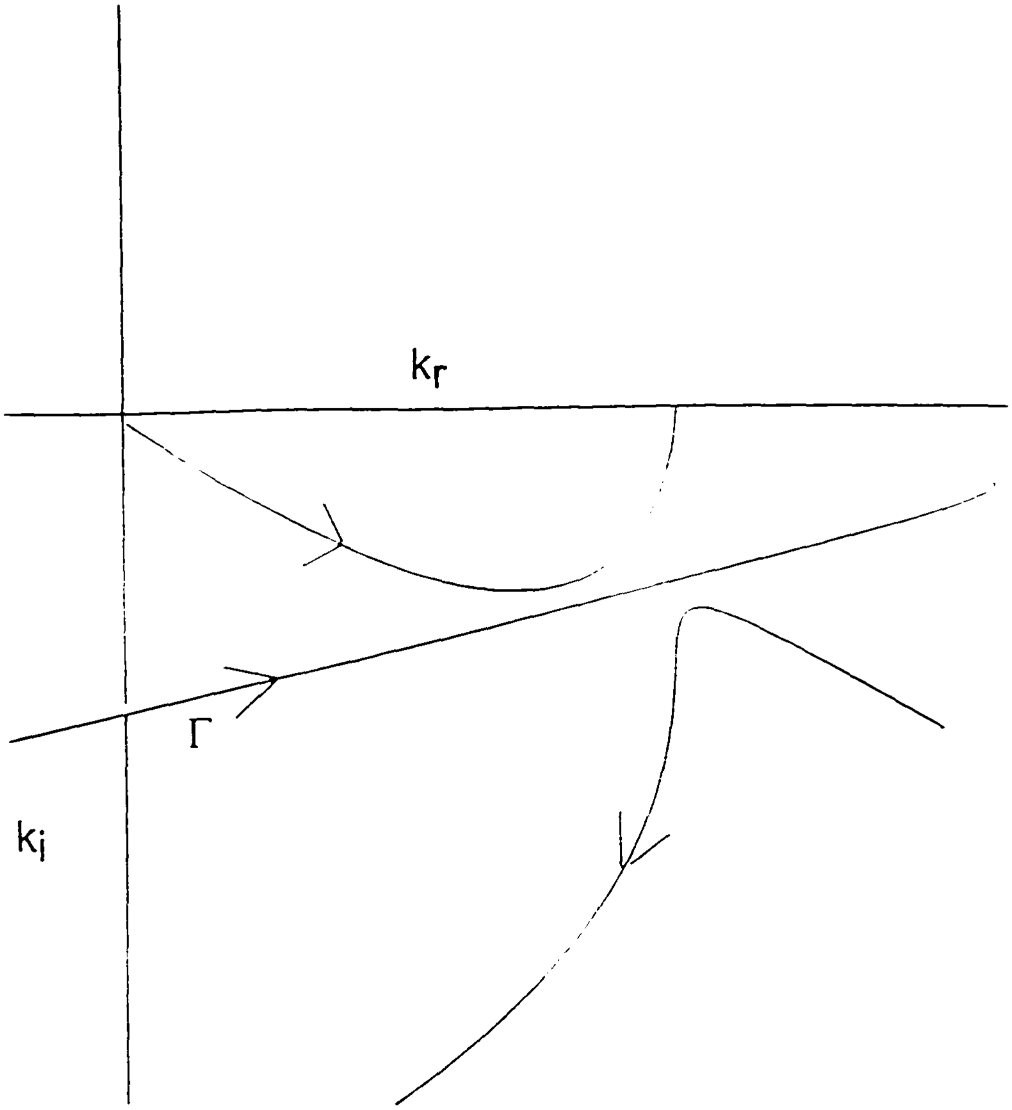

Figure 24 Solutions of k(s) for s_r=0 and the contour for performing the Fourier inversion. (Convective Instability)

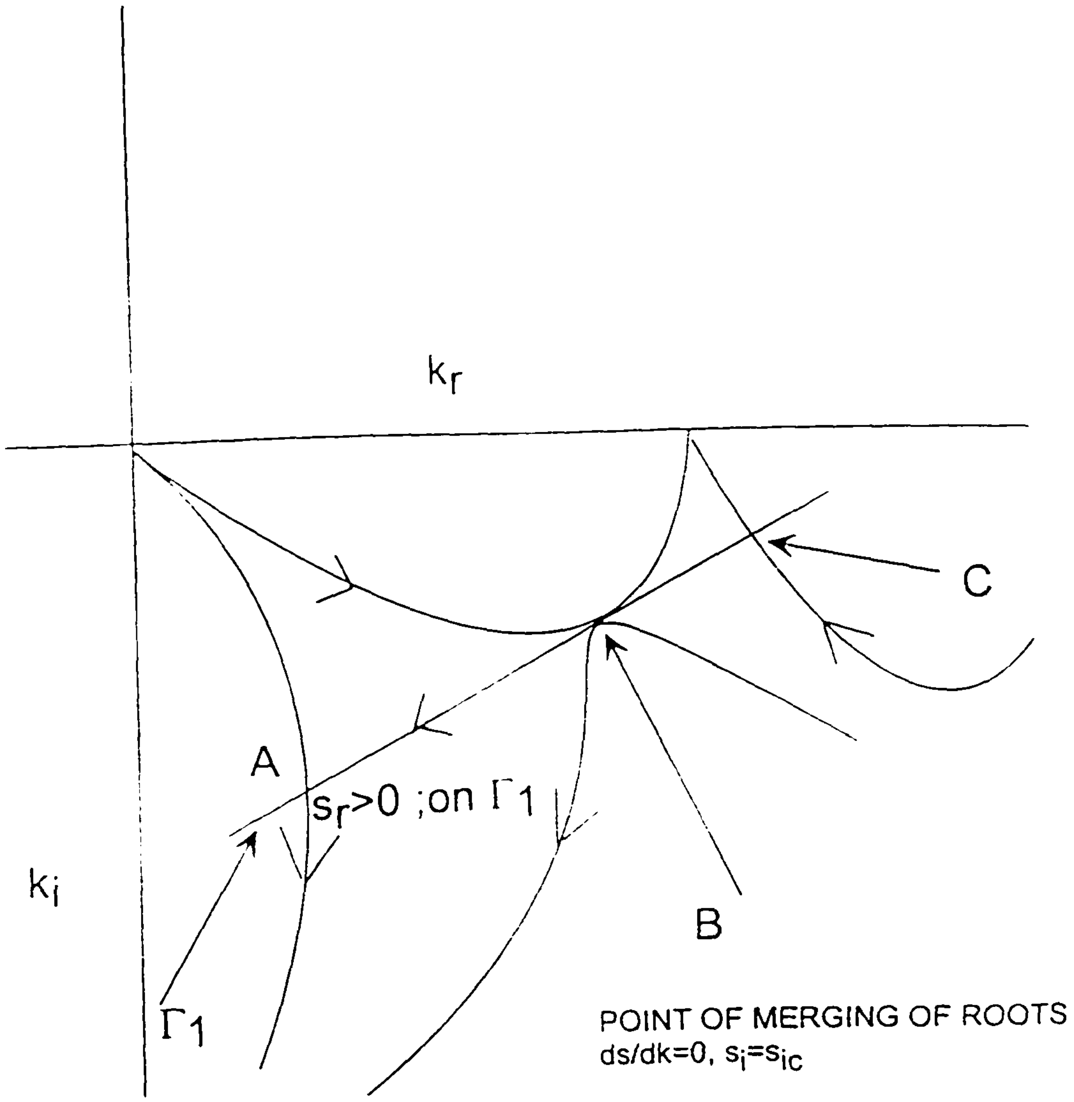

Figure 25 Solutions of k(s) for $s_r=0$ and the contour for performing the Fourier inversion. (Absolute Instability)

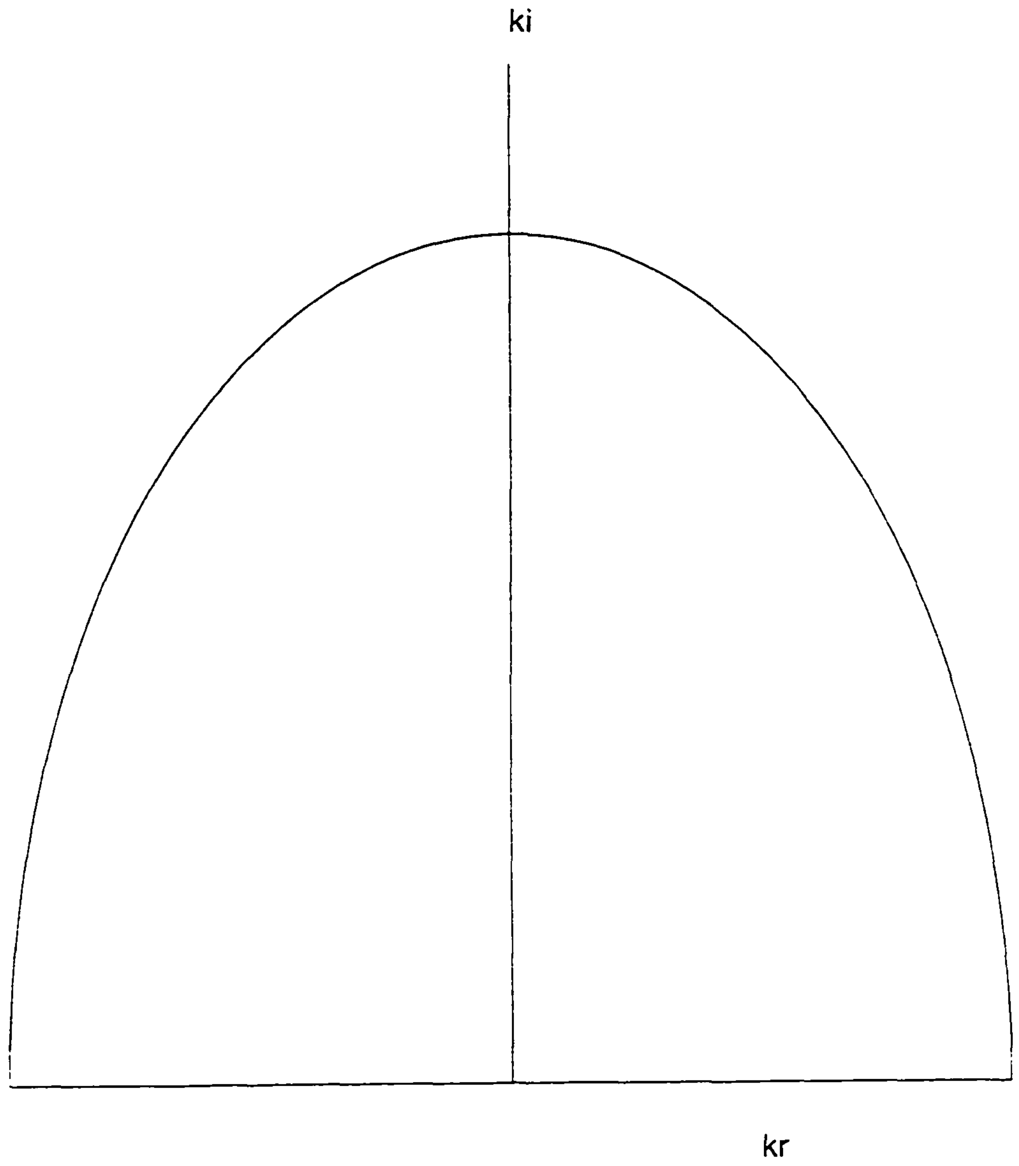

Figure 26 Contour for Fourier inversion, |k|→∞, kr>0

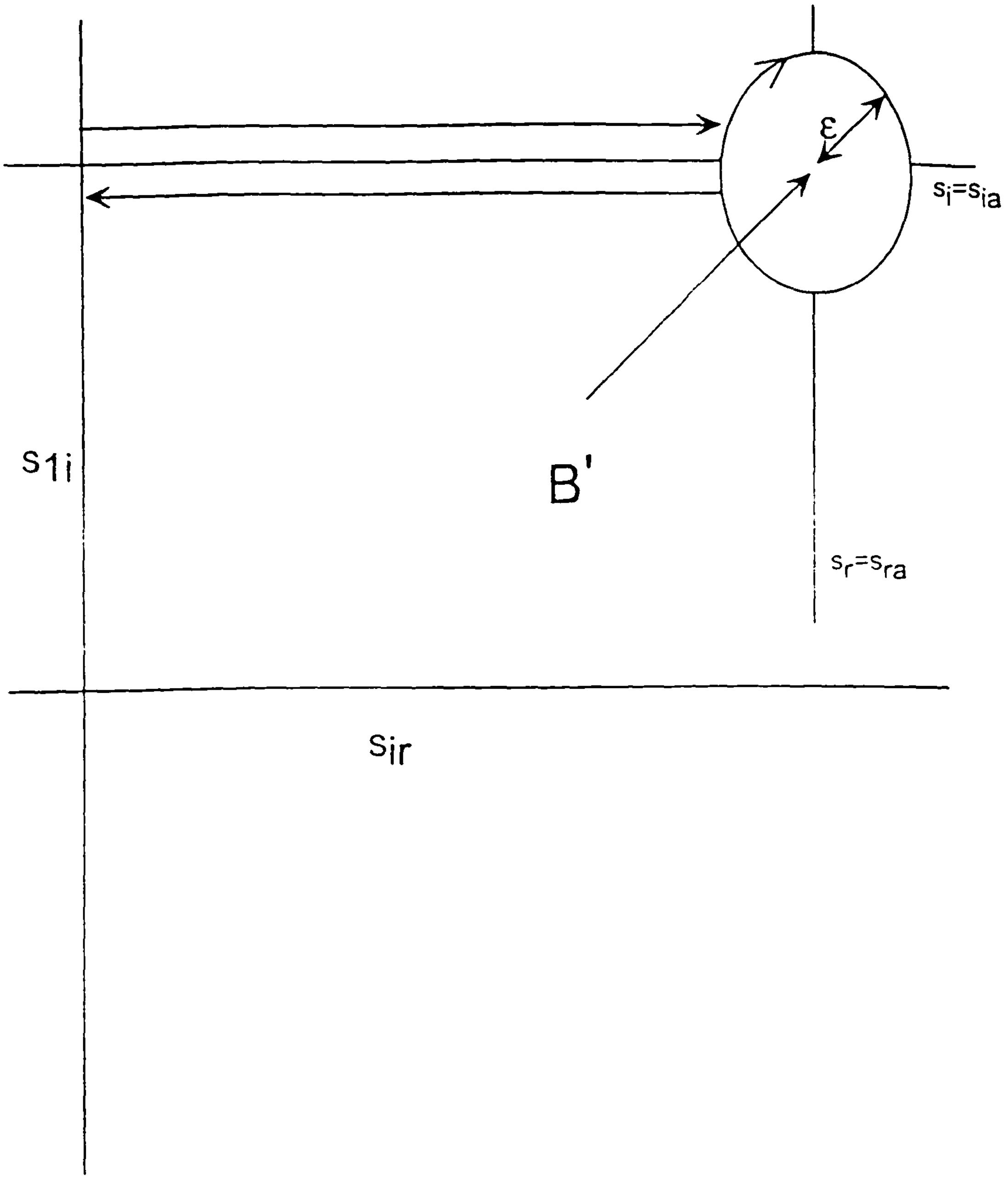

Figure 27(a). Branch cut in the s plane

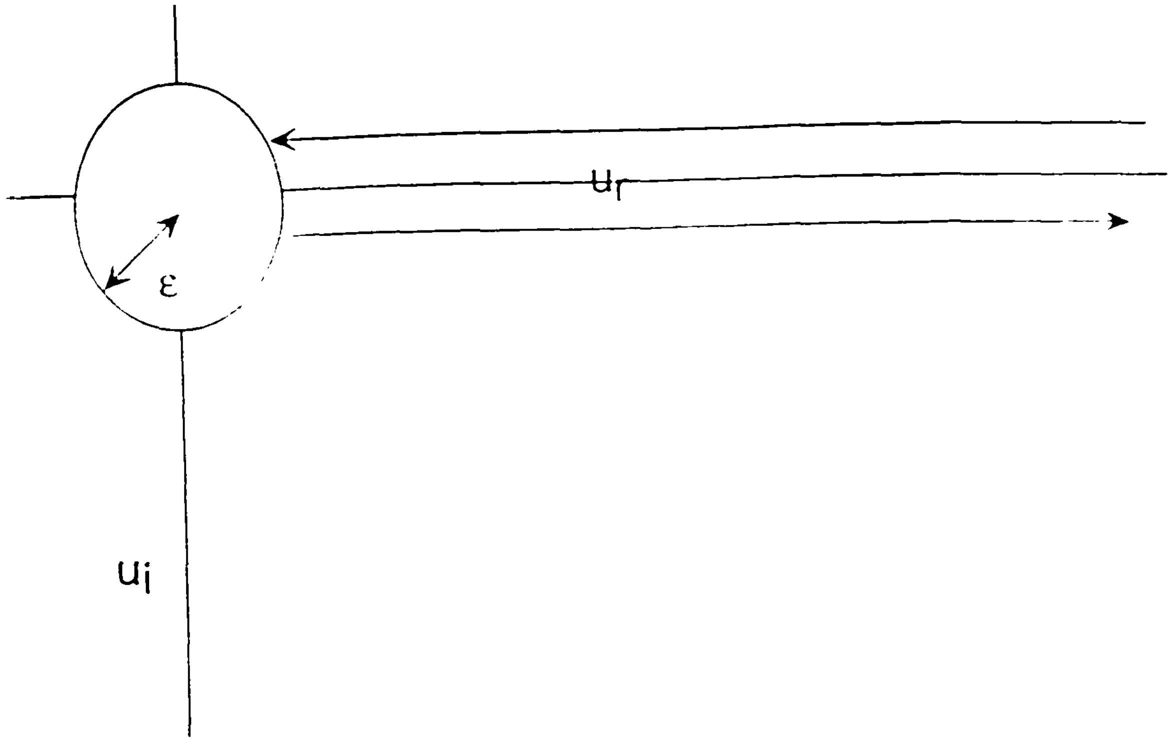

Figure 27(b). Branch cut in the u plane

CHAPTER 5

EXPERIMENTAL INVESTIGATION OF THE CONVECTIVE INSTABILITY IN A SINGLE JET

I. Introduction

A liquid jet issuing out from an orifice is unstable to axisymmetric interfacial disturbances due to destabilizing circumferential capillary forces. Drop break up from jets is important in the technological processes of atomization, ink jet printing (Sweet 1964), fuel injection, particle sorting (Hertzberg, Sweet et al. 1976) and polymer fiber spinning (where it is desirable to arrange for reduced growth rate so that the jets can polymerize before break up). Due to these technological applications, the problem of single jet stability has been widely studied, both experimentally and theoretically. Rayleigh analyzed the *temporal instability* of this base state by imposing, at t=0, an interfacial disturbance with Fourier wave numbers k and n in z and θ directions, respectively. He determined the evolution of this initial disturbance using normal modes ($e^{i(kz+n\theta)+s(k,n)t}$, where z is along the thread axis and s(k,n) is complex). Rayleigh established that only axisymmetric (n=0) modes with wave lengths ($2\pi/k$) larger than the undisturbed thread circumference ($2\pi a$) grow in time ($s_r(k,n=0) > 0$), and that there is a maximum in the growth rate at a wave number k_m equal to 0.696/a. The disturbances grow without traveling, ($s_i(k,n=0)=0$). This temporal stability of the static thread was reconsidered for the case in which the thread fluid is viscous (Chandrasekhar 1961), and is surrounded by a second immiscible viscous liquid (Tomotika 1935). As capillarity drives the instability, the range of unstable wave lengths remains the same when viscous effects are included, but growth rates are reduced and maximally growing waves are shifted to longer wave lengths.

In all the above-mentioned references, the disturbances to the jet are modeled as growing in time. In most applications, the jet issues from an orifice and breaks downstream, i.e., disturbances continually imposed at the nozzle tip (either intentionally through periodic oscillations, or through tip imperfections) grow by the destabilizing capillary action as they are convected downstream, until they cause the jet to break up into drops. Keller et al. (1973) first pointed this fact out. He suggested a base state in which the jet is modeled as a circular (doubly) infinite jet moving with uniform velocity, and interfacial disturbances are imposed locally in space (z=0, for example) and periodic in time, with Fourier frequency modes ω. For an inviscid jet and axisymmetric disturbances of frequency ω, Keller *et al.* determined the spatial growth for the harmonic response ($e^{ik(\omega)z+i\omega t}$; $k(\omega)$ complex, $k_i<0$ for spatial growth) as a function of the Weber number ($W=\rho V^2 a/\sigma$). Keller *et al.* demonstrated that for dimensionless frequencies or Strouhal numbers ($\omega a/V$) between zero and approximately one (the cutoff being a function of W), the localized periodic disturbances grow axially. Thus the spatial analysis allows for the calculation of stable and unstable frequencies. For frequencies in the unstable range, the drop size and distance to break up can be predicted (assuming the linear theory is valid up to break-up; see the experimental verification discussed below) since the drops which are formed then have size which scales as $1/k_r(\omega)$, and the distance downstream from break up is of order $1/k_i(\omega)$. Leib and Goldstein examined the effect of fluid viscosity on growth rates and Lin and Lian (1989) included effects of a surrounding gas phase on the spatial instability.

A large body of experiments studying the break up of jets into drops has been undertaken, usually with a sinusoidal periodic disturbance of frequency ω applied at the nozzle tip (see particularly, (Donnelly and Glaberson 1966), (Goedde and Yuen 1970), (Rutland and Jameson 1970), (Taub 1976), (Pimbley 1976), (Chaudhary and Maxworthy 1980b), (Kowalewski 1996) and the review monograph by (Yarin 1993)).

In all the above studies the wave length of the disturbances was measured by measuring the distance between two successive peaks. The growth rate was measured by measuring the break up length or by measuring the amplitude of the disturbance at two successive peaks and assuming exponential spatial growth. In addition the waves were assumed to convect with the jet velocity and thus the jet velocity was calculated as $n\lambda$ where n is the frequency of the applied disturbance and λ is the measured wave length. The temporal theory is then used to calculate the growth in time, which is then related to the spatial growth rate by $|k_i|V=s_r$ where s_r is the temporal growth rate, V is the jet velocity and k_i is the imaginary part of the wave number which is also the spatial growth rate.

Our study differs from the above in the following regards. First, we digitize the entire jet profile and fit it to the functional form, $\zeta_{nozzle}\exp(-k_i z)\cos(k_r z + \omega t)$ to extract the wave number k_r and the growth rate k_i for a given frequency ω. Since, we make measurements from the digitized image and utilize the entire profile which corresponds to about 250-300 points, our method is expected to yield more reliable and robust measurements. Secondly, we measure the undisturbed jet radius and since we know the flow rate supplied by the pump, we calculate the jet velocity. We independently measure the traveling velocity of the waves by tracking the positions of the maxima with time and compare the wave velocity to the jet velocity. Thirdly, we vary the jet velocity to experimentally study the jet behavior in all velocity regimes. Lastly, we compare the experimental results with the predictions of the convective theory which is the appropriate theory to be used in context to jets coming out of nozzles.

II PROCEDURE

The experimental setup is shown in figure (1). A digital pump (CAVRO SCIENTIFIC) is used to push fluid through a needle to create a jet. Controlling the pump flow rate can control the velocity of the jet. The disturbance to the jet is provided by a piezo crystal, which oscillates with the frequency of the applied voltage. The function generator controls the frequency. An amplifier controls the voltage of the incoming sinusoidal and the voltage controls the amplitude of the piezo crystal. The piezo crystal disturbance is transferred to the base flow of the pump in a special piece made of Plexiglas as shown in figure (2). The modified flow goes through the needle and the liquid emerges from the needle as a jet. The needle is long enough (more than hundred diameters) so that the flow coming out is axisymmetric. The jet flows vertically downward and breaks into droplets downstream. A lamp illuminates the jet from behind and a digital camera records the images of the jet. The camera used in our setup is a KODAK Fast Video Camera which can record at speeds up to 12000 frames per second. The speed used in our experiments is 6000 frames per second. The captured frames are stored in the memory of the camera. They are later downloaded to a computer and digitized. The digitized image is analyzed to detect the interface of the jet. The interface is defined as the pixel or point at which the linearly interpolated intensity between adjacent pixels is 122.5, which is the average of completely, black (0) and completely white (255).

III ANALYSIS OF THE DIGITIZED IMAGE

The digitized image gives the location of the interface, i.e., $r=r(z)$. The disturbance $\zeta = r-a$ where a is the undisturbed radius. From the digitized data, we calculate ζ as a function of z. As stated earlier, the disturbance grows as ζ_{nozzle} $\exp(-k_i z) \cos(k_r z + \omega t)$. We capture the image of the jet in the region where the disturbance is appreciable. It is almost impossible to measure ζ_{nozzle} from the digitized data. Thus we define the amplitude of the disturbance as, $\zeta_0 \exp(-k_i (z+z_0))\cos(k_r (z+z_0))$ where ζ_0 is the amplitude as some location $z=-z_0$. The origin $z=0$ is the axial position of the first data point in the digitized map. Physically, $z=z_0$ represents the first maxima in the fitted image. There are 4 fitting parameters, k_r, k_i, ζ_0, and z_0. If the exact location of the nozzle relative to $z=0$ is known, ζ_{nozzle} can be calculated by using the best-fit solution. The details of the four-parameter fit along with the initial guesses are given in the Appendix. In principle this best fit procedure works even if we have less than one full wave length in the digitized image, clearly with lower accuracy and reliability. Such a situation arises when the growth rate is so large that soon after the disturbances are visible, they grow very fast and break the jet within one wave length. In such situations this best fit method is the only way to measure the wave length. The method to obtain the initial guesses in such situations is different than in the situation in which a few waves are visible in the digitized image. We also note that sometimes the disturbance to the jet is so small that it cannot be picked up by the eye but is still visible in the digitized image. This is another advantage of using the high-speed image analysis to study the single jet instability.

We perform the experiment at different Weber numbers and compare the experimental results with the predictions of the linear stability theory for a doubly infinite jet in the absence of gravity.

IV RESULTS AND DISCUSSION

Experiments at High Weber numbers

The fluid used in the experiment is FC40 fluorocarbon oil. The density and viscosity of FC40 oil are 1.8 g/m^3 and 4cp, respectively. The surface tension of the oil-air interface is 50 dynes/cm. All the experiments were performed at room temperature of approximately 20° C.

We first measure the radius of the jet without imposing any disturbance. The jet still picks up the noise due to friction at the needle top. However, this is small and hence close to the needle tip, we do not see any disturbance. We measure this radius and consider it to be the base state jet radius. The flow rate supplied by the pump is divided by the cross-section area of the jet to get the jet velocity. In the first set of experiments, the jet radius is 0.275 mm and the jet velocity is 1 m/s. Thus, Re=126 and We=36. The frequency of the applied disturbance is varied from 100-600 Hz. The critical frequency, i.e., the frequency above which the jet is stable is $V/(2\pi a)$, where V is the dimensional jet velocity and a is the jet radius. In our experiment the critical frequency is 707 Hz. In the absence of any imposed disturbance the jet breaks due to the small random disturbance at the needle tip, whose magnitude is much smaller than the applied disturbance. Thus, the break up length is fairly large. The fastest growing mode dominates and causes the break up. We seek to study the effect of the frequency of the disturbance on the break up. Since the fastest growing mode grows faster than the imposed disturbance, we need to provide a sufficiently high amplitude at the needle tip to the imposed frequency so that the imposed frequency dominates even at the break up. At the same disturbance needs to be sufficiently small so that the jet does not immediately enter the non-linear regime.

Fig (3) shows an image of the jet along with the digitized image. The real image is at a different scale and is shown inside the digitized image. The frequency of the applied signal is 300 Hz. Fig (4) shows the best fitted curve. As can be seen from the figure, there is a very good match between the digitized shape and the best fitted curve. From the best fit we obtain k_r and k_i. We shall later show the comparison of these with the predictions from the linear stability theory. Fig (5),(7),(9) show the digitized interfaces along with the actual shapes at frequencies of 400,500,600 Hz. Fig (6), (8b), (10) show the best fit shapes along with the digitized images of the jet for the same frequencies. Fig (8a) shows the best fit and the digitized image of the interface instead of the entire jet to increase the resolution. We follow the same procedure to find the wave number and spatial growth rates at these frequencies. At lower frequencies (100

Hz) there is a significant difference between the digitized shape and the best fitted curve. This is caused by the non-linear interaction of the next harmonic of the imposed frequency. At high frequencies the next harmonic lies in the stable regime. But at low frequencies the next harmonic grows faster than the imposed frequency. The next harmonic has double the frequency and hence half the wave length. This results in observable growth around the minima. This growth causes break up, which results in formation of a smaller drop that is called a satellite. This is shown in fig (11). The figure shows a jet issuing from a needle. The white curve is the sum of the intensity at the axial location. A maximum in the intensity corresponds to a maxima. As noted close to the break up there is a second harmonic which leads to satellite formation. Because of this, we can't use the best-fit method to measure the wave length and growth rates at low frequencies. In this regime we rely on all the maxima and calculate wave length as the average distance between them. The growth rates are calculated for each pair of maxima by using eq (10) in the appendix. Figs (12)-(13) show the comparison between the experimental measurements and the predictions of the linear stability theory. Fig(12) compares the wave number and fig(13) compares the growth rate. The error bars in each figure represent the standard deviation in the experimental data. There are at least 20 readings corresponding to each frequency. The comparison is reasonable in both the figures. This is rather remarkable because we are making measurements in the non-linear regime and are comparing the results with the linear theory. All the previous workers (see introduction) have also noticed this. Our experiments are conducted in the high velocity regime so the disturbances are just convected with the jet velocity. To verify this, we measure the velocity of the growing disturbance by tracking a particular maximum and measuring the distance traveled by this crest in a given time. The measured wave velocity is compared with the jet velocity and the comparison is shown in fig(14).

To check for time periodicity at each point in z, we take the average of 20 frames separated by 1 time period. The averaged frame for each frequency is shown in fig (15). The averaged frame looks identical to each of the frames. This shows that the disturbances are growing only in space and are periodic in time.

In most industrial applications involving jet break up, it is important to control the break up size. Thus, we look at the effect of the frequency on the break up size. One would expect each wave length of the disturbance to produce one drop. The volume of fluid contained in one wave length is $\pi a^2\lambda$. Fig (16) compares the measured volume of the drop with the volume contained in one wave length. As can be seen in the figure, the comparison is reasonable at high frequencies but breaks down at lower frequencies. The reason for this is the formation of satellites. As explained above, the satellite formation is due to the next harmonic of the applied frequency, which is unstable only at lower frequencies. To take into account the satellite formation we measure the volume of the satellites as a function of applied frequency. This is shown in figure (17). The vertical line demarcates the region of satellite formation and is based on a non-linear theory by Chaudhary and Redekopp. Their theoretical predictions are based on a third order expansion in δ (the parameter characterizing deviation from the base state) of the temporal problem. We then add the satellite volumes to the drop volumes and the results are shown in fig (18). The comparison of the combined volume with the volume contained in one wave length is reasonable at all frequencies. This shows that each wave length gives rise to one drop at high frequencies and a drop and a satellite at lower frequencies.

Specific Drop Size Production

We can use this system to produce any size of drops at any given rate. Let us assume we need to produce drops N drops per unit time of diameter D. In industrial applications one wants to avoid satellite formation so we want to use a frequency close to the critical frequency. In addition higher frequency also implies higher production rate of drops. But we don't want to choose a frequency very close to the critical frequency because then the growth rate of the imposed disturbance will be too low and hence we will need to impose a much higher initial amplitude to make sure that the imposed disturbance and not the fastest growing mode causes the break up. Based on the above arguments, let us choose a frequency of $0.9n_c$. As mentioned above, for a single jet. $n_c= V/(2\pi a)$. In order to have a high production rate one would like to work at high velocities. Thus we can assume that the disturbance will just convect with the jet velocity. Thus, $\lambda=V/n= V/(0.9n_c)=V/(0.9V/(2\pi a))= (2\pi a)/0.9$. In the absence of satellites each wave length will break into one drop. Thus, the volume of each drop is $(\pi a^2\lambda)= \pi a^2(2\pi a)/0.9 = 2\pi^2a^3/0.9$. The volume of drop is also $(\pi D^3 /6)$. Thus, $2\pi^2a^3/0.9=(\pi D^3 /6) \Rightarrow a=(0.9/12\pi)^{1/3}D=0.288D$. Since each wave length produces one drop, the applied frequency is same as the number of drops that need to be produced per unit time. Thus, $n=N$. The jet velocity is $n\lambda=N (2\pi a)/0.9=N(2\pi)(0.288D)/0.9=2(ND)$. The volumetric flow rate is, $N((\pi D^3 /6)$. This system provides a fairly uniform size distribution of particles and could be very useful in systems in which one needs to produce drops of a given size. The system can change the production rate simply by changing the frequency and the flow rate by the same ratio. The drop size can also be changed on line by changing the frequency. But the variation in drop size is limited to approximately 10% because the satellite formation is negligible only for $k_r<0.7$ {Chaudhary and Redekopp} which corresponds to $n>0.85n_c$. One down side of this setup is the fact that the size of the nozzle scales with the drop size. Thus this system will not be very useful for producing extremely small drops because then the nozzle will need to be extremely small and hence can easily clog. In such situations a system based on much higher frequency is more useful.

Experiments at Intermediate Weber Numbers

At high Weber numbers the experimental results are in close agreement with the spatial theory. Also, the results show that the temporal analysis can be used to analyze the stability problem at high Weber numbers. At intermediate Weber numbers, the waves imposed at the needle tip have non-negligible dispersion. Hence, the predictions of spatial theory begin to differ from the temporal theory on reducing the Weber number. To demonstrate this transition we reduced the Weber number and repeated the above experiments, i.e., we measured the wave lengths and the growth rates of the disturbances as a function of frequency.

We reduce the velocity from 1 m/s to 0.6 m/s giving a Weber number of 6. We use the same fluid so the modified Reynolds number $\frac{\rho a\sigma}{\mu^2}$ stays the same, i.e., 500. Therefore, Reynolds number ($\mathrm{Re} = \frac{\rho U a}{\mu} = \sqrt{\frac{\rho a U^2}{\sigma} \frac{\rho a \sigma}{\mu^2}}$) becomes 55. Fig (19) shows the comparison of the theoretical wave number and the experimental wave number as a function of frequency. As can be seen the comparison is not good. The same holds true for the comparison of the growth rates in fig (20). This disagreement between the experimental and the theoretical results is because of gravity. At high velocities the effect of gravity is not significant and the effect becomes more pronounced on reducing the velocity. To study the effect of gravity further we measured the jet profile in the absence of any imposed disturbances. The noise picked up at the nozzle tip is small enough so that the observable disturbance close to the needle is not significant. The liquid is in a poiseuille (parabolic) flow inside the needle. As it comes out of the needle, the velocity profile relaxes from the poiseuille flow to plug flow. The radius of the jet changes as it emerges in order to conserve the momentum. Neglecting the loss due to friction at the needle edge, conservation of mass and momentum yields,

$$u_j = \frac{4}{3} u_n \qquad\qquad R_j = \frac{\sqrt{3}}{2} R \qquad (1)$$

where u_j is the jet velocity, u_n is the average velocity in the needle, R_j is the jet radius and R is the needle radius. Thus, the jet contracts as it relaxes to a plug flow profile. Since, most authors use a plug flow profile to analyze the jet issuing out of the nozzle, it is important to ensure that the length of the region in which the velocity profile relaxes from parabolic to plug is not too long to affect the stability analysis. The kinetic energy flux is higher in the pipe than in the jet. The difference is dissipated due to viscosity. The difference in the kinetic energy per unit time inside the pipe and in the jet after attaining plug flow is, $19/9\pi\rho R^2 u_n^3$. The viscous dissipation per unit volume $=(\tau:\nabla v)$. In the region of change from poiseuille to plug,

$$\frac{\partial v_r}{\partial r} \sim \frac{\partial v_z}{\partial z} \sim \frac{u_j - u_n}{l} \quad ; \quad \frac{\partial v_z}{\partial r} \sim \frac{4u_n}{R} \quad ; \quad \frac{\partial v_r}{\partial z} \sim \frac{(R - R_j)u_n / l}{l} \sim \frac{0.2u_n R}{l^2}$$

Considering the case when the length of the transition region, l, is greater than R, the viscous dissipation ~ $4\mu u_n/l$. Thus the total viscous dissipation in the transition region ~ $(4\mu u_n/R)(\pi R^2 l)=4\pi\mu u_n R/l$. Equating this to the loss in kinetic energy, one gets, l/R~Re/8. In our experiments, Re~50, thus we expect the jet to travel approximately 6 radii before it relaxes to a plug profile. This is an extremely simplified model to estimate the length of the transition region and much more realistic calculations are available in literature.

The jet further accelerates due to gravity and this acceleration thins it further. The simplest model of the effect of gravity is to assume that the only effect of the gravity is to increase the axial velocity. This increase in axial velocity contracts the jet due to continuity.

$$V^2 - V_0^2 = 2gz \Rightarrow V = \sqrt{2gz + V_0^2} \tag{2}$$

$$R^2 V = R_0^2 V_0 \Rightarrow \frac{R}{R_0} = \sqrt{\frac{V_0}{V}} = \frac{1}{\sqrt{1 + 2gz / V_0^2}} \tag{3}$$

Fig(21) shows the experimental jet profile after exiting from the nozzle. As can be seen in the figure, there is a sudden reduction in the jet diameter as it comes out of the needle. The diameter of the jet after it relaxes to plug flow is 0.8 Rn, which is in close agreement with the theoretical prediction. The figure also shows the theoretical jet profile after the jet is in plug flow and is getting accelerated due to gravity based on eq(18). The agreement is reasonably good. The figure also shows that it takes approximately 3 jet diameters for the velocity to relax from the parabolic profile to plug flow. At this velocity Re=50. Thus the length required to obtain the plug flow velocity is also in reasonable agreement to the theoretical formula obtained above , especially in view of the simplistic model.

Equation (18) shows that the reduction in jet radius is small at high velocities. Thus we cannot reduce the velocity to go into the lower Weber number regime because that would enhance the effect of gravity which we haven't taken into account in our model. We recall that Weber number, $We=\rho RV^2/\sigma$. Thus, Weber number can be reduced by choosing a fluid with a high surface tension and a low density. We choose to use water for performing experiments in the lower Weber number range for the above reason. Water has surface tension approximately three times the surface tension of FC40 oil and its density is approximately half. Thus, the Weber number is reduced by a factor of six without any reduction in velocity.

We kept the velocity at 1m/s and replaced the FC40 oil by Water. The Weber and Reynolds number are 3.8 and 275, respectively. Unfortunately, we were unable to control the frequency of the disturbance applied to the jet. The jet always broke at the wave length corresponding to the fastest growing mode, irrespective of the imposed frequency. We ascribe this fact to the presence of air bubbles in the Plexiglas connection where the base flow from the pump is modulated by disturbance from the piezo-crystal. The bubbles are very compressible and so they absorb the entire disturbance not allowing the disturbance to effect the jet. This does not happen in the experiments done with FC40 oil because it wets the Plexiglas and also Teflon, of which the tubes are made. Thus, we can only compare the fastest growing mode with the theoretical analysis. The experimental wave number and growth rates are 0.58±0.02 and –0.365± 0.045. The theoretical predictions for the k_r, $-k_i$ are 0.77 and –0.363 respectively. Thus, the agreement is better than that for the FC40 oil, but certainly not good. The temporal predictions for this experiment are k_{rmax}= 0.7 and k_{imax}=-0.32. (figure 22). The temporal solutions are reasonably close to the spatial predictions. Thus we are still in a range of Weber numbers where the dispersion is not very significant. This shows that the temporal theory is accurate enough in most circumstances and can be used instead of the more complicated spatial theory unless the Weber number is so low that the jet is or is nearly absolutely unstable.

V CONCLUSIONS

A single jet is unstable due to capillarity. As the jet issues from a nozzle, it picks up disturbances, either specifically imposed or simply due to noise, and these disturbances grow downstream. The growth of these disturbances is very accurately predicted by the linear stability theory. These growing disturbances cause the jet to break into drops. The size of the drops depend on the wave length of the growing disturbance as R~ $\lambda^{1/3}$. In certain situations these big drops are separated by smaller drops, which are called satellites. The formation of satellite has been predicted by non-linear analysis (Chaudhary and Redekopp). The satellite formation takes place at frequencies less than approximately 0.7 times the critical frequency. Chaudhary and Redekopp showed this theoretically and our experimental results agree with their finding. In most industrial applications, satellites are not desirable. Thus, one must impose disturbances of frequencies higher than 0.7 times the critical frequency. Controlling the frequency of the disturbance at the nozzle tip also controls the break up size, i.e., the size of the drops produced on break up. This system can be used to produce a continuous supply of uniform size drops. The production rate can be set arbitrarily and the size can be varied on line by changing the frequency within a range of approximately 10%.

We use the entire jet profile to obtain the wave length and the growth rates by fitting the digitized jet profile to a functional form that is given by the linear stability analysis. The fit of the data is very good, which is rather remarkable because our experiments are clearly in the non-linear regime. The method of using the best-fit curve utilizes the entire jet profile and hence is more reliable than either using just the maxima or using the break up length as a measure of the growth rate.

The effect of gravity on a jet issuing vertically downward from a nozzle is to accelerate it, which reduces the radius of the jet to satisfy continuity. The shape of the interface can be modeled accurately by considering a uniform acceleration in the vertical direction and reducing the jet radius to ensure continuity. The jet is in poiseuille flow inside the needle and, as it comes out, it relaxes to a plug flow. During the course of this process, the radius of the jet decreases to approximately 80% of the needle diameter and hence its velocity increases by approximately 40%. It takes approximately two jet diameters for the profile to relax from poiseuille to plug. These numbers depend in general on the Reynolds number.

The spatial analysis of the jet yields three different regimes in Weber number. At very high Weber number, the disturbances introduced at the nozzle simply convect with the jet velocity and grow as they travel downstream. Since, the disturbances convect with the jet velocity, propagation in space is equivalent to progression in Lagrangian time. Thus, the predictions of the spatial theory match the predictions of the temporal theory. On lowering the jet velocity, the disturbances start getting dispersed as they travel and grow downstream. Still, these disturbances only propagate downstream. In this regime the spatial analysis predicts the break up size and break up lengths that differ from the temporal predictions. In this regime gravity also starts becoming important and thus introduces too much error into our measurements for accurate comparison with theory. However, as noted, for applications requiring high velocities to maximize production, the temporal analysis would probably suffice.

VI APPENDIX

Let the best fit be $\varsigma^* = \varsigma_0 \exp(-k_i(z+z_0))\cos(k_r(z+z_0))$ where k_r, k_i, ς_0, and z_0 are the parameters obtained by the best fit. The experimental data is $\varsigma = \varsigma(z)$ at discrete values of $z=z_i$; $i=1{:}N$. Define the objective function : $F(k_r, k_i, \varsigma_0, z_0) = \sum_i (\varsigma^*(z_i) - \varsigma_i)^2$. The best fit minimizes F.

$$F = \sum_i \varsigma^{*2}(z_i) - 2\varsigma^{*}(z_i)\varsigma_i + \varsigma_i^{2} =$$

$$\sum_i \varsigma_0^{2} \exp(-2k_i(z_i + z_0))\cos^2(k_r(z_i + z_0)) - 2\varsigma_i\varsigma_0 \exp(-k_i(z_i + z_0))\cos(k_r(z_i + z_0)) + \varsigma_i^{2} \tag{1}$$

The minima of F(k_r, k_i, ζ_0, z_0) implies

$$\frac{\partial F}{\partial k_r} = 0 \quad ; \quad \frac{\partial F}{\partial k_i} = 0 ; \quad \frac{\partial F}{\partial \varsigma_0} = 0 \quad ; \quad \frac{\partial F}{\partial z_0} = 0 \tag{2}$$

$$\frac{\partial F}{\partial \varsigma_0} = \sum_i \begin{matrix} 2\varsigma_0 \exp(-2k_i(z_i + z_0))\cos^2(k_r(z_i + z_0)) - \\ 2\varsigma_i \exp(-k_i(z_i + z_0))\cos(k_r(z_i + z_0)) \end{matrix} = 0 \tag{3}$$

Thus,

$$\varsigma_0(k_r, k_i, z_0) = \frac{\sum_i \varsigma_i \exp(-k_i(z_i + z_0))\cos(k_r(z_i + z_0))}{\sum_i \exp(-2k_i(z_i + z_0))\cos^2(k_r(z_i + z_0))} \tag{4}$$

$$\frac{\partial F}{\partial k_r} = \sum_i \begin{matrix} -\varsigma_0^{2} z_i \exp(-2k_i(z_i + z_0))\sin(2k_r(z_i + z_0)) + \\ 2\varsigma_i\varsigma_0 z_i \exp(-k_i(z_i + z_0))\sin(k_r(z_i + z_0)) \end{matrix} = 0 \tag{5}$$

$$\frac{\partial F}{\partial k_i} = \sum_i \begin{matrix} -2\varsigma_0^{2} z_i \exp(-2k_i(z_i + z_0))\cos^2(k_r(z_i + z_0)) + \\ 2\varsigma_i\varsigma_0 z_i \exp(-k_i(z_i + z_0))\cos(k_r(z_i + z_0)) \end{matrix} = 0 \tag{6}$$

$$\frac{\partial F}{\partial z_0} = \sum_i \begin{matrix} -2\varsigma_0^{2} k_i \exp(-2k_i(z_i + z_0))\cos^2(k_r(z_i + z_0)) - \\ \varsigma_0^{2} k_r \exp(-2k_i(z_i + z_0))\sin(2k_r(z_i + z_0)) + \\ 2\varsigma_i\varsigma_0 k_i \exp(-k_i(z_i + z_0))\cos(k_r(z_i + z_0)) + \\ 2\varsigma_i\varsigma_0 k_r \exp(-k_i(z_i + z_0))\sin(k_r(z_i + z_0)) \end{matrix} \tag{7}$$

The equations (3), (5) - (7) are solved simultaneously to give the optimum values of (k_r, k_i, ζ_0, z_0). These equations were solved using Newton Raphson's method. It is important to get as good an initial guess for (k_r, k_i, z_0) as possible for faster convergence. The initial guess for ζ_0 is found by using equation (4).

INITIAL GUESS:

It has been shown that at large jet velocities, the disturbance introduced at the nozzle tip gets convected and grows axially. Thus, the jet velocity is same as the wave velocity. The wave velocity is $\nu\lambda$ where ν is the frequency of the disturbance and λ is the wavelength. $\nu = \omega/2\pi$ and $\lambda = 2\pi/k_r$. The jet velocity $V = Q/(\pi a^2)$ where Q is the flow rate of liquid as supplied by the pump and a is the undisturbed jet radius. Thus, $k_r = \pi a^2\omega/Q$. This is the initial guess for k_r.

If the digitized data has at least 2-3 peaks, the initial guess for k_i is obtained as follows:

$$\varsigma^{*}(z_i) = \varsigma_0 \exp(-k_i(z_i + z_0))\cos(k_r(z_i + z_0)) \tag{8}$$

$$\varsigma^{*}(z_i + 2\pi/k_r) = \varsigma_0 \exp(-k_i(z_i + 2\pi/k_r + z_0))\cos(k_r(z + z_0) - 2\pi) \tag{9}$$

Dividing (9) by (8),

$$\frac{\varsigma^{*}(z_i + 2\pi/k_r)}{\varsigma^{*}(z_i)} = \exp(-k_i(2\pi/k_r)) \quad \Rightarrow \quad k_i = -\frac{k_r}{2\pi}\log\left[\frac{\varsigma^{*}(z_i - 2\pi/k_r)}{\varsigma^{*}(z_i)}\right] \tag{10}$$

For the initial guess, we assume $\varsigma^{*}(z_i) = \varsigma_i$. The initial guess for k_i is the mean of all the k_i's calculated by (10). If the digitized data contains less than one cycle then this method cannot be used. The theoretical solution to the spatial instability yields k_r and k_i as a function of the applied frequency. The theoretical solution is used as the initial guess for k_i in such situations.

The initial guess for z_0 is obtained as follows:

$$\varsigma^{*}(z_i) = \varsigma_0 \exp(-k_i(z_i + z_0))\cos(k_r(z_i + z_0)) \tag{11}$$

$$\varsigma^{*}(z_j) = \varsigma_0 \exp(-k_i(z_j + z_0))\cos(k_r(z_j + z_0)) \tag{12}$$

Dividing (12) by (11)

$$\frac{\varsigma^{*}(z_j)}{\varsigma^{*}(z_i)} = \exp(-k_i(z_j - z_i))\frac{\cos(k_r(z_j + z_0))}{\cos(k_r(z_i + z_0))} \tag{13}$$

Rearranging equation (13) and assuming $\varsigma^{*}(z_i)=\varsigma_i$ we get,

$$z_0(z_i, z_j) = \frac{1}{k_r}\tan^{-1}\{\frac{\varsigma_i\cos(k_r z_j)\exp(k_r z_i) - \varsigma_j\cos(k_r z_i)\exp(k_r z_j)}{\varsigma_i\sin(k_r z_j)\exp(k_r z_i) - \varsigma_j\sin(k_r z_i)\exp(k_r z_j)}\} \tag{14}$$

Thus we get a value of z_0 for each pair of points, i.e., $i,j=1:N$; $i \neq j$. Using the repeated median theorem, the optimum value for z_0 is given by,

$$z_0 = \mathrm{median}(\mathrm{median}(z_0(z_i, z_j; i = 1..N; i \neq j)), j = 1..N) \tag{15}$$

Using these initial guesses we solve the equations (3), (5)-(7) to get the optimum values of (k_r, k_i, ζ_0, z_0).

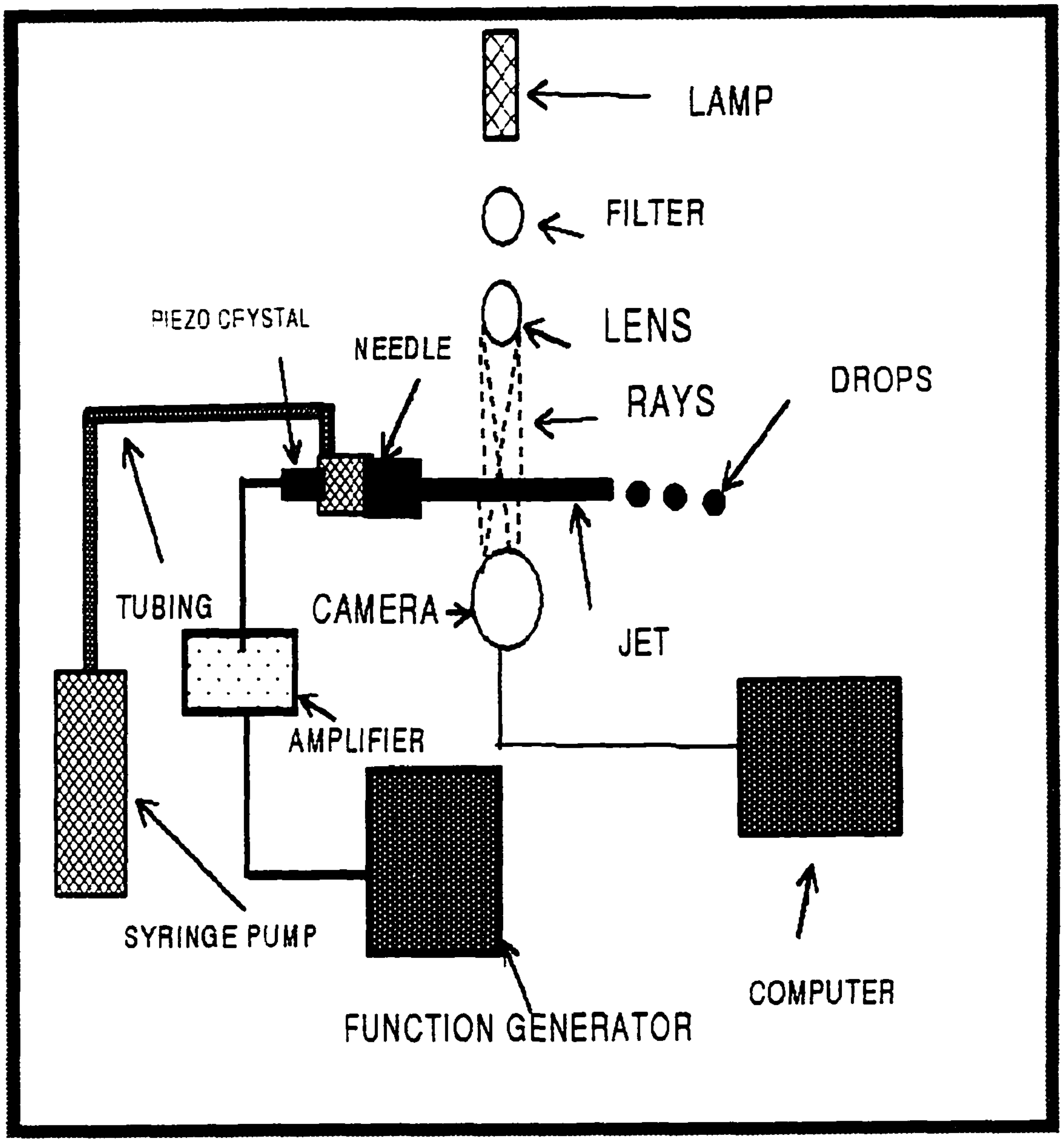

Figure 1. Experimental setup

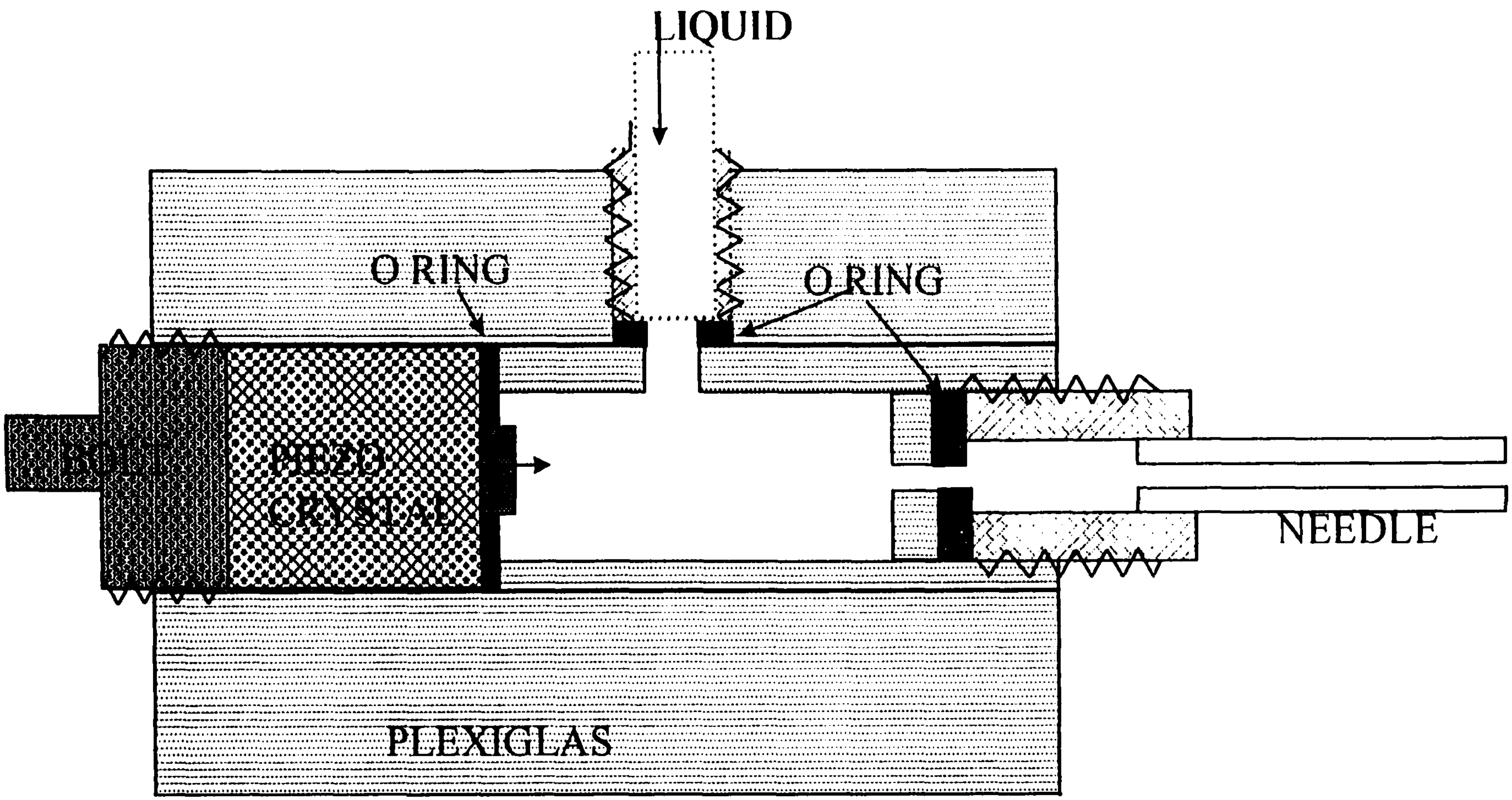

Figure 2. Attenuation of the base flow from pump with the periodic disturbance supplied by the piezo-crystal

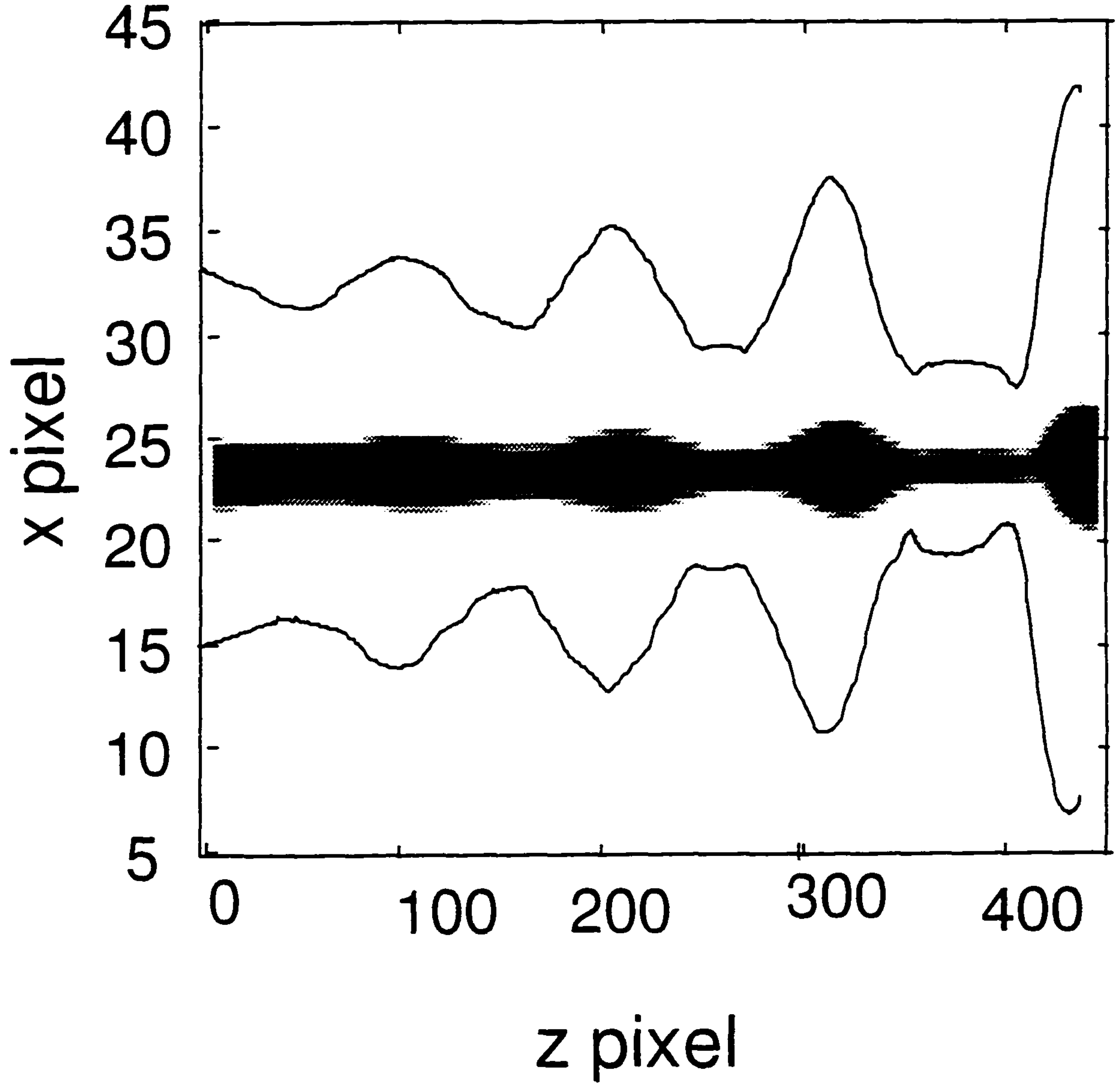

Figure 3. The jet image and the digitized image. Frequency= 300

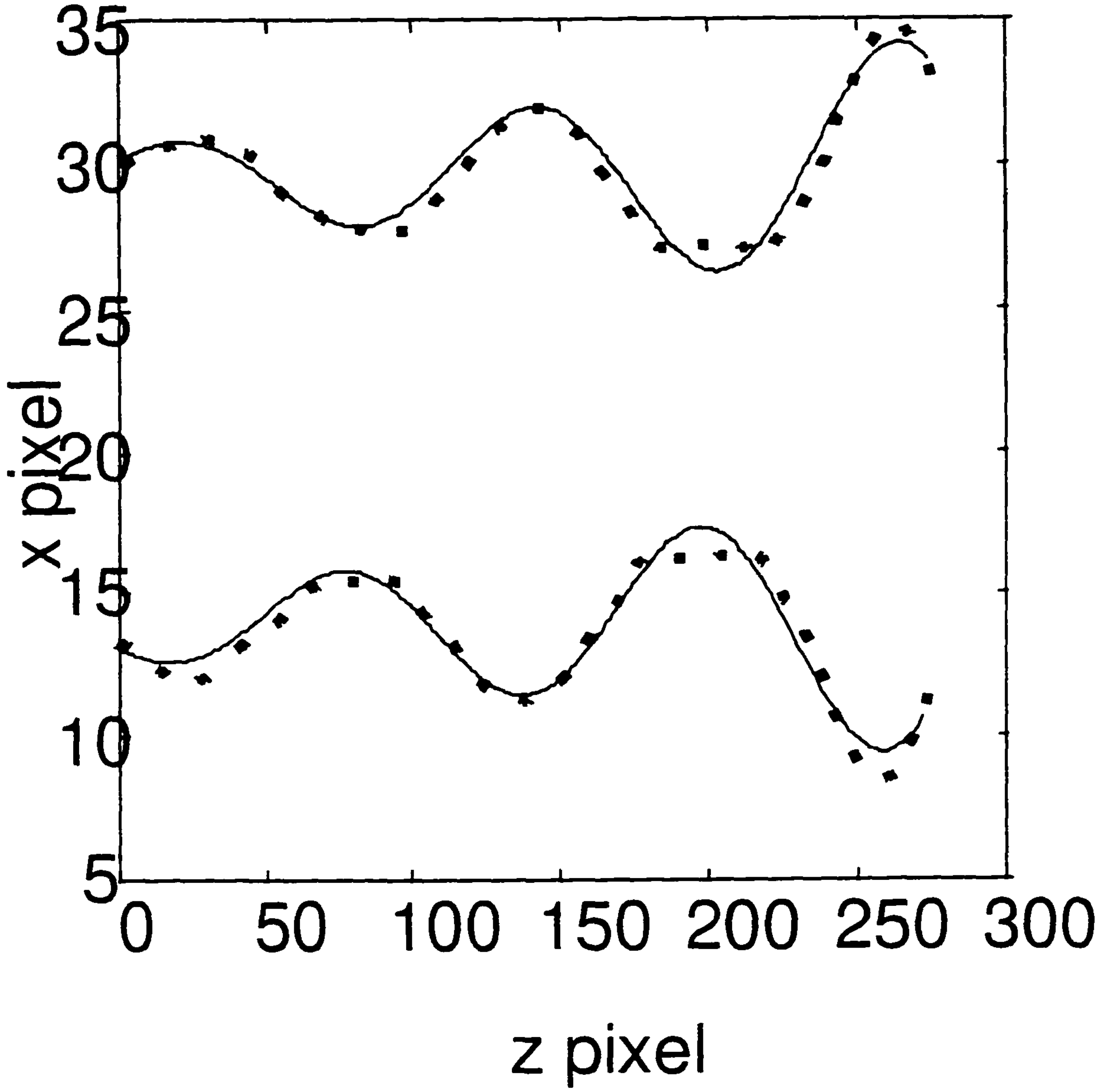

Figure 4. The digitized image along with the best fit of the jet interface at frequency of 300 Hz

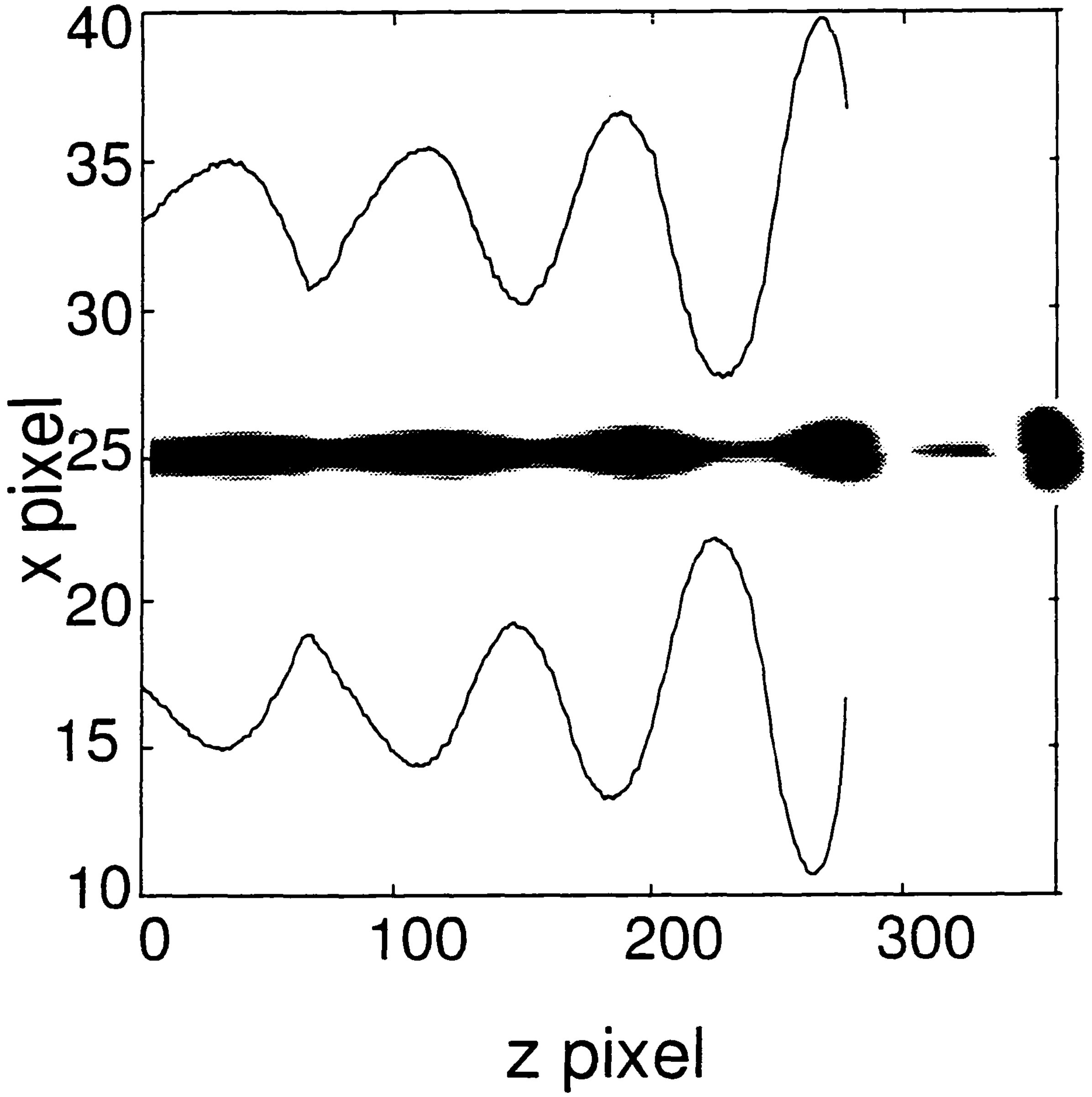

Figure 5. The jet image and the digitized image. Frequency= 400 Hz

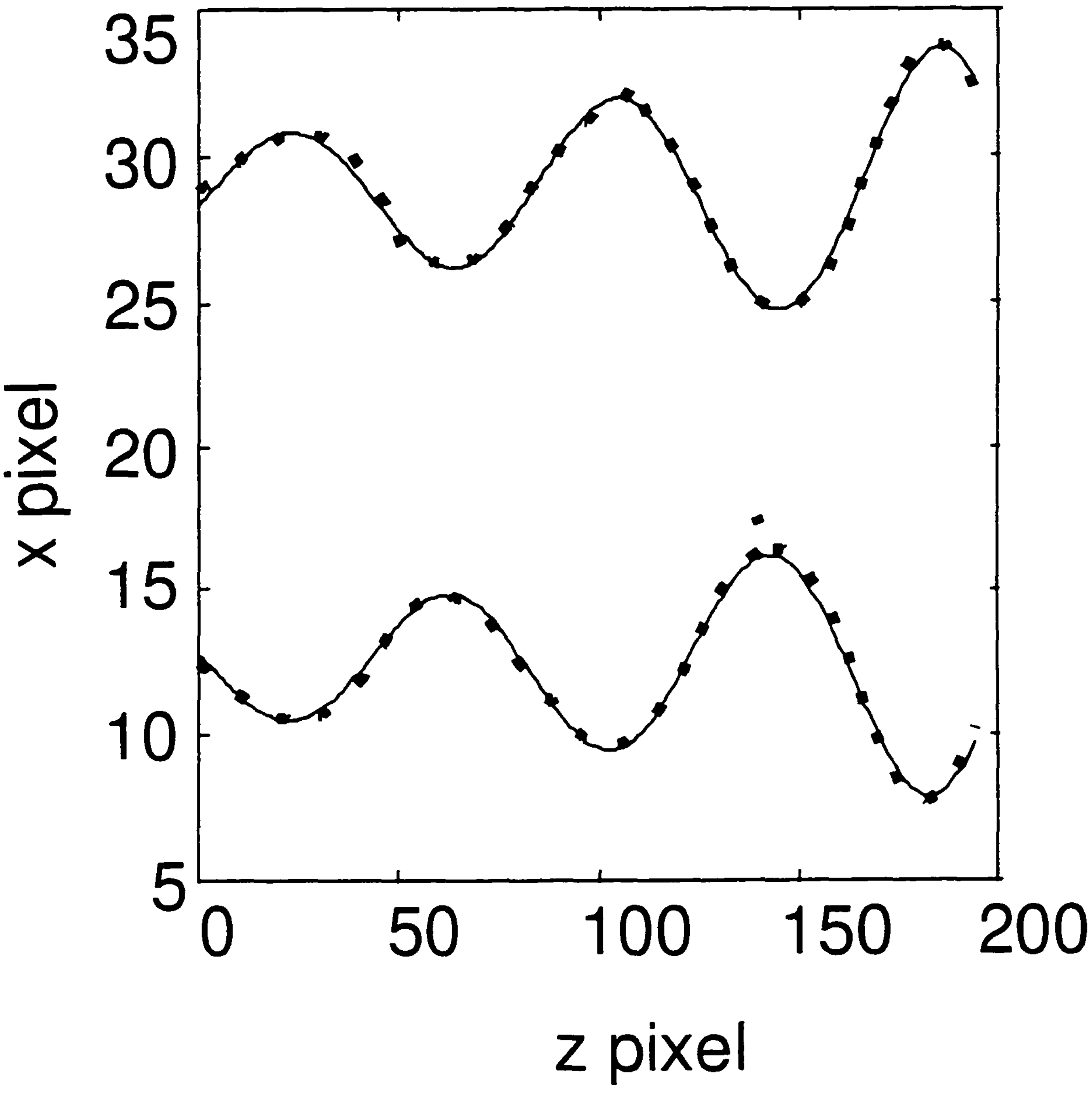

Figure 6. The digitized image along with the best fit of the jet interface at frequency of 400 Hz

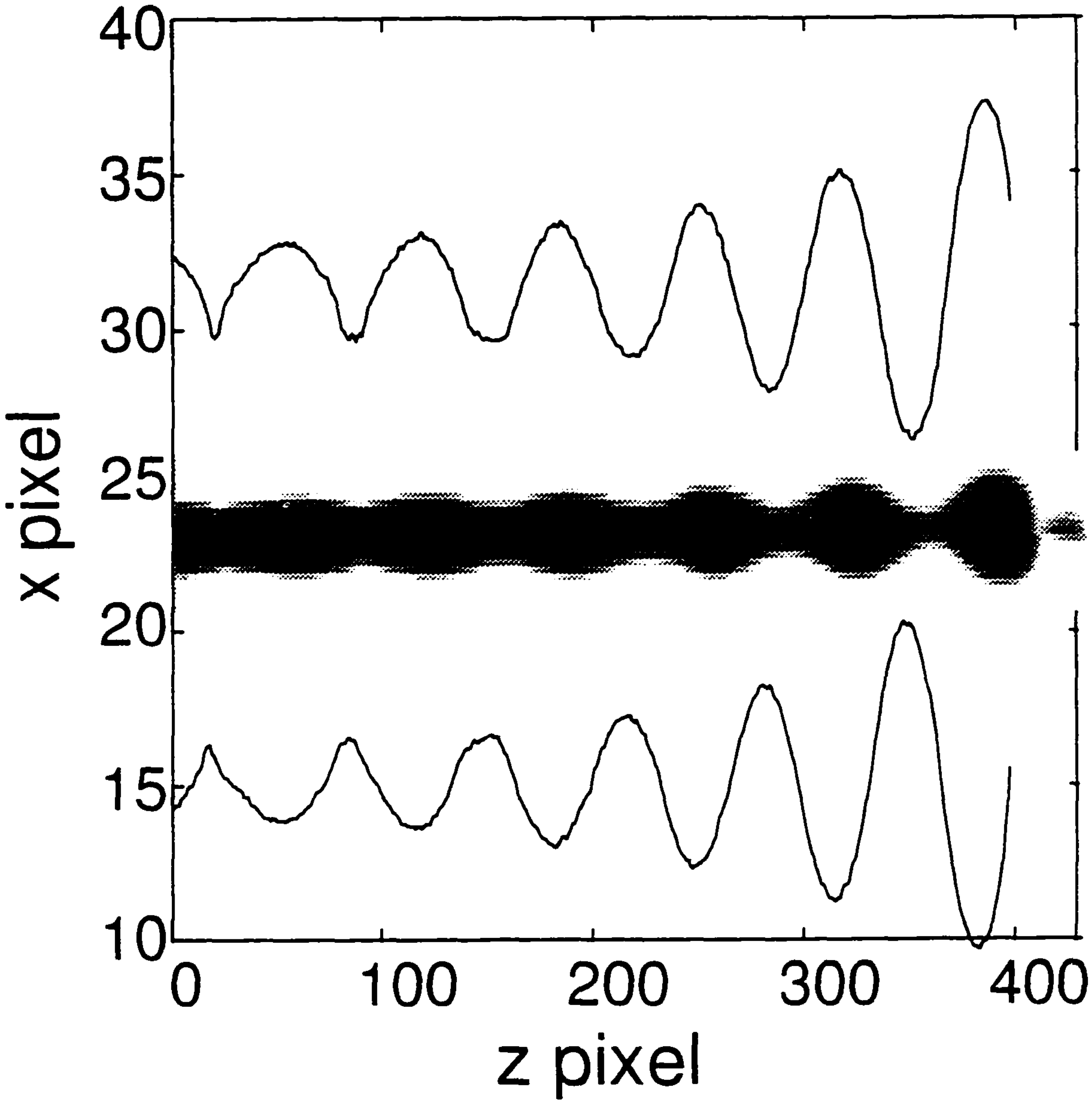

Figure 7. The jet image and the digitized image. Frequency= 500 Hz

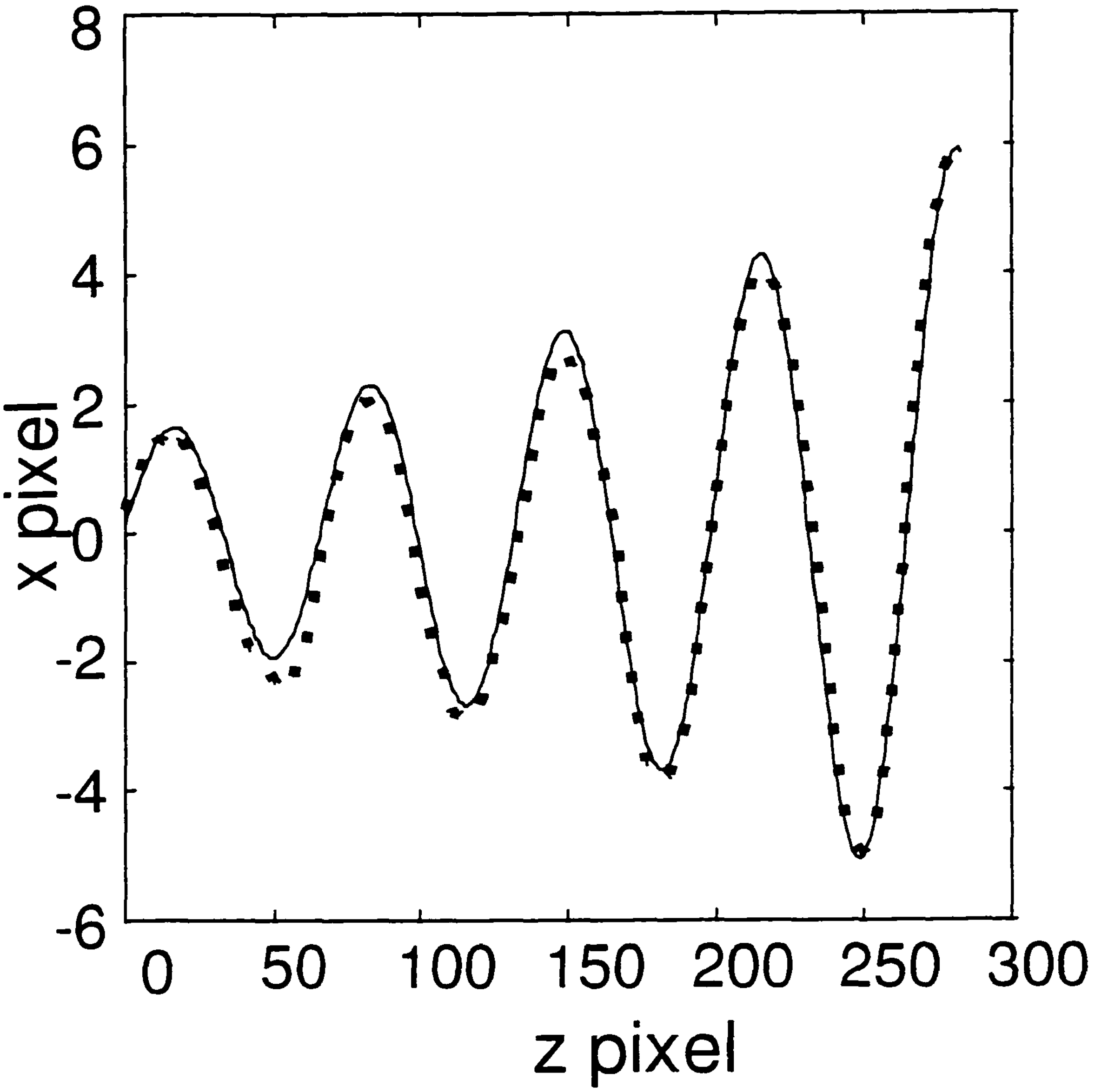

Figure 8(a). The digitized image of the interface along with the best fit at frequency of 500 Hz

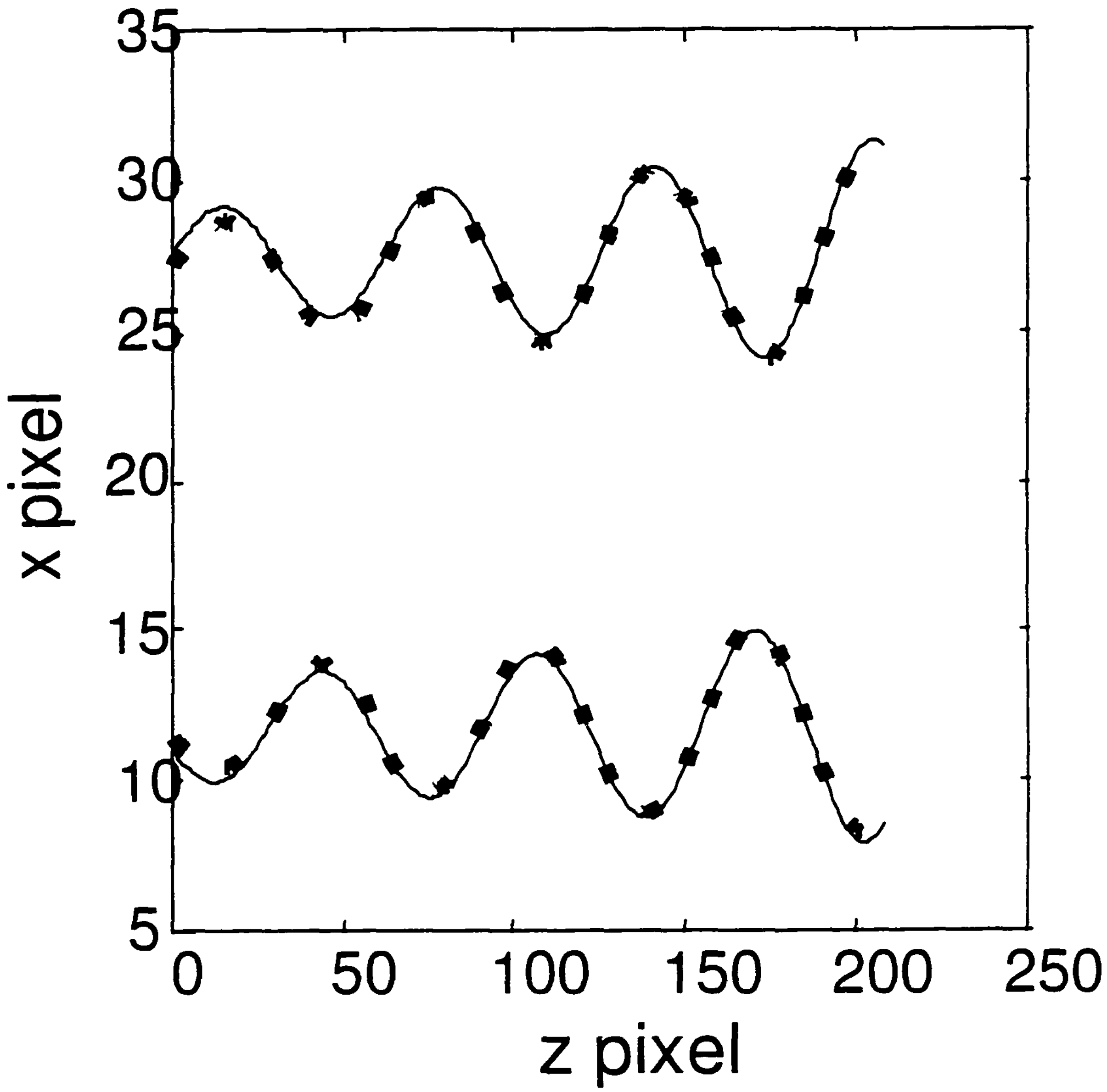

Figure 8(b). The digitized image along with the best fit of the jet interface at frequency of 500 Hz

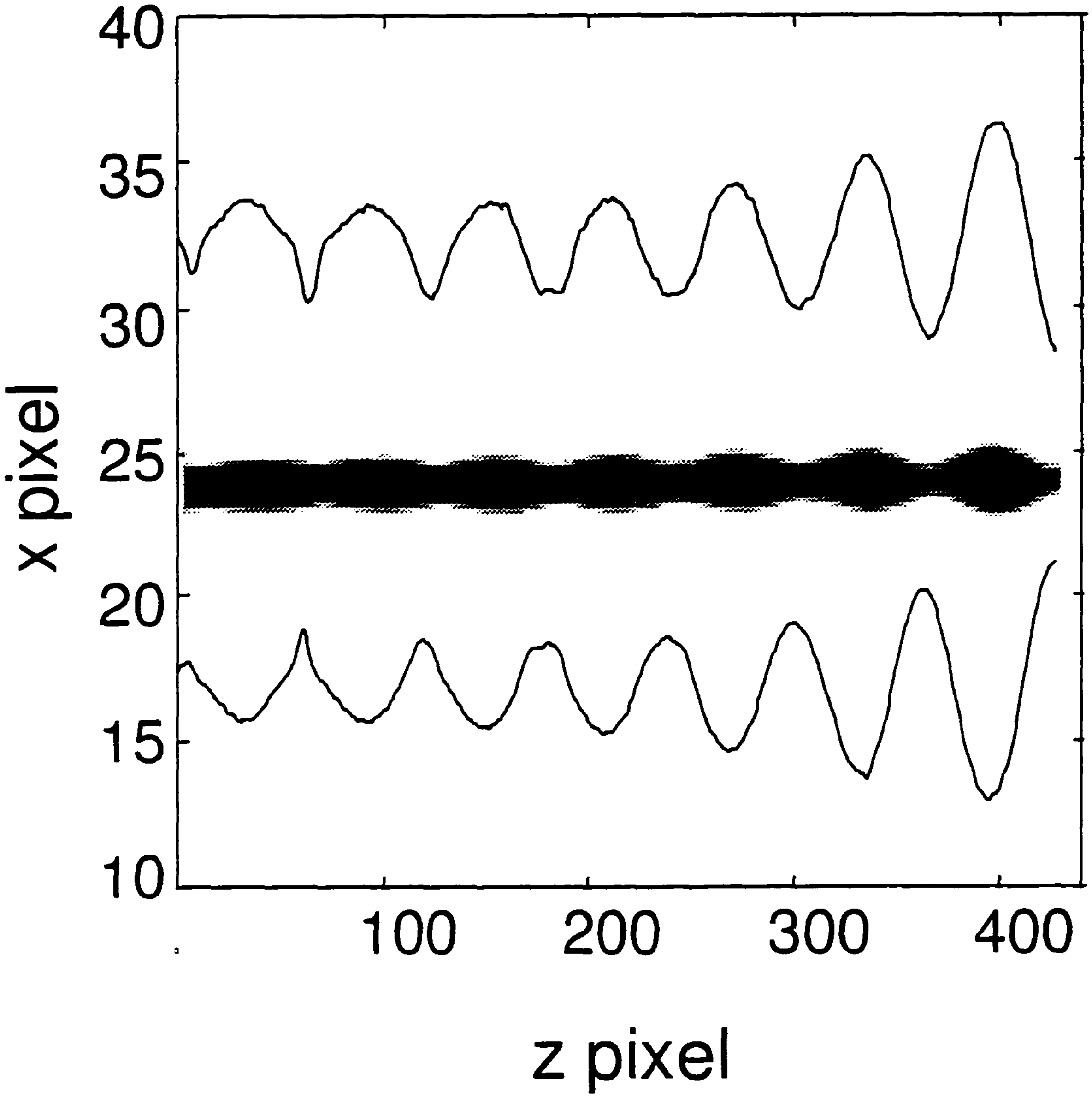

Figure 9. The jet image and the digitized image. Frequency= 600

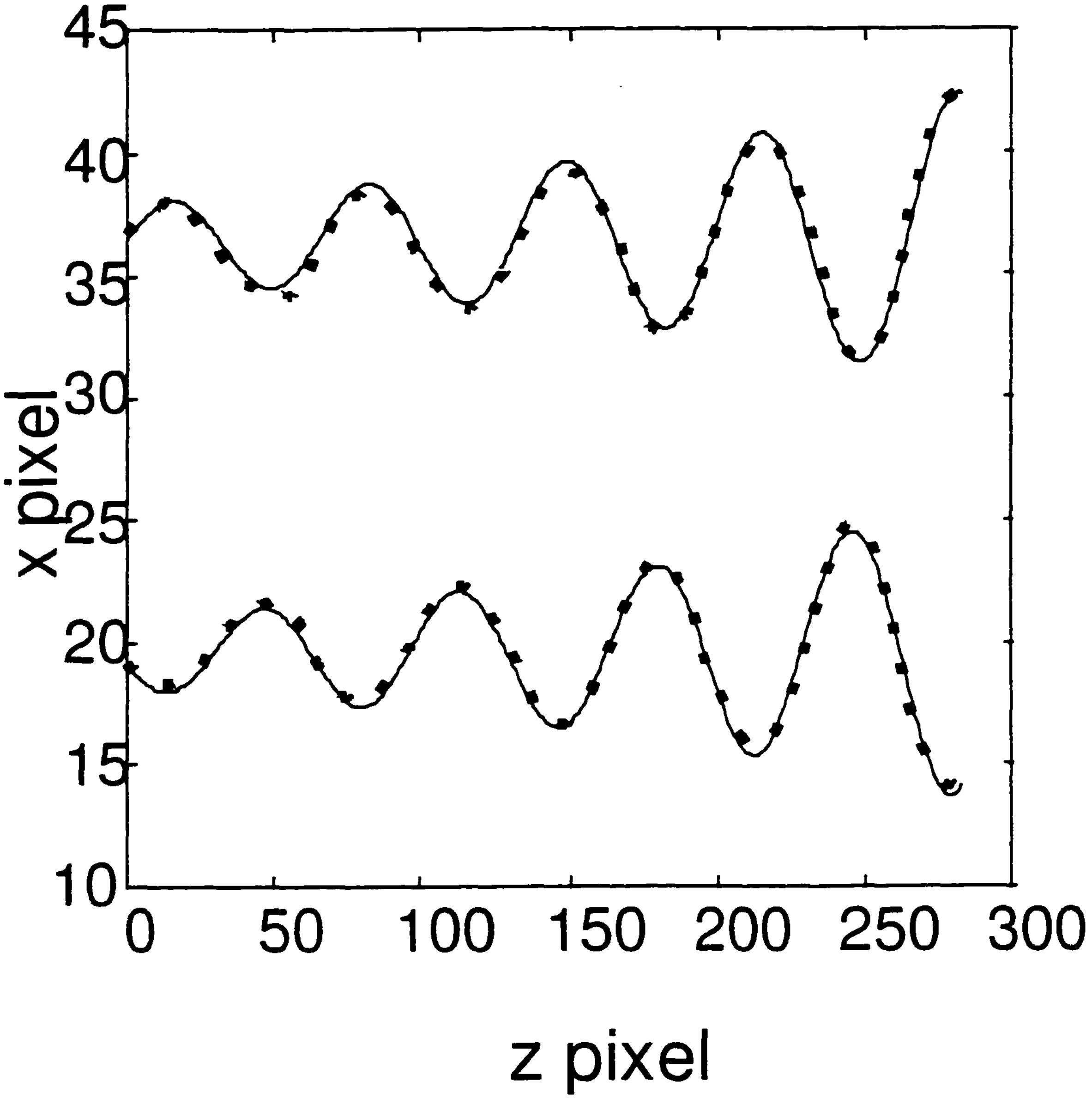

Figure 10. The digitized image along with the best fit of the jet interface at frequency of 600 Hz

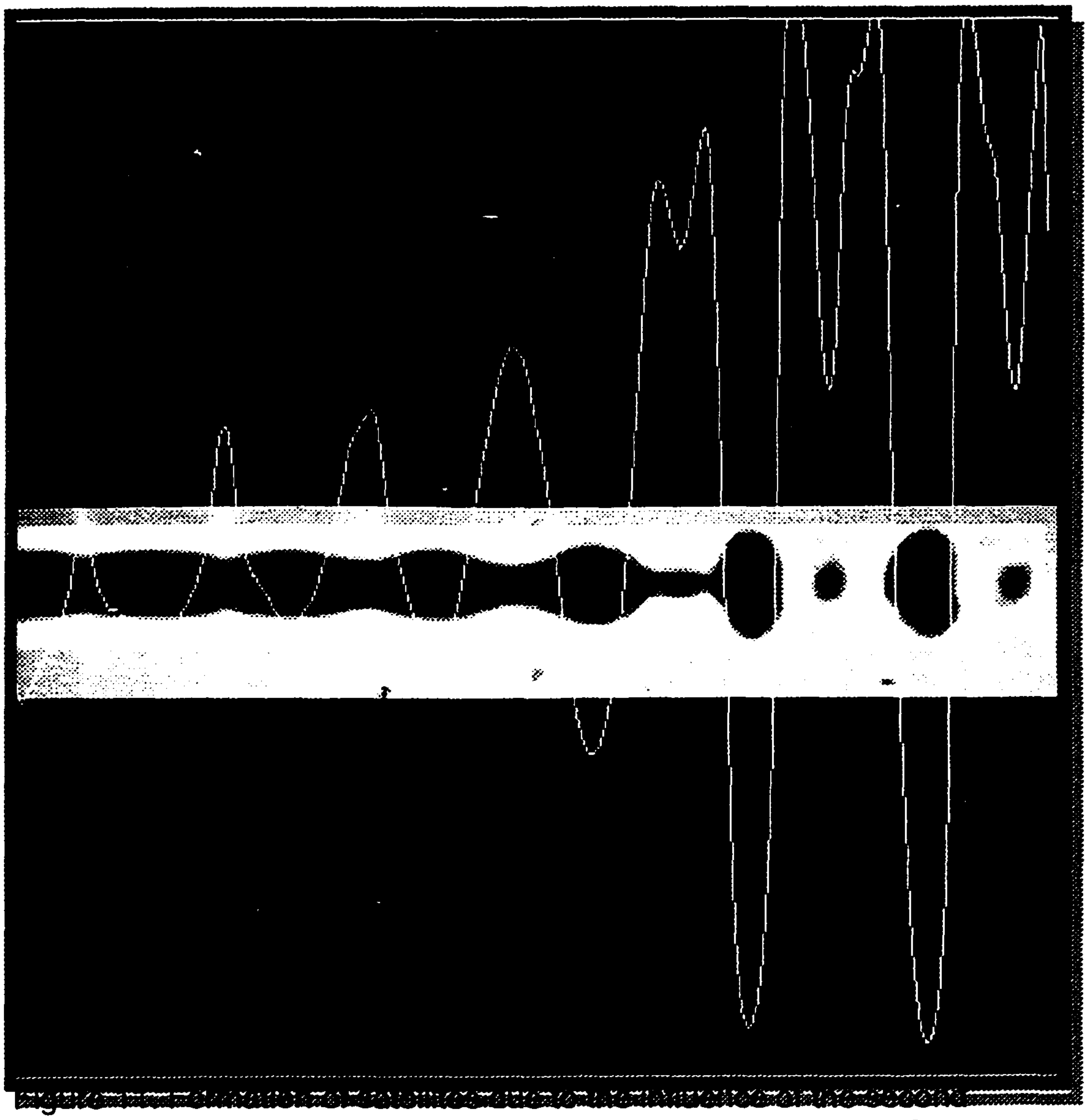

[illegible] of satellites due to the influence of the second harmonic of the imposed frequency. The white line is the sum of the intensity of all the pixelsin the vertical direction as a function of the horizontal location

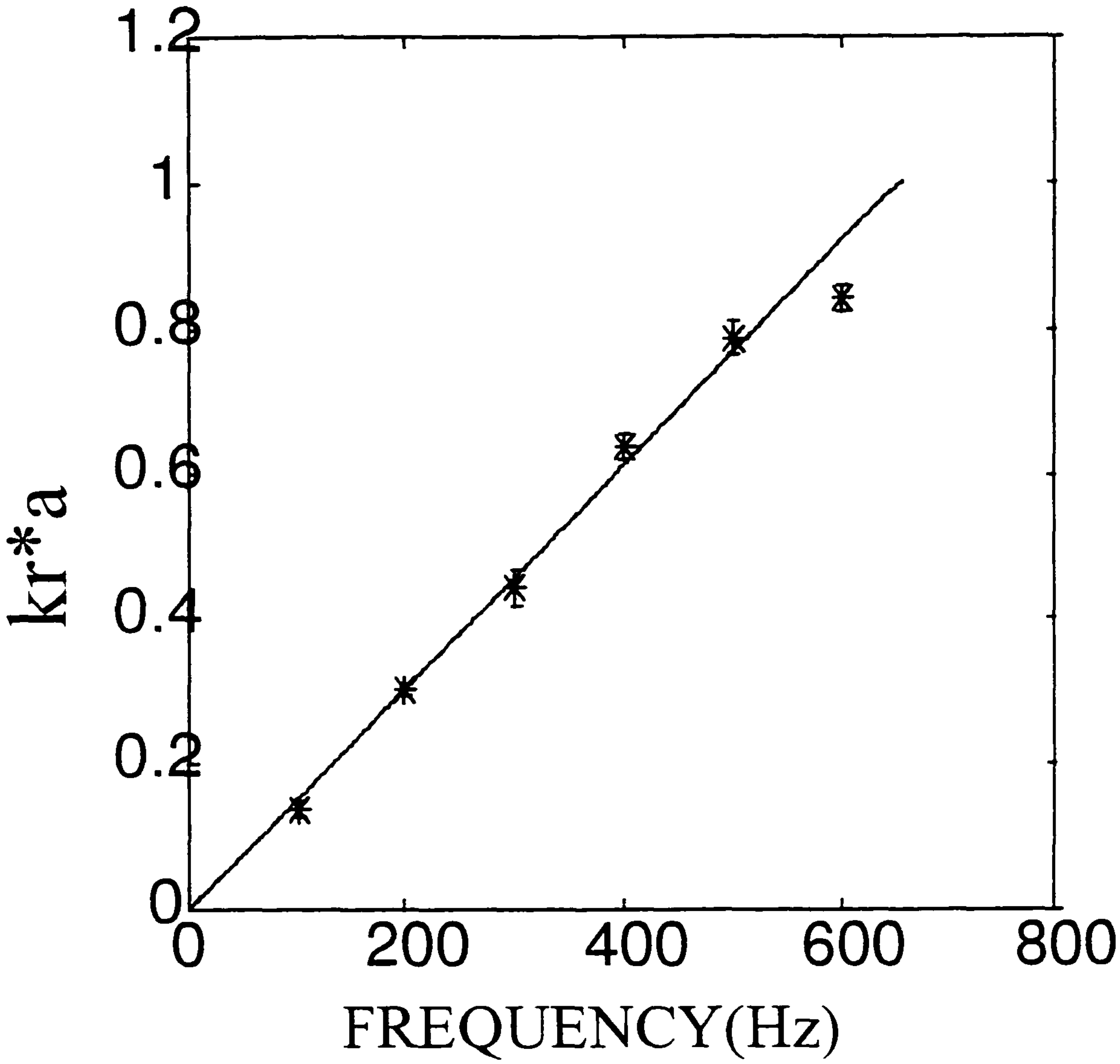

Figure 12. Comparison of the theoretical and the experimental wavenumbers (k,) as a function of frequency at V=lm/s

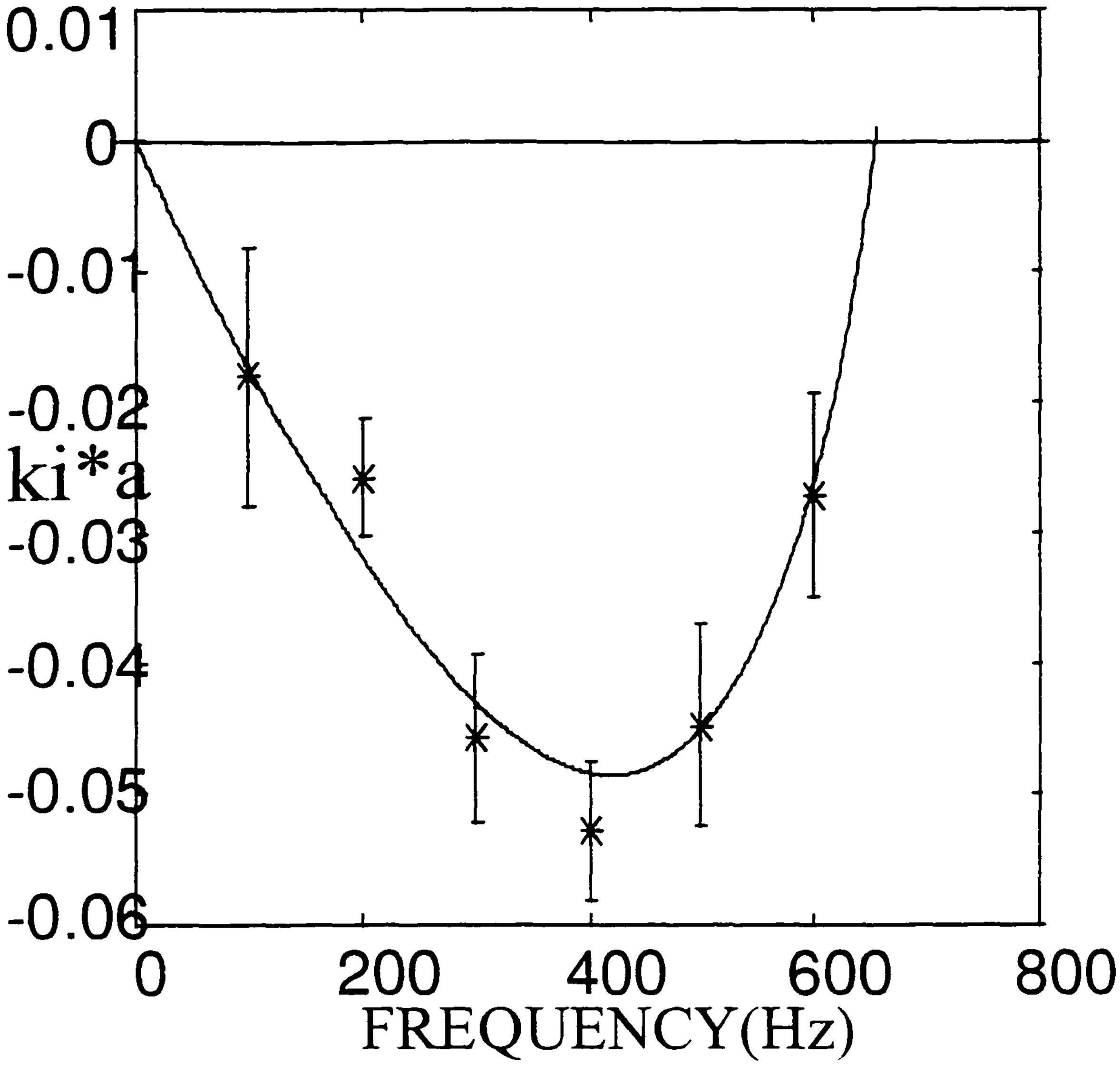

Figure 13. Comparison of the theoretical and the experimental growthrates (ki) as a function of frequency at V=l m/s

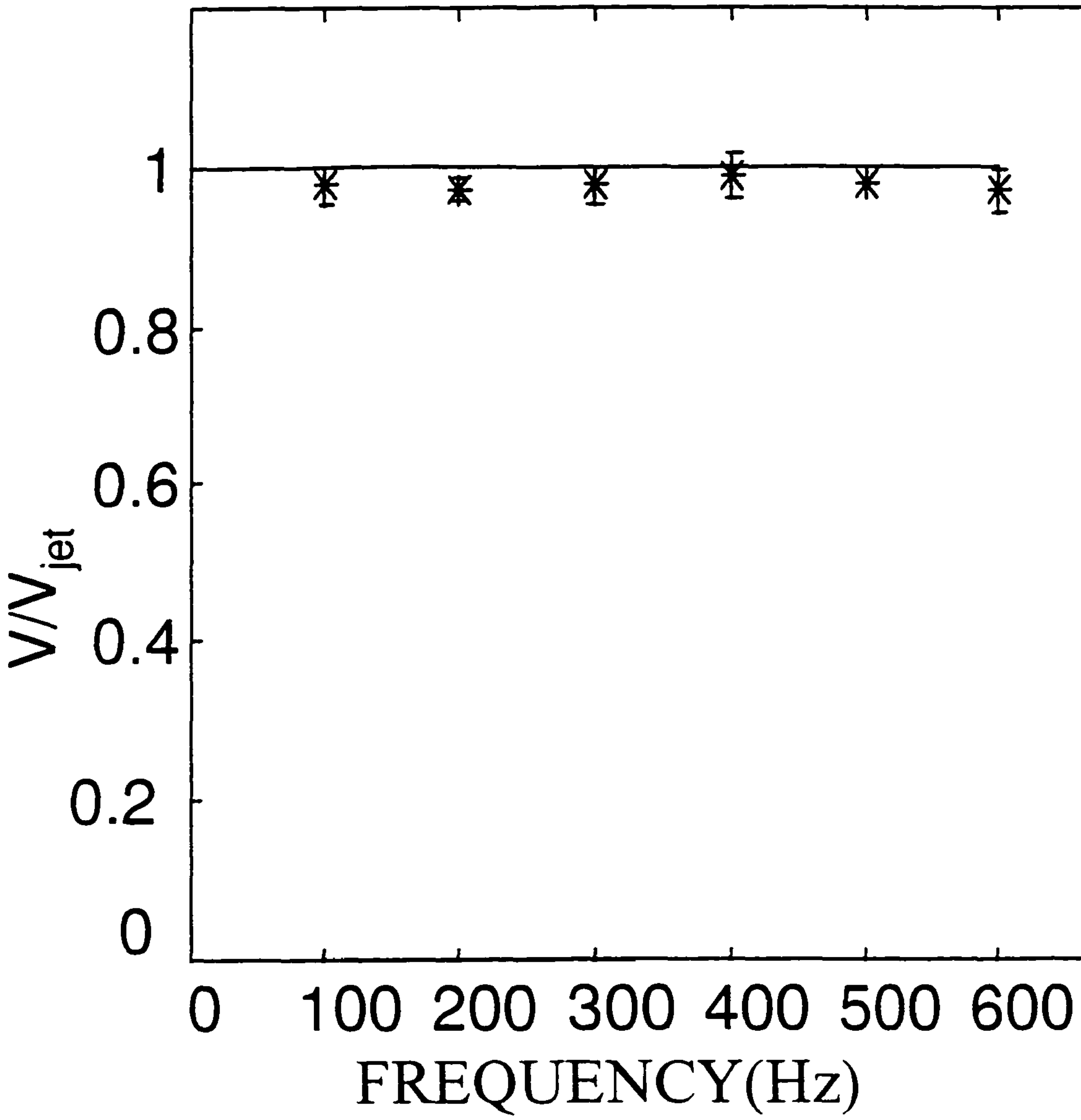

Figure 14. Comparison of the jet and the wave velocity as a function of frequency at V=lm/s

AVERAGE OF 20 IMAGES
SEPARATEDBY 1 PERIOD (1/300s)

Figure 15. Average of 20 images separated by 1 period (1/300 s)
to show the periodicity in the jet profile

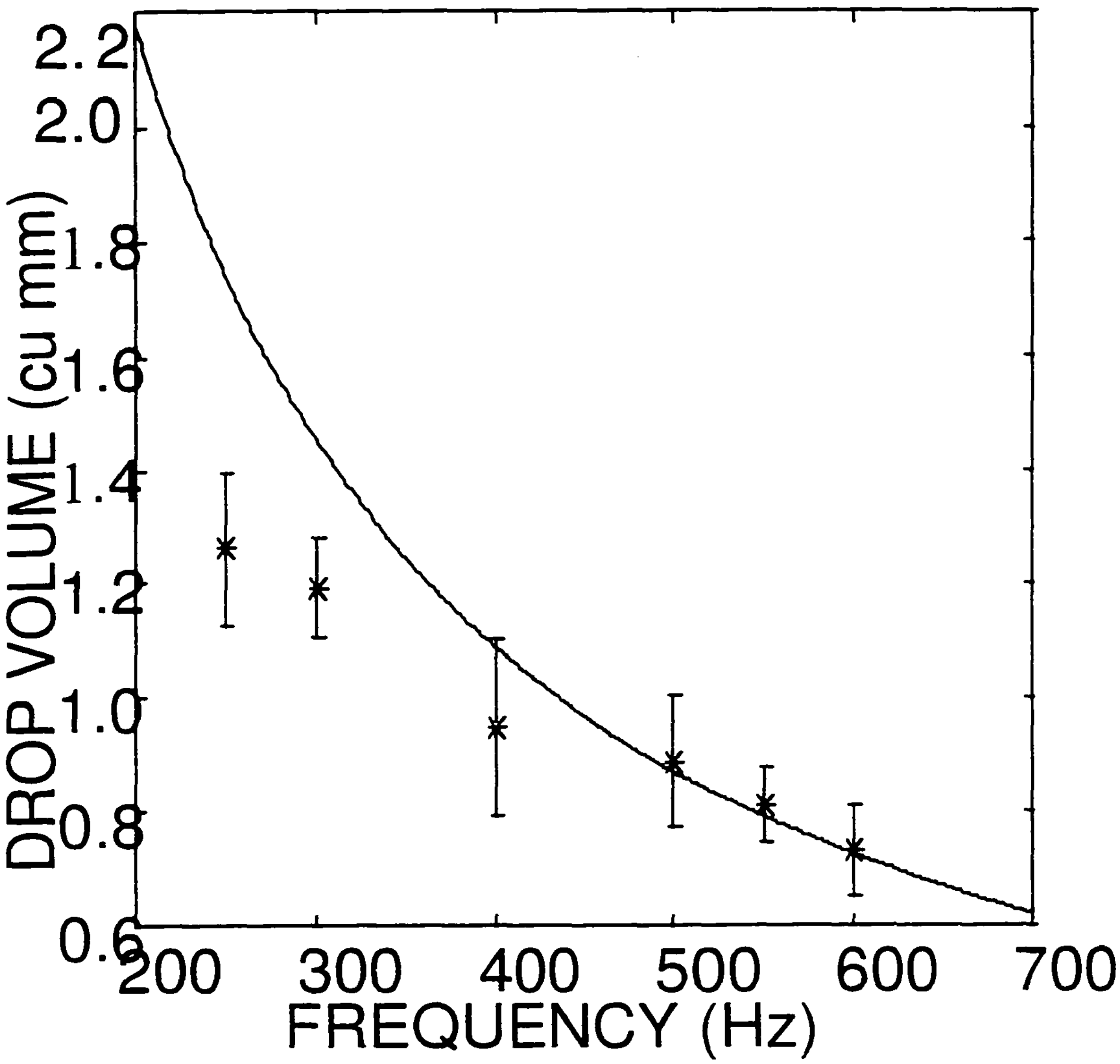

Figure 16. Comparison of the drop volume and the volume contained in one wavelength of the disturbance ($\pi R^2\lambda$) as a function of frequency

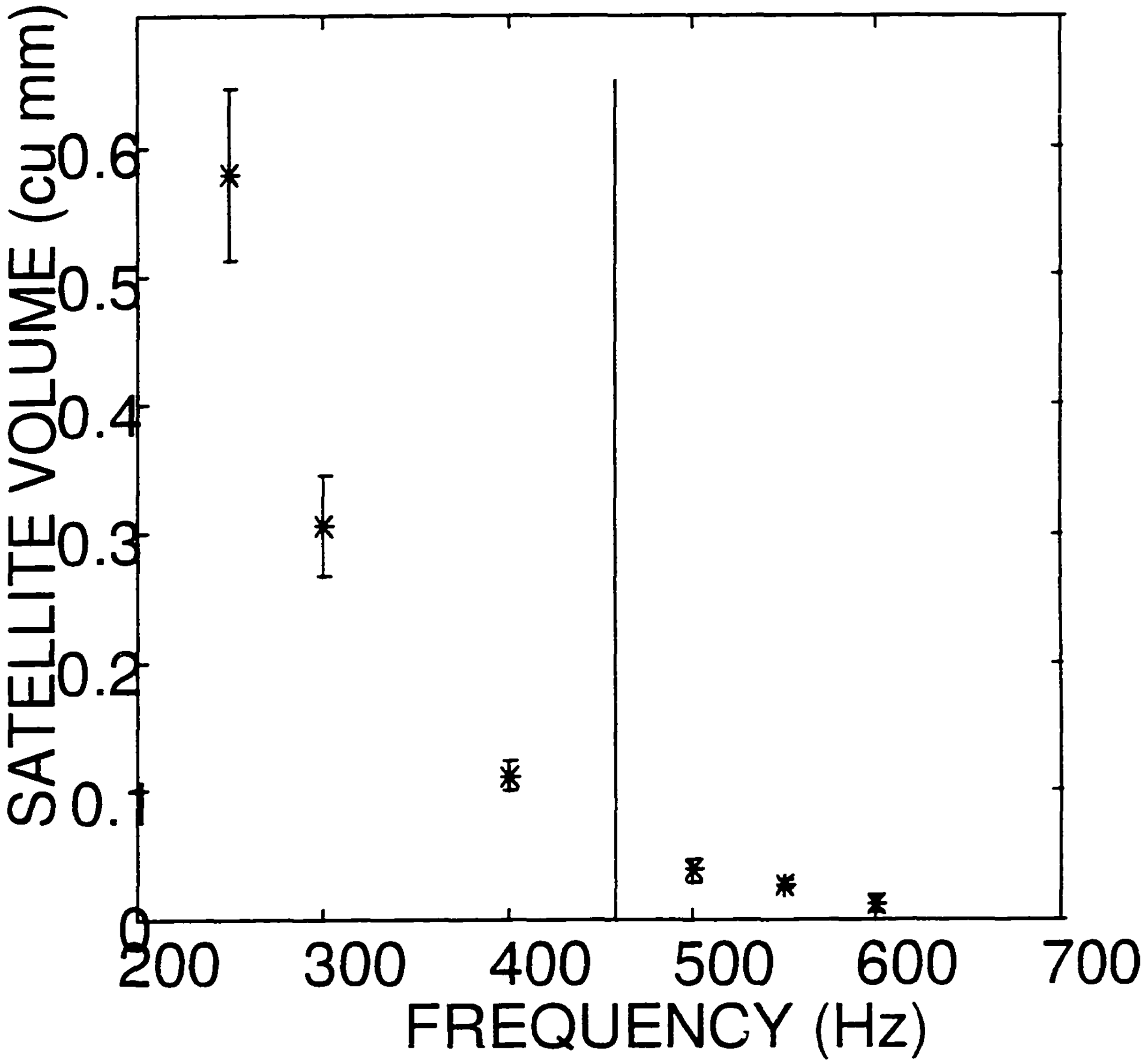

Figure 17. Satellite volume as a function of frequency. The vertical line denotes the transition from satellites to no-satellites according to a theory developed by Chaudhary and Redekopp

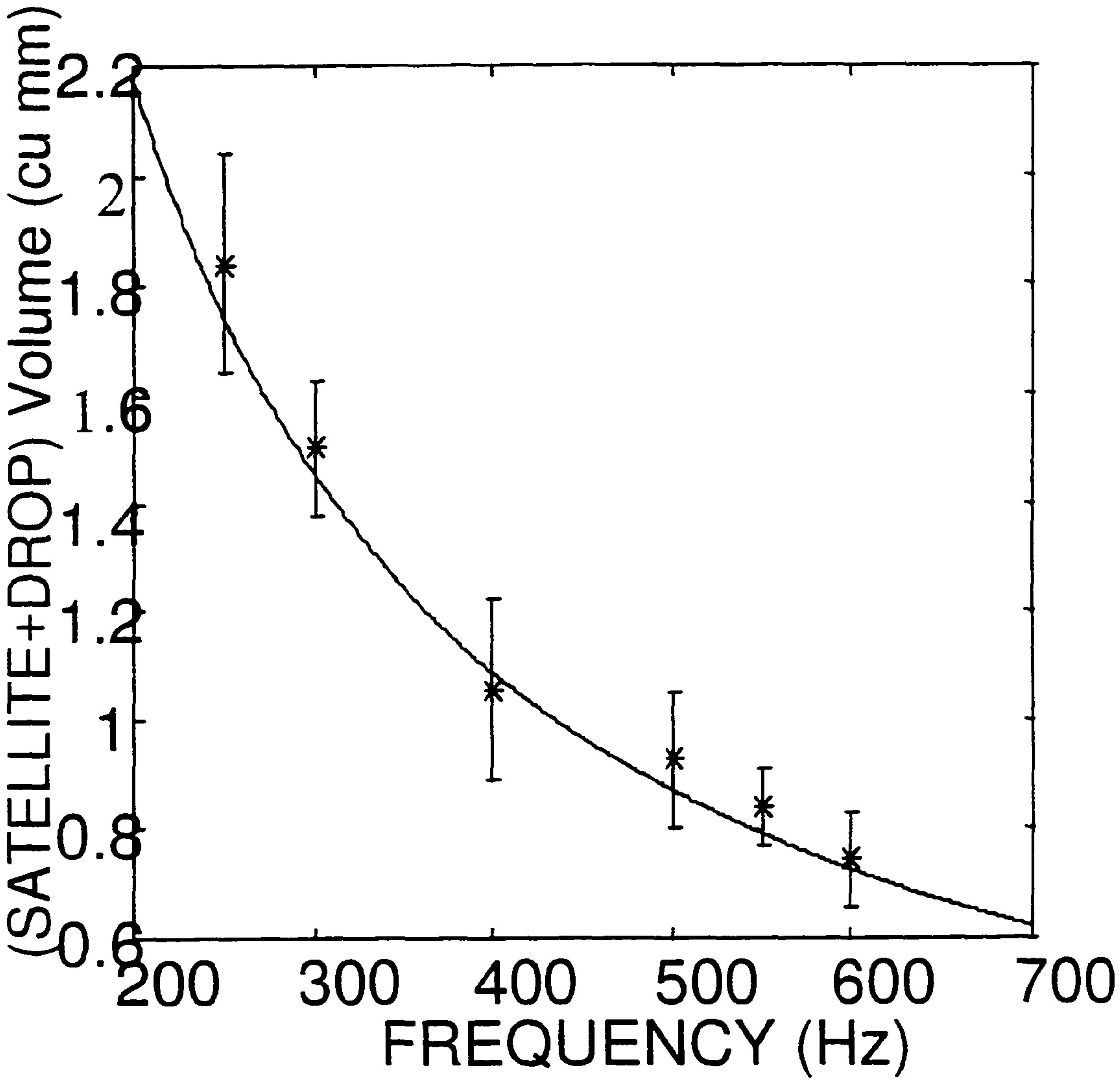

Figure 18. Comparison of the drop volume+satellite volume and the volume contained in one wavelength of the disturbance ($\pi R^2 \lambda$) as a function of frequency

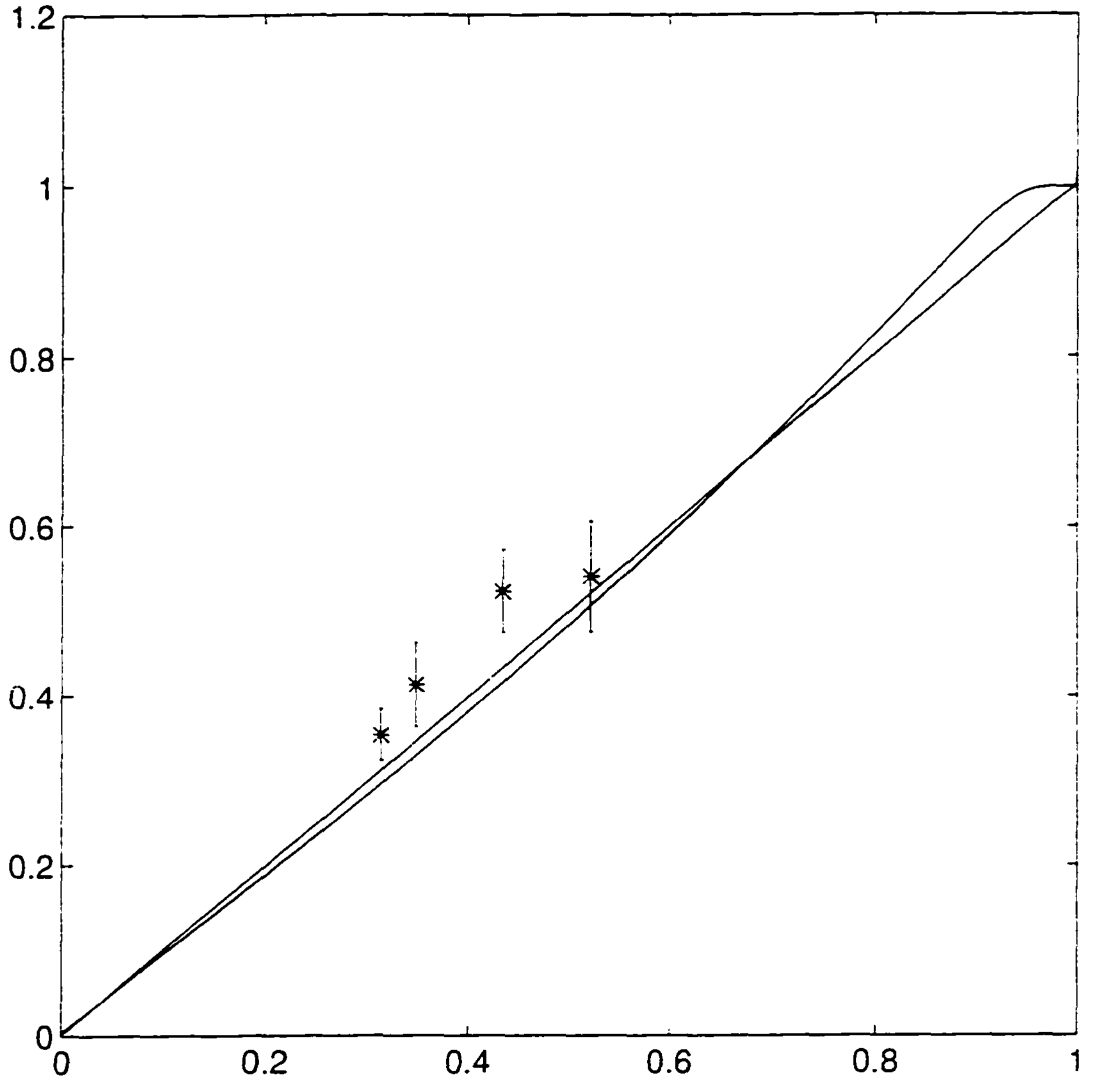

Figure 19. Comparison of the theoretical and the experimental wavenumbers (k_r) as a function of dimensionless frequency at V=0.6 m/s

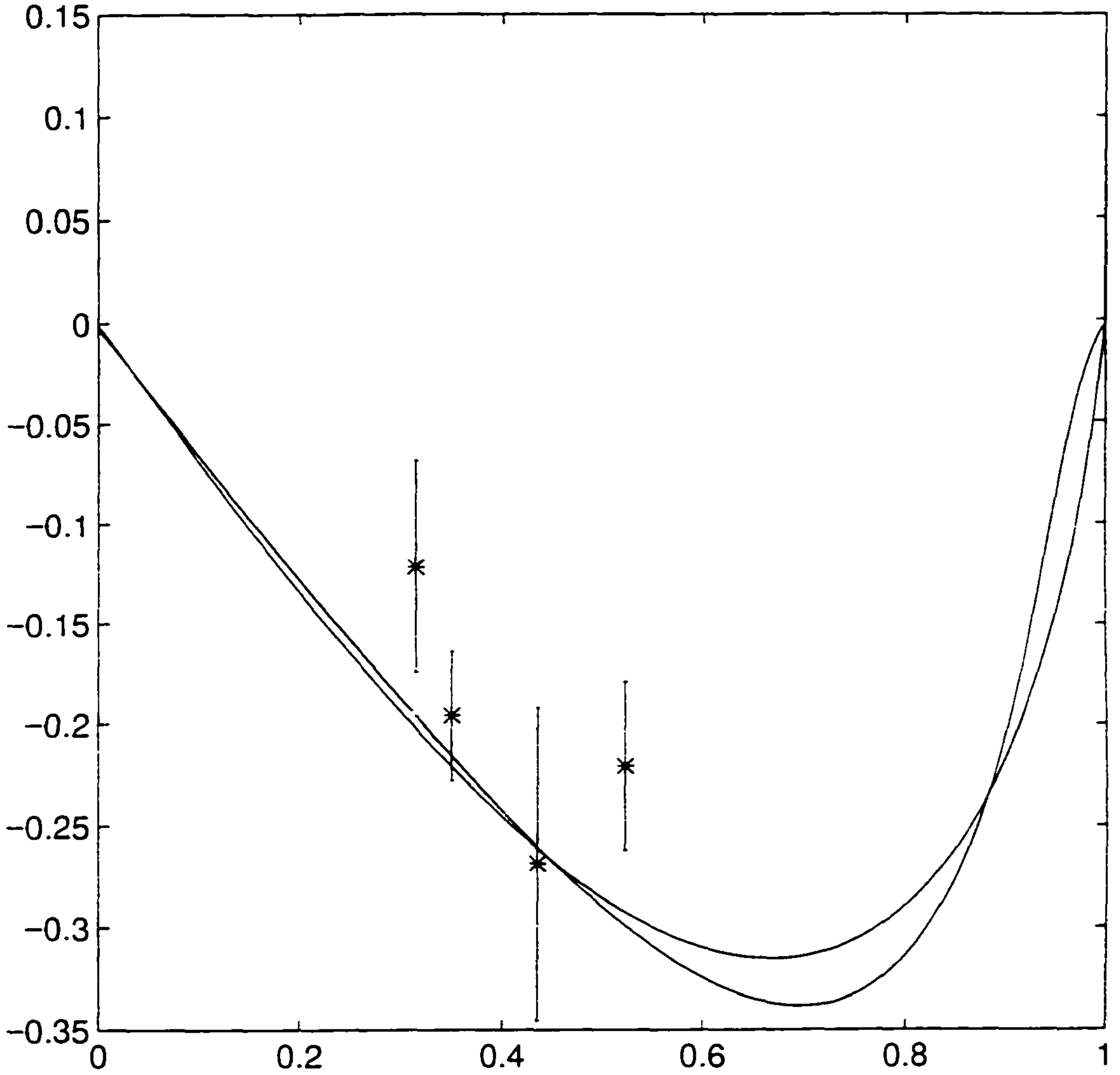

Figure 20. Comparison of the theoretical and the experimental growthrates (k_i) as a function of dimensionless frequency at V=0.6 m/s

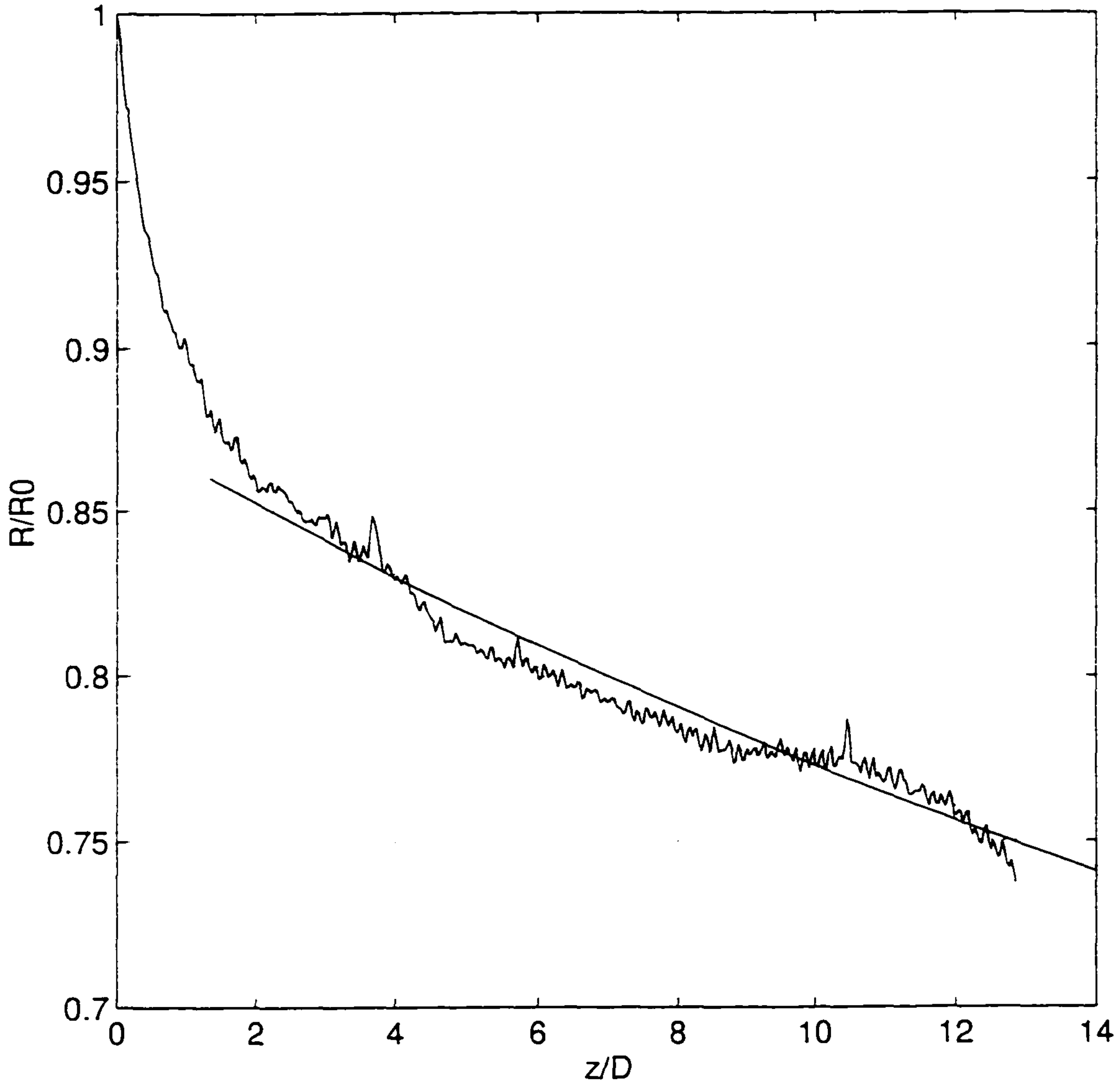

Figure 21. Normalized Jet radius as a function of the axial distance from the needle exit. The plot shows the effect of relaxation in velocity profile to plug flow as the jet exits the nozzle and the further reduction in radius due to the effect of gravity. The solid line is the theoretical prediction of the effect of gravity

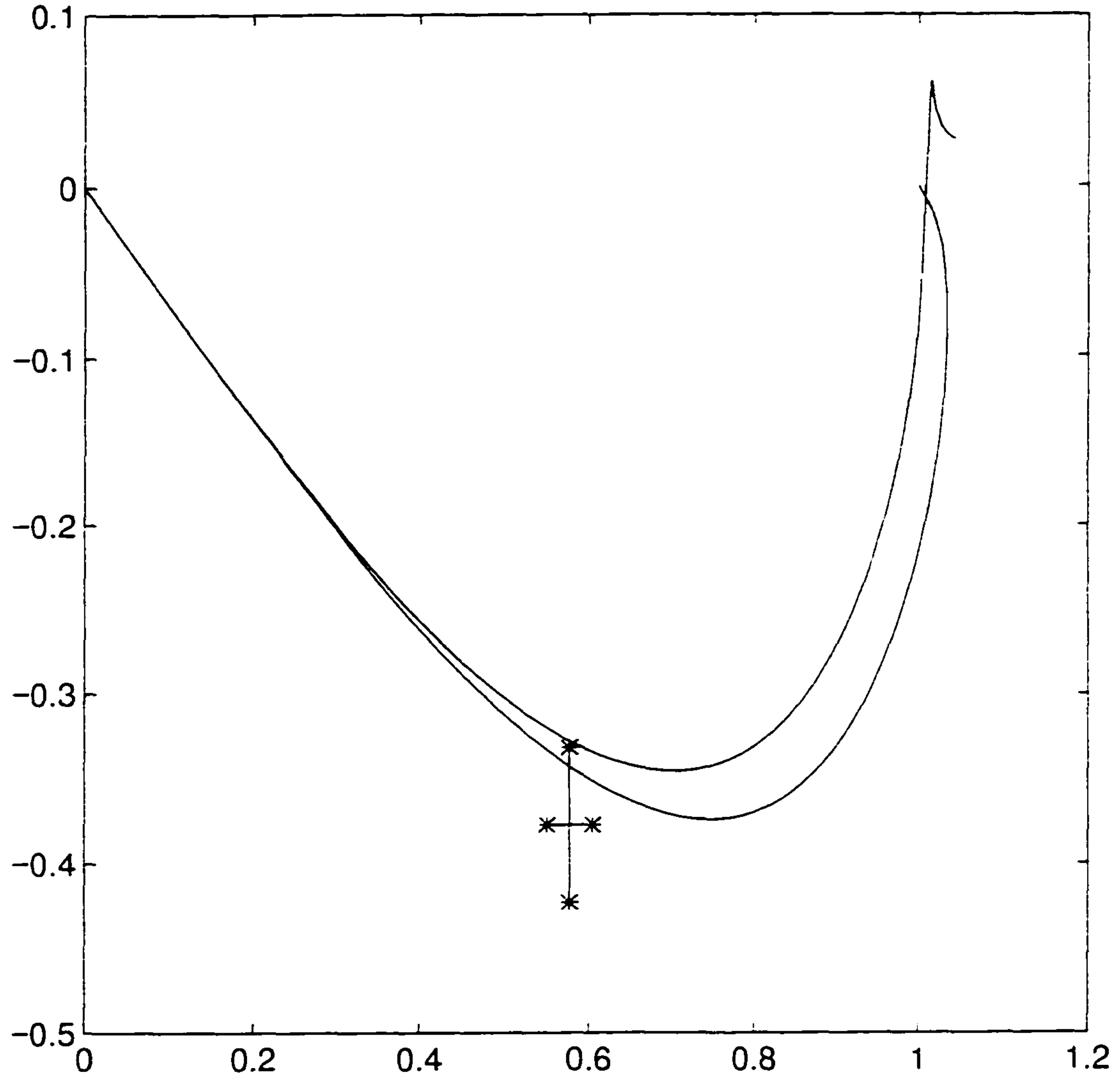

Figure 22. Comparison of the fastest growing convective wave in the experiment and the theoretical predictions based on the spatial and the temporal theories. The lower curve is the spatial prediction. Fluid: Water, Velocity =l m/s

CHAPTER 6

EXPERIMENTAL MANIFESTATION OF ABSOLUTE INSTABILITY IN A SINGLE JET

I. Introduction

The linear stability analysis of a single jet emerging from a nozzle predicts that the stability characteristics depend strongly on the Weber number. There are three regimes in Weber number and the jet behavior is different in each of the three regimes. At very high velocity the disturbances picked up at the nozzle tip convect downstream with the jet velocity. These disturbances grow without any dispersion. In such a scenario the temporal analysis is enough to predict the break up characteristics, namely, break up size and break up length. On lowering the Weber number, these waves begin to disperse as they grow and travel downstream. In this regime one needs to perform a spatial analysis to obtain the stability characteristics. On further lowering the Weber number below a critical value, the jet becomes absolutely unstable, i.e., time periodic disturbances introduced in the jet grow exponentially in time at long times in the linear regime at all spatial locations.

There have been theoretical studies of numerous fluid mechanics problems, which show absolutely unstable behavior. Absolute instability has been shown to exist in; the boundary-layer over a rotating plate (Cooper and Carpenter 1997), (Lingwood 1997b); supersonic shear layer (Lee and Morris

1997); Rayleigh-Benard convection in time-periodic shear flow (Li and Kelly 1997); viscous liquid curtains (Teng et al. 1997); Ekman layer (Lingwood 1997a); Plasma wave guide (Ogura et al. 1992); Couette-Taylor flow with an axial flow (Tsampret and Steinberg 1991); jets (Yakunenko 1995), (Leib and Goldstein 1986a), (Leib and Goldstein 1986b), (Lin and Lian 1989), (Lim and Redekopp 1998), (Shugai and Yakubenko 1997). This list is far from exhaustive. Of all the problems mentioned above, the absolute instability in jets has certainly received the most attention.

While there have been many theoretical studies of absolute instability in the fluid mechanics literature, it is surprising that there are very few experimental studies devoted to observing absolute instability. The only two experimental studies of which we are aware are of a single jet in air (Vihinen et al. 1997) and of a rotating disc boundary-layer flow (Lingwood 1996). Vihinen et. al. (1997) conducted experiments in a drop tower to eliminate the effect of gravity. On lowering the Weber number, they observed a transition from the convective instability in which the jet breaks at some spatial location downstream to another regime in which the disturbances propagate upwards and the jet breaks into two parts, the part next to the nozzle which recoils to form a pendant and the other half that travels downstream and breaks into drops. They take the upstream propagation as a proof of the transition to absolute instability. However, the upstream propagation is not very evident in the pictures. In addition, if the jet became absolutely unstable it is not clear why it caused the break up into two halves, one half moving upstream and the other half continuing to move downstream. This change could be a transition to the dripping regime in which the drop at the nozzle tip grows as a sphere, which is an exact solution of the static Young-Laplace equation in the absence of gravity. However, it is clear from the above study that the reduction in Weber number resulted in a completely different break up configuration. This study (Vihinen et al.) is the first attempt to verify that such a change occurs. Our experimental study is aimed at resolving some of the issues mentioned above. In addition Vihinen et. al. (1997) performed their experiments in the absence of gravity at very low Reynolds and Weber numbers. Our experiments are conducted in the presence of gravity at comparatively much higher Reynolds and Weber numbers. In principle, such an experimental study should be conducted in the absence of gravity but we believe that its presence does not significantly alter the results of our experiments. Before going to the experimental section we would like to discuss the various salient points of absolute instability predicted by theory to ascertain it's distinguishing features from the convective instability. This will tell us what to look for experimentally.

II ABSOLUTE INSTABILITY

Following Briggs (Briggs 1964) we write the Greens function for the single jet as,

$$G(z,t) = \frac{1}{4\pi^2 i}\int_{c-i\infty}^{c+i\infty}\int_{-\infty}^{\infty}\frac{e^{ikz-st}}{f(k,s)}dkds \tag{1}$$

where f(k,s) is the dispersion equation. The Greens function gives the response of the system to a pulse input $\delta(z-z_0)\delta(t-t_0)$. In (1) $z_0=t_0=0$. The response for any other input can easily be found by convoluting the input with the Greens function.

The dispersion equation for a viscous single jet is;

$$f(s,k) = J(k^2 - 1)k I_1(k) I_1(\beta) - 4k^3 \beta I_1(k)(I_0(\beta) - \frac{I_1(\beta)}{\beta}) + 2k^2(I_0(k) - \frac{I_1(k)}{k})(\bar{s} + 2k^2) I_1(\beta) + \bar{s} I_0(k) I_1(\beta)(\bar{s} + 2k^2) \tag{2}$$

where $\beta = \sqrt{k^2 - \bar{s}}$, $\bar{s} = s + ikV$, V is the jet velocity, $J=\rho\sigma R/\mu^2$ and R is the jet radius.

Performing the Fourier integral by closing the contour in the upper half k-plane for z>0 and using the Residue theorem gives,

$$G(z,t) = \frac{1}{2\pi} \int_{c-i\infty}^{c+i\infty} \frac{e^{ik(s)z-st}}{\left.\frac{\partial f}{\partial k}\right|_{s,k(s)}} ds \tag{3}$$

where f(s,k(s))=0.

Merging of two k(s) roots in the k plane gives rise to a non-removable singularity and a branch cut in the s plane. If the real part of s(k) is positive at the point of merger and the two merging roots lie in opposite k halves (above and below the real k line) for large s_r, the system is absolutely unstable. The long time behavior of (3) at long times for a finite z can be evaluated using the method of steepest descent,

$$G(z,t) \sim \frac{1}{2\sqrt{\pi t}} \left.\frac{e^{ikz-st}}{\sqrt{2f_s f_{kk}}}\right|_{s_a,k_a} \tag{4}$$

where k_a is the point of merger in the k plane and $s_a=s(k_a)$. Thus, the solution behaves as $\frac{e^{ik_a z - s_a t}}{\sqrt{t}}$. The real part of k_a, k_{ra} characterizes the absolutely unstable waves. We shall show later that there is a significant difference between the theoretical predictions of the wave lengths of the absolutely unstable wave and the fastest growing convective wave. Thus, a measurement of the wave length could serve as a important differentiating parameter between the absolute and the convective waves. For a single jet, numerical simulations show that Real(k_a)>0. Imag(k_a)<0, Real(s_a)>0 and Imag(s_a)<0. This implies that at long time. the disturbances grow in time everywhere and the phase velocity of the absolutely unstable waves =-Imag(s_a)/Real(k_a) is positive. But the phase velocity of the absolutely unstable waves is not a useful property because (4) is valid only at long times. At short times a more useful characteristic is the velocity of propagation of a wave packet. If the jet is convectively unstable a wave packet or a pulse introduced in the jet grows as it convects. Thus if an observer is fixed at a spatial location. the disturbance passes him by and the disturbance finally decays to zero at that location. However, if the jet is absolutely unstable the wave packet grows and spreads in both directions; hence the disturbance blows up in time everywhere. The wave packet has a front and a back end. In convective instability the velocities of both the front and the back ends are in the same direction, so the wave packet convects as it grows, whereas, in absolute instability the two ends move in opposite directions and hence the wave packet propagates both ways. Following Briggs (Briggs 1964), Triantafyllou (Triantafyllou 1992), we use the above fact is used to determine the velocity of propagation of the front and the back ends. In a reference frame moving with a velocity between the velocity of the front end and the velocity of the back end, the instability will always be convective. Thus, the velocity of the front and the back ends are the velocities of the reference frame at which the transition from convective to absolute instability takes place for a given jet velocity. In a moving reference frame the dispersion equation stays the same as (2) except that $\bar{s} = s + ik(V - V_r)$ where V_r is the velocity of the reference frame. Note that this is valid only in situations when the disturbance is localized in time. We know that the jet becomes absolutely unstable for $-V_c < V < V_c$. This implies. $V-V_r=\pm V_c$. Therefore, $V_r=V\pm V_c$. The velocity of the front end is $V_f= V+V_c$ and the velocity of the back end is $V_b= V-V_c$. If $V<V_c$, V_f and V_b have the same sign which signifies convective instability and if $V>V_c$, V_f and V_b have the opposite sign which signifies absolute instability. This provides another interesting result. $V_c=(V_f+V_b)/2$. Thus the critical velocity can be found by measuring the velocity of the front and the back ends at any jet velocity. At very high velocity. $V>>V_c$, the velocity of the front end is almost the same as the back end and hence there is no dispersion.

An ideal experiment to observe absolute instability would be to create a jet with a Weber number higher than the critical value and impose a disturbance localized in space and time, somewhere in the middle of the jet. This disturbance (wave packet) should grow in space and disperse as it convects downstream. The jet should not be decelerated into the absolutely unstable regime. The disturbance is now expected to grow in time as well and the wave packet should move upstream as well as downstream. Unfortunately such an idealized experiment is almost impossible to perform for a variety of reasons. First, the jet always picks up noise as exits the nozzle. This noise will interfere with the imposed disturbance and might cause the jet break up before the jet reaches the source of imposed disturbance. This is more probable at small velocities because the spatial growth rate becomes very large. Secondly, the attempt to apply a disturbance in the middle might affect the base flow significantly, thereby, rendering the experiment a failure. Thirdly, it is not easy to decelerate the entire jet into the absolutely unstable regime. In addition, gravity acts on the jet and this effect has not been taken into account in the theoretical analysis. Thus, we simplify our experiment by relying on the noise to provide the disturbance. The jet picks up noise not only at the nozzle tip but also while moving through air. This disturbance might propagate both ways signifying absolute instability. In addition we will rely on measuring the wave length to identify the absolutely unstable waves. We will conduct experiments at high Reynolds number so that the critical Weber number is as high as possible. In addition, we will use Water in our experiments because it has a high surface tension and relatively low density so one can achieve the critical Weber number at a relatively higher velocity than most other fluids. The reduction in the jet radius due to the effect of gravity decreases with an increase in jet velocity and hence gravity does not have a considerable influence in our experiments.

III EXPERIMENT

The experimental apparatus is the same as described in the previous chapter. The Weber number is controlled by controlling the flow rate supplied by the pump. In the experiments described below, we do not impose any specific disturbance at the needle tip. However, we verified that imposing the disturbance did not have any noticeable effect on these experiments. In the experiments at high Weber numbers we observe convective growth and break up. The wave length and growth rates agree reasonably with the spatial instability theory. At Weber numbers below the critical, we observed disturbances moving in both directions. Fig (1) shows the disturbances moving upstream. At high Weber numbers disturbances clearly move downstream and the upstream moving disturbances are not present. Vihinen et. al. (1997) also reported observing upstream propagating disturbances and attributed it to absolute instability. Thus, our observations could be the experimental manifestation of absolute instability. To the best of our knowledge, these upstream moving disturbances have not been reported in literature in the presence of gravity at such high Weber and Reynolds numbers.

IV DISCUSSION

(1) ABSOLUTE INSTABILITY

The chief attribute of absolute instability is propagation of a wave packet in both directions. As mentioned above, we observe upstream propagating modes at Weber number below the critical. The wave number of these upstream propagating disturbances is 1.2, which is close to the theoretical wave number of the absolutely unstable waves, which is 1.1. These disturbances do not grow upstream which is also in agreement with the theoretical growth rate of the absolutely unstable modes. However, these disturbances do not grow in time and never cause the break up of jet. This is in contradiction to the absolute instability. This could be because the absolutely unstable waves have wave lengths shorter than the jet circumference and so they are non-linearly stable even though they grow exponentially in the linear regime. This is simply a speculation and one needs to perform a non-linear spatial stability analysis at low Weber numbers to confirm it. The absolute instability has a cutoff Weber number. If these upstream propagating waves are the absolutely unstable waves, they should disappear above the critical Weber number. We started increasing the velocity so observe its effect on these modes. On increasing the velocity these modes disappear from the region near the needle but they are still present near the break up. We increased the Weber number to above the critical value. But these modes still persist near the break up. The theoretical analysis on which we base the critical Weber number neglects the presence of ambient air. Lin and Lian (Lin and Lian 1989) showed that the presence of air increases the critical Weber number and the increase depends on the velocity of the ambient air. We do not have any measurement on the velocity of the ambient air so we cannot quantify this effect. However we note that this could explain why the absolutely unstable modes are present above what we consider as the critical Weber number. The video images of these modes show that they seem to arise out of the break up, i.e.. the forward traveling capillary waves cause the jet to break up and this break up releases/creates the waves which propagate upstream. Thus, the break up is serving as a source of wave packet and since this source is located in the break up region the forward motion of the wave packet cannot be observed. But this raises the question, why is the noise at the needle tip not generated the forward traveling absolutely unstable waves? This could be because the spatial growth rate of the absolutely unstable waves is almost zero. The noise at the needle tip is very small so unless the waves grow spatially they cannot be observed. In addition the time growth of the absolutely unstable waves is small because we are close to the critical Weber number, hence, it might take prohibitively long to observe them near the needle exit. All the above arguments show that the observed backward propagating modes could be the manifestation of absolute instability. However, the proof is not so convincing so as to eliminate all other possibilities. Below we present another plausible explanation for these upstream propagating waves.

(2) IF NOT ABSOLUTE INSTABILITY, THEN WHAT?

This explanation is based on the observation that these modes originate from the break up and are only present near the break up. Also they disappear, as the Weber number becomes very large. They decay as they travel upstream and the decay rate increases with the increase in velocity. This suggests that the break up serves as a source of disturbance of all wave numbers. For this source of disturbance the upstream jet lies in the region $z<z_s$ or $z<0$ if one defines the origin at the source. We now need to consider the stability of the negative half of a doubly infinite jet. The dispersion equation of a single jet is given in eq (1). Fig (2) shows the two solutions of the dispersion equation in the k plane for purely imaginary s ($s=-i\omega$) at two different velocities and at J=3000. At v=1.7 the jet is convectively unstable and at v=1.5 it is absolutely unstable. Above the critical velocity, the mode labeled [1] is included in the inversion for z>0 and the one-labeled [2] is included for z<0. Mode [1] causes the growth for z>0 because k_i is negative, hence, e^{ikz} grows in positive z direction. Mode [2] implies decay in the negative z direction for the same reason. The direction of the arrow marks the direction of increasing frequency. The phase velocity (ω/k_r) is positive for [1], positive for a part of [2] and negative for the rest of [2]. The part of [2] to the right of the curve s=0 (see figure) has a negative phase velocity. We hypothesize that the break up of the jet creates disturbances of large amplitude and of all frequencies. Some of these waves have negative phase velocity (the waves in the region to the right of s=0). These waves propagate upstream but decay because k_i is negative. The one with the slowest decay, i.e., smallest $|k_i|$ is the observable wave. At the conditions corresponding to the experiment, the k_r of the observable waves with negative phase velocity is greater than 3.0. This is clearly not in agreement to the experimental value of 1.2. However as can be seen in the figure the minimum k_r with negative phase velocity (s=0 curve) decreases on reducing the velocity. The theoretical wave length becomes close to the observable values on reducing the velocity in the simulations to 50% of the measured value. If the above explanation of the upstream propagating waves is the correct one, the wave length of these backward propagating waves should reduce with an increase in jet velocity (see figure 2). Experimentally the wave length of the backward propagating waves do not change appreciably with changes in the jet velocity. The curve [2] moves downwards on increasing the jet velocity and thus the minimum $|k_i|$ of the waves moving in the -z direction increase. This results in a faster decay. This is collaborated by the experiments. In our model, we neglect the effect of gravity and that of the ambient air. Addition of these effects might shift the wave lengths corresponding to negative phase velocities to smaller values. However, the big difference in the theoretical and the experimental wave lengths renders the above explanation suspect.

V CONCLUSIONS

At high Weber numbers, the jet is convectively unstable and disturbances only propagate upstream. At Weber number below the critical, the jet becomes absolutely unstable. On lowering the Weber number, but still above the critical Weber number, we begin to see waves propagating both ways. The forward propagating waves are the usual disturbances picked up at the needle tip due to noise. These disturbances grow downstream and cause the jet break up. The break up release waves which propagate upstream and decay. Hence, they are visible only near the break up region. These waves are much shorter than the downstream propagating waves. Infact, they are shorter than the jet circumference. Their wave length is very close to the absolutely unstable waves. The theory of absolute instability provides reasonable explanation for all the observations but not convincing enough to not consider other plausible explanations. We interpret these waves as being introduced at the break up. Thus the upstream jet is like the negative half of the doubly infinite jet. We analyze the negative half of the jet and observe that there is a branch that has a negative phase velocity and a negative k_i. Thus, the waves corresponding to this branch travel and decay in the negative direction. The one that decays the slowest is the observable one in the experiment. However, the wave length of the slowest decaying wave is not close to the experimentally observed wave length.

On further lowering the Weber number we do not see any qualitative change in the break up of the jet. Thus, if we attribute the upstream propagating waves to convective waves with negative phase velocity, we do not observe the break up due to absolute instability. This could be because of a variety of reasons. Firstly, the backward propagating waves that we observe could be the absolutely unstable waves. They may be non-linearly stabilized and hence we do not see them growing in time. The theory may not predict the critical velocity for the transition to absolute instability and thus these waves persist at velocities higher than the predicted critical velocity. The motion of ambient air. which we neglected, also increases the critical Weber number. Secondly, in our analysis we neglect the effect of gravity. The gravity effects are negligible at high Weber numbers but they become increasingly important at lower velocities. which implies low Weber numbers. Thus, the gravity is accelerating the jet and this might bring it out of the absolute instability regime. Thirdly, at small Weber numbers, the liquid starts to drip out of the needle. Theory predicts a transition to absolute instability above the velocity at which we experimentally observed dripping but the theoretical prediction might not be very accurate and the actual critical velocity might be below the velocity at which dripping starts. In that case the absolute instability cannot be observed. Some authors have speculated that the 'dripping' might be caused due to absolute instability (Lin and Lian 1989). (Monkewitz 1990). This does not seem probable for the following reason: when the liquid is dripping there is no base state of a jet on which one performs the stability analysis. Thus, the theory based on a base state that does not exist at all cannot be expected to predict the experiments. Interestingly, in our experiments we found a significant hysteresis in the transition from dripping to jetting, i.e., if one starts with a dripping needle and increases the velocity, the velocity at which jetting starts is different from the one at which the jet transforms to a dripping needle on reducing the velocity.

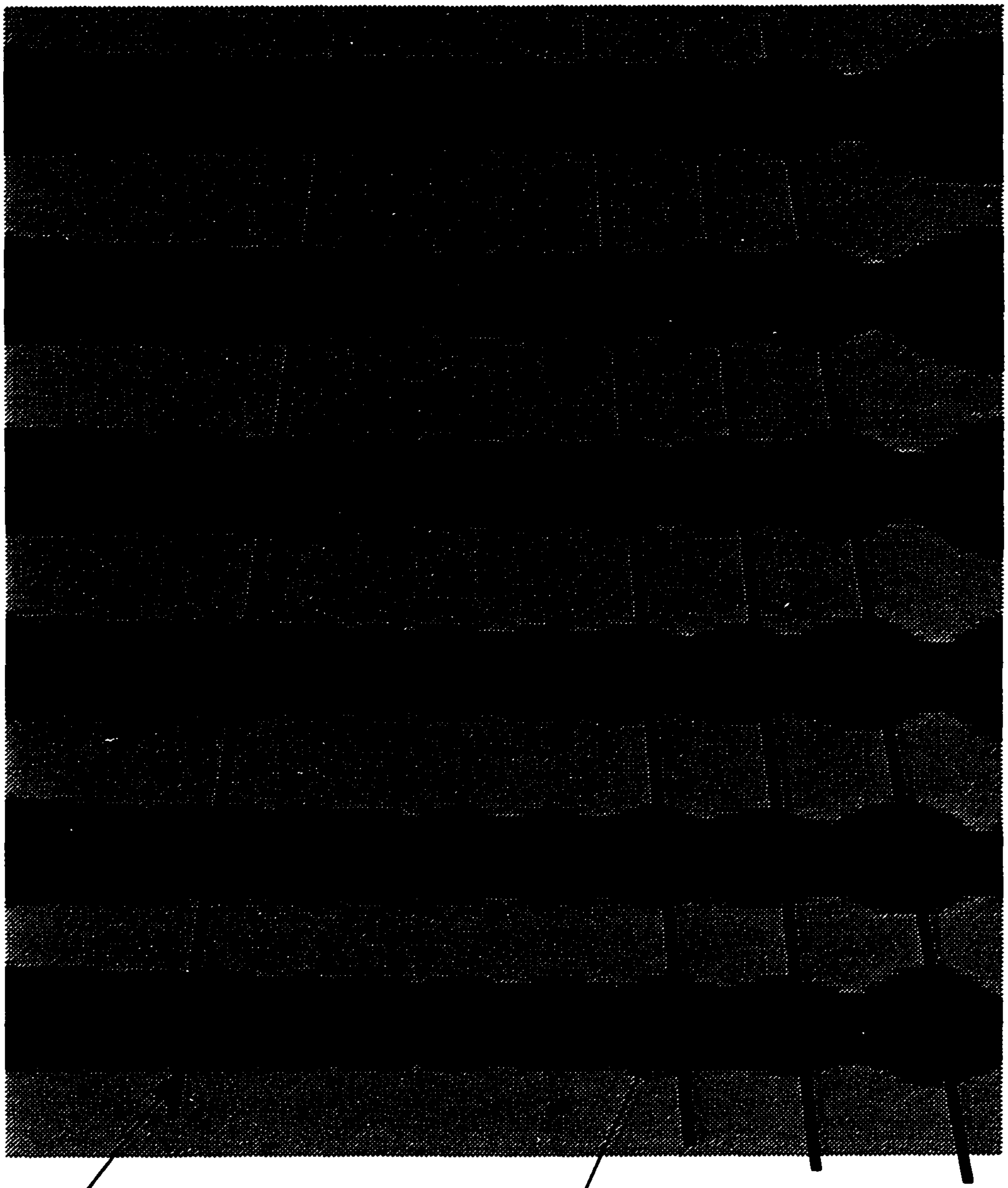

BACK END OF THE WAVE PACKET (TR AVELLING UPSTREAM)

ABSOLUTELY UNSTABLE WAVES WITH POSITIVE PHASE VELOCITY

Figure 1. Upstream propogating modes at Weber number below the critical

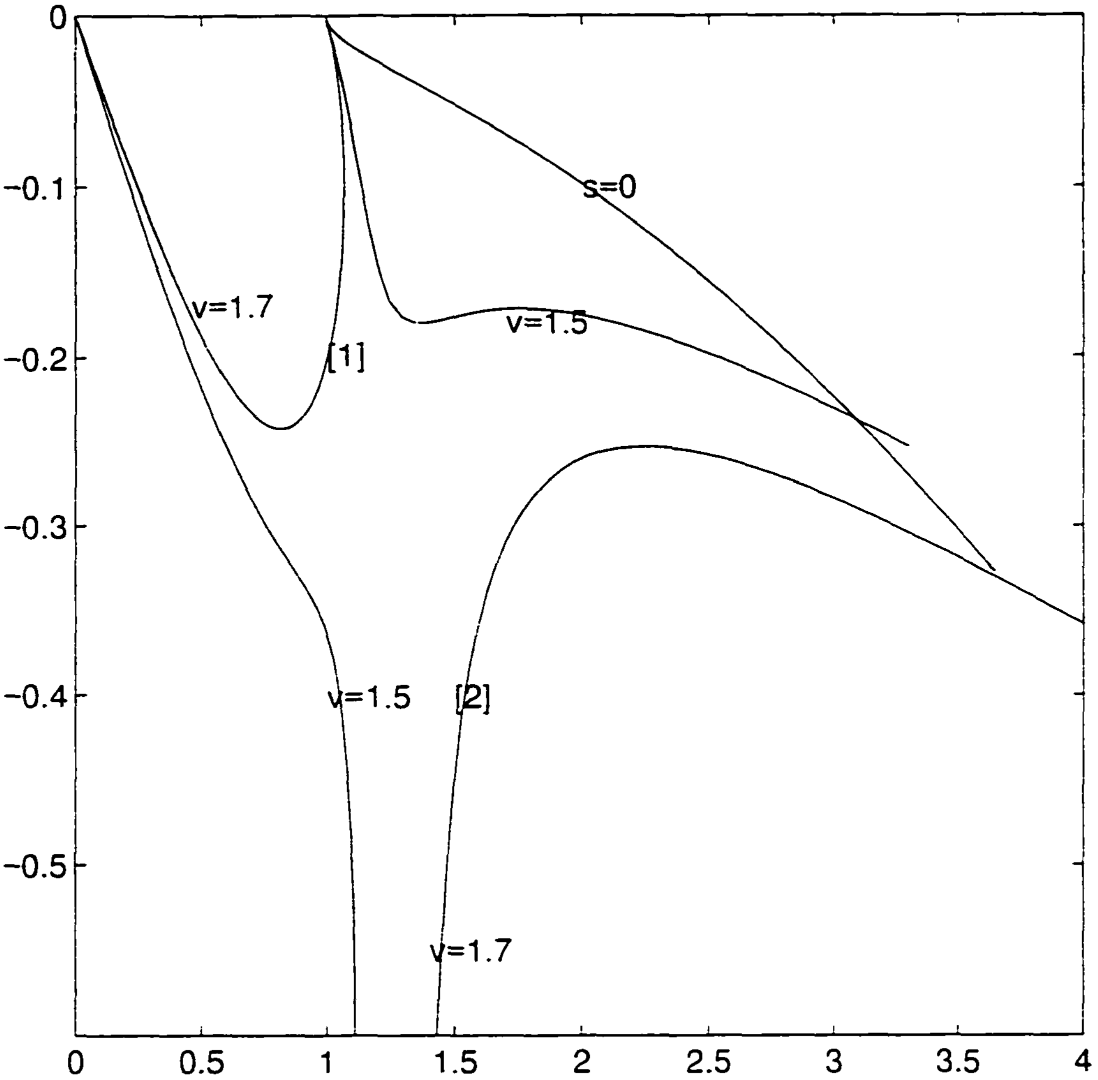

Figure 2. Plots of k(-iω) for a single jet

CHAPTER 7

CONCLUSIONS

A compound jet is unstable due to capillarity. We solved the spatial stability problem for an inviscid compound jet and the temporal problem for an inviscid and a viscous compound jet. The presence of two interfaces in the compound jet results in two growing modes in the temporal and also the spatial analysis.

In the temporal analysis, one of the modes grows exactly in phase, i.e., the two interfaces are in phase at all times and the other mode grows out of phase. The mode with in phase growth is called the stretching mode and the one with out of phase growth is called the squeezing mode. The stretching mode grows if the wavelength of the disturbances is longer than the inner circumference and the squeezing mode grows if the wavelength of the disturbances is longer than the outer circumference. The growth of the stretching mode is larger than the squeezing mode so it is expected to dominate the breakup dynamics. In the stretching mode, extrapolating the growth beyond the linear regime will result in the breakup of the core leading to drops of primary fluid in the secondary fluid. If the system continues to follow its pre-breakup dynamics, further non-linear stretching growth will finally cause rupture of film to form compound drops. In the squeezing mode when extrapolating the linear dynamics, either the film or the core can break first depending on the film thickness. In experiments, both modes grow and the one with the higher growth rate will dominate; it will become the observable mode at long times if the system is still in the linear regime. The growth rate of the stretching mode appears to be always higher, and so it dominates the long time, linear regime and presumably the breakup dynamics. On the other hand, the squeezing mode can cause breakup for very thin films. To see this note that, for film breakup in the squeezing mode, $|\zeta_2|+|\zeta_1| \sim \varepsilon$ and for the film breakup in stretching mode, $|\zeta_2-\zeta_1| \sim \varepsilon$. For the core to break in either mode, $|\zeta_1| \sim 1$. If the film is not thin, the stretching mode dominates and results in the formation of drops of the primary (core) fluid in the secondary (annular) fluid. If the linear dynamics persist the instability results in compound drops. If the fluids are inviscid, the wavelengths longer than the inner and the outer circumferences for the stretching and the squeezing modes respectively, result in undamped oscillations. This is expected because in the absence of viscosity the energy imparted to the system cannot be dissipated. Addition of viscosity results in reduction of growth rates for the waves that grow and cause the waves with wavelengths smaller than the critical value to decay. In the absence of any specific frequency disturbance the system is expected to follow the dynamics dictated by the fastest growing mode. The size of the drops that are produced by breakup scale as $1/k_{max}$ and the time taken for the jet to break scales as $1/s_{max}$, where s_{max} is the maximum temporal growth rate and k_{max} is the wave number corresponding to the maximum growth rate. Industrial applications require a good control on the breakup size and time scales. An appropriate choice of the system parameters can control these scales. This is of advantage in a compound jet because it possesses more manipulatable variables than the single jet. The system parameters that can be manipulated in a compound jet are the surface tension ratio of the outer interface and the inner interface, the viscosity ratio and the density ratio of the secondary and the primary fluids and the modified Reynolds number ($\mathbf{J} = \frac{\rho_1 \sigma_1 \mathbf{R}_1}{\mu_1^2}$). Of these the surface tension ratio has the most significant effect on k_{max} and s_{max}. In the limit of the viscosity ratio approaching zero and J approaching infinity the dispersion equation of the viscous compound jet reduces to the inviscid dispersion equation. As the film thickness goes to zero, the stretching mode solution reduces to the dispersion equation for a single jet with surface tension equal to the sum of the surface tension of the inner and the outer interfaces of the compound jet. The squeezing mode's growth rate goes as $\varepsilon^{1/2}$ ($\varepsilon=(R_2-R_1)/R_1$) in this limit for the inviscid jet and as ε^2 for the viscous compound jet. As the film thickness goes to infinity the squeezing mode disappears and the stretching mode approaches the Tomotika's solution of a single jet in an infinite liquid. As the wavelength of the disturbances tends to infinity the growth rate tends to zero because there is no pressure gradient to accelerate the fluid in the axial direction. In the inviscid long wave solution both the modes go linearly in k and in the viscous solution the stretching mode goes linearly and the squeezing mode goes as k^2. In an experiment, in general, both the stretching and the squeezing modes are present. However, if the initial disturbances applied to the compound jet are exactly out of phase and the amplitude ratio corresponds to the amplitude ratio for the squeezing mode, the compound jet always stays in the squeezing mode, i.e., the disturbances grow and the two interfaces are out of phase at all times. Similarly, if the initial disturbances are exactly in phase with amplitude ratio corresponding to the stretching mode, the jet always stays in the stretching mode. The temporal analysis is relevant in situations where the compound jet is stationary, i.e., it is like a compound thread. Such situations arise in context to liquid bridges, molding applications etc. In other situations where the jet issues out from a nozzle the spatial instability is the proper framework to analyze the problem.

In the spatial analysis the compound jet is modeled as a doubly infinite jet. The disturbances are introduced at z=0. The spatial analysis predicts that the positive half of the jet, i.e., downstream of the disturbance is unstable and the negative half is stable. The growth of the disturbances initiated at z=0 in the axial direction causes the compound jet to break to break into compound particles. The spatial analysis also shows the existence of two modes, one corresponding to each interface. The critical Strouhal number is approximately 1 and 1/a {a is the ratio of the outer to the inner radius} for the modes corresponding to the inner and the outer interfaces respectively. Once again the mode corresponding to the inner interface grows faster and is called the primary mode. The other mode is called the secondary mode. There is a maximum in the axial growth rates as a function of frequency for each mode. Thus, if a specific frequency disturbance is not applied at the nozzle exit, the system picks up all the frequencies and the one corresponding to the fastest spatial growth rate is the observable one. If the breakup dynamics follow the linear regime, the drop size will then scale as $1/k_{r,max}$ and the breakup length will scale as $1/k_{i,max}$ where $k_{i,max}$ is the maximum spatial growth and $k_{r,max}$ is the real part of the wave number corresponding to the maximum spatial growth. The growth rates of both the modes depend strongly on the Weber number. The rates increase on reducing the Weber number. In the limit of large Weber number the waves introduced at the nozzle exit grow and convect with the jet velocity. There is no dispersion and the motion of the waves in the axial direction is equivalent to a progression of a stationary jet in time in a Lagrangian frame. In this limit the spatial analysis predicts the same growth rates as the temporal analysis. The primary mode approaches the stretching mode and the secondary mode approaches the squeezing mode as the Weber number becomes large. Thus. the temporal analysis is relevant not only in the context of stationary threads but also in the context of fast moving jets which are frequently encountered in industrial applications. On lowering the Weber number below a critical value which depends on the system parameters the compound jet becomes absolutely unstable. Each mode has a different critical Weber number. In the absolutely unstable regime. i.e.. Weber number below the critical. there are three absolutely unstable modes. These three modes arise as a result of multiple intersections of the primary and the secondary modes with the evanescent modes. One of these three modes becomes absolutely stable at Weber numbers close to zero. The growth rates in time of the other two modes approach the maxima of the two temporal growing modes as the Weber number approaches zero. In this limit the absolutely unstable waves do not grow in space and their wavelength corresponds to the wavelength associated with the fastest growing temporal waves. The merging pattern of the primary and the secondary modes with the evanescent modes changes with the Weber number. The intersection with the highest absolute growth rate in time represents the dominant absolutely unstable mode. As mentioned above, there are three absolutely unstable modes and a different mode is dominant in different Weber number regimes. This gives rise to a discontinuity in the observable absolutely unstable characteristics. i.e.. the characteristics of the dominant mode. such as. the wavelength. phase velocity. and frequency, as a function of the Weber number. There is a significant difference between the wavelengths and the phase velocities of the fastest growing convective wave and the dominant absolutely unstable mode. atleast in certain Weber number regimes. This difference is important in an experiment designed to observe absolute instability. The conditions necessary to experimentally observe absolute instability in a compound jet coming out of a nozzle are: (1) $|k_i|R_1<<1$. where k_i is the maximum convective growth and R_1 is the inner radius of the compound jet. This insures that the jet breaks far away nozzle so there is a region in the axial direction where a transition from convective to absolute on reducing the Weber number. can be observed. (2)$1/\mathrm{Real}(s_a)<<R_1/V$, where s_a is the growth rate associated with the absolute instability and V is the jet velocity. This insures that once the exponential growth due to absolute instability breaks the jet. the time scales of the absolute instability are slower than the time scale of the formation of the jet so that the jet can form and be broken again by the absolute instability. This will result in an intermittent jet. The same conditions are needed for observing absolute instability in a single jet.

We solved the spatial instability problem in the Fourier Laplace domain and inverted the solution to real space time domain. The order of inversion of the solution from the Fourier Laplace domain is immaterial. The same results and the same criterion for determining if the system is stable, convectively unstable or absolutely unstable are obtained by first inverting the Fourier integral and then the Laplace (as done by Briggs) or first inverting the Laplace and then the Fourier integral.

The experimental setup designed in our lab superimposes a periodic perturbation on the base state of uniform flow of a single jet. We use the entire jet profile to measure the spatial growth rates and wavelengths as a function of the frequency imposed at the needle tip. This provides a more reliable measurement as compared to using the breakup length as a measure of the growth rate. It also shows that the experimental jet profile is in very good agreement with the predictions of the linear stability theory, even in regions close to the breakup. At high Weber numbers, the experimental results for the spatial growth rates and the wavelengths as a function of frequency are in good agreement with the spatial and the temporal predictions. In the intermediate Weber number regime, the theoretical predictions do not match the experimental data as closely because of the effect of gravity, which has not been accounted for in our model. A simple model based on uniform axial acceleration due to gravity, which contracts the jet diameter due to continuity matches the experimental jet profile near the nozzle, where the deviation from the base state is not significant. The jet is in a poiseuille flow inside the needle and relaxes to a plug flow in the air. Conservation of mass and momentum yields simple equations that predict the diameter and the velocity of the jet after it has relaxed to a plug flow. We also predict the distance that the jet travels before it is in a plug flow. The experimental data matches these predictions.

The breakup size of the jet, i.e., the drop size formed on breakup scales as $n^{-1/3}$, where n is the frequency of the applied disturbance. Controlling the amplitude of the disturbance applied at the needle tip can control the breakup length. The satellite formation can be avoided by applying a frequency greater than 0.7 times the critical frequency, i.e., the frequency beyond which the jet is stable. Thus, our system can be used to provide a continuous supply of uniformly sized drops of a given diameter at a given rate. Changing the frequency can change the drop size on the line, but the formation of satellites at lower frequencies restricts the size change to within a range of 10%.

At small jet velocities, the pattern of the jet breakup changes significantly. In the region near the breakup, we notice very short waves propagating upstream. They decay spatially as they travel upstream. The wavelength of these waves is close to the predicted wavelength of the absolutely unstable waves. The jet is expected to become absolutely unstable at small velocities and the presence of upstream propagating waves is consistent with the predictions of the absolute instability. Thus, this could be the experimental manifestation of absolute instability. However, these waves do not grow in time. In addition they persist at Weber numbers greater than the critical. This suggests that these waves are probably not the absolutely unstable waves. We believe that the breakup of the jet is still caused by the convective growth of the disturbances picked up at the needle tip. The breakup acts as a source of disturbance in a doubly infinite jet and release waves of all wavelengths. Some of these wavelengths have a negative phase velocity, hence, they propagate upstream. Numerical simulations reveal that these upstream propagating waves decay spatially. Thus the waves with the slowest decay rate will be observed in the experiment. The minimum decay rate increases with an increase in Weber number and hence, these waves are not observable at high velocities. But, the theoretical prediction of the wavelength of these disturbances is not close to the experimental value.

We do not see any further changes in the breakup pattern on reducing the Weber number below the critical value. Thus we do not see the absolute instability in our experiments. This could be attributed to a variety of reasons: Firstly, the backward propagating waves that we observe could be the absolutely unstable waves. These waves might be nonlinearly stable and hence they do not grow in time. The theoretical prediction of the critical Weber number might not be accurate enough and hence these waves persist at Weber numbers higher than the predicted critical Weber number. Secondly, in our analysis we neglect the effect of gravity. The gravity become increasingly important at lower Weber numbers. The effect of gravity is to accelerate the jet velocity and this could possibly increase the Weber number beyond the critical. Thirdly, at small Weber numbers, the liquid starts to drip out of the needle. The predicted critical velocity for transition to absolute instability is above the dripping velocity but the theoretical prediction might not be very accurate and the actual critical velocity could be below the velocity at which dripping starts. In that case the absolute instability cannot be observed.

BIBLIOGRAPHY

(1) Bechtel, S. E.; Carlson, C. D.; Forest, M. G. *Phys. Fluids* **1995**, *7*, 2956-2971.

(2) Berger, S. A. *SIAM J. Appl. MATH* **1988**, *48*, 973-991.

(3) Bogy, D. B. *Phys. Fluids* **1978**, *21*, 190.

(4) Bogy, D. B. *Annu. Rev. Fluid Mech.* **1979**, *11*, 207-228.

(5) Briggs, R. J. *Electron Stream Interaction with Plasmas*; MIT Press: Cambridge, MA, 1964.

(6) Chandrasekhar, S. *Hydrodynamic and Hydromagnetic Stability*; Dover: New York, 1961.

(7) Chaudhary, K. C.; Maxworthy, T. *J. Fluid Mech.* **1980a**, *96*, 275-286.

(8) Chaudhary, K. C.; Maxworthy, T. *J. Fluid Mech.* **1980b**, *96*, 287-297.

(9) Chaudhary, K. C.; Redekopp, L. G. *J. Fluid Mech.* **1980**, *96*, 257-274.

(10) Chauhan, A.; Maldarelli, C.; Rumschitzki, D.; Papageorgiou, D. T. *Rheol. Acta.* **1996**, *35*.

(11) Cooper, A. J.; Carpenter, P. W. *Journal of Fluid Mechanics* **1997**, *350*, 261-270.

(12) Donnelly, R. J.; Glaberson, W. *Proc. Roy. Soc. Lond.* **1966**, *A 290*. 547-556.

(13) Eggers, J.; Dupont , T. F. *J. Fluid Mech.* **1994**, *262*, 205-221.

(14) Epikhin, V. E.; Shkadov, V. Y. *Fluid Dynam.* **1978**, *13*. 50-59.

(15) Felderhof. B. U. *J. Chem. Phys.* **1968**, *49*. 44-51.

(16) Goedde, E. F.; Yuen. M. C. *J. Fluid Mech.* **1970**, *33*. 151.

(17) Hertz. C. H.; Hermanrud. B. *J. Fluid Mech* **1983**, *131*. 271-287.

(18) Hertzberg, L. A.; Sweet, R. G.; Herzberg, L. A. *Sci. Am.* **1976**, *234*. 97.

(19) Kamenov. O.; Radev. S. *Theor. Appl. Mech. (in Bulgarian)* **1987**. *18*, 44-53.

(20) Kamenov. O.; Radev. S. *Theor. Appl. Mech.* **1988**, *18*. 44-53.

(21) Keller. J. B.; Rubinow. S. L.; Tu. Y. O. *Phys. Fluids* **1973**. *16*. 2052-2055.

(22) Kowalewski. T. A. *Fluid Dynamics Research* **1996**. *17*. 121-145.

(23) Lafrance, P. *Phys. Fluids* **1975**, *18*. 428.

(24) Lee, H. C. *IBM J. Res. Dev.* **1974**. *18*. 364-369.

(25) Lee. L. S.; Morris. P. J. *Journal of Propulsion and Power* **1997**. *13*. 763-767.

(26) Leib, S. J.; Goldstein. M. E. *Phys. Fluids* **1986**. *29*. 952-954.

(27) Leib, S. J.; Goldstein. M. E. *J. Fluid Mech.* **1986**. *168*. 479-500.

(28) Li, H. S.; Kelly, R. E. *Physics of Fluids* **1997**, *9*, 1273-1276.

(29) Lim, D. W.; Redekopp, L. G. *European Journal of Mechanics B - Fluids* **1998**, *17*, 165-185.

(30) Lin, S. P.; Lian, Z. W. *Phys. Fluids* **1989**, 490-493.

(31) Lingwood, R. J. *Journal of Fluid Mechanics* **1996**, *314*, 373-405.

(32) Lingwood, R. J. *Journal of Fluid Mechanics* **1997**, *331*, 405-428.

(33) Lingwood, R. J. *Physics of Fluids* **1997**, *9*, 1317-1328.

(34) Monkewitz, P. A. *European Journal of Mechanics B - Fluids* **1990**, *9*, 395-413.

(35) Nayfeh, A. H. *Phys. Fluids* **1970**, *13*, 841.

(36) Ogura, K.; Ali, M. M.; Miname, K.; Watanabe, S. A. O. *Journal of the physical society of Japan* **1992**, *61*, 4022-4032.

(37) Papageorgiou, D. T. "Analytical description of the breakup of liquid jets in air." ICASE. 1993.

(38) Pimbley, W. T. *IBM J. Res. Dev.* **1976**, *20*, 148-156.

(39) Pimbley, W. T.; Lee, H. C. *IBM J. Res. Dev.* **1977**, *21*, 21-30.

(40) Prosperetti, A. *J. Fluid Mech.* **1980**, *100*, 333-347.

(41) Radev, S.; Shkadov, V. *Theor. Appl. Mech.* **1985**, *16*, 68-75.

(42) Radev, S.; Tchavdarov, B. *Int. J. Multiphase Flow* **1988**, *14*, 67-69.

(43) Rayleigh, L. *Proc. Lond. Math. Soc.* **1879**, *10*, 4-13.

(44) Rutland, D. F.; Jameson, G. J. *Chem. Eng. Sci.* **1970**, *25*, 1689.

(45) Rutland, D. F.; Jameson, G. J. *J. Fluid Mech.* **1971**, *46*, 267.

(46) Sanz, A.; Masseguer, J. *J. Fluid Mech.* **1985**, *159*, 55-68.

(47) Schulkes, R. M. S. M. *J. Fluid Mech.* **1993**, *250*, 635-650.

(48) Shkadov, V. Y.; Sisoev, G. M. *J. Multiphase Flow* **1996**, 363-377.

(49) Shugai, G. A.; Yakubenko, P. A. *Physics of Fluids* **1997**, *9*, 1928-1932.

(50) Sweet, R. G. *Stanford Univ. Tech. Rep.* **1964**, *1722*.

(51) Taub, H. H. *Phys. Fluids* **1976**, *19*, 1124-1129.

(52) Taylor, G. I. *Proc Roy Soc A* **1959**, *253*, 296-312.

(53) Teng, C. H.; Lin, S. P.; Jn, C. *Journal of Fluid Mechanics* **1997**, *332*.

(54) Ting, L.; Keller, J. B. *SIAM J. Appl. Math.* **1990**, *50*, 1533.

(55) Tomotika, S. *Proc. R. Soc. London* **1935**, *A 150*. 322-337.

(56) Triantafyllou, G. S. *Physics of Fluids A- Fluid Dynamics* **1992**, *4*, 277-282.

(57) Tsamopoulos, J.; Poslinski, A.; Ryan, M. *J. Fluid Mech.* **1988**, *197*, 523-549.

(58) Tsampret, A.; Steinberg, V. *Europhysics Letters* **1991**, *14*, 331-336.

(59) Vihinen, I.; Honohan, A. M.; Lin, S. P. *Physics of Fluids* **1997**, *9*, 3117-3119.

(60) Wang, D. P. *J. Fluid Mech.* **1968**, *34*, 299.

(61) Yakunenko, P. A. *Eur. J. Mech., B/Fluids* **1995**, *6*, 823-830.

(62) Yarin, A. L. *Free liquid jets and films: hydrodynamic and rheology*; Longman Sci. and Tech.: Essex, 1993.

(63) Yuen, M. C. *J. Fluid Mech.* **1968**, *33*, 151.

IMAGE EVALUATION TEST TARGET (QA-3)

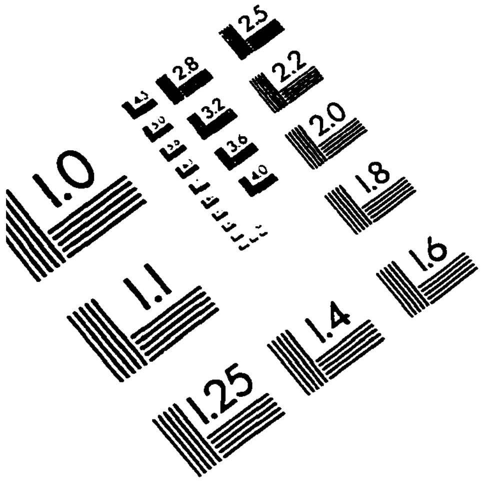

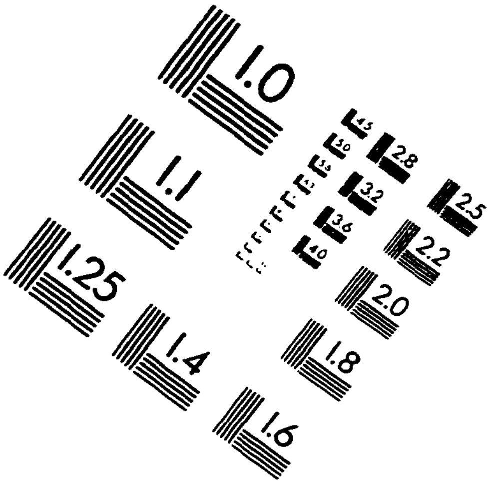

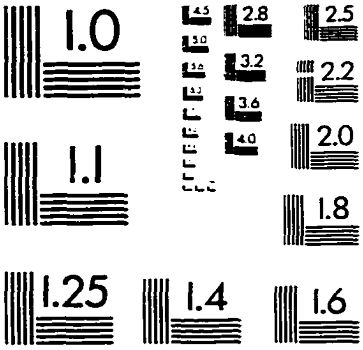

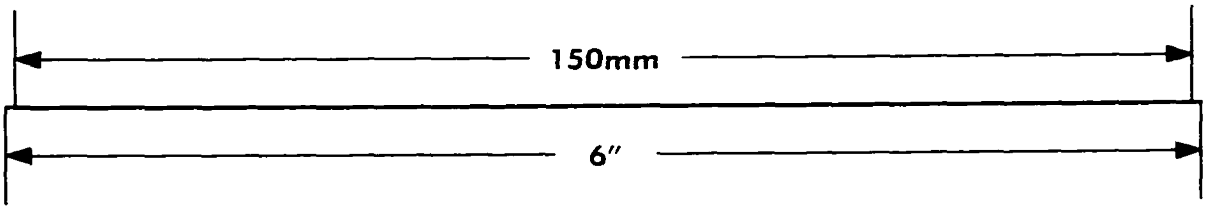

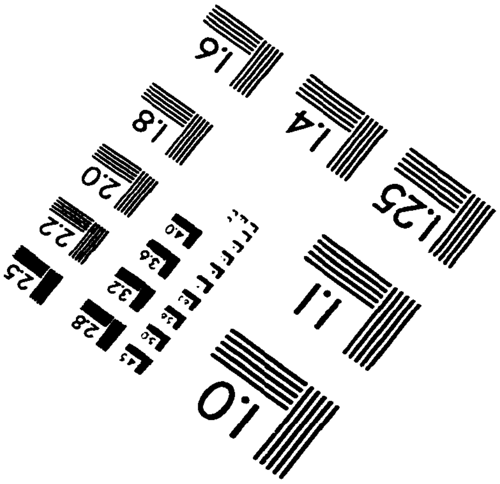

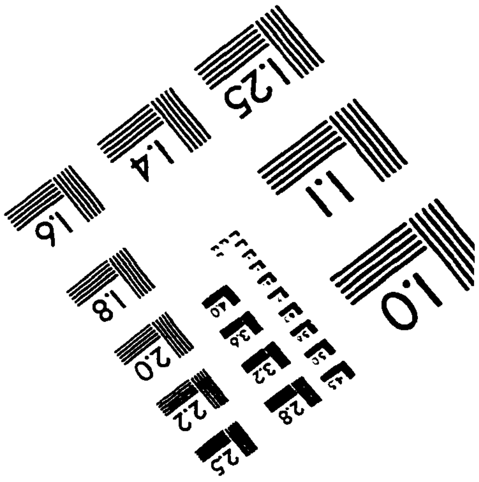

APPLIED IMAGE . Inc
1653 East Main Street
Rochester, NY 14609 USA
Phone: 716/482-0300
Fax: 716/288-5989